Joint Positioning and Multipath Radio Channel Estimation and Prediction

Mannesson, Anders

2016

Document Version:
Publisher's PDF, also known as Version of record

Joint Positioning and Multipath Radio Channel Estimation and Prediction

Anders Mannesson

LUND
UNIVERSITY

Department of Automatic Control

Ph.D. Thesis
ISRN LUTFD2/TFRT--1113--SE
ISBN 978-91-7623-713-7 (print)
ISBN 978-91-7623-714-4 (web)
ISSN 0280–5316

Department of Automatic Control
Lund University
Box 118
SE-221 00 LUND
Sweden

Printed in Sweden by Holmbergs i Malmö AB.
Lund 2016

Till Julia, Folke
och Yngve

Abstract

This thesis investigates the topic of joint positioning and radio channel estimation and prediction. Both positioning and radio channel estimation have a long history of research with many publications but the combination of the two has so far at large been left unexplored. The reason for studying this topic is twofold: improvement of positioning and improvement of radio channel prediction. Positioning is of interest in many situations, such as, e.g., localization in an unknown environment. Better radio channel estimates and prediction enable improved transmission rates with fewer lost data packages in wireless networks. In this thesis, both areas are covered with analysis and simulations and the improvement in positioning performance is also demonstrated with measurements from experiments.

A well established approach for positioning is using an inertial measurement unit (IMU) which contains sensors measuring, e.g., acceleration and angular velocity. Due to noise in the sensors, the dead reckoning performance of the stand-alone unit is quickly degraded. The degradation has previously been combated by fusing the accelerometer and gyroscope signals with other sensor information such as GPS or wheel encoders in order to correct for the errors of the IMU. This is achieved by establishing a model that combines the information from the sensors. In this thesis, such a model is established between the accelerometer and gyroscope readings and the radio channel estimates obtained from pilot signals transmitted in a wireless network. The transfer characteristics of the narrowband radio channel are described with multipath components, where amplitude and angle of arrival are associated with each component. Since it is believed that the performance of the solution is greatly affected by imperfections in the receiver, its frequency error is also included in the modeled.

The joint model is estimated using Bayesian methods, suitable for nonlinear systems. By simultaneously estimating the variables of the multipath components, the frequency error, and the location of the receiver, it is shown that the positioning performance using an IMU, with similar quality found in a modern day cellular phone, can be greatly improved. Since all the sig-

nals needed are present in a typical cellular phone, the proposed solution does not require any extra infrastructure. Both simulations and experiments show that the technique has a potential to give a breakthrough in positioning performance using low-cost inertial measurement units.

With the established model, the variables that describe the future radio channel can also be predicted. By knowing beforehand what signal reception the cellular phone can expect, the transmissions can be adjusted in terms of modulation and transmission power to suit the future channel condition that occurs at the moment when the transmission is received. This is commonly known as link adaptation. Simulations show that the data transmission rates to the end user can be greatly improved in communication systems such as the LTE system.

The thesis also includes an investigation of performance bounds that extends previously known results for the angle of arrival estimation problem and also contributions to joint estimation of angle of arrival and frequency error estimation. These results give an intuitive understanding of how the receiver's trajectory of movement impacts the accuracy achievable when estimating the local radio channel landscape. In mathematical terms this can be stated as that the space-time moments of the trajectory determine the Cramér-Rao lower bound of the variables for joint estimation of angle of arrival and frequency error.

Acknowledgments

So, my journey as a Ph.D. student at the Department of Automatic Control has now reached its final destination. As I joined the department, after spending a few years in industry, coming back to the university was not the obvious career move to make. However, in retrospect, I am thankful that I did. During a night while listening to swing music, my friend and now also my colleague, Anton Cervin encouraged me to apply for an open position as a Ph.D. student at the department. I was a bit reluctant to join at first, but after a few persuading phone calls from former administrator Eva Schildt, I was convinced. During one of the first meetings at the department, I was introduced to Bo Bernhardsson, who would become my main supervisor. Bo, your contribution in terms of support and guidance to the final work is incalculable. You have always taken the time to explain difficult topics in a nice and elegant way, making everything easier to understand. Your enthusiasm for the subject, your broad knowledge, and your humor are invaluable sources for a Ph.D. student and I am truly grateful for you being my supervisor during these years. You also introduced me to my second supervisor, Fredrik Tufvesson from the EIT department. I want to thank you Fredrik for making me and Bo aware of the interesting and challenging core ideas for this project. I also highly value your knowledge of radio systems and radio channel modeling which has helped me in this work. I also want to thank you for all comments and feedback on my work and for making the equipment I have used for the experiments available. I have also enjoyed working with Atif Yaqoob, also from the EIT department. Thank you for sharing your ideas and comments, knowledge of the equipment, and also for being a great travel company a couple of times.

During my studies I have had the honor of working at a great department. To all my present and former colleagues I want to say thank you for making this department a fantastic workplace with a friendly and open atmosphere. Among the Ph.D. students, I specifically want to send special thanks to Karl Berntorp, Jerker Nordh, and Jacob Antonsson for sharing the same research interest and together we have had many inspiring dis-

cussions. I also want to thank Erik Johannesson, Martin Hast, and Jonas Dürango for making lunch and coffee breaks enjoyable and memorable. Ola Johnsson deserve a special thanks for proof reading parts of this thesis. Without your help, the end result would have been far less readable. For computer support, I acknowledge Anders Nilsson and Anders Blomdell and a special thanks goes to Leif Andersson; having a true LaTeX typesetting wizard next door is a great resource when preparing a document like this.

Finally, I would like to thank my friends, parents, and brothers for always believing in me and encouraging me in my work. And lastly but most importantly; all my love and gratitude goes to my amazing wife Julia and our son Folke. Without your love, support, and understanding this work would never have been possible.

Financial Support

I acknowledge the following for financial support: Vetenskapsrådet through the project 621-2012-4969, the Swedish Research Council through the LCCC Linnaeus Center, and VINNOVA through the ELLIIT Excellence Center.

Contents

1. Introduction **13**
- 1.1 The Radio Channel . . . 13
- 1.2 Positioning . . . 16
- 1.3 Joint Position and Radio Channel Estimation . . . 20
- 1.4 Publications . . . 23
- 1.5 Outline . . . 25

2. Radio Channel Modeling **26**
- 2.1 MIMO Communication Systems . . . 26
- 2.2 MIMO Radio Channel Model . . . 27
- 2.3 Cluster Modeling . . . 39
- 2.4 Receiver Imperfections Modeling . . . 41
- 2.5 Summary . . . 43

3. Joint Radio Channel and Position State-Space Model **44**
- 3.1 Inertial Measurement Unit . . . 44
- 3.2 Kinematic Modeling . . . 47
- 3.3 Joint Radio Channel and Kinematic Modeling . . . 50

4. Nonlinear Estimation Techniques **54**
- 4.1 Recursive State-Space Estimation . . . 55
- 4.2 Angle of Arrival Estimation . . . 62

5. Fundamental Performance Bounds **79**
- 5.1 Cramér-Rao Lower Bound for Space-Time Arrays . . . 81
- 5.2 Worst-case-optimal Array Configurations . . . 88
- 5.3 Sensitivity Analysis . . . 95
- 5.4 Recursive Cramér-Rao Lower Bound . . . 101

6. Joint Positioning and Radio Channel Estimation **106**
- 6.1 Simulations for SISO Configuration . . . 108
- 6.2 Simulations for MIMO Configuration . . . 110
- 6.3 Summary and Discussion . . . 118

7. Positioning Experiments **121**
7.1 Hardware 121
7.2 Data Gathering 124
7.3 Experiment Results and Analysis 128
7.4 Discussion 130
8. Link Adaptation **133**
8.1 Introduction 133
8.2 System Overview 134
8.3 Particle CQI Prediction 136
8.4 Simulations 140
9. Summary and Conclusions **151**
9.1 Directions for Future Work 153
Bibliography **155**
A. The Particle Filter **164**
B. Information Matrices for Multiple Components **167**
B.1 Fisher Information Matrix for Multiple Components 167
B.2 Hybrid Information Matrix for Multiple Components . . . 169

Nomenclature

Nomenclature	**Description**
$\mathrm{Re}\{\cdot\}$	Real part
$\mathrm{Im}\{\cdot\}$	Imaginary part
$\mathbb{R}$	Real numbers
$\mathbb{R}^n$	Real-valued column vectors of length n
$\mathbb{R}^{n\times m}$	Real-valued matrices of dimension $n \times m$
$\mathbb{C}$	Complex numbers
$\mathbb{C}^n$	Complex-valued column vectors of length n
$\mathbb{C}^{n\times m}$	Complex-valued matrices of dimension $n \times m$
$\mathbf{I}_n$	The identity matrix of size $n \times n$
$\exp\{\cdot\}$	Exponentiation
$\langle \cdot, \cdot \rangle$	Scalar product
$\otimes$	Kronecker product
$\lvert \cdot \rvert$	Matrix determinant
$\lVert \cdot \rVert$	Euclidean norm
$\lVert \cdot \rVert_F$	Frobenius norm
$(\cdot)^T$	Matrix transpose
$(\cdot)^*$	Matrix Hermitian transpose
$\mathrm{vec}\{\cdot\}$	Matrix vectorization
$\mathrm{tr}\{\cdot\}$	Matrix trace
$\mathcal{N}(m, \sigma^2)$	Normal distribution with mean m and variance σ^2
$\mathcal{CN}(m, \sigma^2)$	Circular symmetric complex Gaussian distribution with mean m and variance σ^2
$\mathcal{U}(a, b)$	Uniform distribution between a and b
$\mathbb{E}\{\cdot\}$	Expectancy operator

Throughout this thesis scalars are denoted by lower case italic symbols, vectors by lower case boldface italic symbols, and matrices with upper case boldface symbols.

Abbreviation	**Description**
AoA	Angle of Arrival
AWGN	Additive White Gaussian Noise
BLER	BLock Error Rate
CRLB	Cramér-Rao Lower Bound
CQI	Channel Quality Indicator
EKF	Extended Kalman Filter
eNB	e-Node B
GPS	Global Positioning System
H-ARQ	Hybrid Automatic Repeat Request
IMU	Inertial Measurement Unit
INS	Inertial Navigation System
LOS	Line-Of-Sight
LTE	Long-Term Evolution
LTV	Linear Time Variant
LUT	Look-Up Table
MEMS	MicroElectroMechanical System
MIMO	Multiple-Input Multiple-Output
MMSE	Minimum Mean Square Error
MPC	MultiPath Component
NLOS	Non Line-Of-Sight
OFDM	Orthogonal Frequency Division Multiplexing
RMSE	Root Mean Square Error
RSS	Received Signal Strength
RX	Receiver
SBL	Sparse Bayesian Learning
SINR	Single to Interference and Noise Ratio
SISO	Single-Input Single-Output
SLAM	Simultaneous Localization And Mapping
SNR	Signal to Noise Ratio
TDOA	Time Difference Of Arrival
TOA	Time Of Arrival
TX	Transmitter
UE	User Equipment
UKF	Unscented Kalman Filter
UWB	Ultra-WideBand

1

Introduction

This thesis investigates the topic of joint estimation and tracking of a radio receiver's position and the radio channel. The underlying concept of the work is fusion of information from different sensors by using statistical estimation algorithms and models. Both positioning and radio channel estimation are topics with a long history of research but the combination of the two areas is at large unexplored. There are two motives for exploring this field: to enable long-term positioning and to improve radio channel prediction. Positioning is of great interest in many scenarios, e.g., localization in an unknown environment. Reliable and accurate radio channel prediction can significantly increase the rate at which application data can be transmitted to the end user in a wireless network. At the same time the frequency spectrum is used more efficiently. This thesis describes the background, investigates suitable algorithms, and analyzes the performance of what can be achieved when position and radio channel estimates are combined and jointly estimated.

1.1 The Radio Channel

In radio communication, the transmission medium between the transmitter (TX) and the receiver (RX) can be modeled as a linear time variant (LTV) system which is called *the radio channel*. The radio channel is a description of the propagation properties such as attenuation and scattering of the transmitted signal along the propagation path. The propagation properties are determined by the physical surroundings, e.g., buildings and the landscape.

One way of representing the radio channel is in the time-frequency domain. In Figure 1.1, an example of the magnitude of the transfer function is shown as a function of time and frequency. As seen there, the channel changes over time as well as over frequency. There are regions of the channel that are strong, which correspond to good reception at the receiver. But there

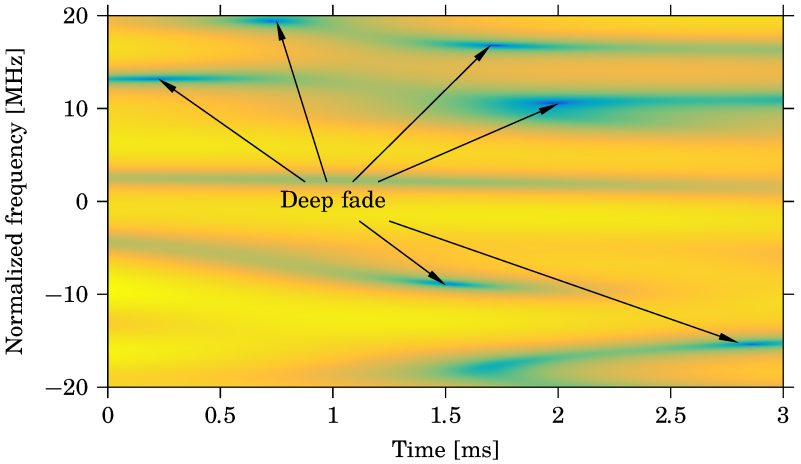

Figure 1.1 The magnitude of the channel frequency response as a function of time and frequency. Light colors indicate strong channel conditions while dark colors indicate fading dips.

are also some parts with fading dips in the magnitude transfer function. These dips correspond to bad reception at the receiver. The origin of the pattern can be described by *multipath wave propagation* and the origin of the multipath components (MPC) can be explained by four phenomena: reflection, transmission, diffraction, and scattering [Molisch, 2005]. Which of the four phenomena that an object causes depends on the material and size of the object compared to the wavelength of the radio wave. When the object is much larger than the wavelength, the major energy of the impinging radio wave is typically reflected by the object. In which direction and to what amount the energy is reflected depends — amongst other things — on the material of the obstacle, the wavelength, and the polarization. When a wave hits an edge of an object, diffraction occurs, i.e., the radio waves bend around the object according to the Huygens-Fresnel principle. The fourth phenomenon, scattering, occurs when the wave hits an irregular surface and energy is scattered in all directions.

Due to these phenomena, multiple time-shifted multipath components of the transmitted signal reach the receiver unit. The scenario is illustrated in Figure 1.2 where there are three MPCs reaching the receiver from different directions. 'MPC 1' is the line-of-sight (LOS) path between the TX and the RX while 'MPC 2' and 'MPC 3' are both scattered by nearby buildings. If the time duration of the transmitted signal is larger than the difference in time it takes for all components to reach the receiver the components add up, constructively or destructively, at the receiver. This scenario is usually

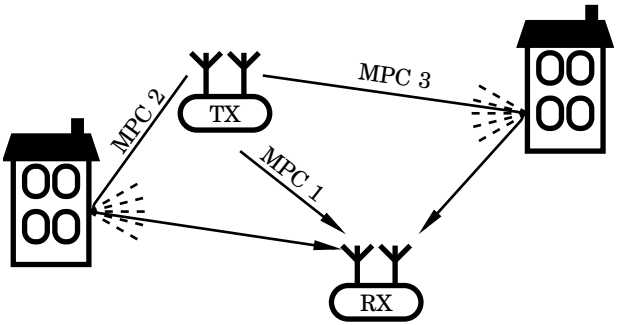

Figure 1.2 A multipath environment where the TX communicates with the RX over a wireless link. The transmitted signal reaches the receiver through a direct path, 'MPC 1', and also via two scattered components, 'MPC 2' and 'MPC 3'. Note that both units are equipped with two antennas each. Also note that in a system where both units communicate with each other, the roles of TX and RX are constantly switched.

referred to as *narrowband* [Molisch, 2005]. Since the interference pattern is dependent on the amplitude and phase of each component at the point of interference, the pattern becomes dependent on the physical location of the receiver unit. Hence, the received signal strength will fluctuate as the receiver is moved. This is what could be seen in Figure 1.1 and the effect is commonly referred to as *small scale fading* as opposed to large scale fading which is related to shadowing and absorption loss due to physical obstacles such as building or dense vegetation [Molisch, 2005]. The relationship between the transfer function of the radio channel and the location of the receiver will be established in Chapter 2.

Channel Estimation Using Pilots

Since the radio channel alters the amplitude and phase of the transmitted signal, the decoding of the received signal would be unsuccessful if no measures were taken to cancel the impact of the channel. Hence, most efficient modern communication systems rely on *channel estimation* [Paulraj et al., 2003]. One way of obtaining the channel estimates is by using training sequences or *pilots*. The pilot is a predetermined symbol or symbol sequence inserted in the transmitted data stream. The pilot symbols are extracted from the received data stream and treated separately in the receiver in order to obtain a channel estimate. The principle of a pilot-based communication system is shown in Figure 1.3. Consider for example a time-frequency communication system where multiple symbols can be transmitted simultaneously on orthogonal subcarriers. This is known as an *orthogonal frequency division multiplexing* (OFDM) system and a commercial application of this

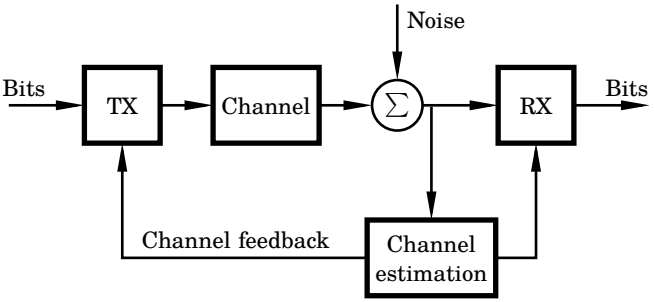

Figure 1.3 Data transmission in a pilot-based communication system where the channel estimates are extracted and used by the receiver and also communicated back to the transmitter for link adaptation.

is the 3GPP LTE system [3GPP, 2016a; Ghosh et al., 2011]. In such a system, the pilots are inserted in both time and frequency as seen in Figure 1.4 where one subframe consisting of 14 symbols and 12 subcarriers is depicted. The channel estimate obtained from the pilot signal is valid for that specific time slot and subcarrier it was transmitted on. If the channel does not change too rapidly in time and frequency, the channel estimates can be used for transmissions close to the pilot symbol.

The second usage area of the channel estimates is *link adaptation* [Goldsmith and Chua, 1998]. Modern communication systems employ coding to transform bits into symbols which are then transmitted. By changing the number of bits per symbol, the number of error coding bits inserted, the signal strength, and also the number of parallel data streams, the amount of transmitted user data can be adjusted. The likelihood for the receiver to successfully decode the received data is dependent on the current channel quality. If the transmitter can adapt the next transmission to the quality of the channel that applies during transmission, the likelihood is increased and the data does not have to be re-transmitted. Since there is an inevitable delay between the time instant the channel estimate is obtained and the next transmission, a predicted channel estimate should be used to adapt the link properties for future transmissions. Channel prediction and link adaptation will be further examined in Chapter 8.

1.2 Positioning

Positioning and orientation relative to a fixed frame is one of the ingredients in navigation and device tracking. The other part in navigation is the map, which is usually thought of as a representation of the physical surroundings but it could just as well be a description of the surroundings as seen by a

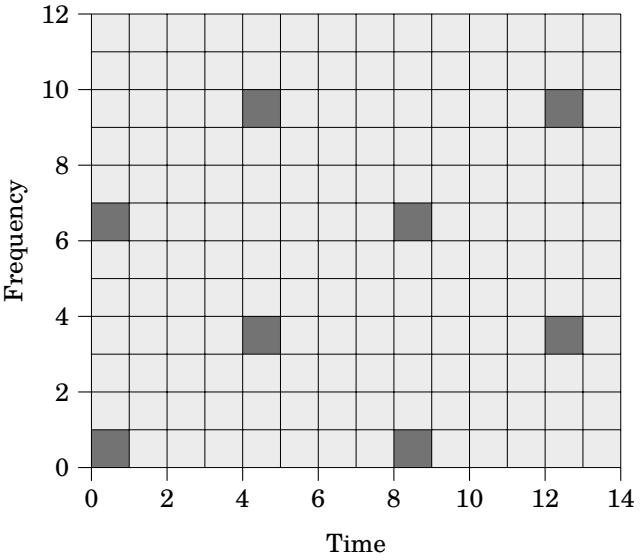

Figure 1.4 The typical pilot scheme in an LTE subframe. A subframe consists of two slots with 14 symbols in total and 12 subcarriers. The duration of the subframe is 1 ms with a total bandwidth of 180 kHz. The dark squares mark where the pilot symbols are inserted.

sensor. In some situations, the map is known beforehand and can be used for improving the localization of the unit. However, if the map is unknown, it needs to be constructed at the same time as the positioning is performed. This problem is called simultaneous localization and mapping (SLAM) and has been studied thoroughly in the literature over the last years [Bailey and Durrant-Whyte, 2006a; Bailey and Durrant-Whyte, 2006b; Davison, 2003].

With the development of microelectromechanical systems (MEMS) accelerometers and gyroscopes, which are the key components of an inertial measurement unit (IMU), are today small and inexpensive. An accelerometer measures proper acceleration of the device while the gyroscope measures the angular velocity. The price for an IMU ranges from $1 to several $1000 for high-precision units. The expensive ones exhibit lower noise levels in general compared to the inexpensive ones and they may also include software and other sensors on the board, e.g., magnetometers for measuring the magnetic field. Also, the size and power consumption differ between different IMUs.

An IMU can be used for building an inertial navigation system (INS), able to measure relative position [Titterton and Weston, 2004]. Due to its simplicity, a tempting solution for positioning using an IMU is the dead reck-

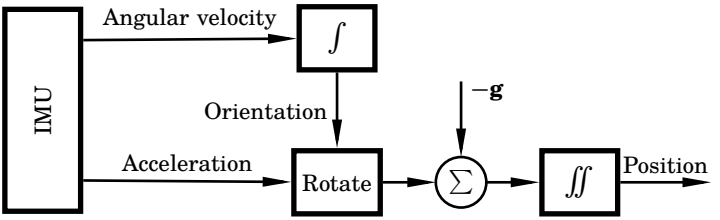

Figure 1.5 An IMU-based navigation system. The gyroscope signal is integrated once to obtain the orientation with respect to the initial orientation of the device. The accelerometer signal is then rotated using the estimated orientation before gravity is canceled. The position is obtained by double integration of the residual acceleration. Due to the integrators, the position estimates will be correlated in time.

oning approach depicted in Figure 1.5. Gyroscope readings are integrated once in order to obtain the orientation of the device. The accelerometer readings are then rotated based on the knowledge of the orientation of the device before gravity is canceled and double integration then yields the position. Such a system however fails to deliver good performance for any longer period of time due to noise and imperfections inherent in the IMU. Since the noise is integrated, the variance of the estimated position grows unboundedly. Also, constant offsets or biases in the signals will keep adding up to the orientation and position leading to an ever increasing estimation error.

Depending on noise and bias levels, the IMUs are usually classified into different grades. Common names for these grades are consumer, industrial, and tactical grade. Consumer grade IMUs are found in cellular phones and other consumer products, industrial grade IMUs can be used for enabling detailed motion capture in, e.g., robotics while the tactical grade IMUs are the most expensive and found in, e.g., high-precision weapons. In Figure 1.6, the typical dead reckoning position error using an IMU from each class is shown. The noise values used for simulations are presented in Table 1.1. The noise processes of the IMU will be further explained in Section 3.1.

The performance of the accelerometers is improved a factor or two comparing the consumer grade and the tactical grade IMU while the performance of the gyroscope is improved 100 times, see Table 1.1. The conclusion is that the rapid growth of the position error as seen in Figure 1.6 is mainly due to accumulation of gyroscope noise. The accumulated gyroscope noise translates to an incorrect orientation estimation of the device and thereby also an inability to cancel the contribution from gravity present in the accelerometer signals. Hence, the IMU needs other sensor information in order to be able to estimate orientation and position for any longer period of time.

Table 1.1 Noise level for the accelerometer and the gyroscope for three different IMU grades. The bias stability time is defined as the time when the contribution from the angle random walk noise process is exceeded by the contribution from the angle bias stability noise process. The values for the different grades are approximative and correspond to products available on the public market as of 2016 [Phidgets, 2016; Xsens, 2016; Systron, 2016].

	Consumer	**Industrial**	**Tactical**
Velocity random walk [m/s/$\sqrt{\text{h}}$]	0.1	0.07	0.05
Angle random walk [deg/$\sqrt{\text{h}}$]	2	0.5	0.02
Angle bias stability [deg/h]	20	10	1
Stability time [s]	300	120	60

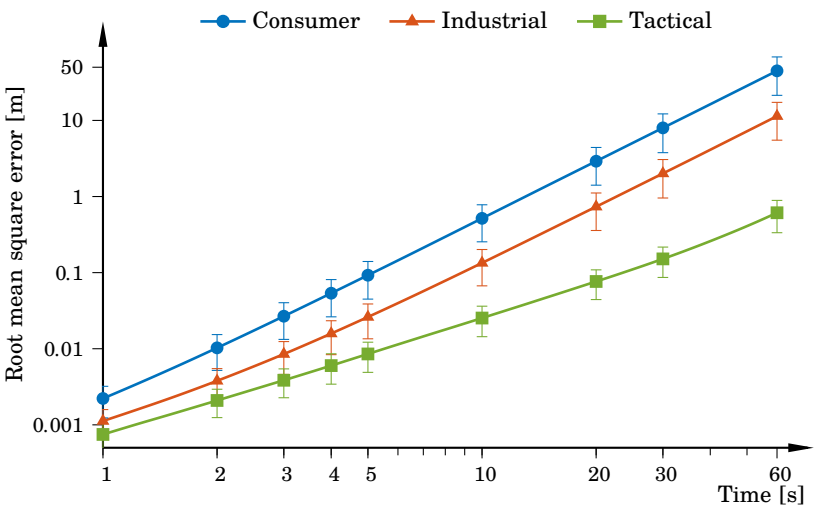

Figure 1.6 Root mean square error of distance as a function of time for three different grades of IMUs, see Table 1.1 for corresponding noise specifications. The vertical bars indicate one standard deviation. The accumulated error compared to a wavelength of approximately 15 cm, used in many modern communication systems, is reached in 6 seconds by a consumer grade IMU and in 30 seconds by a tactical grade IMU.

IMU-Based Positioning

There are many different proposals in the literature on how to improve positioning accuracy by combining information from IMU sensors with data from other sensors. This concept is usually referred to as *sensor fusion* but the subject is not limited to using IMUs and serves as a general framework for estimation. By creating a model of how different variables depend on the measurements and of how they evolve over time, all information the measurements give can be combined and the variables can thereby be estimated. The work of [Gustafsson, 2010] serves as a good starting point for the subject and it also presents several successful examples of sensor fusion.

The concept of IMU-based sensor fusion is illustrated in Figure 1.7. For improving IMU-based positioning, the Global Positioning System (GPS) has been a viable source of additional position estimates for sensor fusion. The GPS provides low bandwidth drift-free position estimates which is well complemented by the higher acquisition bandwidth of the IMU. Together, the units can give reliable position estimates with high bandwidth, see [Sukkarieh et al., 1999; Carvalho et al., 1997]. Another approach, which is particularly useful in situations where the estimates provided by the GPS are unreliable, e.g., in an indoor environment, is fusion with information from other available radio signals. In [Li et al., 2013; Fink et al., 2010], the authors use the received signal strength (RSS) which is dependent on the distance between the receiver and the access point. In [Jourdan et al., 2005; Hol et al., 2009], the time of arrival is used a as distance measure in an ultra-wideband (UWB) network. Together with an IMU, the solutions provide high-accuracy positioning.

In a scenario when a wireless network is unavailable, pedestrian localization has been researched by [Woodman and Harle, 2008; Sabatini et al., 2005; Skog et al., 2010]. The common solution is to mount the IMU to a boot and then to detect when the IMU has zero velocity during a step. This can then be used for re-calibration of the IMU to remove the drift in the velocity estimates and the positioning results are promising [Woodman and Harle, 2008; Skog et al., 2010].

1.3 Joint Position and Radio Channel Estimation

Angle of arrival (AoA) estimation with either active or passive arrays is a research area with many applications and several estimation approaches have been presented over the years. The central problem within the field is to estimate the AoA of a propagating wave that impinges on an array of sensors [Krim and Viberg, 1996]. The applications are, e.g., radio transmission source localization, active radar, seismic sensing, and astronomy to mention

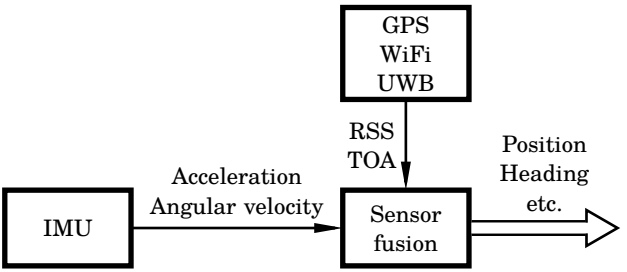

Figure 1.7 Tight integration by sensor fusion between IMU sensors and information acquired from wireless networks. The sensor fusion block combines the information provided by the different sensors and produces an estimate of the underlying variables such as position, heading etc.

a few [Van Trees, 2004]. For radio source localization, the sensor array consists of several receive antenna elements placed at known locations and a synchronized receiver which measures the phase of the received baseband signal. Using the phase information of the received signals from the different receiver antenna elements, the AoA can be estimated. The problem can also be stated the other way around as localization of the sensors when the transmitter locations are known. A survey of different localization methods where the transmitter locations are known is given in [Yanying et al., 2009]. The novelty in our work is to jointly estimate the position of the receiver, and at the same time estimate the location of the transmitters in the sense of AoA.

As mentioned before, the radio channel can be described with a set of parameters such as, signal strength, AoA, and Doppler shift. Accurate estimation of these parameters enables detailed radio channel models and development of advanced wireless communication systems. In the literature there are many competing algorithms for parameter estimation, e.g., [Schmidt, 1986; Roy and Kailath, 1989; Veen et al., 1997; Fleury et al., 1999]. Today there is a growing interest in channel parameter estimation with tracking using a Bayesian approach such as an extended Kalman filter (EKF) as presented in [Richter et al., 2005] or a sequential Monte Carlo approach using a particle filter [Kirkelund et al., 2008]. These approaches use a state-space model to describe how the channel parameters evolve over time and how the channel response depends on them, but there is no motion model of the receiver included. In [Olama et al., 2006], the authors show how the position and velocity can be tracked when radio channel measurements are available at the receiver. They compare estimation performance of a particle filter and an EKF and the particle filter turns out to be the superior choice. However, they do not include any variables in the estimation

that describe the radio channel. In [Broumandan et al., 2007], the authors used an IMU to make a synthetic antenna array, i.e., an antenna array that is formed with a single movable receive element. By using it, the authors performed AoA estimation for interference suppression in a GPS receiver. The single receive antenna was placed together with the IMU on a revolving stick, and the radius of the circle was estimated from the IMU data which also becomes the radius of the synthetic antenna array. However, no tracking results for positioning was considered. In summary, none of the sources address the problem of jointly estimating the position and tracking the multipath component parameters.

In contrast to these sources, we will establish a state-space model that combines a description of the radio channel and the location of the receiver. The state-space of the model will be estimated using a nonlinear state estimator. The purpose of joint position and radio channel estimation is double: improving the long-term IMU-based positioning performance and improving radio channel prediction. The radio channel will be modeled with MPCs and each component is described with a set of states. These states will be tracked and estimated using information obtained from the IMU and the radio channel estimates. We will specifically study narrowband systems, even though a wideband system where the individual MPCs could be retrieved is deemed an easier problem. Since the states explain the small scale fading pattern, the pattern will be seen as a map which is simultaneously constructed while using it for positioning of the receiver. With the estimated state-space model, predictions of the radio channel can also be calculated and used for adaptation of the link parameters for future transmissions. For illustrative purposes, and for showing the benefit on transmission data rates, the LTE system is used, but the approach is not limited to this system alone. Instead any pilot-based system where the receiver is equipped with inertial sensors may be used.

Contributions

The contributions of this thesis are:

- a state-space model that combines a motion model and a radio channel model for a narrowband system,
- identification of suitable algorithms for joint estimation of position and the radio channel states,
- simulation results showing significantly improved performance of long-term positioning,
- proof of concept experiments of using a low-cost IMU with good results,

- investigation of fundamental performance bounds of space-time virtual arrays under imprecise position estimates,
- a new method based on sparse Bayesian learning for joint estimation of angle of arrival and frequency error under imprecise position estimates, and
- link adaptation based on prediction of the joint position and radio channel model to increase data throughput in the LTE system.

1.4 Publications

The work presented in this thesis is based on the following peer reviewed publications, all mainly written by A. Mannesson.

Mannesson, A., M. A. Yaqoob, B. Bernhardsson, and F. Tufvesson (2015). "Tightly coupled positioning and multipath radio channel tracking". *IEEE Transactions on Aerospace and Electronic Systems*. Accepted.

This article covers the joint state-space model and includes positioning results for both synthetic signals and for a set of measurements acquired by experiments. The work concerns SISO systems. A. Mannesson was responsible for modeling, implementation, analysis, and writing the article. The measurements were performed together with M. A. Yaqoob who had the main responsibility for the experiment equipment and planning of the experiments. He also contributed with ideas on the modeling and the manuscript. F. Tufvesson and B. Bernhardsson contributed with the core idea and assisted on modeling, choice of algorithms, and structuring the manuscript.

Mannesson, A., M. A. Yaqoob, B. Bernhardsson, and F. Tufvesson (2012). "Radio and IMU based indoor positioning and tracking". In: *Proceedings of IEEE International Conference on Systems, Signals and Image Processing (IWSSIP)*. Vienna, Austria, pp. 32–35.

Preliminary work on positioning using experiment data. The work distribution among the authors is identical to the previous article.

Mannesson, A., B. Bernhardsson, M. A. Yaqoob, and F. Tufvesson (2014). "Optimal virtual array length under position imperfections". In: *Proceedings of IEEE 8th Sensor Array and Multichannel Signal Processing Workshop (SAM)*. A Coruña, Spain.

This article is an extension of the angle of arrival estimation presented in the licentiate thesis by the author. A. Mannesson stated the problem and

was responsible for the implementation, analysis, and writing the article. The other authors contributed with feedback on the problem definition and the manuscript.

Mannesson, A. and B. Bernhardsson (2015). "Cramér-Rao lower bound for imprecise space-time virtual antenna arrays". *IEEE Transactions on Signal Processing*. Submitted.

Cramér-Rao lower bound calculations and analysis for space-time antenna arrays. The core idea was initiated by B. Bernhardsson while A. Mannesson was responsible for calculations, implementation, validation, and writing the manuscript.

Mannesson, A., B. Bernhardsson, and F. Tufvesson (2015). "Link adaption for MIMO systems using sensor fusion based channel prediction". *IEEE Transactions on Wireless Communications*. Submitted.

An extension of the joint state-space model used in previous publications to cover MIMO systems. The article also presents work on channel prediction and link adaptation. A. Mannesson was responsible for the problem definition, implementation, and writing of the manuscript. B. Bernhardsson and F. Tufvesson contributed with the underlying idea and gave valuable feedback on the problem definition and the manuscript.

Preliminary work concerning positioning, performance bounds, particle filter initialization, and experiment series has also been published in the author's licentiate thesis.

Mannesson, A. (2013). *Joint Pose and Radio Channel Estimation*. Licentiate Thesis ISRN LUTFD2/TFRT–3263–SE. Department of Automatic Control, Lund University, Sweden.

The work in the following publications is not included in this thesis but A. Mannesson has been involved and has contributed with ideas for the work and has also provided feedback on the manuscripts as well as helped out with the measurement series.

Yaqoob, M. A., A. Mannesson, F. Tufvesson, and B. Bernhardsson (2013). "Direction of arrival estimation with arbitrary virtual antenna arrays using low cost inertial measurement unit". In: *Proceedings of IEEE International Conference on Communications - Workshop*. Budapest, Hungary, pp. 79–83.

Yaqoob, M. A., A. Mannesson, F. Tufvesson, B. Bernhardsson, and N. R. Butt (2014). "On the performance of random antenna arrays for direction of arrival estimation". In: *Proceedings of IEEE International Conference on Communications - Workshop*. Sydney, Australia, pp. 193–199.

Yaqoob, M. A., A. Mannesson, N. R. Butt, and F. Tufvesson (2015). “Source localization using virtual antenna arrays”. In: *2015 International Conference on Localization and GNSS (ICL-GNSS)*. Gothenburg, Sweden.

All published publications are available to download from `http://www.control.lth.se/Publications.html`.

1.5 Outline

This thesis consists of nine chapters. In Chapter 2, a model for the radio channel is presented and a connection between it and the location of the receiver is derived. This connection will be used in the joint position and radio channel state-space model derived in Chapter 3. In Chapter 4 algorithms suitable for estimation of the joint state-space model is presented. The fundamental estimation limitations are studied in Chapter 5 and in Chapter 6, simulation results of the full estimation problem are presented. Chapter 7 describes and presents results from a series of measurement that has been conducted during the work and the results serve as a proof of concept. In Chapter 8, the possible increase in end user data rates using link adaptation with the predicted state-space model is investigated. Finally, the work is summarized and future research directions are pointed out in Chapter 9.

2

Radio Channel Modeling

2.1 MIMO Communication Systems

In a multiple-input multiple-output (MIMO) system, the transmitter and receiver are equipped with two or more antennas each and use them simultaneously for communication. Compared to a single-input single-output (SISO) system with one active channel between the transmitter and the receiver, MIMO systems provide several important benefits that can improve link reliability and data transfer rates [Paulraj et al., 2003]. In Figure 2.1, a simple generic MIMO system is shown. The transmitter pre-processes the bits to be transmitted, what steps that are used depend on the particular system but may include coding, modulation mapping, and antenna mapping, before finally modulating the information onto the carrier signal. The carrier frequency used is system specific and ranges from approximately 450 MHz to 6 GHz for typical cellular and WiFi networks. Many systems use several different frequency bands in order to increase the data transfer rates or to serve more users and the given frequency interval is therefore densely occupied with different radio standards. The modulated carrier signal is fed to the transmit antennas and when the receiver detects the carrier signal, the RX retrieves the transmitted bits by, e.g., reverting the pre-processing operations of the TX.

The MIMO scheme enables techniques which are not available for single-channel systems. These techniques enhance the communication link in different ways which can be divided into three categories described briefly below [Paulraj et al., 2003].

- **Diversity**. As seen in Figure 1.1, the wireless link can go into deep fading dips due to multipath wave propagation. Since a MIMO system enables more channels, and by combining the received signal from all receive antennas, the likelihood of losing a transmission is decreased.
- **Multiplexing**. Since the MIMO technique enables several channels between the TX and the RX, parallel data streams can be transmitted

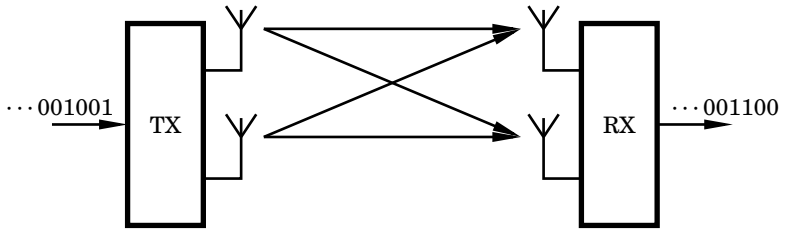

Figure 2.1 A MIMO scenario with two transmit antennas to the left and two receive antennas to the right. The pre-processing of the TX includes, e.g., coding and modulation while the post-processing reverts these steps in order to retrieve the transmitted bits.

using the same transmission bandwidth and time slot. In a single-channel system, increased transmission capacity can only be gained by either increasing the signal to noise ratio (SNR) or increasing the bandwidth used. While these options increase the throughput to one user, all other users will be negatively affected by them.

- **Beamforming**. By adjusting the amplitude and phase of the transmitted signal at each transmitting antenna, the energy can be directed towards the receiver. An analogy to this is an optical lens which focuses rays of light into a single point. Since less energy is emitted towards other users, the general noise level in the system is lowered which enables higher data rates in the wireless network.

The benefits of the MIMO technique and an increased demand on high data transfer rates in wireless devices have resulted in several commercial implementations of it, e.g., the LTE [3GPP, 2016a] system for 4G as well as the IEEE 802.11 n/ac [IEEE S.A., 2016] for WiFi. Therefore, a MIMO system is used in the derivation below.

2.2 MIMO Radio Channel Model

As discussed in Section 1.1, wireless transmissions are subject to multipath wave propagation. We will now derive an MPC based radio channel model which allows tracking of the individual MPCs in a MIMO system. It is more advanced than traditionally used, but newer radio channel models such as COST 2100 [Verdone and Zanella, 2012; Liu et al., 2012] is an application of the geometry based radio channel modeling which is the basis of our model. The derivation presented here follows [Pedersen, 2009] closely.

Consider a MIMO system with M_T transmit antennas and M_R receive antennas, compare Figure 2.1. The transmitted and received signal can be

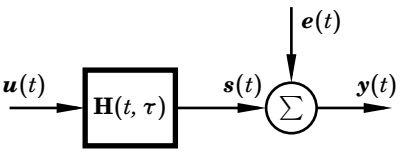

Figure 2.2 The radio channel can be modeled as an LTV system with additive complex valued Gaussian noise $\boldsymbol{e}(t)$. The input to the channel is the baseband equivalent $\boldsymbol{u}(t)$ while the output is $\boldsymbol{y}(t)$. The channel is described by the time-variant impulse response function $\mathbf{H}(t, \tau)$.

represented with their complex baseband signals, respectively, as

$$\boldsymbol{u}(t) = \begin{bmatrix} u_1(t) & \dots & u_m(t) & \dots & u_{M_T}(t) \end{bmatrix}^T$$

and

$$\boldsymbol{y}(t) = \begin{bmatrix} y_1(t) & \dots & y_n(t) & \dots & y_{M_R}(t) \end{bmatrix}^T,$$

where $(\cdot)^T$ denotes matrix transpose, $u_m(t)$ is the input signal of transmit antenna m, and $y_n(t)$ the output signal of receive antenna n, see [Paulraj et al., 2003]. If the radio channel is modeled as an LTV system, the observed noisy signal $\boldsymbol{y}(t)$ will be

$$\boldsymbol{y}(t) = \int_0^\infty \mathbf{H}(t, \tau)\boldsymbol{u}(t - \tau)\, d\tau + \boldsymbol{e}(t), \tag{2.1}$$

where t is the time when the receive antenna observes the signal, τ is the time delay in the channel, and $\boldsymbol{e}(t) \sim \mathcal{CN}(\mathbf{0}, \boldsymbol{\Sigma})$ is additive zero mean circular symmetric complex Gaussian noise with a positive definite covariance matrix $\boldsymbol{\Sigma} \in \mathbb{R}^{n_x \times n_x}$. The probability density function of the distribution is given by

$$\mathcal{CN}(\boldsymbol{x}|\boldsymbol{m}, \boldsymbol{\Sigma}) = \frac{1}{\pi^{n_x}|\boldsymbol{\Sigma}|} \exp\{-(\boldsymbol{x} - \boldsymbol{m})^* \boldsymbol{\Sigma}^{-1}(\boldsymbol{x} - \boldsymbol{m})\}, \tag{2.2}$$

where $\boldsymbol{m} \in \mathbb{C}^{n_x}$ denotes the mean, $\boldsymbol{x} \in \mathbb{C}^{n_x}$ denotes the random variable, $(\cdot)^*$ denotes Hermitian transpose, and $|\cdot|$ denotes determinant. Furthermore, the integral kernel $\mathbf{H}(t, \tau) \in \mathbb{C}^{M_R \times M_T}$ is called the *time-variant impulse response* [Molisch, 2005]. The noise can represent different things, e.g., thermal noise in the receiver or interference in the radio channel. The channel operations are illustrated in Figure 2.2.

In (2.1), the transfer function is given in the time-delay domain. In Chapter 1, the transfer function of the radio channel was illustrated in the time-frequency domain and their relationship is given by

$$\mathbf{L}(t, f) = \int_{-\infty}^{\infty} \mathbf{H}(t, \tau) \exp\{-i2\pi f \tau\}\, d\tau, \tag{2.3}$$

which is the Fourier transform with respect to the delay. An example of $\mathbf{L}(t, f)$ is given in Figure 1.1.

If the channel is assumed to be time-invariant, i.e., the kernel function is constant over time, its impulse response function is of the form $\mathbf{H}(t, \tau) \triangleq \mathbf{H}_t(\tau), \ \forall\, t$. Furthermore, if the channel is assumed to be *non-dispersive*, the kernel function is of the form $\mathbf{H}(t, \tau) \triangleq \mathbf{H}_\tau(t)\delta(\tau - \tau_0)$, where $\delta(t)$ is the Dirac delta function. If both these assumptions hold, then the channel operations in (2.1) can be simplified and become

$$\boldsymbol{y}(t) = \mathbf{H}_{t,\tau}\boldsymbol{u}(t - \tau_0) + \boldsymbol{e}(t), \tag{2.4}$$

where $\mathbf{H}_{t,\tau} \in \mathbb{C}^{M_R \times M_T}$ is the non-dispersive time constant kernel function. This matrix will be referred to as the *channel matrix*.

Time-invariance may be assumed for channels where changes of the channel transfer function occur slowly compared to the considered transmission time duration. Similarly, a channel may be considered non-dispersive if the corresponding time-frequency transfer function $\mathbf{L}(t, f)$ is approximately constant in the frequency domain over the bandwidth of the transmitted signal. This is also referred to as *frequency non-selective channels* [Molisch, 2005].

Antenna Modeling

In this thesis it is assumed for simplicity that the antennas are isotropic, i.e., the channel matrix $\mathbf{H}$ will not depend on the rotation of the receiver which simplifies the models significantly. However, for future research, the models describing the influence of the antennas on the radio channel model are presented here.

By assuming that the antennas at the transmitters and the receivers are time-invariant and non-dispersive with respect to their field pattern, the antennas can be described by their direction dependent complex transfer functions. For each antenna element, the complex electric field pattern is a two-dimensional complex function. For the mth transmit antenna element, it is described by

$$\begin{bmatrix} c^{\phi}_{\mathrm{TX},m}(\boldsymbol{\varrho}) \\ c^{\theta}_{\mathrm{TX},m}(\boldsymbol{\varrho}) \end{bmatrix}, \tag{2.5}$$

where $c^{\phi}_{\mathrm{TX},m}(\boldsymbol{\varrho})$ and $c^{\theta}_{\mathrm{TX},m}(\boldsymbol{\varrho})$ are the horizontal and vertical components of the complex electric field pattern respectively and $\boldsymbol{\varrho}$ is the direction vector defined in Figure 2.3. Define the transmit antenna response matrix as

$$\mathbf{C}_{\mathrm{TX}} = \begin{bmatrix} c^{\phi}_{\mathrm{TX},1} & \cdots & c^{\phi}_{\mathrm{TX},m} & \cdots & c^{\phi}_{\mathrm{TX},M_T} \\ c^{\theta}_{\mathrm{TX},1} & \cdots & c^{\theta}_{\mathrm{TX},m} & \cdots & c^{\theta}_{\mathrm{TX},M_T} \end{bmatrix} \in \mathbb{C}^{2 \times M_T}, \tag{2.6}$$

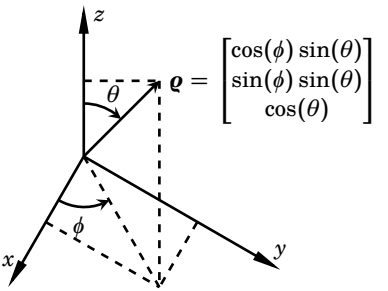

Figure 2.3 Definition of the direction vector $\boldsymbol{\varrho}$.

where ϕ denotes azimuth and θ elevation. Similarly, for the receive antenna, a complex $2 \times M_R$ response matrix $\mathbf{C}_{\mathrm{RX}}$ is introduced. The impulse response function for the radio channel can then be written as

$$\mathbf{H}(t, \tau) = \iint [\mathbf{C}_{\mathrm{RX}}(\boldsymbol{\varrho}_{\mathrm{RX}})]^T \mathbf{G}(t, \tau, \boldsymbol{\varrho}_{\mathrm{TX}}, \boldsymbol{\varrho}_{\mathrm{RX}}) [\mathbf{C}_{\mathrm{TX}}(\boldsymbol{\varrho}_{\mathrm{TX}})] \, d\boldsymbol{\varrho}_{\mathrm{TX}} \, d\boldsymbol{\varrho}_{\mathrm{RX}}, \tag{2.7}$$

where the 2×2 kernel $\mathbf{G}(t, \tau, \boldsymbol{\varrho}_{\mathrm{TX}}, \boldsymbol{\varrho}_{\mathrm{RX}})$ is the *bi-directional impulse response function* of the radio channel. It describes the propagation properties for different combinations of transmit-receive polarization pairs as

$$\mathbf{G}(t, \tau, \boldsymbol{\varrho}_{\mathrm{TX}}, \boldsymbol{\varrho}_{\mathrm{RX}}) = \begin{bmatrix} g^{\phi\phi}(t, \tau, \boldsymbol{\varrho}_{\mathrm{TX}}, \boldsymbol{\varrho}_{\mathrm{RX}}) & g^{\phi\theta}(t, \tau, \boldsymbol{\varrho}_{\mathrm{TX}}, \boldsymbol{\varrho}_{\mathrm{RX}}) \\ g^{\theta\phi}(t, \tau, \boldsymbol{\varrho}_{\mathrm{TX}}, \boldsymbol{\varrho}_{\mathrm{RX}}) & g^{\theta\theta}(t, \tau, \boldsymbol{\varrho}_{\mathrm{TX}}, \boldsymbol{\varrho}_{\mathrm{RX}}) \end{bmatrix}. \tag{2.8}$$

Multipath Wave Propagation Assumption

The multipath wave propagation introduced in Section 1.1 is used to describe the result of scattering. It is a commonly used model which is intuitive and fits many other observed phenomena like channel delay and Doppler power spectra. The multipath assumption also allows for physical interpretation of observed changes in the radio channel due to movement of the receiver. We will now establish this relationship.

The received signal is modeled as a superposition of N_R multipath components

$$\boldsymbol{s}(t) = \sum_{r=1}^{N_R} \boldsymbol{s}^{(r)}(t), \tag{2.9}$$

where $\boldsymbol{s}^{(r)}(t)$ denotes the signal contribution by the rth MPC. For a multipath model, the impulse response function is decomposed as

$$\mathbf{H}(t, \tau) = \sum_{r=1}^{N_R} \mathbf{H}^{(r)}(t, \tau) = \sum_{r=1}^{N_R} \begin{bmatrix} h_{1,1}^{(r)}(t, \tau) & \dots & h_{1,M_T}^{(r)}(t, \tau) \\ \vdots & \ddots & \vdots \\ h_{M_R,1}^{(r)}(t, \tau) & \dots & h_{M_R,M_T}^{(r)}(t, \tau) \end{bmatrix} \tag{2.10}$$

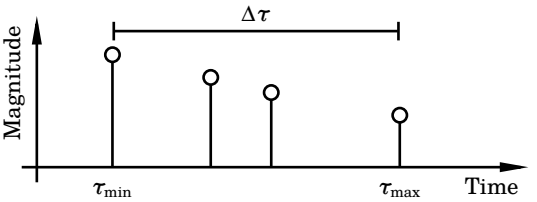

Figure 2.4 Time delayed and attenuated multipath components arriving at the receiver between $\tau_{\min}$ and $\tau_{\max}$. The coherence bandwidth of the channel is approximately $1/\Delta\tau$. If the bandwidth of the transmitted signal is significantly lower than the coherence bandwidth, the radio channel is said to be non-dispersive or frequency flat over the signal bandwidth. A consequence of this is that the individual multipath components can not be resolved after they add up at the receiver.

where $\mathbf{H}^{(r)}(t, \tau)$ denotes the time-variant impulse response function for the rth MPC. Multipath wave propagation in the time domain is illustrated in Figure 2.4 where there are four time shifted components arriving at the receiver after different propagation times τ. The scenario is similar to Figure 1.2 where there are three multipath components arriving at the receiver.

Let the difference in time delay between the first and the last multipath component be denoted by $\Delta\tau$, see Figure 2.4. For such a channel, the coherence bandwidth is approximately given by $B_{\text{coh}} = 1/\Delta\tau$. If the bandwidth of the transmitted signal $\boldsymbol{u}$ in (2.1) is denoted B_{u} and fulfills $B_{\text{u}} \ll B_{\text{coh}}$, the frequency response of the channel can be considered to be flat over the signal bandwidth. This assumption is commonly referred to as *the narrowband assumption* [Molisch, 2005]. A consequence of the narrowband scenario is that the individual multipath components can not be resolved at the receiver. If the opposite holds, i.e., the signal bandwidth is significantly larger than the coherence bandwidth, the difference between the absolute delays of the components can be resolved. If so, time of arrival (TOA) information can be obtained with time synchronized receivers and time difference of arrival (TDOA) otherwise. The wideband transmission case would supply more information about the radio channel, but in this thesis the investigation is focused on the more challenging narrowband case and the wideband case is left for future research. The narrowband assumption will be used later on in our derivation.

Since an isotropic antenna transmits energy with the same intensity in all directions, the wavefront becomes a sphere in free space. If the distance between the transmitter and the receiver is large, the curvature of the wavefront can be neglected and then it can be considered to be a plane

wave instead. This is known as *the plane wave assumption*. This implies that all points on a plane, perpendicular to the propagation direction, is assumed to have the same traveling distance and time delay, and thus the same phase offset. If the plane wave assumption holds for all propagation paths, the individual impulse response function for each MPC becomes

$$h_{n,m}^{(r)}(t,\tau) = \iint [\mathbf{C}_{\mathrm{RX},n}(\boldsymbol{\varrho}_{\mathrm{RX}})]^T \mathbf{G}_{n,m}^{(r)}(t,\tau,\boldsymbol{\varrho}_{\mathrm{TX}},\boldsymbol{\varrho}_{\mathrm{RX}})[\mathbf{C}_{\mathrm{TX},m}(\boldsymbol{\varrho}_{\mathrm{TX}})]\, d\boldsymbol{\varrho}_{\mathrm{TX}}\, d\boldsymbol{\varrho}_{\mathrm{RX}}, \quad (2.11)$$

where $\mathbf{C}_{\mathrm{RX},n}$ and $\mathbf{C}_{\mathrm{TX},m}$ are the nth and mth column of $\mathbf{C}_{\mathrm{RX}}$ and $\mathbf{C}_{\mathrm{TX}}$ respectively. Consequently, the (n,m)th element of $\mathbf{H}(t,\tau)$ is

$$h_{n,m}(t,\tau) = \iint [\mathbf{C}_{\mathrm{RX},n}(\boldsymbol{\varrho}_{\mathrm{RX}})]^T \sum_{r=1}^{N_R} \mathbf{G}_{n,m}^{(r)}(t,\tau,\boldsymbol{\varrho}_{\mathrm{TX}},\boldsymbol{\varrho}_{\mathrm{RX}})[\mathbf{C}_{\mathrm{TX},m}(\boldsymbol{\varrho}_{\mathrm{TX}})]\, d\boldsymbol{\varrho}_{\mathrm{TX}}\, d\boldsymbol{\varrho}_{\mathrm{RX}}. \quad (2.12)$$

Specular Multipath Representation

A multipath component is called *specular* [Pedersen, 2009] when its impulse response function has the form

$$\mathbf{G}_{n,m}^{(r)}(t,\tau,\boldsymbol{\varrho}_{\mathrm{TX}},\boldsymbol{\varrho}_{\mathrm{RX}}) = \mathbf{A}^{(r)} \exp\{-i2\pi\nu^{(r)}t\}\delta(\tau-\tau_{n,m}^{(r)})\delta(\boldsymbol{\varrho}_{\mathrm{TX}}-\boldsymbol{\varrho}_{\mathrm{TX}}^{(r)})\delta(\boldsymbol{\varrho}_{\mathrm{RX}}-\boldsymbol{\varrho}_{\mathrm{RX}}^{(r)}), \quad (2.13)$$

where $\mathbf{A}^{(r)}$ is a complex 2×2 polarization matrix, ν_r is the Doppler frequency, $\tau^{(r)}$ is the delay, $\boldsymbol{\varrho}_{\mathrm{TX}}^{(r)}$ is the angle of departure, and $\boldsymbol{\varrho}_{\mathrm{RX}}^{(r)}$ is the AoA of component r. Inserting this expression in (2.11) and integrating over $\boldsymbol{\varrho}_{\mathrm{TX}}$ and $\boldsymbol{\varrho}_{\mathrm{RX}}$ yields

$$h_{n,m}^{(r)}(t,\tau) = [\mathbf{C}_{\mathrm{RX},n}(\boldsymbol{\varrho}_{\mathrm{RX}}^{(r)})]^T \mathbf{A}^{(r)} [\mathbf{C}_{\mathrm{TX},m}(\boldsymbol{\varrho}_{\mathrm{TX}}^{(r)})] \exp\{-i2\pi\nu^{(r)}t\}\delta(\tau-\tau_{n,m}^{(r)}). \quad (2.14)$$

Thus, component r is determined by the parameters $\mathbf{A}^{(r)}$, $\boldsymbol{\varrho}_{\mathrm{TX}}^{(r)}$, $\boldsymbol{\varrho}_{\mathrm{RX}}^{(r)}$, $\tau_{n,m}^{(r)}$, and $\nu^{(r)}$. Since $\mathbf{A}^{(r)}$ is a complex matrix with four elements and the directions can be described by two real parameters each, a total of 14 parameters is needed for each transfer function and multipath component. To simplify the model and reduce the number of parameters, some assumptions will be made.

We will start by assuming that the scatterers do not contribute to the Doppler shifts, i.e., $\nu^{(r)} = 0,\ \forall\, r \in \{1,\ldots,N_R\}$. This is the case if all MPCs have been scattered by stationary objects. The next assumption is isotropic antennas which leads to

$$[\mathbf{C}_{\mathrm{RX},n}(\boldsymbol{\varrho}_{\mathrm{RX}}^{(r)})]^T \mathbf{A}^{(r)} [\mathbf{C}_{\mathrm{TX},m}(\boldsymbol{\varrho}_{\mathrm{TX}}^{(r)})] = a^{(r)},\ \forall\, r \in \{1,\ldots,N_R\} \quad (2.15)$$

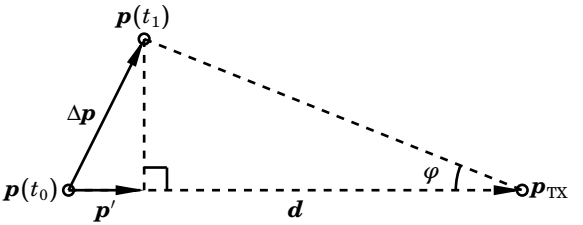

Figure 2.5 The receive antenna is moved from location $\boldsymbol{p}(t_0)$ to $\boldsymbol{p}(t_1)$ and a stationary transmitter is placed in $\boldsymbol{p}_{\mathrm{TX}}$. Note that $\boldsymbol{d} \triangleq \boldsymbol{p}_{\mathrm{TX}} - \boldsymbol{p}(t_0)$.

where $a^{(r)}$ is a complex scalar for the rth MPC.

Furthermore, assume that the transmitter is stationary, i.e., the delay in the channel $\tau^{(r)}$ is only dependent on the position of the receiver.

To establish how a translation of the receiver affects the delay of the signal, the scenario in Figure 2.5 is considered. Introduce the location of the receiver at time t as $\boldsymbol{p}(t) \in \mathbb{R}^3$ and introduce the vectors $\Delta\boldsymbol{p} \triangleq \boldsymbol{p}(t_1) - \boldsymbol{p}(t_0)$ and $\boldsymbol{d} \triangleq \boldsymbol{p}_{\mathrm{TX}} - \boldsymbol{p}(t_0)$, where $\boldsymbol{p}_{\mathrm{TX}} \in \mathbb{R}^3$ is the location of the transmitter. If the vector $\Delta\boldsymbol{p}$ is projected onto vector $\boldsymbol{d}$ as

$$\boldsymbol{p}' = \frac{\langle \Delta\boldsymbol{p}, \boldsymbol{d} \rangle}{\|\boldsymbol{d}\|^2}\boldsymbol{d}, \tag{2.16}$$

where $\langle \cdot, \cdot \rangle$ denotes scalar product, the distance between the stationary transmitter in $\boldsymbol{p}_{\mathrm{TX}}$ and the receiver in $\boldsymbol{p}(t_1)$ is

$$\|\boldsymbol{p}_{\mathrm{TX}} - \boldsymbol{p}(t_1)\| = \frac{\|\boldsymbol{d} - \boldsymbol{p}'\|}{\cos(\varphi)}. \tag{2.17}$$

If $\|\Delta\boldsymbol{p}\| \ll \|\boldsymbol{d}\|$, φ becomes small and thus

$$\|\boldsymbol{p}_{\mathrm{TX}} - \boldsymbol{p}(t_1)\| \approx \|\boldsymbol{d} - \boldsymbol{p}'\| = \|\boldsymbol{d} - \frac{\langle \boldsymbol{d}, \Delta\boldsymbol{p} \rangle}{\|\boldsymbol{d}\|^2}\boldsymbol{d}\| = \|\boldsymbol{d}\| - \langle \frac{\boldsymbol{d}}{\|\boldsymbol{d}\|}, \Delta\boldsymbol{p} \rangle. \tag{2.18}$$

The vector $\dfrac{\boldsymbol{d}}{\|\boldsymbol{d}\|}$ is the vector $\boldsymbol{\varrho}_{\mathrm{RX}}$, compare Figure 2.3, pointing in the direction of the impinging MPC. Introduce the notation of the nth receive antenna position at time t by $\boldsymbol{p}_n(t) \in \mathbb{R}^3$. With these assumptions and this notation, the travel time from transmit antenna m to receive antenna n of the rth MPC can be written as

$$\tau_{n,m}^{(r)} = \overline{\tau}_m^{(r)} - \frac{1}{v_c}\langle \boldsymbol{p}_n(t), \boldsymbol{\varrho}(\phi^{(r)}, \theta^{(r)}) \rangle, \tag{2.19}$$

where $\overline{\tau}_m^{(r)}$ is a constant and v_c is the speed of propagation. Using these assumptions, the elements $h_{n,m}^{(r)}(t, \tau)$ of (2.10) are given by

$$h_{n,m}^{(r)}(t, \tau) = a^{(r)} \delta \left(\tau - \overline{\tau}_m^{(r)} + \frac{1}{v_c} \langle \boldsymbol{p}_n(t), \boldsymbol{\varrho}(\phi^{(r)}, \theta^{(r)}) \rangle \right). \tag{2.20}$$

We are now ready to formulate the relationship between the input RF signal to the channel from the mth transmit antenna

$$u_{\mathrm{RF},m}(t) = \mathrm{Re}\{\exp\{i2\pi f_c t\} u_m(t)\},$$

and output RF signal of the channel at the nth receive antenna

$$y_{\mathrm{RF},n}(t) = \mathrm{Re}\{\exp\{i2\pi f_c t\} y_n(t)\},$$

where $u_m(t) \in \mathbb{C}$ and $y_n(t) \in \mathbb{C}$ are the baseband equivalents [Molisch, 2005] of $u_{\mathrm{RF},m}(t)$ and $y_{\mathrm{RF},n}(t)$ respectively. The relationship is given by

$$y_{n,m}^R(t) = \sum_{r=1}^{N_R} a^{(r)} \exp\{-i\beta_m^{(r)}\} \exp\left\{ -i2\pi \frac{f_c}{v_c} \langle \boldsymbol{p}_n(t), \boldsymbol{\varrho}(\phi^{(r)}, \theta^{(r)}) \rangle \right\} \times u_m \left(t + \overline{\tau}_m^{(r)} - \frac{1}{v_c} \langle \boldsymbol{p}_n(t), \boldsymbol{\varrho}(\phi^{(r)}, \theta^{(r)}) \rangle \right), \tag{2.21}$$

where the index of the output signal y denotes the active receive-transmit antenna pair with N_R impinging multipath components. The phase shift $\beta_m^{(r)}$ is a result of the unknown time delay $\overline{\tau}_m^{(r)}$. If the baseband signal $u_m(t)$ is slowly varying and thereby has its energy contained in a frequency interval $[0, u_{\mathrm{BW}}]$, then the approximation

$$u_m(t + \overline{\tau}_m^{(r)} - \frac{1}{v_c} \langle \boldsymbol{p}_n(t), \boldsymbol{\varrho}(\phi^{(r)}, \theta^{(r)}) \rangle) \approx u_m(t + \overline{\tau}_m^{(r)}), \ \forall\, m \in \{1, \ldots, M_R\} \tag{2.22}$$

is valid if $\tau_n^{(r)}(t) \triangleq \frac{1}{v_c} \langle \boldsymbol{p}_n(t), \boldsymbol{\varrho}(\phi^{(r)}, \theta^{(r)}) \rangle$ satisfies

$$\tau_n^{(r)}(t_1) - \tau_n^{(r)}(t_0) \ll \frac{1}{u_{\mathrm{BW}}}, \ \forall\, r \in \{1, \ldots, N_R\},$$

i.e., the approximation holds if the delay in the channel is not significantly changed by the movement of the receiver during the transmission time $t_1 - t_0$ of a symbol.

If the transmitter is transmitting a known baseband signal as it does during the pilot sequence, its contribution to $y_n(t)$ can be included in the complex amplitude $a_{n,m}^{(r)}$. Also, if the scenario is limited to $\mathbb{R}^2$ the position

of the receive antenna n at time t is denoted by $\boldsymbol{p}_n(t) \in \mathbb{R}^2$ and the unit vector $\boldsymbol{\varrho}$ is given by

$$\boldsymbol{\varrho}(\phi^{(r)}) \triangleq \left[\cos(\phi^{(r)}) \quad \sin(\phi^{(r)})\right]^T. \tag{2.23}$$

The azimuth angle ϕ is hereafter called the *angle of arrival* (AoA). If the AoA ϕ and amplitude a are slowly varying and only the mth transmit antenna is active, the baseband model in (2.21) simplifies to

$$y^R_{n,m}(t) = \sum_{r=1}^{N_R} a^{(r)}_{n,m}(t) \exp\{-i2\pi \frac{f_c}{v_c} \langle \boldsymbol{p}_n(t), \boldsymbol{\varrho}[\phi^{(r)}(t)] \rangle\}, \tag{2.24}$$

where $\boldsymbol{p}_n(t)$ denotes the position of the nth receive antenna at time t, $a^{(r)}_{n,m}$ is the complex MPC amplitude, unique for each transmit-receive antenna pair (m, n) and component r, and $\boldsymbol{\varrho}(\phi^{(r)})$ is a unit vector pointing in the azimuth direction of $\phi^{(r)}$. This is the relationship between the channel impulse response and the location of the receiver in the channel. This configuration with a moving antenna is usually referred to as a *virtual antenna array*, see [Molisch, 2005]. Note that $a^{(r)}_{n,m}(t)$ has taken into account all different contributions to the amplitude and phase that are independent of the location of the receiver and it is hereafter referred to as the *complex MPC amplitude*.

Illustrations

Before investigating (2.24) further, the impulse response function of (2.20) is illustrated in Figure 2.6. The figure shows how the first component arrives at 0.4 μs together with two MPCs arriving around 0.8 μs and 1.5 μs later. The curvature of the delay profile is due to the movement of the receiver which changes the distance to the scattering objects.

With the expression in (2.24) we have established a connection between the physical position of the receiver and the baseband signal. The measured baseband signal $y^R_{n,m}(t)$ is a sum of N_R complex valued contributions and depending on whether the receiver is approaching or leaving the scattering object, the contribution from each component is rotating clockwise or anti-clockwise in the complex plane as illustrated in Figure 2.7. Thus, the components interfere constructively and destructively with each other depending on the current receiver location and AoA. This is what was visualized in Figure 1.1 where destructive interference of the MPCs gave rise to fading dips in the time-frequency power spectra. Equation (2.24) can consequently be used to model the small scale fading pattern of the radio channel.

If we study the argument of the measured baseband signal $y^R_{n,m}(t)$, the pattern resembles a map, see figures 2.8, 2.9, and 2.10. The three figures

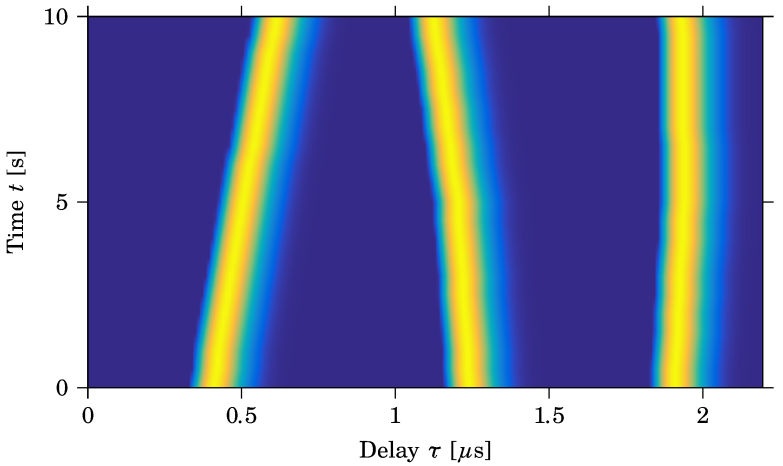

Figure 2.6 The impulse response function of a radio channel with delay τ on the x-axis and time t on the y-axis. The color indicates $|h(t, \tau)|$. Three multipath components give responses at around 0.4 μs, 1.2 μs, and 1.9 μs respectively. As time progresses and the receiver is moved, the delay time increases or decreases as the physical distances to the sources change.

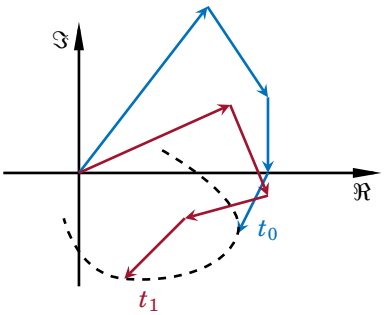

Figure 2.7 The contribution from four MPCs added together. As the receiver is moved between time instance t_0 and t_1, the components rotate dependent on the AoA for the specific component.

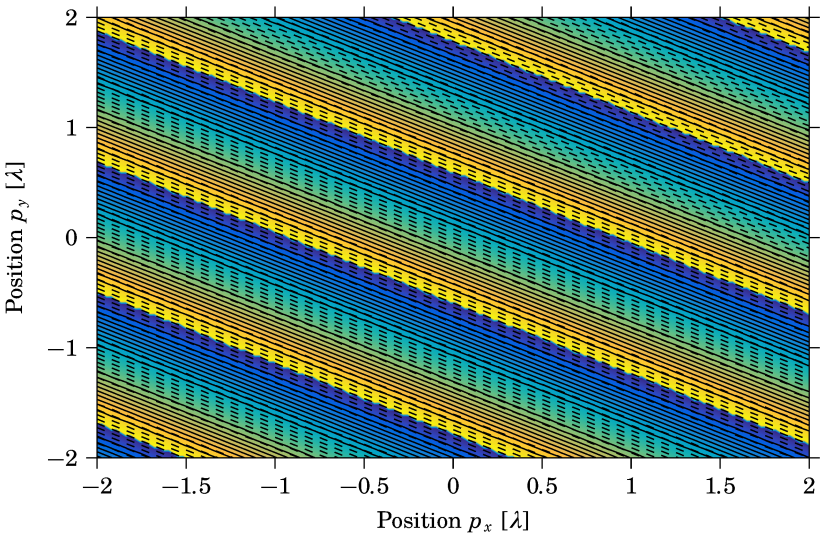

Figure 2.8 Map of the radio channel with one impinging MPC with level curves for the real (-) and imaginary (- -) value of the received complex signal $y^R_{n,m}(t)$. The colors indicate the argument of the complex signal. The plane wave assumption is clearly visible as straight phase lines, perpendicular to the AoA.

show this pattern where the number of impinging MPCs are one, two, and three respectively and have constant amplitude and AoA. In the figures, the real and imaginary parts, as well as the argument of the received complex signal (2.24), are shown as a function of the receiver's location.

The map in Figure 2.8 shows interesting characteristics of the radio channel. The far field assumption is clearly visible as straight lines of the color pattern where the argument is constant in the direction perpendicular to the impinging MPC. Hence, the argument of the received signal will not give any information about the position perpendicular to the direction of the impinging MPC. Further, if the receiver is moved a wavelength in the direction of the MPC, the argument of the signal revolves 2π during the movement and ends up back at the same value as it was when the movement was initiated. Clearly, the phase information is not usable for determining the absolute distance to the scattering object, but relative movements can be tracked.

In Figure 2.9, two MPCs are impinging on the receiver. The constant argument lines have now become "wavy" due to superposition of the two components. There are still areas wherein the argument is constant but now the real and imaginary parts of the received signal are changing. This

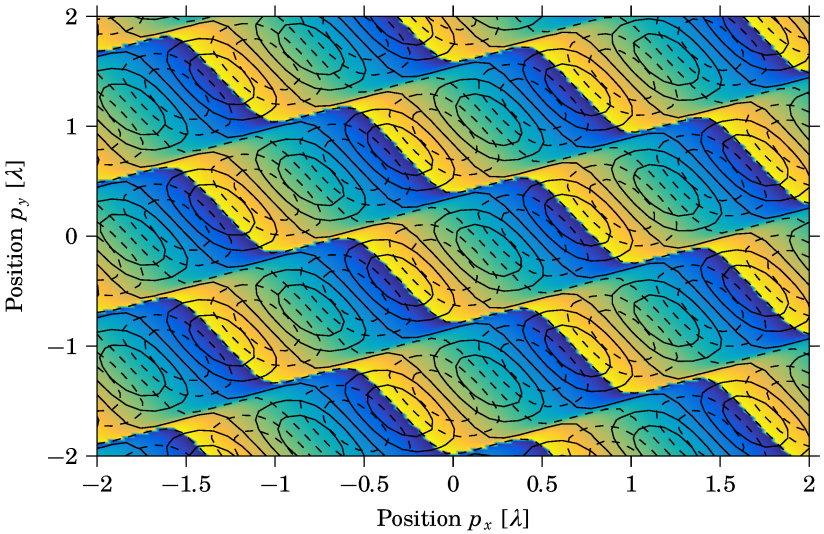

Figure 2.9 Same as Figure 2.8 but with two impinging MPCs giving a more informative map.

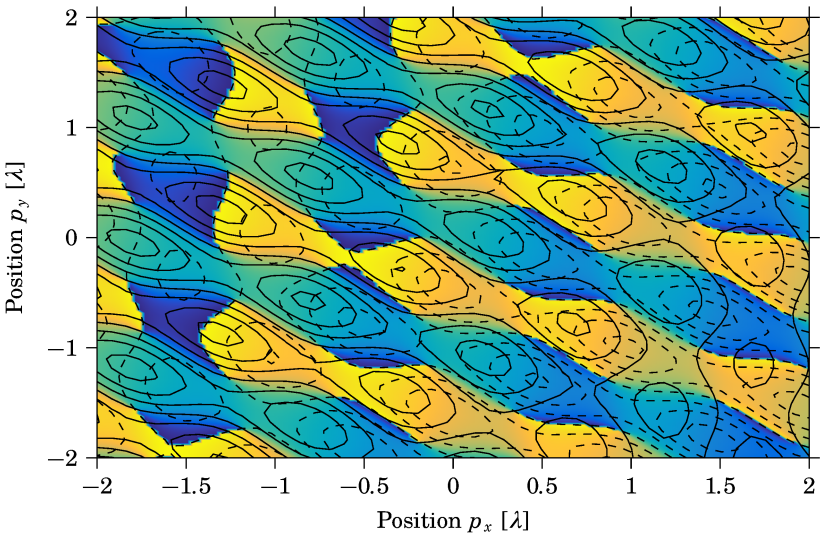

Figure 2.10 Same as Figure 2.8 but with three impinging MPCs giving an even more informative map.

information can be used to distinguish two points having the same argument from each other. Finally, for the case with three MPCs in Figure 2.10, the pattern becomes even more descriptive. There are several positions in the plane that will be indistinguishable from each other when looking at the real and the imaginary value of the received signal. Hence, the map of the radio environment alone will not provide a unique location of the receiver but rather multiple possible locations. This will have implications on estimating the location of the receiver in the radio channel later on. Finally, each transmit-receive antenna pair has its own unique map so for a 2×2 MIMO system, there will be four maps in total.

2.3 Cluster Modeling

So far we have used a point scatter description for the interfering objects; the incident energy of the radio wave is spread out in all different directions but only one component from each scatterer reaches the receiver. However, radio channel measurements show that several MPCs tend to reach the receiver from the same direction with low angular separation and low delay spread [Liu et al., 2012]. This can be explained by scattering in many nearby points of the same object. Therefore, radio channel models like COST 2100 include *clusters* to explain this phenomenon [Verdone and Zanella, 2012]. In the COST 2100 radio channel model, three different types of clusters are defined: single-bounce cluster, double-bounce cluster, and local cluster. The different cluster types are illustrated in Figure 2.11. In this thesis, the analysis is limited to single-bounce clusters.

The spatial description of a cluster is an ellipsoid. The cluster is oriented towards the TX so that the width, depth, and height of the cluster represent azimuth, delay, and elevation spread respectively. In this thesis, the analysis is restricted to include azimuth and delay spread. Hence, the contribution of a cluster consisting of N_L components originating from transmit antenna m to the baseband measurement on receive antenna n will be modeled as

$$y_{n,m}^{(c)}(t) = \sum_{l=1}^{N_L} a_{n,m}^{(l)} \exp\{-i2\pi \frac{f_c}{v_c} \langle \boldsymbol{p}_n(t), \boldsymbol{\varrho}(\phi^{(l)}) \rangle\}, \tag{2.25}$$

where $\phi^{(l)} \sim \mathcal{U}(\phi_0 - \overline{\mu}_\phi, \phi_0 + \overline{\mu}_\phi)$, $\arg\{a_{n,m}^{(l)}\} \sim \mathcal{U}(-\pi, \pi)$, and $|a_{n,m}^{(l)}| = 1, \ \forall\, l \in \{1, \ldots, N_L\}$. Furthermore, ϕ_0 is the center of the cluster and $\overline{\mu}_\phi$ is the azimuth spread of the cluster. If N_C clusters are present in the environment, the total response from all cluster on the baseband signal will be

$$y_{n,m}^{C} = \sum_{c=1}^{N_C} y_{n,m}^{(c)}(t). \tag{2.26}$$

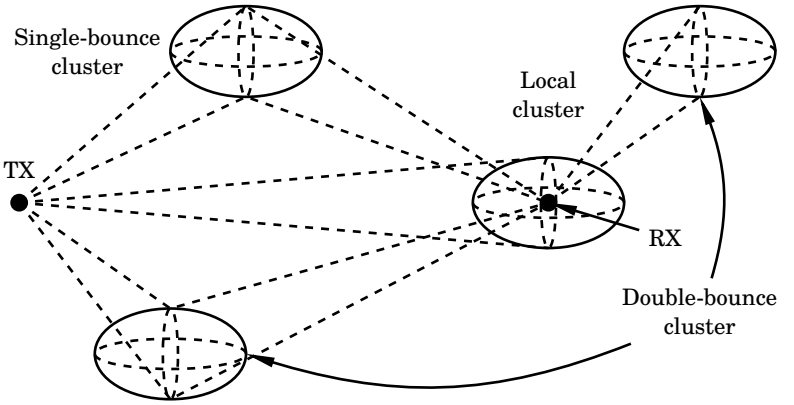

Figure 2.11 Cluster types in the COST 2100 radio channel model. The local cluster is a description of scatterers near the receiver. The single bounce cluster describes a scattering object that resides between the transmitter and the receiver while the double-bounce cluster contains two identical images of one cluster.

Cluster Characteristics

In [Zhu et al., 2013] and [Poutanen et al., 2011], different radio environments have been investigated with respect to occurrence of clusters and cluster parameters. In the former, two different outdoor radio channels, a non line-of-sight (NLOS) channel and a line-of-sight (LOS) channel, are characterized at a carrier frequency of 300 MHz while the latter focuses on indoor channels at 5.3 GHz. From the extensive set of channel parameters presented in the cited articles, Table 2.1 summarizes what we are interested in: the azimuth spread, delay spread, and the number of multipath components per cluster. The spread values are given using log-normal distributions to avoid negative values. Hence, the azimuth spread of a cluster can be drawn from the log-normal distribution as

$$\overline{\mu}_\phi \sim \mu_\phi 10^{\sigma_\phi \eta/10},$$

where μ_ϕ is the mean value for the azimuth spread, σ_ϕ is the standard deviation of the spread, and $\eta \sim \mathcal{N}(0,1)$ and similarly regarding the delay spread. However, since the mean delay spread corresponds to several wavelengths for carrier frequencies in cellular systems, it is justified to regard the complex MPC amplitude $a^{(l)},\ \forall\, l \in \{1,\ldots,N_L\}$ as a uniform random number on the unit circle.

Table 2.1 Number of multipath components per cluster, azimuth spread, and delay spread of the cluster for three different scenarios. Scenario 1 and 2 correspond to the NLOS and LOS outdoor channels of [Zhu et al., 2013], while scenario 3 is the indoor scenario of [Poutanen et al., 2011].

		1	**2**	**3**
Carrier frequency [GHz]	f_c	0.3	0.3	5.3
Number of MPCs [-]	N_L	27	48	4
Mean of azimuth spread [deg]	μ_ϕ	14.8	19.0	3.57
Std. of azimuth spread [dB]	σ_ϕ	2.68	2.03	2.05
Mean of delay spread [μs]	μ_τ	0.14	0.32	$1.16 \cdot 10^{-3}$
Std. of delay spread [dB]	σ_τ	3.66	2.05	3.65

2.4 Receiver Imperfections Modeling

The local oscillators of the transmitter and the receiver in the channel model in Section 2.2 were assumed to be perfectly synchronized. The local oscillators found in the base stations are usually of high quality and experience minor drift. A closer look at the receiver reveals that especially noise in the local oscillator will be transformed into a phase/frequency error of the receiver. The frequency error will accumulate into a phase error which slowly deteriorates the radio map and thereby limits the information the radio signal gives to the sensor fusion algorithm for the joint position and radio channel estimation. Consequently, it is important to model the phase noise carefully.

The local oscillator output of the receiver can be modeled as

$$z(t) = a(t)\cos(2\pi f_c t + \xi(t)), \tag{2.27}$$

where $\xi(t)$ is a perturbation of the phase of the output signal, f_c is the carrier frequency and $a(t)$ is the amplitude. If $\xi(t)$ is assumed to be small, then

$$z(t) \approx a(t)\cos(2\pi f_c t) - a(t)\xi(t)\sin(2\pi f_c t). \tag{2.28}$$

Thus, the perturbation is modulated onto the carrier frequency and this noise is termed *phase noise*. It can be quantified as the noise power in a 1 Hz band at an offset of Δf from the carrier frequency. The spectral noise density then becomes

$$\mathcal{S}(\Delta f) = 10\log\left(\frac{S_\xi(f_c + \Delta f)}{P(f_c)}\right) \quad \left[\frac{\text{dBc}}{\text{Hz}}\right], \tag{2.29}$$

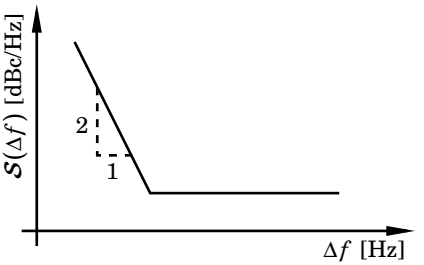

Figure 2.12 Output phase noise from the local oscillator of the receiver as a function of frequency offset from the carrier Δf in logarithmic scale. In practice, the spectrum is more complicated but this simplification is deemed to capture the largest error contribution.

where $P(f_c)$ denotes the signal power of the carrier frequency and $S_\xi(f)$ is the noise power per unit frequency noise power spectral density of $\xi(t)$ in (2.28) at frequency f. A simplified output noise spectrum of the local oscillator is shown in Figure 2.12.

The noise in the oscillator can be divided into different parts; a noise floor with flat noise power at large offset frequencies and a $1/f^2$ part near the carrier. The noise floor is due to thermal noise in the circuits while the $1/f^2$ noise comes from electronic noise in the oscillator circuits. However, in practice both $1/f$ and $1/f^3$ noise is typically present in the output of the oscillator [Staszewski et al., 2005]. We decide to limit the analysis to the white noise floor and the $1/f^2$ noise. As in [Staszewski et al., 2005], the noise floor part can be seen as an uncertainty of the phase in the oscillator output (2.28). Since the error from one time step to another is approximately independent, it is modeled as white Gaussian noise on $z(t)$. Furthermore, the $1/f^2$ part is modeled as an accumulative process leading to a drift in the phase of the oscillator. To model this effect, an integrator

$$v(t) = \int_0^t \delta_f(\tau)\, d\tau \tag{2.30}$$

is introduced where $\delta_f(t)$ is a frequency error in Hz which is added to the argument of $y^R_{n,m}(t)$ and $y^C_{n,m}(t)$ from (2.24) and (2.26) respectively.

Several other types of imperfections exist in the transmitters and the receivers, e.g., nonlinearities and thermal noise in the amplifiers, noise from digital and analog converters, and radio signal interference but for simplicity they are all approximated to be covered by the zero mean circular symmetric complex Gaussian noise $\boldsymbol{e}(t)$, see Figure 2.2.

2.5 Summary

The baseband signal, measured on receive antenna n when transmit antenna m is active is the sum of N_R specular components $y^R_{n,m}$ and the contribution from the clusters $y^C_{n,m}$. After adding the contribution of the frequency error from (2.30) to $y^R_{n,m}\ \forall\ (n,m)$ as well as scaling the positions with $2\pi\dfrac{f_c}{v_c}$ and the frequency error δ_f with 2π, (2.24) becomes

$$y^R_{n,m}(t) = \sum_{r=1}^{N_R} a^{(r)}_{n,m}(t)\exp\{-i\langle \boldsymbol{p}_n(t), \boldsymbol{\varrho}[\phi^{(r)}(t)]\rangle - i\nu(t)\}, \tag{2.31}$$

and similarly for the contribution from the clusters in (2.26)

$$\begin{aligned} y^C_{n,m}(t) &= \sum_{c=1}^{N_C} y^{(c)}_{n,m}(t) \\ y^{(c)}_{n,m}(t) &= \sum_{l=1}^{N_L} a^{(l)}_{n,m}\exp\{-i\langle \boldsymbol{p}_n(t), \boldsymbol{\varrho}[\phi^{(l)}(t)]\rangle - i\nu(t)\}. \end{aligned} \tag{2.32}$$

In both equations $\boldsymbol{p}_n(t)$ denotes the location of the nth receive antenna at time t with respect to its initial position $\boldsymbol{p}_n(t_0)$. The derived equation gives a connection between the AoA of the impinging MPCs and how the channel fading pattern will vary with the position of the receiver. The sum of the two, with added zero mean circular symmetric complex Gaussian noise $e_{n,m}(t)$ becomes

$$y_{n,m}(t) = y^R_{n,m}(t) + y^C_{n,m}(t) + e_{n,m}(t). \tag{2.33}$$

3

Joint Radio Channel and Position State-Space Model

3.1 Inertial Measurement Unit

An IMU consists of accelerometers and gyroscopes and optionally magnetometers and pressure sensors. In order to be able to measure acceleration and rotation around all axes, three accelerometers and gyroscopes are needed. The gyroscope measures the angular velocity of the IMU's body coordinate frame with respect to the static coordinate frame. Rotation is thereby defined as the orientation of the body coordinate frame with respect to the static coordinate frame. The accelerometer measures the forces acting upon the device, in the coordinate frame of the IMU. Acceleration of the device leads to a displacement between the static coordinate frame and the body coordinate frame called translation. Rotation and translation is illustrated in Figure 3.1. The fixed coordinate frame is the coordinate system relative to which position and orientation is defined and it is hereafter called the *world frame* while the coordinate system attached to the moving body is called the *body frame*. All frames throughout the thesis are assumed to be right handed.

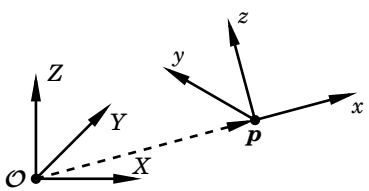

Figure 3.1 Translation and rotation of the body frame in relation to the world frame. The world frame is fixed in $\mathcal{O}$ while the body frame is translated to $\boldsymbol{p}$.

IMU Noise Sources

Various types of disturbances distort the IMU measurements. The main distortion contributors are random noise, bias, calibration errors, and temperature effects [Woodman, 2010]. Both the accelerometer and gyroscope are subject to these noise sources.

Random Noise The random noise from the accelerometer and gyroscope circuits is modeled as zero mean white Gaussian noise. For the gyroscope, the random noise will be integrated once when calculating the orientation resulting in so-called *angular random walk*. The standard deviation of the orientation will therefore grow proportionally to $\sqrt{t}$. The unit for the standard deviation of the angular random walk is usually given as $\text{deg}/\sqrt{\text{h}}$. However, the mean value of the orientation is unaffected by this noise since the integral of zero mean white Gaussian noise has zero mean.

For the accelerometer, the random noise is integrated once into a velocity random walk noise source. The unit for the standard deviation of the noise becomes $\text{m/s}/\sqrt{\text{h}}$. As mentioned before, position is obtained by double integration of the accelerometer signal. Thus, the noise from the accelerometer will also be integrated twice and the standard deviation of the position estimate will grow proportionally to $t^{3/2}$. The mean value is left unaffected due to the same reason as for the gyroscope.

Constant and Varying Bias If the IMU is kept at rest, the mean value of the measurements from the gyroscope might differ from zero. Possible reasons for this deviation are scale errors or periodic behavior in the circuits. This offset is called bias and usually consists of one constant part and one slowly time-varying part [Woodman, 2010]. The constant part can quite easily be removed with a calibration scheme such as in [Skog and Händel, 2006]. Any remaining calibration errors in the gyroscope will be integrated once leading to an orientation error that grows proportionally to t. The effect on the position is an error that grows proportionally to t^3 due to the constant error. The time-varying part must be modeled and is usually done so with a first-order Gaussian random walk process on the measurements, see [Woodman, 2010] and [Gustafsson, 2010]. For the gyroscope, this noise will be integrated once more into a second-order random walk process. The standard deviation of the angular random walk process will then have the unit $\text{deg}/\text{h}^{3/2}$.

The same applies to the accelerometer; the constant part of the bias can be removed by calibration but any remaining error will be integrated twice to obtain position. The time-varying offset is also modeled with a first-order random walk which yields a third-order random walk in the estimated position. The unit for the standard deviation of the position noise process is $\text{m}/\text{h}^{5/2}$.

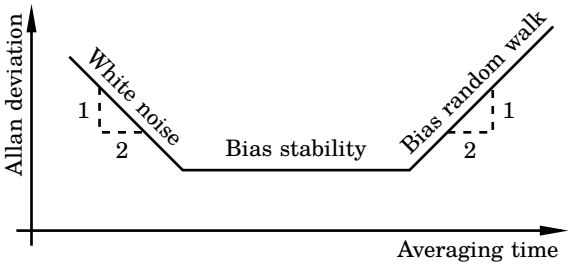

Figure 3.2 Typical log-log plot of the Allan deviation as a function of averaging time [IEEE Std 952-1997, 1998].

Note that in order to simulate a true bias stability process with the units of deg/h and m/h^2 for gyroscope and accelerometer respectively, a noise source with intensity $1/f$ must be used. Due to the challenge of simulating this, only $1/f^2$ noise is considered here giving the noise sources described previously [Staszewski et al., 2005; Kasdin, 1995]. The chosen noise sources have other properties but it is deemed to capture the noise behavior of the IMU needed in simulation during suitable time intervals.

Temperature Effects Temperature variations affect the accelerometers and gyroscopes as changing bias and noise levels, etc. The temperature dependence of the circuits can be modeled but this model will be difficult to obtain if no temperature information is available from the device used. Thus, the temperature dependence of the IMU sensors is left unmodeled.

Allan Variance

To determine which noise sources that are present in the measured signals, a technique known as *Allan variance* can be used. A thorough description of the technique can be found in [IEEE Std 952-1997, 1998]. To characterize the IMU, data is gathered over a long period of time when the IMU is kept at complete rest. The data sequence is then divided into N bins of length T. For each bin, the mean value is calculated giving a set of averages denoted by $[a(T)_1, \ldots, a(T)_N]$. The Allan variance for the averaging time T is calculated as

$$\mathrm{AVAR}(T) = \frac{1}{2(N-1)} \sum_{n=1}^{N-1} [a(T)_{n+1} - a(T)_n]^2.$$

The Allan deviation, $\mathrm{AD}(T) = \sqrt{\mathrm{AVAR}(T)}$, is plotted against the averaging interval T. A typical such curve is shown in Figure 3.2.

From the Allan deviation plot, the white noise intensity and bias stability can be obtained as well as other noise sources. The white noise gives a slope

of -0.5 at short averaging times. As more samples are lumped together and averaged, the variance of the mean value becomes lower. The bias stability can be determined by the flat part in the plot and the bias random walk is seen as the ramp with slope 0.5. If the signal contains correlated noise, it will be visible as a hump in the plot. In this work, random noise and bias are considered to be the two most important noise sources and are therefore modeled. The bias is modeled as a first-order random walk process, individual for each sensor axis. The measurements from the 3-axis accelerometer and gyroscope sensors in the body frame are denoted by $\boldsymbol{u}_{a,k}^b \in \mathbb{R}^3$ and $\boldsymbol{u}_{\omega,k}^b \in \mathbb{R}^3$ respectively and become

$$\boldsymbol{u}_{a,k}^b = \boldsymbol{a}_k^b + \boldsymbol{\delta}_{a,k} + \boldsymbol{n}_{a,k}, \tag{3.1a}$$

$$\boldsymbol{u}_{\omega,k}^b = \boldsymbol{\omega}_k^b + \boldsymbol{\delta}_{\omega,k} + \boldsymbol{n}_{\omega,k}, \tag{3.1b}$$

where k denotes sample index, $\boldsymbol{a}_k^b \in \mathbb{R}^3$ are the acceleration forces acting on the three axes of the device measured in m/s^2, and $\boldsymbol{\omega}_k^b \in \mathbb{R}^3$ is the angular velocity of the device measured in rad/s. Furthermore, $\boldsymbol{\delta}_{a,k} \in \mathbb{R}^3$ and $\boldsymbol{\delta}_{\omega,k} \in \mathbb{R}^3$ are modeled as independent first-order random walk processes given by

$$\boldsymbol{\delta}_{a,k+1} = \boldsymbol{\delta}_{a,k} + T_s \boldsymbol{n}_{\delta_a,k},$$
$$\boldsymbol{\delta}_{\omega,k+1} = \boldsymbol{\delta}_{\omega,k} + T_s \boldsymbol{n}_{\delta_\omega,k},$$

where T_s is sample time, $\boldsymbol{n}_{\delta_a,k}$ and $\boldsymbol{n}_{\delta_\omega,k}$ are zero mean white Gaussian noise processes with covariance matrices $\boldsymbol{\Sigma}_{\delta_a}$ and $\boldsymbol{\Sigma}_{\delta_\omega}$ respectively. Finally, the noise processes $\boldsymbol{n}_{a,k} \in \mathbb{R}^3$ and $\boldsymbol{n}_{\omega,k} \in \mathbb{R}^3$ are white Gaussian noise processes

$$\boldsymbol{n}_{a,k} \sim \mathcal{N}(\boldsymbol{0}, \boldsymbol{\Sigma}_a),$$
$$\boldsymbol{n}_{\omega,k} \sim \mathcal{N}(\boldsymbol{0}, \boldsymbol{\Sigma}_\omega),$$

where $\boldsymbol{\Sigma}_a$ and $\boldsymbol{\Sigma}_\omega$ are diagonal covariance matrices of appropriate sizes.

3.2 Kinematic Modeling

Kinematics is the dynamical description of how bodies move. To be able to predict or evaluate the likelihood of the movements, a kinematic model is of essence. The model derived here is for movements in three dimensions even though simulations and experiments in this thesis are carried out in two dimensions.

Orientation Representation

There are two widely used ways of representing rotation, Euler angles and quaternions [Gustafsson, 2010]. Euler angles represent the rotation

as three rotations around the coordinate axes. The Euler angles are easy to understand but suffer from singularities when two of the rotational axes coincide. The other representation, quaternions, does not have this shortcoming and will therefore be used in our work. A quaternion $\boldsymbol{q}$ is defined as

$$\boldsymbol{q} \triangleq \begin{bmatrix} q_0 & q_1 & q_2 & q_3 \end{bmatrix}^T = \begin{bmatrix} q_0 & \boldsymbol{q}_v^T \end{bmatrix}^T \in \mathbb{R}^4 \tag{3.2}$$

with the internal restriction

$$\|\boldsymbol{q}\|_2 = 1. \tag{3.3}$$

Let $\boldsymbol{p}^b = \begin{bmatrix} p_x^b & p_y^b & p_z^b \end{bmatrix}^T$ be a vector in the body frame and $\boldsymbol{q}$ the quaternion describing the relation between the body and the world frame. Rotation of the vector $\boldsymbol{p}^b$ from the body coordinate system to $\boldsymbol{p}^w = \begin{bmatrix} p_x^w & p_y^w & p_z^w \end{bmatrix}^T$ in the world frame is calculated as

$$\boldsymbol{p}^w = \mathbf{R}(\boldsymbol{q})\boldsymbol{p}^b, \tag{3.4}$$

where $\mathbf{R}(\boldsymbol{q})$ denotes a rotation matrix from body coordinates to world coordinates. The rotation matrix is given by

$$\mathbf{R}(\boldsymbol{q}) = \begin{bmatrix} q_0^2 + q_1^2 - q_2^2 - q_3^2 & 2q_1q_2 - 2q_0q_3 & 2q_1q_3 + 2q_0q_2 \\ 2q_1q_2 + 2q_0q_3 & q_0^2 - q_1^2 + q_2^2 - q_3^2 & 2q_2q_3 - 2q_0q_1 \\ 2q_1q_3 - 2q_0q_2 & 2q_2q_3 + 2q_0q_1 & q_0^2 - q_1^2 - q_2^2 + q_3^2 \end{bmatrix}. \tag{3.5}$$

Continuous Time Dynamics

Let the orientation of a rigid body be represented by the quaternion $\boldsymbol{q}$ and let the angular velocity of the body be $\boldsymbol{\omega}$. The continuous state dynamics for the quaternion written with matrix multiplication is [Kuipers, 1999; Coutsias and Romero, 1999]

$$\dot{\boldsymbol{q}}(t) = \frac{1}{2}\mathbf{P}[\boldsymbol{q}(t)]\boldsymbol{\omega}(t) = \frac{1}{2}\mathbf{Q}[\boldsymbol{\omega}(t)]\boldsymbol{q}(t), \tag{3.6}$$

where

$$\mathbf{P}(\boldsymbol{q}) = \begin{bmatrix} -q_1 & -q_2 & -q_3 \\ q_0 & -q_3 & q_2 \\ q_3 & q_0 & -q_1 \\ -q_2 & q_1 & q_0 \end{bmatrix} \tag{3.7}$$

and

$$\mathbf{Q}(\boldsymbol{\omega}) = \begin{bmatrix} 0 & -\omega_x & -\omega_y & -\omega_z \\ \omega_x & 0 & \omega_z & -\omega_y \\ \omega_y & -\omega_z & 0 & \omega_x \\ \omega_z & \omega_y & -\omega_x & 0 \end{bmatrix} \tag{3.8}$$

with $\boldsymbol{\omega} = \begin{bmatrix} \omega_x & \omega_y & \omega_z \end{bmatrix}^T$.

For translation, there are several different motion models available [Li and Jilkov, 2003]. If the movement of the object is constrained, e.g., a car can not drive sideways, there are models that include this constraint. In our scenario, the choice is to assume no prior information about the movement of the device. This is provided by the Newton equations for free body movement. The relationship between position, velocity, and acceleration is given by

$$\dot{\boldsymbol{p}}(t) = \boldsymbol{v}(t), \tag{3.9a}$$

$$\dot{\boldsymbol{v}}(t) = \boldsymbol{a}(t), \tag{3.9b}$$

where $\boldsymbol{p}(t) \triangleq \begin{bmatrix} p_x(t) & p_y(t) & p_z(t) \end{bmatrix}^T$, and $\boldsymbol{v}(t) \triangleq \begin{bmatrix} v_x(t) & v_y(t) & v_z(t) \end{bmatrix}^T$ are the position and velocity in the world frame at time t respectively. Before the position and velocity states can be updated using the accelerometer measurements from an IMU, they have to be rotated from the body frame to the world frame using (3.5), and the contribution of the gravity $\bar{\boldsymbol{g}} \triangleq \begin{bmatrix} 0 & 0 & g \end{bmatrix}^T$ must be canceled. Together, these operations yield

$$\boldsymbol{a}^w(t) = \mathbf{R}[\boldsymbol{q}(t)]\boldsymbol{a}^b(t) - \bar{\boldsymbol{g}}, \tag{3.10}$$

where $\boldsymbol{a}^w(t)$ will be used as the time derivative of the velocity in (3.9b).

Discrete Time Dynamics

The continuous dynamic models above must be discretized to fit the estimation framework later. The rotational dynamics in (3.6) are discretized as [Gustafsson, 2010]

$$\boldsymbol{q}_{k+1} = \left\{ \mathbf{I}_4 + \frac{T_s}{2}\mathbf{Q}(\boldsymbol{\omega}_k) \right\} \boldsymbol{q}_k + \frac{T_s}{2}\mathbf{P}(\boldsymbol{q}_k)\boldsymbol{n}_{\omega,k} \tag{3.11}$$

and the translational dynamics in (3.9) are discretized as

$$\boldsymbol{p}_{k+1} = \boldsymbol{p}_k + T_s\boldsymbol{v}_k + \frac{T_s^2}{2}\boldsymbol{a}_k \tag{3.12a}$$

$$\boldsymbol{v}_{k+1} = \boldsymbol{v}_k + T_s\boldsymbol{a}_k. \tag{3.12b}$$

When the IMU measurement equations from (3.1) are inserted and the bias states are included, the state equations of the kinematics are given by

$$\boldsymbol{p}_{k+1} = \boldsymbol{p}_k + T_s\boldsymbol{v}_k + \frac{T_s^2}{2}\left\{ \mathbf{R}(\boldsymbol{q}_k)[\boldsymbol{u}_{a,k}^b + \boldsymbol{\delta}_{a,k}] - \bar{\boldsymbol{g}} + \boldsymbol{n}_{a,k} \right\} \tag{3.13a}$$

$$\boldsymbol{v}_{k+1} = \boldsymbol{v}_k + T_s\left\{ \mathbf{R}(\boldsymbol{q}_k)[\boldsymbol{u}_{a,k}^b + \boldsymbol{\delta}_{a,k}] - \bar{\boldsymbol{g}} + \boldsymbol{n}_{a,k} \right\} \tag{3.13b}$$

$$\boldsymbol{\delta}_{a,k+1} = \boldsymbol{\delta}_{a,k} + T_s\boldsymbol{n}_{\delta_a,k} \tag{3.13c}$$

$$\boldsymbol{q}_{k+1} = \left\{ \mathbf{I}_4 + \frac{T_s}{2}\mathbf{Q}(\boldsymbol{u}_{\omega,k}^b + \boldsymbol{\delta}_{\omega,k}) \right\} \boldsymbol{q}_k + \frac{T_s}{2}\mathbf{P}(\boldsymbol{q}_k)\boldsymbol{n}_{\omega,k} \tag{3.13d}$$

$$\boldsymbol{\delta}_{\omega,k+1} = \boldsymbol{\delta}_{\omega,k} + T_s\boldsymbol{n}_{\delta_\omega,k}, \tag{3.13e}$$

where $\mathbf{I}_4$ is the unit matrix of size 4 and T_s is the sample time. In total, 16 states are used to describe the kinematics of a rigid body. In the discretization step, without loss of generality, the sign on the bias states and the white noise processes for both accelerometer and gyroscope has been changed. Note that (3.13d) does not preserve the relation (3.3). This will be dealt with when implementing algorithms for state estimation.

3.3 Joint Radio Channel and Kinematic Modeling

The radio channel model presented in Chapter 2 introduced two parameters for each MPC, the complex amplitude and the angle of arrival. The AoA was assumed to be independent of the transmit-receive antenna pair. Adding to these two is the frequency error δ_f, which is assumed common for all MPCs. These parameters will now be added as states in the model. The complex MPC amplitude is separated into two individual states as

$$\begin{aligned} \alpha(t) &\triangleq |a(t)| \\ \beta(t) &\triangleq \arg\{a(t)\}. \end{aligned} \tag{3.14}$$

The absolute value of the complex MPC amplitude is regarded independently of the antenna pairs considered, but the phase varies since the physical displacement between the antenna elements leads to a difference in phase offset. Let vector $\boldsymbol{z}_n \in \mathbb{R}^3$ be the displacement between the center of the IMU, denoted $\boldsymbol{p}$, and the nth receive antenna. Then,

$$\boldsymbol{p}_n = \boldsymbol{p} + \mathbf{R}[\boldsymbol{q}]\boldsymbol{z}_n, \tag{3.15}$$

and $\boldsymbol{z}_n,\ \forall\, n = \{1, \ldots, M_R\}$ are assumed known. The phase offset due to receive antenna displacement can thereby be accounted for. Hence, β is modeled as dependent on the transmit antenna and a particular MPC. Adding the phase error $\nu(t)$ to all βs makes β an integrator of the frequency error. The absolute value, the AoA, and the frequency error are all modeled as random walk processes and the dynamic equations for the states become

$$\phi_{k+1} = \phi_k + T_s n_{\phi,k}, \tag{3.16a}$$

$$\alpha_{k+1} = \alpha_k + T_s n_{\alpha,k}, \tag{3.16b}$$

$$\beta_{k+1} = \beta_k + T_s \delta_{f,k} + T_s n_{\beta,k} + \frac{T_s^2}{2} n_{\delta,k} \tag{3.16c}$$

$$\delta_{f,k+1} = \delta_{f,k} + T_s n_{\delta,k} \tag{3.16d}$$

where $n_\phi, n_\alpha, n_\beta,$ and n_δ are white Gaussian noise processes. By choosing a random walk process for the complex amplitude, any path loss variation that

arises as the distance to the transmitter changes, is not modeled. However, the model can still track a changing amplitude.

We assume that there is no mutual information between the different MPCs except for the frequency error that is common for all. Consequently, equations (3.16a) – (3.16c) are reused for all ϕ, α, and β. The noise term n_β is kept as a roughening noise term to let the phases slowly drift even though they are assumed to be constant.

For the clusters presented in Section 2.3, the angular spread is so small that they are not individually resolvable. Also, since the number of states in the filter grows proportionally to N_R, the number of states needed to track all components of a cluster would rule out this modeling approach. Instead, a cluster will be modeled as a single multipath component with one exception. In the cluster model (2.25), the βs are unique for every cluster component and consequently the interference pattern between the components will not be the same for different transmit antennas. Therefore, the absolute value of the complex MPC amplitude must be separated for different transmit antennas. To investigate the change rate of the amplitude such a model imposes, 20000 datasets with each of the three clusters in Table 2.1 is generated and the amplitude change rate is calculated as the receiver is moving in a straight line with a heading ranging from a perpendicular movement to straight towards the cluster. The result is presented in Figure 3.3. From the figure it is seen that moving perpendicularly to the cluster gives the largest amplitude change rates and the rate drops as the movement is directed towards the cluster. The change rates are considerably larger than what the amplitude of a distinct MPC is believed to be.

All the states are added to the state vector, which now becomes

$$\begin{aligned} \boldsymbol{x} = \begin{bmatrix} \boldsymbol{p}^T & \boldsymbol{v}^T & \boldsymbol{\delta}_a^T & \boldsymbol{q}^T & \boldsymbol{\delta}_\omega^T & \boldsymbol{\phi}^T & \boldsymbol{\alpha}^T & \boldsymbol{\beta}^T & \delta_f \end{bmatrix}^T \\ \in \mathbb{R}^{17+N_R(2+M_T)+N_C(1+2M_T)}, \end{aligned} \tag{3.17}$$

where N_R is the number of MPCs present in the radio channel, N_C is the number of clusters present, M_T is the number of transmit antennas, and

$$\begin{aligned} \boldsymbol{\phi} &= \begin{bmatrix} \phi_1^R & \dots & \phi_{N_R}^R & \phi_1^C & \dots & \phi_{N_C}^C \end{bmatrix}^T \in \mathbb{R}^{N_R+N_C} \\ \boldsymbol{\alpha} &= \begin{bmatrix} \alpha_1^R & \dots & \alpha_{N_R}^R & \alpha_{1,1}^C & \dots & \alpha_{1,N_C}^C & \dots & \alpha_{M_T,N_C}^C \end{bmatrix}^T \in \mathbb{R}^{N_R+N_C M_T} \\ \boldsymbol{\beta} &= \Big[\beta_{1,1}^R \quad \dots \quad \beta_{1,N_R}^R \quad \dots \quad \beta_{M_T,N_R}^R \\ &\qquad \beta_{1,1}^C \quad \dots \quad \beta_{1,N_R}^C \quad \dots \quad \beta_{M_T,N_C}^C \Big]^T \in \mathbb{R}^{M_T(N_R+N_C)}. \end{aligned}$$

Equations (3.13) together with (3.16) is the final dynamic state-space representation of the kinematics and the radio channel model together. The

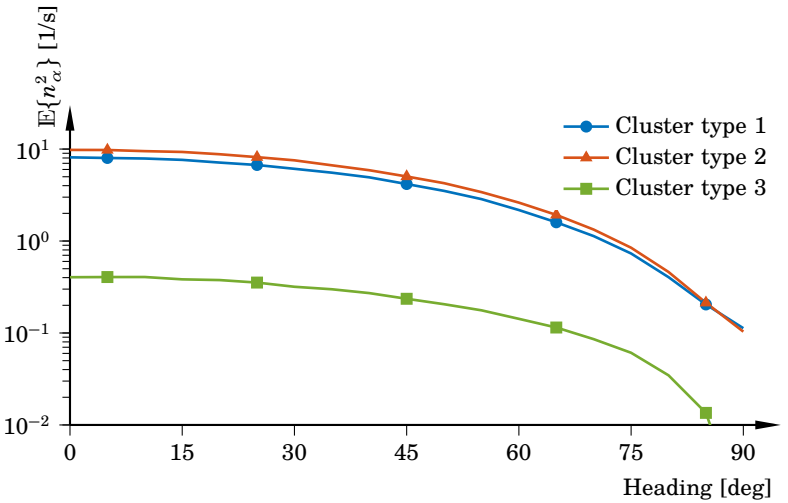

Figure 3.3 Amplitude change rate as a function of movement heading for the three different clusters in Table 2.1. The cluster is located at 90 deg and consequently a heading of 0 deg equals a movement perpendicular to the cluster. The cluster energy is normalized to 1.

equation from (2.33) is sampled with sample rate T_s and becomes

$$y_{n,m,k} = y^R_{n,m,k} + y^C_{n,m,k} + e_{n,m,k} \tag{3.18}$$

where $e_{n,m,k}$ is zero mean circular symmetric complex Gaussian noise,

$$y^R_{n,m,k} = \sum_{r=1}^{N_R} \alpha^R_{r,k} \exp\{-i\beta^R_{m,r,k}\} \exp\{-i\langle \boldsymbol{p}_{n,k}, \boldsymbol{\varrho}(\phi^R_{r,k})\rangle\}, \tag{3.19}$$

and

$$y^C_{n,m,k} = \sum_{c=1}^{N_C} \alpha^C_{m,c,k} \exp\{-i\beta^C_{m,c,k}\} \exp\{-i\langle \boldsymbol{p}_{n,k}, \boldsymbol{\varrho}(\phi^C_{c,k})\rangle\}. \tag{3.20}$$

Remember that $\boldsymbol{p}_{n,k}$ is normalized with the constant $2\pi\frac{f_c}{v_c}$ to facilitate the notation, i.e., distances are measured in the unit of wavelengths. The equation (3.18) will be referred to as the *measurement equation* in subsequent chapters.

Observability of the States

Since all MPCs are assumed to impinge on the receiver in 2D, neither the measurement equation (3.18) nor any other states depend on the position

along the z-axis. This state is therefore unobservable in this model. The estimated position along the z-axis will therefore be the dead reckoning estimate. To include estimation of p_z, the elevation angle θ mentioned in Section 2.2 can be used. Another possibility would be to include pressure sensors in the IMU if they provide enough accuracy. Furthermore — as long as the receiver unit has a displacement between the antennas and the IMU center — the yaw angle, i.e., the rotation of the unit around the z-axis, is observable.

4

Nonlinear Estimation Techniques

In an ideal case, all variables of a system are measurable. In the real world this is however not the case; some quantities are difficult to measure with reasonable accuracy under given noise levels or simply impossible to measure at all. In such cases, we have to rely on an estimation. When estimating, an estimate is sought of a latent variable given a set of noisy measurements that are dependent on the latent variable. Furthermore, we also seek an optimal estimate given some criterion by which the estimator can be evaluated. A natural criterion is to minimize the mean square error,

$$\text{minimize} \quad \mathbb{E}\{\|\hat{\boldsymbol{x}} - \boldsymbol{x}\|^2\},$$

where $\hat{\boldsymbol{x}}$ is a vector containing the estimates and $\boldsymbol{x}$ are the true values of the latent variables. For practical purposes such an estimator is generally not available, so instead the estimator has to be restricted. If the problem of finding the estimator is restricted to the linear class, i.e., the estimator is linear in the measurements, then the well-known least squares solution turns out to be the minimum mean square error (MMSE) estimator [Kay, 1993]. This estimator falls in the category of batch estimators, i.e., it collects a set of measurements and finds the best linear estimate of the latent variable. Another class of estimators is the recursive estimators where instead the samples are processed one at a time and the estimate is updated recursively given the new information provided by the measurements. This kind of estimators are suitable for online estimation or where the underlying latent variables are constantly changing. One of the most widely used estimators of this kind is the Kalman filter [Kalman, 1960]. In this thesis we will use both kind of estimators; they will be addressed in this chapter.

4.1 Recursive State-Space Estimation

Consider the discrete state-space model

$$\boldsymbol{x}_{k+1} = \boldsymbol{f}(\boldsymbol{x}_k, \boldsymbol{u}_k, \boldsymbol{n}_k) \tag{4.1a}$$

$$\boldsymbol{y}_k = \boldsymbol{h}(\boldsymbol{x}_k) + \boldsymbol{e}_k, \tag{4.1b}$$

where $\boldsymbol{x}_k \in \mathbb{R}^{n_x}$ is the state vector at sample k, $\boldsymbol{y}_k \in \mathbb{R}^{n_y}$ is the measurement vector, $\boldsymbol{u}_k \in \mathbb{R}^{n_u}$ the exogenous signal vector, and $\boldsymbol{n}_k \in \mathbb{R}^{n_w}$ and $\boldsymbol{e}_k \in \mathbb{R}^{n_y}$ are noise processes acting on the states and measurements respectively. Furthermore, $\boldsymbol{f} : \mathbb{R}^{n_x} \times \mathbb{R}^{n_u} \times \mathbb{R}^{n_n} \to \mathbb{R}^{n_x}$ are the dynamic equations and $\boldsymbol{h} : \mathbb{R}^{n_x} \to \mathbb{R}^{n_y}$ are the measurement equations, both sets of functions are potentially nonlinear. Clearly, the state-space model is a recursive formulation where the state vector propagates with time and produces a set of measurements for each sample point k.

Let the posterior state distribution be denoted by $p(\boldsymbol{x}_{s:k}|\boldsymbol{y}_{1:K})$, $s \leq k$, where $\boldsymbol{x}_{s:k} \triangleq \{\boldsymbol{x}_s, \ldots, \boldsymbol{x}_k\}$ and $\boldsymbol{y}_{1:K} \triangleq \{\boldsymbol{y}_1, \ldots, \boldsymbol{y}_K\}$. Depending on the choice of s and k, three different estimation problems can be formulated.

- If $s \leq k < K$ the problem is called smoothing.
- If $s = k = K$ the problem is called filtering.
- If $k \geq s > K$ the problem is called prediction.

In this thesis we will deal with filtering and prediction but smoothing could be interesting for future research, see Section 9.1.

The Kalman Filter

As mentioned before, one of the most widely used filters for state-space estimation is the Kalman filter [Kalman, 1960] which is an elegant recursive formulation of the filtering problem. The original formulation of the filter is applicable for linear systems with additive Gaussian noise processes $\boldsymbol{n}$ and $\boldsymbol{e}$. It represents the states by a Gaussian distribution and the linear transformation of updating the states and the measurement equation maintains the Gaussianity. The Kalman filter has several nice properties, e.g., it minimizes the mean square error as $K \to \infty$ and convergence of the estimate to the true state vector is guaranteed if the noise covariance matrices for $\boldsymbol{n}$ and $\boldsymbol{e}$ are positive definite.

For the more general problem of state estimation, where the state equations are nonlinear, a problem arises. A nonlinear transform of a Gaussian distribution does not preserve the Gaussianity. To tackle this problem, two commonly used formulations are available: the extended Kalman filer (EKF) [Anderson and Moore, 2012] and the unscented Kalman filter (UKF)

[Julier and Uhlmann, 2004]. The EKF propagates the covariance of the states and the measurements using linearized equations instead, while the UKF propagates sigma points through the nonlinearity and approximates a Gaussian distribution to these propagated sigma points. Both formulations thereby maintain a Gaussian description of the states but the convergence of the filters is not guaranteed anymore. Still, the formulations are widely and successfully used in many nonlinear scenarios. The equations for the extended Kalman filter are given in Algorithm 4.1.

Algorithm 4.1—The extended Kalman filter

Input: Initial state estimate $\hat{\boldsymbol{x}}_{1|0}$, and initial covariance $\mathbf{P}_{1|0}$.
State noise covariance matrix $\mathbf{Q}_k$
Measurement noise covariance matrix $\mathbf{R}_k$.

1: **for** $k = 1$ **to** K **do**

2: Measurement update:

$$\hat{\boldsymbol{x}}_{k|k} = \hat{\boldsymbol{x}}_{k|k-1} + \mathbf{K}_k[\boldsymbol{y}_k - \boldsymbol{h}(\hat{\boldsymbol{x}}_{k|k-1})] \tag{4.2a}$$

$$\mathbf{P}_{k|k} = [\mathbf{I}_{n_x} - \mathbf{K}_k\mathbf{H}_k]\mathbf{P}_{k|k-1} \tag{4.2b}$$

$$\mathbf{K}_k = \mathbf{P}_{k|k-1}\mathbf{H}_k^T[\mathbf{H}_k\mathbf{P}_{k|k-1}\mathbf{H}_k^T + \mathbf{R}_k]^{-1} \tag{4.2c}$$

$$\mathbf{H}_k = \left.\frac{\partial \boldsymbol{h}(\boldsymbol{x})}{\partial \boldsymbol{x}^T}\right|_{\boldsymbol{x}=\hat{\boldsymbol{x}}_{k|k-1}}$$

3: Time update:

$$\hat{\boldsymbol{x}}_{k+1|k} = \boldsymbol{f}(\hat{\boldsymbol{x}}_{k|k}, \boldsymbol{u}_k, \mathbf{0}) \tag{4.3a}$$

$$\mathbf{P}_{k+1|k} = \mathbf{F}_k\mathbf{P}_{k|k}\mathbf{F}_k^T + \mathbf{G}_k\mathbf{Q}_k\mathbf{G}_k^T \tag{4.3b}$$

$$\mathbf{F}_k = \left.\frac{\partial \boldsymbol{f}(\boldsymbol{x}, \boldsymbol{u}, \boldsymbol{n})}{\partial \boldsymbol{x}^T}\right|_{\substack{\boldsymbol{x}=\hat{\boldsymbol{x}}_{k|k},\\ \boldsymbol{u}=\boldsymbol{u}_k}} \quad \mathbf{G}_k = \left.\frac{\partial \boldsymbol{f}(\boldsymbol{x}, \boldsymbol{u}, \boldsymbol{n})}{\partial \boldsymbol{n}^T}\right|_{\substack{\boldsymbol{x}=\hat{\boldsymbol{x}}_{k|k}\\ \boldsymbol{u}=\boldsymbol{u}_k}}$$

4: **end for**

Output: Posterior state estimate $\hat{\boldsymbol{x}}_{K|K}$ and posterior covariance $\mathbf{P}_{K|K}$ ■

Note that the formulation in Algorithm 4.1 is applicable for the linear case as well. In such a case, the derivatives become trivial. For the UKF algorithm, refer to [Julier and Uhlmann, 2004].

The Particle Filter

The nonlinear state estimator that has gained the largest attention in the last decade is the particle filter [Gordon et al., 1993; Doucet et al., 2000b; Arulampalam et al., 2001]. The underlying idea of the particle filter is to represent the state posterior distribution $p(\boldsymbol{x}_k|\boldsymbol{y}_{1:k})$ using *particles*, each

carrying a hypothesis of the state vector $\hat{\boldsymbol{x}}_k$ and a weight w_k as a measure of the likelihood of that hypothesis when evaluated against the measurements [Arulampalam et al., 2001]. The posterior filtering distribution is then represented by the particles. The main benefits of the particle filter compared to the EKF and UKF are that nonlinearities can be dealt with without making linearizations and that the posterior distribution is no longer limited to a Gaussian distribution. The particle filter has found its use in many different applications and there are also extensions, e.g., for the smoothing problem [Godsill et al., 2004]. A derivation of the particle filter can be found in Appendix A. The recursive formulation of the filter with a measurement update and a time update, similar to the structure of the Kalman filter of the filter, is given in Algorithm 4.2 and the approximation of the posterior distribution can be written as

$$\hat{p}(\boldsymbol{x}_k|\boldsymbol{y}_{1:k}) \propto \sum_{i=1}^{N_p} w_{k|k}^{(i)} \delta(\boldsymbol{x}_k - \tilde{\boldsymbol{x}}_k^{(i)}), \tag{4.4}$$

where $\delta(\cdot)$ is the Dirac delta function.

Resampling The particle filter has a problem with degeneracy or depletion which means that after a few time steps, most particles have negligible weight. The implication is that the approximation of the posterior distribution $\hat{p}(\boldsymbol{x}_k|\boldsymbol{y}_{1:k})$ will be concentrated to a few particles. To make sure that the approximation is a good description of the true posterior distribution, the particles are *resampled*. The resampling is carried out using draw and replace so that particles having a large weight w are more likely to be reproduced several times compared to particles with low weights. The resampling step has some theoretical implications for the filter but it has proven to be a good solution for the depletion problem, see [Gordon et al., 1993; Gustafsson, 2010]. Resampling can be performed in every time step but in order to save time, we resample when the effective number of particles, calculated as

$$N_{\text{eff}} = \left[\sum_{i=1}^{N_p} \left(w_{k|k}^{(i)} \right)^2 \right]^{-1}, \tag{4.5}$$

drops below a predetermined level N_{th}. After resampling has been performed, the weights are reinitialized as $w_{k|k}^{(i)} = 1/N_p, \ \forall\, i \in \{1, \ldots, N_p\}$.

Convergence The convergence of the particle filter is sensitive to the initialization of the states as opposed to the Kalman filter which always converges given positive definite covariance matrices. For the particle filter, the state estimates might converge to a local maximum in the likelihood function and the filter will be unable to find the global maximum. To

facilitate convergence to the global optimum an initialization algorithm to the filter, tailored to our estimation problem, will be derived in Section 4.2.

Algorithm 4.2—The particle filter

Input: Particles $\boldsymbol{x}_{1|0}^{(i)} \sim p(\boldsymbol{x}_{1|0})$ and weights $w_{1|0}^{(i)} = 1/N_p,\ \forall\, i \in \{1, \ldots, N_p\}$.

1: **for** $k = 1$ **to** K **do**

2: Measurement update: evaluate importance weights as

$$w_{k+1|k}^{(i)} = \frac{p(\boldsymbol{y}_k|\boldsymbol{x}_k^{(i)})}{\sum_{j=1}^{N_p} p(\boldsymbol{y}_k|\boldsymbol{x}_k^{(j)}) w_{k|k-1}^{(j)}} w_{k|k-1}^{(i)},\ \forall\, i \in \{1, \ldots, N_p\}.$$

3: **if** $N_{\text{eff}} < N_{\text{th}}$ **then**

4: Resample N_p particles using draw and replace with weights $w_{k+1|k}^{(i)}$.

5: Reinitialize weights to $w_{k+1|k}^{(i)} = 1/N_p,\ \forall\, i \in \{1, \ldots, N_p\}$.

6: **end if**

7: Time update: draw new particles from the proposal distribution as

$$\boldsymbol{x}_{k+1}^{(i)} \sim q(\boldsymbol{x}_{k+1|k}^{(i)}|\boldsymbol{x}_{1:k}^{(i)}, \boldsymbol{y}_{1:k}),\ \forall\, i \in \{1, \ldots, N_p\}.$$

8: **end for**

Output: Posterior distribution $\hat{p}(\boldsymbol{x}_K|\boldsymbol{y}_{1:K})$, see (4.4). ■

The Marginalized Particle Filter

By representing the posterior distributions with particles instead of using mean and covariance, as in the Kalman filter, the posterior distributions can now be non-Gaussian. To obtain a good description of the filtering densities, the particles must cover the true distribution. Therefore, more particles are needed as the state dimension grows and the computing power and time needed for solving the problem then increases linearly with the number of particles, [Karlsson et al., 2005].

One solution to reduce the computational burden of the particle filter is to use marginalization of the linear states. This means that the state vector is split into a linear and a nonlinear part. The linear state vector holds the states that can be estimated by using a Kalman filter while the nonlinear state vector is still estimated by using the particle filter. This filter is called the marginalized particle filter or Rao-Blackwellized particle filter [Doucet et al., 2000a]. The derivations of the marginalized particle filter are long and have been left out but can be found in [Schön et al., 2005]. The filter is however summarized here for convenience.

Let $\boldsymbol{x}_k^l$ denote the linear state vector and $\boldsymbol{x}_k^n$ the nonlinear state vector at sample instant k. The system in (4.1) is rewritten as

$$\boldsymbol{x}_{k+1}^n = \boldsymbol{f}_k^n(\boldsymbol{x}_k^n) + \mathbf{A}_k^n(\boldsymbol{x}_k^n)\boldsymbol{x}_k^l + \mathbf{G}_k^n(\boldsymbol{x}_k^n)\boldsymbol{n}_k^n, \tag{4.6a}$$

$$\boldsymbol{x}_{k+1}^l = \boldsymbol{f}_k^l(\boldsymbol{x}_k^n) + \mathbf{A}_k^l(\boldsymbol{x}_k^n)\boldsymbol{x}_k^l + \mathbf{G}_k^l(\boldsymbol{x}_k^n)\boldsymbol{n}_k^l, \tag{4.6b}$$

$$\boldsymbol{y}_k = \boldsymbol{h}_k(\boldsymbol{x}_k^n) + \mathbf{C}_k(\boldsymbol{x}_k^n)\boldsymbol{x}_k^l + \boldsymbol{e}_k. \tag{4.6c}$$

The filtering algorithm for the decoupled case, i.e.,

$$\boldsymbol{n}_k = \begin{bmatrix} \boldsymbol{n}_k^n \\ \boldsymbol{n}_k^l \end{bmatrix} \sim \mathcal{N}(\mathbf{0}, \mathbf{Q}_k), \quad \mathbf{Q}_k = \begin{bmatrix} \mathbf{Q}_k^n & \mathbf{0} \\ \mathbf{0} & \mathbf{Q}_k^l \end{bmatrix}, \tag{4.7}$$

is summarized in Algorithm 4.3.

Algorithm 4.3—The marginalized particle filter

Input: Particles $\boldsymbol{x}_{1|0}^{n,(i)} \sim p(\boldsymbol{x}_{1|0}^n)$ and weights $w_{1|0}^{(i)} = 1/N_p,\ \forall\, i \in 1, \ldots, N_p$.
Initial state estimate $\boldsymbol{x}_{1|0}^{l,(i)} = \boldsymbol{x}_0^l$,
and initial covariance $\mathbf{P}_{1|0}^{(i)} = \mathbf{P}_0,\ \forall\, i \in 1, \ldots, N_p$,

1: **for** $k = 1$ **to** K **do**

2: Measurement update: evaluate importance weights as

$$\tilde{w}_{k+1|k}^{(i)} = p(\boldsymbol{y}_k | \boldsymbol{x}_{1:k}^{n,(i)}, \boldsymbol{y}_{1:k-1}) w_{k|k-1}^{(i)}, \tag{4.8}$$

and normalize as $w_{k+1|k}^{(i)} = \dfrac{\tilde{w}_{k+1|k}^{(i)}}{\sum_{j=1}^{N_p} \tilde{w}_{k+1|k}^{(j)}},\ \forall\, i \in \{1, \ldots, N_p\}$.

3: **if** $N_{\text{eff}} < N_{\text{th}}$ **then**

4: Resample N_p particles using draw and replace with weights $w_{k+1|k}^{(i)}$.

5: Reinitialize weights to $w_{k+1|k}^{(i)} = 1/N_p,\ \forall\, i \in \{1, \ldots, N_p\}$.

6: **end if**

7: Measurement update of the Kalman filter:

$$\begin{aligned}
\hat{\boldsymbol{x}}_{k|k}^{l,(i)} &= \hat{\boldsymbol{x}}_{k|k-1}^{l,(i)} + \mathbf{K}_k^{(i)}[\boldsymbol{y}_k - \boldsymbol{h}_k^{(i)} - \mathbf{C}_k \hat{\boldsymbol{x}}_{k|k-1}^{l,(i)}] \\
\mathbf{P}_{k|k}^{(i)} &= \mathbf{P}_{k|k-1}^{(i)} - \mathbf{K}_k^{(i)} \mathbf{S}_k^{(i)} [\mathbf{K}_k^{(i)}]^T \\
\mathbf{S}_k^{(i)} &= \mathbf{C}_k \mathbf{P}_{k|k-1}^{(i)} \mathbf{C}_k^T + \mathbf{R}_k \\
\mathbf{K}_k^{(i)} &= \mathbf{P}_{k|k-1}^{(i)} \mathbf{C}_k^T [\mathbf{S}_k^{(i)}]^{-1}
\end{aligned}$$

8: Draw new particles from the proposal distribution

$$\boldsymbol{x}_{k+1|k}^{n,(i)} \sim p(\boldsymbol{x}_{k+1|k}^n | \boldsymbol{x}_{1:k}^{n,(i)}, \boldsymbol{y}_{1:k}),\ \forall\, i \in \{1, \ldots N_p\}. \tag{4.9}$$

9: Time update of the Kalman filter:

$$\begin{aligned}
\hat{\boldsymbol{x}}_{k+1|k}^{l,(i)} &= \mathbf{A}_k^l \hat{\boldsymbol{x}}_{k|k}^{l,(i)} + \boldsymbol{f}_k^l + \mathbf{L}_k^{(i)}[\boldsymbol{x}_{k+1|k}^{n,(i)} - \boldsymbol{f}_k^n - \mathbf{A}_k^n \hat{\boldsymbol{x}}_{k|k}^{l,(i)}] \\
\mathbf{P}_{k+1|k}^{(i)} &= \mathbf{A}_k^l \mathbf{P}_{k|k}^{(i)} [\mathbf{A}_k^l]^T + \mathbf{G}_k^l \mathbf{Q}_k^l [\mathbf{G}_k^l]^T - \mathbf{L}_k^{(i)} \mathbf{M}_k^{(i)} [\mathbf{L}_k^{(i)}]^T \\
\mathbf{M}_k^{(i)} &= \mathbf{A}_k^n \mathbf{P}_{k|k}^{(i)} [\mathbf{A}_k^n]^T + \mathbf{G}_k^n \mathbf{Q}_k^n [\mathbf{G}_k^n]^T \\
\mathbf{L}_k^{(i)} &= \mathbf{A}_k^l \mathbf{P}_{k|k}^{(i)} [\mathbf{A}_k^n]^T [\mathbf{M}_k^{(i)}]^{-1}
\end{aligned}$$

10: **end for**

Output: Posterior distributions $\hat{p}(\boldsymbol{x}_K^n|\boldsymbol{y}_{1:K})$ and $\hat{p}(\boldsymbol{x}_K^l|\boldsymbol{y}_{1:K})$, see (4.11). ■

The distributions in (4.8) and (4.9) are given by

$$p(\boldsymbol{y}_k|\boldsymbol{x}_{1:k}^n, \boldsymbol{y}_{1:k-1}) = \mathcal{N}(\boldsymbol{y}_k|\boldsymbol{h}_k(\boldsymbol{x}_k^n) + \mathbf{C}_k(\boldsymbol{x}_k^n)\hat{\boldsymbol{x}}_{k|k-1}^l, \mathbf{S}_k) \tag{4.10a}$$

$$p(\boldsymbol{x}_{k+1|k}^n|\boldsymbol{x}_{1:k}^n, \boldsymbol{y}_{1:k}) = \mathcal{N}(\boldsymbol{x}_{k+1|k}^n|\boldsymbol{f}_k^n(\boldsymbol{x}_k^n) + \mathbf{A}_k^n(\boldsymbol{x}_k^n)\hat{\boldsymbol{x}}_{k|k}^l, \mathbf{M}_k) \tag{4.10b}$$

and the point estimates of the mean and covariance for the linear states become

$$\hat{\boldsymbol{x}}_{k|k}^l = \sum_{i=1}^{N_p} w_{k|k}^{(i)} \hat{\boldsymbol{x}}_{k|k}^{l,(i)}, \tag{4.11a}$$

$$\widehat{\mathbf{P}}_{k|k} = \sum_{i=1}^{N_p} w_{k|k}^{(i)} \left[\mathbf{P}_{k|k}^{(i)} + (\hat{\boldsymbol{x}}_{k|k}^{l,(i)} - \hat{\boldsymbol{x}}_{k|k}^l)(\hat{\boldsymbol{x}}_{k|k}^{l,(i)} - \hat{\boldsymbol{x}}_{k|k}^l)^T\right]. \tag{4.11b}$$

Marginalization of the State-Space Model For our purposes, the marginalized filter above is a suitable candidate for the state estimation problem. The states in the state vector (3.17) must be divided into linear and nonlinear in order to use the filter. The goal is to keep as many of the states in the linear domain as possible. Due to the nonlinearities in the measurement equation (3.18), position $\boldsymbol{p}$, angle of arrival $\boldsymbol{\phi}$, and the argument of the complex amplitude $\boldsymbol{\beta}$ are clearly part of the nonlinear domain. The nonlinear state vector becomes

$$\boldsymbol{x}^n = \begin{bmatrix}\boldsymbol{p}^T & \boldsymbol{\phi}^T & \boldsymbol{\beta}^T\end{bmatrix}^T \in \mathbb{R}^{3+(N_R+N_C)(1+M_T)}. \tag{4.12}$$

The states of the quaternion $\boldsymbol{q}$ have nonlinear state dynamics but the EKF has successfully been used in, e.g., [Sabatini, 2006] to estimate the quaternion after the dynamics have been linearized. The success of the linearization will depend on the angular velocity. For the angular velocities used in the experiments, the linearization has been found to be a good approximation and the quaternion is arranged with the rest of the linear states as

$$\boldsymbol{x}^l = \begin{bmatrix}\boldsymbol{v}^T & \boldsymbol{\delta}_a^T & \boldsymbol{q}^T & \boldsymbol{\delta}_\omega^T & \boldsymbol{\alpha}^T & \delta_f\end{bmatrix}^T \in \mathbb{R}^{14+N_R+N_C M_T}. \tag{4.13}$$

For the state-space model with the dynamic equations in (3.13) and (3.16), with the two state vectors in (4.12) and (4.13), the matrices defined in (4.6) for the marginalized particle filter become

$$\mathbf{A}_k^l = \begin{bmatrix} \mathbf{I}_3 & T_s\mathbf{R}(\boldsymbol{q}_k) & T_s\mathbf{Q}'(\boldsymbol{q}_k, \boldsymbol{u}_{a,k} + \boldsymbol{\delta}_{a,k}) & \mathbf{0} & \mathbf{0} & \mathbf{0} \\ \mathbf{0} & \mathbf{I}_3 & \mathbf{0} & \mathbf{0} & \mathbf{0} & \mathbf{0} \\ \mathbf{0} & \mathbf{0} & \mathbf{I}_4 + \frac{T_s}{2}\mathbf{Q}(\boldsymbol{u}_{\omega,k}) & \frac{T_s}{2}\mathbf{P}(\boldsymbol{q}_k) & \mathbf{0} & \mathbf{0} \\ \mathbf{0} & \mathbf{0} & \mathbf{0} & \mathbf{I}_3 & \mathbf{0} & \mathbf{0} \\ \mathbf{0} & \mathbf{0} & \mathbf{0} & \mathbf{0} & \mathbf{I}_{N_R+N_CM_T} & \mathbf{0} \\ \mathbf{0} & \mathbf{0} & \mathbf{0} & \mathbf{0} & \mathbf{0} & 1 \end{bmatrix} \tag{4.14a}$$

$$\mathbf{G}_k^l = \begin{bmatrix} T_s\mathbf{I}_3 & \mathbf{0} & \mathbf{0} & \mathbf{0} & \mathbf{0} & \mathbf{0} \\ \mathbf{0} & T_s\mathbf{I}_3 & \mathbf{0} & \mathbf{0} & \mathbf{0} & \mathbf{0} \\ \mathbf{0} & \mathbf{0} & \frac{T_s}{2}\mathbf{P}(\boldsymbol{q}_k) & \mathbf{0} & \mathbf{0} & \mathbf{0} \\ \mathbf{0} & \mathbf{0} & \mathbf{0} & T_s\mathbf{I}_3 & \mathbf{0} & \mathbf{0} \\ \mathbf{0} & \mathbf{0} & \mathbf{0} & \mathbf{0} & T_s\mathbf{I}_{N_R+N_CM_T} & \mathbf{0} \\ \mathbf{0} & \mathbf{0} & \mathbf{0} & \mathbf{0} & \mathbf{0} & T_s \end{bmatrix} \tag{4.14b}$$

$$\mathbf{A}_k^n = \begin{bmatrix} T_s\mathbf{I}_3 & \frac{T_s^2}{2}\mathbf{I}_3 & \frac{T_s^2}{2}\mathbf{Q}'(\boldsymbol{q}_k, \boldsymbol{u}_{a,k} + \boldsymbol{\delta}_{a,k}) & \mathbf{0} & \mathbf{0} & \mathbf{0} \\ \mathbf{0} & \mathbf{0} & \mathbf{0} & \mathbf{0} & \mathbf{0} & \mathbf{0} \\ \mathbf{0} & \mathbf{0} & \mathbf{0} & \mathbf{0} & \mathbf{0} & T_s\mathbf{1}_{M_T(N_R+N_C)} \end{bmatrix} \tag{4.14c}$$

$$\mathbf{G}_k^n = \begin{bmatrix} \frac{T_s^2}{2}\mathbf{I}_3 & \mathbf{0} & \mathbf{0} \\ \mathbf{0} & T_s\mathbf{I}_{N_R+N_C} & \mathbf{0} \\ \mathbf{0} & \mathbf{0} & T_s\mathbf{I}_{M_T(N_R+N_C)} \\ \mathbf{0} & \mathbf{0} & \frac{T_s^2}{2}\mathbf{1}_{M_T(N_R+N_C)} \end{bmatrix}, \tag{4.14d}$$

where $\mathbf{1}_K$ is a column vector of length K with ones, and the matrix $\mathbf{Q}'(\boldsymbol{q}, \boldsymbol{p})$ is defined as

$$\begin{aligned} \mathbf{Q}'(\boldsymbol{q}, \boldsymbol{p}) &= \frac{\partial(\mathbf{R}(\boldsymbol{q})\boldsymbol{p})}{\partial \boldsymbol{q}^T} \\ &= 2\begin{bmatrix} p_xq_0 - p_yq_3 + p_zq_2 & p_xq_3 + p_yq_0 - p_zq_1 & p_yq_1 - p_xq_2 + p_zq_0 \\ p_xq_1 + p_yq_2 + p_zq_3 & p_xq_2 - p_yq_1 - p_zq_0 & p_xq_3 + p_yq_0 - p_zq_1 \\ p_yq_1 - p_xq_2 + p_zq_0 & p_xq_1 + p_yq_2 + p_zq_3 & p_yq_3 - p_xq_0 - p_zq_2 \\ p_zq_1 - p_yq_0 - p_xq_3 & p_xq_0 - p_yq_3 + p_zq_2 & p_xq_1 + p_yq_2 + p_zq_3 \end{bmatrix}^T, \end{aligned} \tag{4.15}$$

where $\boldsymbol{q} = \begin{bmatrix} q_0 & q_1 & q_2 & q_3 \end{bmatrix}^T$ and $\boldsymbol{p} = \begin{bmatrix} p_x & p_y & p_z \end{bmatrix}^T$. As mentioned before, the state update of the quaternion does not preserve the relation of (3.3). This is dealt with by normalizing the predicted quaternion every time step in order to maintain the unit norm.

4.2 Angle of Arrival Estimation

As stated before, the particle based filtering solution intended for the estimation problem is sensitive to initialization of the states. If no initialization is used and the complete state-space of the AoA and amplitude is to be searched by the filter, the number of particles needed will disqualify the particle filter solution for any online estimation purposes. Also, if the filter is initialized in an erroneous state, convergence to the true movement and channel parameters would be a rare occasion. Thus, the filter needs to be initialized with not only the number of MPCs to track but also with the amplitude and AoA parameters describing each MPC. Consequently, we will now derive an algorithm that can provide initial estimates for the filter to use.

Background

The problem formulation of angle of arrival estimation can be applied to widely different scenarios and several different estimation techniques have been developed. Early solutions are based on beamforming like Bartlett and Capon [Krim and Viberg, 1996; Capon, 1969], subspace decomposition like MUSIC and ESPRIT [Schmidt, 1986; Roy and Kailath, 1989; Veen et al., 1997], while later solutions like SAGE [Fessler and Hero, 1994; Fleury et al., 1999] applied to AoA estimation separate the estimation problem into several one-dimensional problems instead.

Another way to solve the AoA estimation problem is to use sparse signal reconstruction. The idea is to reconstruct the measurements using as few components as possible out of a predetermined dictionary, where each dictionary component represents a hypothetical AoA. Since sparse reconstruction based on norm minimization with a dictionary is a convex problem and efficient frameworks for solving such problems are available, the solution can be easily found [Tibshirani, 1996; Boyd and Vandenberghe, 2004]. For an overview and comparison to previously mentioned techniques, see, e.g., [Malioutov et al., 2005]. The conclusion is that the sparse reconstruction is well suited for these problems and the performance is very good.

Sparse signal reconstruction can also be seen from a Bayesian viewpoint known as *sparse Bayesian learning* (SBL). Bayesian inference is based on finding a set of parameters which maximizes the likelihood of the posterior distribution for the parameters given the measurements [Tipping, 2001; Tipping and Faul, 2003]. For AoA estimation, the method also uses a dictionary of hypothetical source locations and several contributions to the field have been made [Wipf and Rao, 2007; Ji et al., 2008; Babacan et al., 2010]. For our purpose, we will study the convex formulation and also SBL for estimating as many parameters associated with the MPCs as possible to initialize the particle filter.

Problem Formulation

In the AoA estimation literature, the problem is usually formulated assuming a number of narrowband sources. However, we intend to use the approach to estimate the AoA of multipath components. Since the MPCs are also considered to be narrowband sources, the two formulations are interchangeable.

By assuming the existence of N_R multipath components, and a virtual array consisting of K antenna elements placed in the far field, the baseband equivalent can be written as

$$y_k = \sum_{r=1}^{N_R} a^{(r)} \exp\{-i\langle \boldsymbol{p}_k, \boldsymbol{\varrho}(\phi^{(r)})\rangle - i\delta_f T_s k\} + e_k, \tag{4.16}$$

where the $\boldsymbol{p}_k$ is the location of the kth receiver element, $\phi^{(r)}$ and $a^{(r)}$ is the AoA and complex amplitude of the rth MPC, and δ_f is the frequency error. The signal is also subject to additive zero mean circular symmetric complex Gaussian noise e_k. This is a repetition of the equation presented as (2.33) assuming one receive antenna element and that no clusters are present in the environment. Note that the AoA, complex amplitude, and the frequency error are assumed to remain constant during the acquisition period.

If the frequency error is neglected, the problem of finding the remaining parameters can be formulated as a convex problem. Introduce the set of all possible angles $[-\pi, \pi]$ and cover this set with L equidistant angles $\{\phi_1, \ldots, \phi_L\}$. Then let $\boldsymbol{\Phi} = \begin{bmatrix}\boldsymbol{\phi}_1 & \boldsymbol{\phi}_2 & \ldots & \boldsymbol{\phi}_L\end{bmatrix} \in \mathbb{C}^{K\times L}$ be a dictionary with these L hypothetical AoA directions. The lth base vector $\boldsymbol{\phi}_l$ in the dictionary is then given by

$$\boldsymbol{\phi}_l = \begin{bmatrix} \exp\{-i\langle \boldsymbol{p}_1, \boldsymbol{\varrho}(\phi_l)\rangle\} \\ \exp\{-i\langle \boldsymbol{p}_2, \boldsymbol{\varrho}(\phi_l)\rangle\} \\ \vdots \\ \exp\{-i\langle \boldsymbol{p}_K, \boldsymbol{\varrho}(\phi_l)\rangle\} \end{bmatrix} \in \mathbb{C}^K, \tag{4.17}$$

where $\boldsymbol{\varrho}(\phi) = \begin{bmatrix}\cos(\phi) & \sin(\phi)\end{bmatrix}^T$. The problem can now be stated as

$$\underset{\boldsymbol{a}}{\text{minimize}} \quad \|\boldsymbol{y} - \boldsymbol{\Phi}\boldsymbol{a}\|^2, \tag{4.18}$$

where $\boldsymbol{a} = [a_1 \ \ldots \ a_L]^T$ is a vector containing the sought complex MPC amplitudes and $\boldsymbol{y} = \begin{bmatrix}y_1 & y_2 & \ldots & y_K\end{bmatrix}^T$ are the K measurements. This formulation has the nice property of being a convex problem that can be efficiently solved. However, since most AoA hypotheses are wrong the vector $\boldsymbol{a}$ should be sparse, i.e., most elements are most likely zero. This can be achieved by introducing ℓ_1 regularization [Tibshirani, 1996; Boyd and Vandenberghe, 2004]; re-weighted ℓ_1 minimization has also been proposed in

[Candes et al., 2008] to increase sparsity even more. The latter approach is formulated as

$$\underset{\boldsymbol{a}}{\text{minimize}} \quad \|\boldsymbol{y} - \boldsymbol{\Phi a}\|^2 + \kappa \sum_{l=1}^{L} |\mu_l a_l|, \tag{4.19}$$

where $\kappa > 0$ is a weight of the regularization term and $\mu_l > 0$ are the costs for each element in $\boldsymbol{a}$. The weighting coefficients $\{\mu_1, \ldots, \mu_L\}$ can be updated with an iterative algorithm, presented in [Candes et al., 2008] and restated here as Algorithm 4.4.

Algorithm 4.4—Iteratively reweighted ℓ_1 minimization

Input: $\boldsymbol{\Phi}$, $\boldsymbol{y}$, κ, $i_{\max}$
Initialize: Set $\mu_l^{(1)} = 1, \ \forall\, l \in \{1, \ldots, L\}$
1: **for** $i = 1$ **to** $i_{\max}$ **do**
2: Solve (4.19) with $\mu_l = \mu_l^{(i)} \ \forall\, l \in \{1, \ldots, L\}$
3: Update μ_l as

$$\mu_l^{(i+1)} = \frac{1}{|a_l^{(i)}| + \epsilon}, \tag{4.20}$$

where $\boldsymbol{a}^{(i)}$ is the solution from (4.19).
4: Set $i = i + 1$
5: **end for**
Output: $\boldsymbol{a}$ ■

The value $\epsilon > 0$ is suggested in [Candes et al., 2008] to be chosen smaller than the largest value expected in $\boldsymbol{a}$. Thus, the reweighting scheme will penalize small elements in $\boldsymbol{a}$, forcing them to zero and thereby improving sparsity as the algorithm is repeated. Choosing κ has been studied in the literature, e.g., [Ohlsson et al., 2010]. With

$$\kappa = c\|\boldsymbol{\Phi}^* \boldsymbol{y}\|_\infty \tag{4.21}$$

where $\|\cdot\|_\infty$ denotes infinity norm and $0 < c < 1$ is a constant, a good trade-off between the two norm expressions in (4.19) is achieved. Hence, the iteratively reweighted ℓ_1 minimization has three parameters to adjust, κ, ϵ, and $i_{\max}$.

Extended Problem Formulation In the formulation (4.18), the frequency error δ_f is not taken into account. Given (4.16), the problem can be reformulated as

$$\underset{\boldsymbol{a}, \delta_f}{\text{minimize}} \quad \|\boldsymbol{y} - \boldsymbol{\Delta}(\delta_f)\boldsymbol{\Phi a}\| \tag{4.22}$$

where

$$\boldsymbol{\Delta}(\delta_f)_{[k,k]} = \exp\{-i\delta_f T_s k\}, \quad k \in \{1, 2, \ldots, K\} \tag{4.23}$$

and zero outside the diagonal. An important property of $\mathbf{\Delta}$ is that

$$\mathbf{\Delta}^*\mathbf{\Delta} = \mathbf{\Delta}\mathbf{\Delta}^* = \mathbf{I}.$$

However, the loss in the reformulation is that the cost function is no longer convex in δ_f and hence the convex optimization approach is not applicable. Consequently, we will now look closer on sparse Bayesian learning instead and also reformulate it to fit our problem.

Sparse Bayesian Learning

Let the measurements $\boldsymbol{y}$ be dependent on a set of unknown parameters collected in the vector $\boldsymbol{\psi}$. Then the sought parameters $\boldsymbol{\psi}$ can be obtained as the maximum a posteriori (MAP) estimate

$$\widehat{\boldsymbol{\psi}} = \arg\max_{\boldsymbol{\psi}} p(\boldsymbol{\psi}|\boldsymbol{y}),$$

where $p(\boldsymbol{\psi}|\boldsymbol{y})$ is the distribution of $\boldsymbol{\psi}$ given $\boldsymbol{y}$. By using Bayes' theorem, a relationship between the posterior, observation likelihood, and the prior distribution for the unknown parameters can be established as

$$p(\boldsymbol{\psi}|\boldsymbol{y}) \propto p(\boldsymbol{y}|\boldsymbol{\psi})p(\boldsymbol{\psi}).$$

The concept of treating unknown parameters of the prior distribution as a stochastic variable and then place a prior on them can be repeated endlessly, but the increasing number of parameters to estimate will also make the problem more complex and difficult to solve. For the problem stated in the previous section, two layers of priors will be used. The derivations below follow [Babacan et al., 2010] closely but the algorithm is adjusted so that the frequency error can be estimated.

The observations in (4.16) can be formulated as a multivariate stochastic distribution given by

$$p(\boldsymbol{y}|\boldsymbol{a}, \delta_f, \varrho) = \prod_{k=1}^{K} p(y_k|\boldsymbol{a}, \delta_f, \varrho) = \prod_{k=1}^{K} \mathcal{CN}(y_k|\mathbf{\Delta}(\delta_f)\mathbf{\Phi}\boldsymbol{a}, \varrho^{-1}\mathbf{I}_K), \tag{4.24}$$

i.e., a product of circular symmetric complex Gaussian distributions with mean $\mathbf{\Delta}(\delta_f)\mathbf{\Phi}\boldsymbol{a}$ and covariance $\varrho^{-1}\mathbf{I}_K$. Consequently, ϱ is the precision parameter of the noise e_k and a Gamma prior is placed on it as

$$p(\varrho|a^\varrho, b^\varrho) = \Gamma(\varrho|a^\varrho, b^\varrho), \tag{4.25}$$

where a^ϱ is the shape parameter and b^ϱ is the scale parameter. Since the Gamma prior is the conjugate prior to the precision of a Gaussian

distribution, the posterior will also be a Gaussian distribution. This fact will become useful later when solving the optimization problem.

As shown in [Babacan et al., 2010], a Laplace prior on the weight parameters $\boldsymbol{a}$ enforces sparsity. However, the Laplace distribution is not a conjugate prior to the mean of the Gaussian observation model and therefore a two layer hierarchical model is used. The first layer is a complex Gaussian distribution given by

$$p(\boldsymbol{a}|\boldsymbol{\gamma}) = \prod_{l=1}^{L} \mathcal{CN}(a_l|0, \gamma_l) \tag{4.26}$$

and $\boldsymbol{\gamma} = [\gamma_1 \quad \gamma_2 \quad \dots \quad \gamma_L]^T$. For the second layer, the conjugate prior of the variance γ_l is applied which again is a Gamma prior given by

$$p(\gamma_l|\eta) = \Gamma(\gamma_l|1, \eta/2) = \frac{\eta}{2} \exp\left\{-\frac{\eta\gamma_l}{2}\right\}. \tag{4.27}$$

Finally, for η, the Gamma prior

$$p(\eta|a^\eta, b^\eta) = \Gamma(\eta|a^\eta, b^\eta) \tag{4.28}$$

is used. This prior can easily be transformed into a so-called noninformative prior if $a^\eta \to 0$ and $b^\eta \to 0$. For the frequency error δ_f a uniform prior

$$p(\delta_f) = \mathcal{U}(\delta_f| - T_s/2, T_s/2), \tag{4.29}$$

where T_s is the sampling time, is used. The choice of this prior is done with the Nyquist criterion in mind.

The joint distribution, including the parameters and measurements, is given by

$$p(\boldsymbol{y}, \boldsymbol{a}, \boldsymbol{\gamma}, \varrho, \eta, \delta_f) = p(\boldsymbol{y}|\boldsymbol{a}, \varrho, \delta_f)p(\varrho)p(\boldsymbol{a}|\boldsymbol{\gamma})p(\boldsymbol{\gamma}|\eta)p(\eta)p(\delta_f) \tag{4.30}$$

and all distributions on the right hand side have been introduced in (4.24) – (4.29). The sought set of parameters $\boldsymbol{a}, \boldsymbol{\gamma}, \varrho, \eta, \delta_f$ is given as the MAP estimate as

$$(\hat{\boldsymbol{a}}, \hat{\boldsymbol{\gamma}}, \hat{\varrho}, \hat{\eta}, \hat{\delta_f}) = \arg\max\ p(\boldsymbol{a}, \boldsymbol{\gamma}, \varrho, \eta, \delta_f|\boldsymbol{y}) \tag{4.31}$$

and the distribution $p(\boldsymbol{a}, \boldsymbol{\gamma}, \varrho, \eta, \delta_f|\boldsymbol{y})$ is decomposed as

$$p(\boldsymbol{a}, \boldsymbol{\gamma}, \varrho, \eta, \delta_f|\boldsymbol{y}) = p(\boldsymbol{a}|\boldsymbol{\gamma}, \varrho, \eta, \delta_f, \boldsymbol{y})p(\boldsymbol{\gamma}, \varrho, \eta, \delta_f|\boldsymbol{y}).$$

The concept of conjugate priors [Robert, 2007] leads to the conclusion that $p(\boldsymbol{a}|\boldsymbol{\gamma}, \varrho, \eta, \delta_f, \boldsymbol{y})$ must be a multivariate complex Gaussian distribution $\mathcal{CN}(\boldsymbol{a}|\boldsymbol{\mu}, \boldsymbol{\Sigma})$ with

$$\boldsymbol{\mu} = \varrho\boldsymbol{\Sigma}\boldsymbol{\Phi}^*\boldsymbol{\Delta}^*\boldsymbol{y}^*, \tag{4.32a}$$

$$\boldsymbol{\Sigma} = [\boldsymbol{\Lambda} + \varrho\boldsymbol{\Phi}^*\boldsymbol{\Delta}^*\boldsymbol{\Delta}\boldsymbol{\Phi}]^{-1} = [\boldsymbol{\Lambda} + \varrho\boldsymbol{\Phi}^*\boldsymbol{\Phi}]^{-1}, \tag{4.32b}$$

where $\mathbf{\Lambda} = \text{diag}(\gamma_l^{-1})$ and the property of $\mathbf{\Delta}^*\mathbf{\Delta} = \mathbf{I}$ has been used. Now, the parameters $\boldsymbol{\gamma}, \varrho, \eta$, and δ_f can be estimated as the MAP estimate of $p(\boldsymbol{\gamma}, \varrho, \eta, \delta_f|\boldsymbol{y})$. By noting that

$$p(\boldsymbol{\gamma}, \varrho, \eta, \delta_f|\boldsymbol{y}) \propto p(\boldsymbol{y}, \boldsymbol{\gamma}, \varrho, \eta, \delta_f)$$

this distribution is used instead to estimate the hyperparameters from $p(\boldsymbol{y}, \boldsymbol{a}, \boldsymbol{\gamma}, \varrho, \eta, \delta_f)$ after marginalization over the weights $\boldsymbol{a}$

$$\begin{aligned} p(\boldsymbol{y}, \boldsymbol{\gamma}, \varrho, \eta, \delta_f) &= \int p(\boldsymbol{y}|\boldsymbol{a}, \boldsymbol{\gamma}) p(\boldsymbol{a}|\boldsymbol{\gamma}) p(\boldsymbol{\gamma}|\eta) p(\eta) p(\varrho) p(\delta_f)\, d\boldsymbol{a} \\ &= \left(\frac{1}{\pi}\right)^L |\mathbf{C}|^{-1} \exp\{-\boldsymbol{y}^*\mathbf{C}^{-1}\boldsymbol{y}\} p(\boldsymbol{\gamma}|\eta) p(\eta) p(\varrho) p(\delta_f), \end{aligned} \quad (4.33)$$

with $\mathbf{C} = \varrho^{-1}\mathbf{I} + \mathbf{\Delta}\mathbf{\Phi}\mathbf{\Lambda}^{-1}\mathbf{\Phi}^*\mathbf{\Delta}^*$. Taking the logarithm of the marginalized distribution yields

$$\begin{aligned} \mathcal{L} = &-L\log(\pi) - \log|\mathbf{C}| - \boldsymbol{y}^*\mathbf{C}^{-1}\boldsymbol{y} + L\log\frac{\eta}{2} - \frac{\eta}{2}\sum_{l=1}^{L}\gamma_l \\ &+ a^\eta \log b^\eta - \log\Gamma(a^\eta) + (a^\eta - 1)\log\eta - b^\eta\eta \\ &+ (a^\varrho - 1)\log\varrho - b^\varrho\varrho + \frac{1}{T_s}. \end{aligned} \quad (4.34)$$

If $a^\eta \to 0$ and $b^\eta \to 0$, the prior for η becomes noninformative and the expression can be further simplified to

$$\begin{aligned} \mathcal{L} = &-\log|\mathbf{C}| - \boldsymbol{y}^*\mathbf{C}^{-1}\boldsymbol{y} + L\log\frac{\eta}{2} - \frac{\eta}{2}\sum_{l=1}^{L}\gamma_l \\ &- \log\eta + (a^\varrho - 1)\log\varrho - b^\varrho\varrho \end{aligned} \quad (4.35)$$

where constants have been removed. The following expressions will be useful when the maximization problem is solved.

$$\begin{aligned} |\mathbf{C}| &= |\mathbf{\Lambda}^{-1}||\varrho^{-1}\mathbf{I}||\Sigma^{-1}| \\ \log|\mathbf{C}| &= \sum_{l=1}^{L}\log\gamma_l - L\log\varrho - \log|\mathbf{\Sigma}| \\ \mathbf{C}^{-1} &= \varrho\mathbf{I} - \varrho\mathbf{\Delta}\mathbf{\Phi}\mathbf{\Sigma}\mathbf{\Phi}^*\mathbf{\Delta}^*\varrho \\ \boldsymbol{y}^*\mathbf{C}^{-1}\boldsymbol{y} &= \varrho\boldsymbol{y}^*\boldsymbol{y} - \varrho\boldsymbol{y}^*\mathbf{\Delta}\mathbf{\Phi}\mathbf{\Sigma}\mathbf{\Phi}^*\mathbf{\Delta}^*\boldsymbol{y}\varrho \\ &= \varrho\|\boldsymbol{y} - \mathbf{\Delta}\mathbf{\Phi}\boldsymbol{\mu}\|^2 + \boldsymbol{\mu}^*\mathbf{\Lambda}\boldsymbol{\mu} \end{aligned}$$

To maximize the likelihood, given the current distribution of $\boldsymbol{a}$, the derivatives of $\mathcal{L}$ in (4.35) are calculated with respect to γ_l, ϱ, and η and become

$$\frac{\partial \mathcal{L}}{\partial \gamma_l} = -\frac{1}{\gamma_l} + \frac{|\mu_l|^2}{\gamma_l^2} - \frac{\eta}{2}, \tag{4.36a}$$

$$\frac{\partial \mathcal{L}}{\partial \varrho} = \frac{L}{\varrho} - \|\boldsymbol{y} - \boldsymbol{\Delta}\boldsymbol{\Phi}\boldsymbol{\mu}\|^2 + \frac{a^\varrho - 1}{\varrho} - b^\varrho, \tag{4.36b}$$

$$\frac{\partial \mathcal{L}}{\partial \eta} = \frac{L}{\eta} - \frac{1}{2}\sum_{l=1}^{L} \gamma_l - \frac{1}{\eta}. \tag{4.36c}$$

Finally, the derivative of the likelihood function $\mathcal{L}$ with respect to the frequency error δ_f becomes

$$\dot{\mathcal{L}}(\delta_f) = \frac{\partial \mathcal{L}}{\partial \delta_f} = -2\varrho \,\mathrm{Re}\{\boldsymbol{y}^* \dot{\boldsymbol{\Delta}}\boldsymbol{\Delta}\boldsymbol{\Phi}\boldsymbol{\mu}\}, \tag{4.37}$$

where

$$\dot{\boldsymbol{\Delta}}_{[k,k]} = \frac{\partial \boldsymbol{\Delta}}{\partial \delta_f} = (-i2\pi T_s k)\boldsymbol{\Delta}_{[k,k]}, \ \forall\, k \in \{1, 2, \ldots, K\} \tag{4.38}$$

and zero outside the diagonal. By equating the derivatives of (4.36) to zero, an update strategy for the parameters is obtained as

$$\gamma_l^{\text{new}} = \begin{cases} \dfrac{1}{\eta}\left(-1 + \sqrt{1 + 2\eta|\mu_l|^2}\right) & \eta > 0 \\ |\mu_l|^2 & \eta = 0 \end{cases} \tag{4.39}$$

$$\varrho^{\text{new}} = \frac{L + a^\varrho - 1}{\|\boldsymbol{y} - \boldsymbol{\Delta}\boldsymbol{\Phi}\boldsymbol{\mu}\|^2 + b^\varrho}, \tag{4.40}$$

and

$$\eta^{\text{new}} = \frac{2(L-1)}{\sum_{l=1}^{L} \gamma_l}. \tag{4.41}$$

For the frequency error, a closed form expression is unavailable so instead a Newton step is performed as

$$\delta_f^{\text{new}} = \delta_f - \frac{\dot{\mathcal{L}}(\delta_f)}{\ddot{\mathcal{L}}(\delta_f)} \tag{4.42}$$

where $\dot{\mathcal{L}}(\delta_f)$ is given by (4.37) and

$$\ddot{\mathcal{L}}(\delta_f) = -2\varrho \,\mathrm{Re}\{\boldsymbol{y}^* (\dot{\boldsymbol{\Delta}})^2 \boldsymbol{\Delta}\boldsymbol{\Phi}\boldsymbol{\mu}\}. \tag{4.43}$$

The algorithm for finding the distribution for the weight vector $\boldsymbol{a}$ is then carried out as described in Algorithm 4.5.

Algorithm 4.5—Compressive sensing with frequency error detection

Input: $\boldsymbol{y}$, $\boldsymbol{\Phi}$, $\delta_{f,0}$, $\hat{\varrho}$
1: Set $\gamma_l = 0, \ \forall\, l \in \{1, 2, \ldots, L\}$, $\eta = 0$,
2: **while** $\|\boldsymbol{\gamma} - \boldsymbol{\gamma}^{\text{old}}\| > \kappa$ **do**
3: Update γ_l by (4.39) $\quad \forall\, l \in \{1, 2, \ldots, L\}$
4: Update η by (4.41)
5: Update δ_f by (4.45)
6: Calculate $\boldsymbol{\mu}$ and $\boldsymbol{\Sigma}$ with (4.32).
7: **end while**
Output: $\mathcal{CN}(\boldsymbol{a}|\boldsymbol{\mu}, \boldsymbol{\Sigma})$, $\hat{\delta}_f$ ■

Since the likelihood function $\mathcal{L}$ is nonlinear in the frequency error δ_f, a grid search is done to initialize the algorithm since the Newton steepest decent search in (4.42) would not converge to the global minimum otherwise. Also, as discussed in [Babacan et al., 2010], the noise precision ϱ is not updated in the algorithm due to unreliability of the estimate. As argued by [Wipf and Rao, 2007] a heuristic estimate of the noise precision as

$$\hat{\varrho} = \frac{3K}{\|\boldsymbol{y}\|^2}\text{SNR}, \tag{4.44}$$

where SNR is assumed known and K is the number of data points, is used instead. Furthermore, the update of δ_f has proven to be unstable when $\boldsymbol{\gamma}$ is far away from the true values as it is for early iterations. Therefore the updating of δ_f is disabled for the first few runs of Algorithm 4.5. Since the initial grid search is supposed to find a value close to the true frequency error, the updated rate of δ_f is limited to avoid unrealistically large changes. Hence, the update rate is limited between -0.1 and 0.1 as

$$\delta_f^{\text{new}} = \delta_f - \left[\frac{\dot{\mathcal{L}}(\delta_f)}{\ddot{\mathcal{L}}(\delta_f)}\right]_{-0.1}^{0.1}, \tag{4.45}$$

which is used instead of (4.42).

As shown in [Tipping and Faul, 2003], the algorithm can be altered into a suboptimal version where one element of $\boldsymbol{\gamma}$ is updated in each run of the algorithm. This lowers the complexity of the algorithm significantly and is especially recommended for embedded systems. However, in this thesis, we are only interested in the performance of the algorithm and decide to not derive a sequential version of the algorithm.

Evaluation

To evaluate the iteratively reweighted ℓ_1 minimization approach against the SBL algorithm, the following setup is used. The movement shown in

Figure 4.1 is generated and noise levels similar to a consumer grade IMU are added to the accelerometer and gyroscope signals representing that movement. It is assumed that the movement is to be carried out in the far field of the sources and that path loss is negligible over the virtual array the movement creates. The position estimates are obtained by dead reckoning of the signals, see Figure 1.5 for the operations. These estimates are used when forming $\mathbf{\Phi}$ in (4.22) with an angular resolution of 2.5 deg. Based on findings that will be presented in the next chapter, an array that stretches a larger physical area will have a better estimation performance compared to a small one. Consequently, a large array would be preferred if the position estimates are good. Since the position estimates supplied by the dead reckoning scheme will deteriorate after a few seconds, it is of interest to see how many seconds of data that can be used for reliable joint AoA and frequency error estimation. Also, the number of data points gathered during the movement will be altered in order to see how it affects the reconstruction performance.

The iteratively reweighted ℓ_1 algorithm is implemented in MATLAB using the convex optimization package CVX [CVX, 2016] and executed twice since it has been proven to yield a satisfying result. However, since the algorithm is unable to detect the frequency error, no adjustment is made for it. To initialize the sparse Bayesian learning algorithm, a grid search is performed where the likelihood in (4.35) is calculated after a few iterations of Algorithm 4.5 with a fixed η. This is to enable comparison of the likelihoods calculated for the different grid points. The δ_f in the grid that yields the highest likelihood is chosen as starting point as the algorithm is run the second time with varying η and the frequency error is updated with (4.45).

To test the algorithms over different noise realizations, 1000 datasets were generated where four MPCs and no clusters are present in the measurement signal. The AoA for the MPCs are spread out randomly as $\mathcal{U}(-\pi, \pi)$ with a minimum angular distance of 18 deg between any two. The amplitude of an MPC is drawn from $\mathcal{U}(0.5, 1.5)$. Furthermore, the frequency error, constant for each dataset, is drawn from $\mathcal{N}(\delta_0, 0.1)$ and δ_0 is varied. Both algorithms are using the same dataset with either 50, 75, or 100 data points to investigate how the reconstruction performance depends on the number of data points. After the algorithms have finished, the four highest peaks in the resulting sparse solution are selected and they are matched with the four true AoA sorted in such a way that the root mean square error (RMSE), given by

$$\mathrm{RMSE}_\phi = \sqrt{\frac{1}{N_R}\sum_{r=1}^{N_R}\left|\hat{\phi}^{(r)} - \phi^{(r)}\right|^2} \tag{4.46}$$

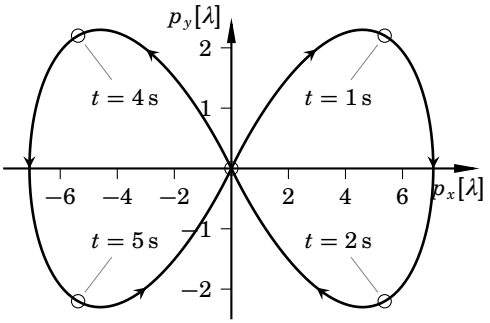

Figure 4.1 The movement of the receiver, the total traveled distance is approximately 36 λ which yields an average speed of 1 m/s assuming a carrier frequency of 1.8 GHz. The direction of movement is indicated by the arrows and the markings on the curve indicate the time at different positions. At 0, 3, and 6 seconds the receiver is in the origin. Note that the movement is larger in p_x than p_y but the movement is assumed to be in the far field so that the plane wave assumption holds and path loss is negligible over the virtual array.

is minimized where $\hat{\phi}$ and ϕ denote the estimated and true AoA respectively and $N_R = 4$. The complex amplitude estimates are then finally calculated as the least squares solution of

$$\boldsymbol{y} = \boldsymbol{\Phi}\boldsymbol{a} + \boldsymbol{e} \tag{4.47}$$

where $\boldsymbol{\Phi}$ has been reduced to only contain the vectors of the four detected peaks.

Simulation Results For zero average frequency error and 50 measurement points for reconstruction, the result is found in Figure 4.2. The two algorithms perform well but the sparse Bayesian learning yields a lower median RMSE for AoA and complex amplitude over a larger integration time. There is a clear performance degradation for integration times larger than 3 seconds for the iteratively reweighted ℓ_1 algorithm where the median error increases. For the SBL algorithm, the median of angle of arrival ϕ and amplitude α stays almost unaffected while the 75th percentile increases. Estimation of β is clearly more sensitive to the position errors accumulated by the dead reckoning than AoA and the amplitude are.

In Figure 4.3 the average frequency error is larger, $\delta_0 = 0.6\,\mathrm{Hz}$ and the iteratively reweighted ℓ_1 minimization algorithm is unable to find the AoA at all while the SBL algorithm has comparable performance with the low frequency error case in Figures 4.2. In Figure 4.4 a box plot for the estimation error of δ_f is shown. It is clear that the sparse Bayesian learning

algorithm is able to estimate the frequency error with good accuracy and that the estimation is insensitive to the accumulated position errors as time progresses. Furthermore, the frequency error estimation is improved by updating it continuously with (4.45), the results are shown in the right panel in Figure 4.4 compared to the value which the grid solver yields in the left panel. In all, the result shows the necessity of estimating the frequency error and that the derived SBL algorithm is able to produce more accurate AoA estimates with a reasonable number of measurement points.

In Figure 4.5, the median RMSE for complex amplitude and AoA is presented as a function of time for 50, 75, and 100 reconstruction points for the small and large frequency error cases. The iteratively reweighted ℓ_1 algorithm benefits from more data points but the SBL suffers from it. The number of points must however be chosen with the Nyquist criterion in mind in order to estimate the frequency error. Finally, robustness to increased measurement noise is investigated and presented in Figure 4.6 where the SNR has been decreased to 10 dB. The conclusion is that the algorithms are quite insensitive to measurement noise.

Finally, the mean and standard deviation of the error is calculated based on 80% of the estimation results. The mean value of the estimation error is close to zero for all four variables. The results for standard deviation for both 10 and 20 dB are presented in Figure 4.7. At 20 dB the standard deviation attains its lowest value after approximately 2.5 seconds. Beyond this time, the uncertainty in the estimate increases due to the accumulated position errors. Worth noting is that for 10 dB, the performance is better at longer integration time. The explanation is that the algorithm assumes more noise in the measurements and later ones will therefore not deteriorate the estimates as they will at 20 dB. This fact points towards a solution that applies weights to the measurements so that the ones coming in the beginning will be highly weighted while more uncertain measurements coming from the later part of the array are assigned a lower weight.

Conclusions

The performance of the sparse Bayesian learning algorithm is promising. While the iteratively reweighed ℓ_1 approach is shown to be very sensitive even to small frequency errors, the combination of the grid search and the recursive frequency error estimation has been shown to give superior performance. In a real world scenario, the attainable performance is yet to be investigated. The simulations are crafted to mimic real signals but one potential error source not investigated here is how static the amplitude and the frequency error really are during the movement. Also, if the movement does not span the horizontal plane well, the estimation performance in some direction might be bad. A third source of errors is vertical displacement which is not accounted for here.

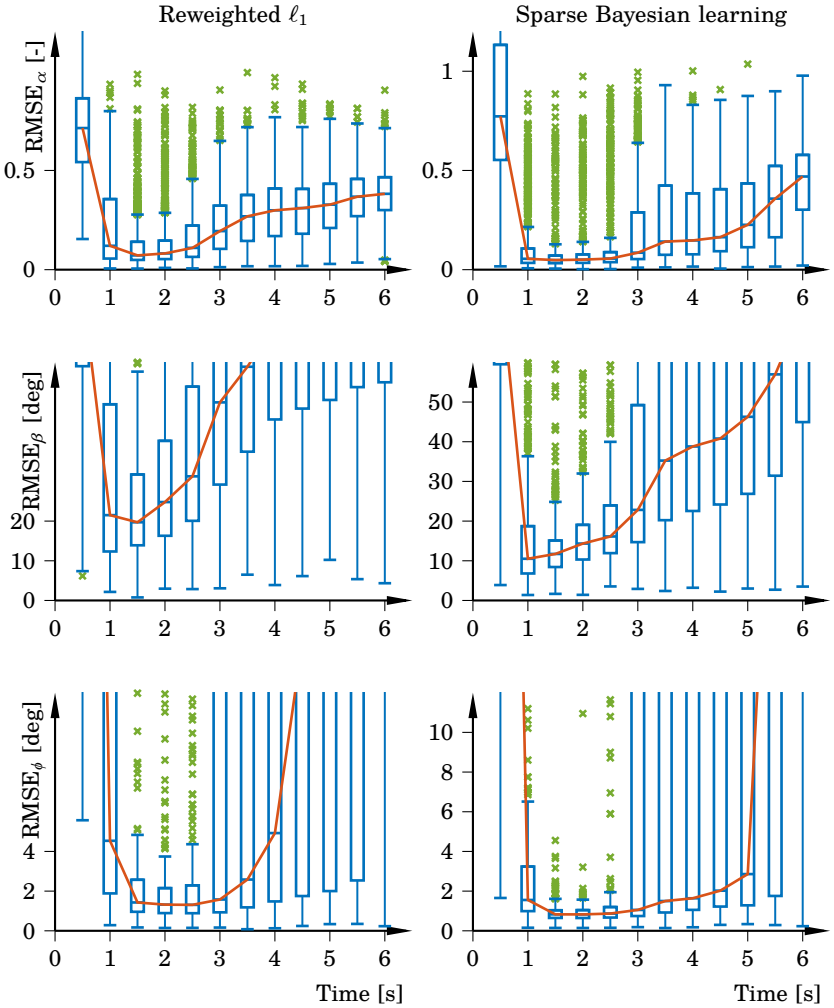

Figure 4.2 Box plot of RMSE for complex amplitude $\alpha \exp\{i\beta\}$ and AoA ϕ for the iteratively reweighted ℓ_1 and the SBL algorithms. The average frequency error δ_0 is 0 Hz, the SNR 20 dB, 50 data points are used for reconstruction, and there are 1000 simulations. The solid line in each plot marks the median and the crosses mark outliers. The RMSE for both AoA and complex amplitude are comparable for integration times up until 3 seconds but for larger ones, the SBL algorithm produces a lower RMSE.

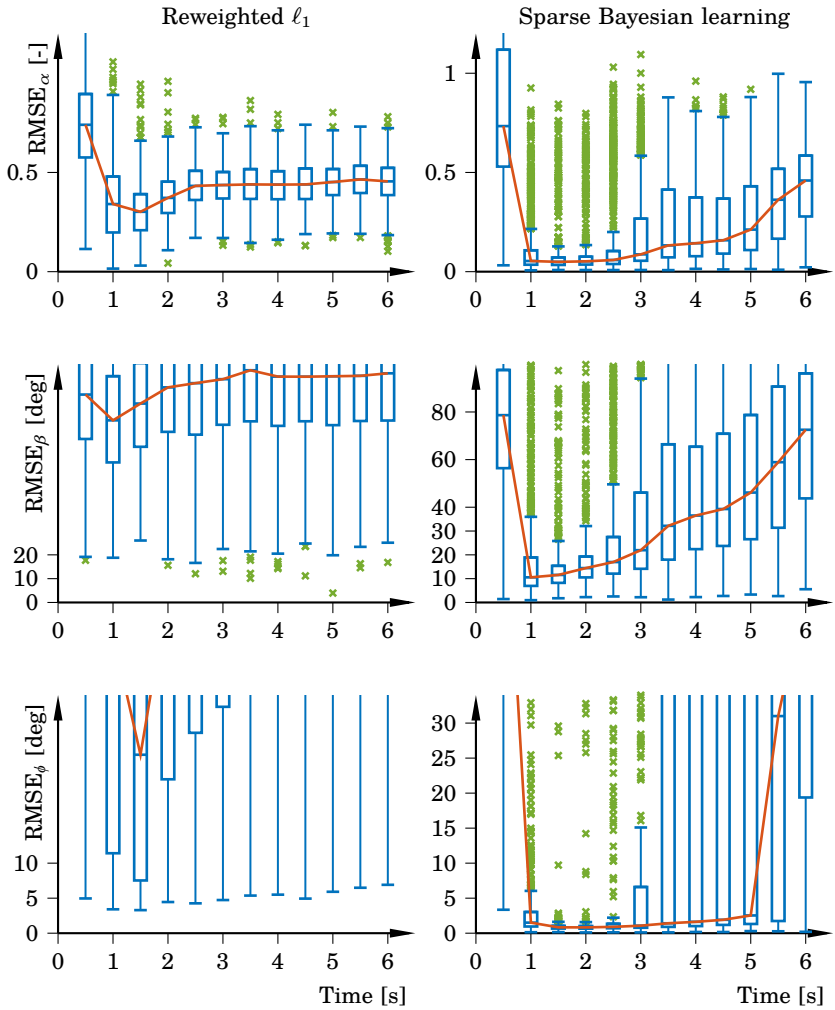

Figure 4.3 Box plot of RMSE for complex amplitude $\alpha \exp\{i\beta\}$ and AoA ϕ for the for the iteratively reweighted ℓ_1 and the SBL algorithms. The average frequency error δ_0 is 0.6 Hz, the SNR 20 dB, 50 data points are used for reconstruction, and there are 1000 simulations. The solid line in each plot marks the median and the crosses mark outliers. The iteratively reweighted ℓ_1 algorithm fails to estimate the AoA at all. After 5 seconds both algorithms fail due to the accumulated position errors.

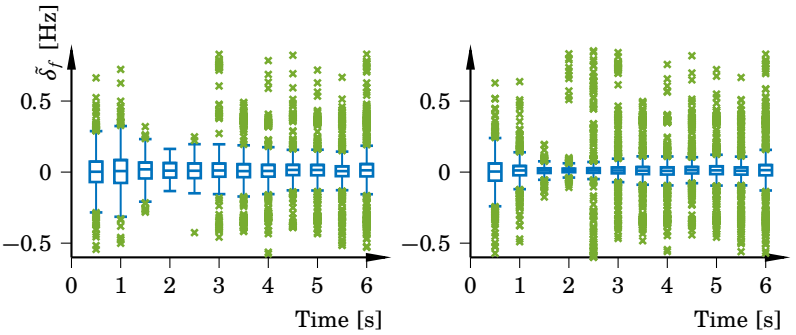

Figure 4.4 Box plot of the estimation error $\tilde{\delta}_f = \hat{\delta}_f - \delta_f$ for the SBL algorithm with the same color coding as in Figure 4.3. The average frequency error is 0.6 Hz, the SNR 20 dB, 50 data points are used for reconstruction, and there are 1000 simulations. To the left, the estimation error yielded by the grid search is presented and to the right is the error after Algorithm 4.5 has finished. There is a small but noticeable lowering of the estimation error using the adaptive frequency error estimation to the right.

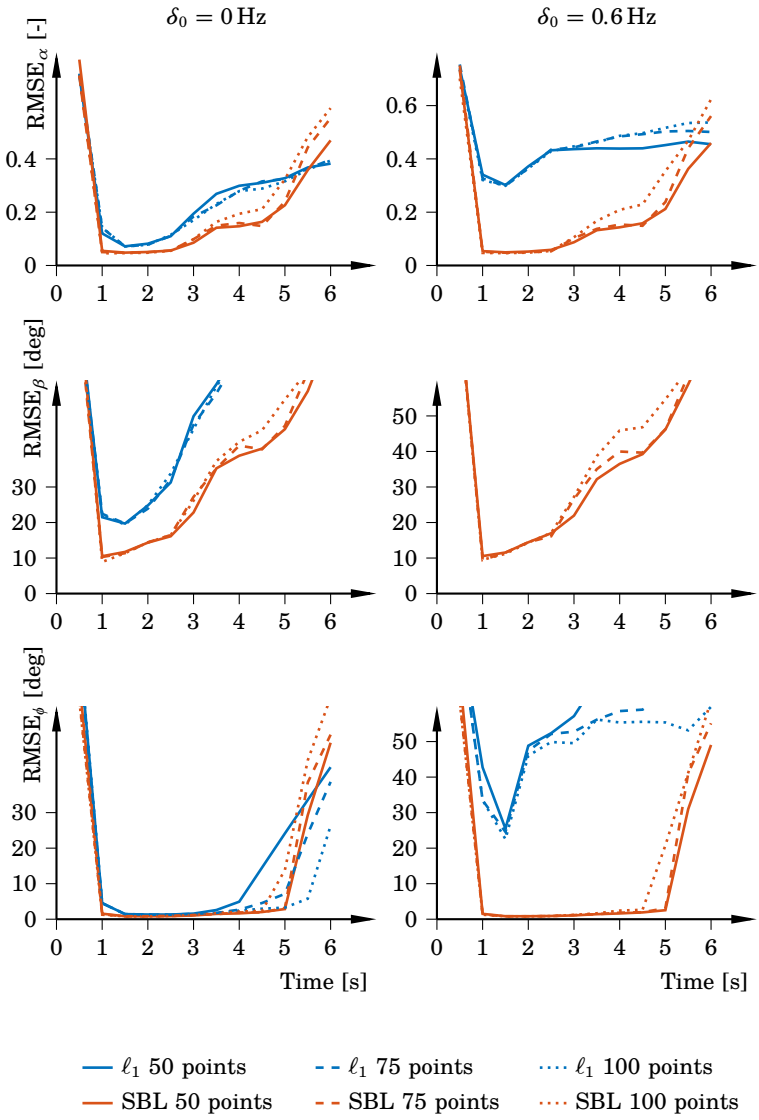

Figure 4.5 Comparison of the median RMSE error with 50, 75, and 100 data points used for reconstruction at an SNR of 20 dB. There is no big difference in the performance by increasing the number of points. The iteratively reweighted ℓ_1 algorithm benefits from more points while the SBL suffers slightly from it. The iteratively reweighted ℓ_1 algorithm yields an RMSE$_\beta$ larger than 50 deg for all integration times when δ_0=0.6 Hz.

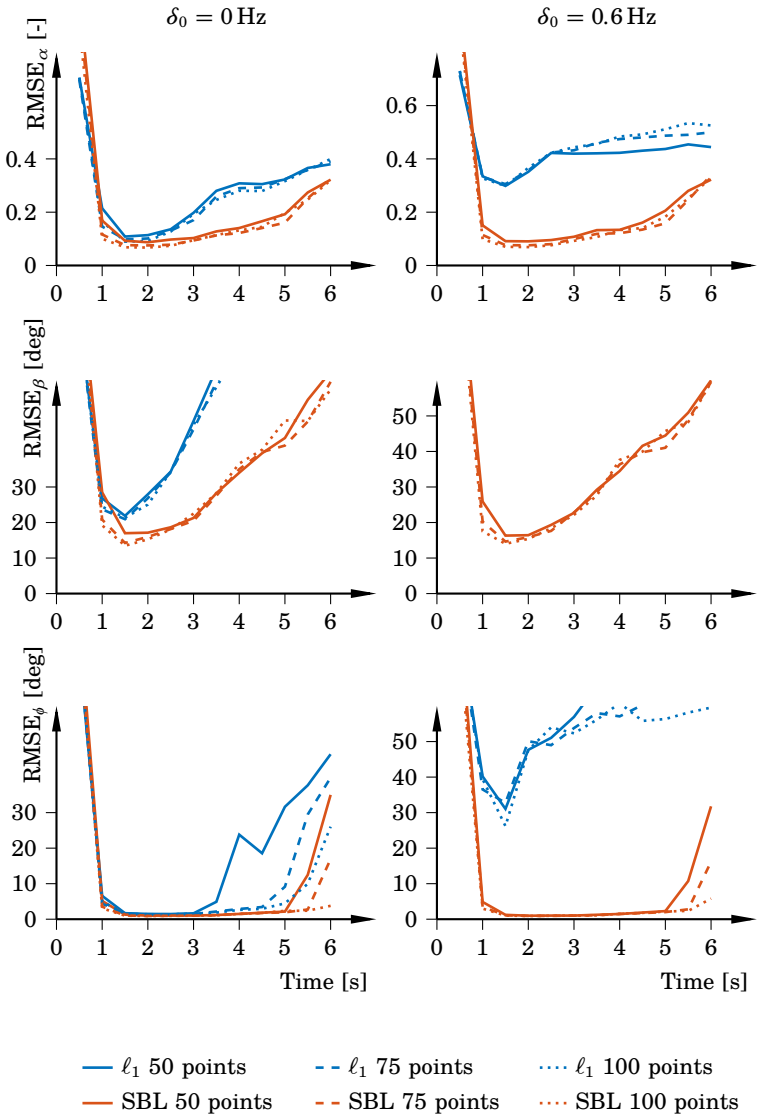

Figure 4.6 Comparison of the median RMSE error with 50, 75, and 100 data points used for reconstruction at an SNR of 10 dB. There is no big difference in the performance apart from ϕ for the iteratively reweighted ℓ_1 when the number of reconstruction points are increased. There is an improvement in estimation performance as the number of reconstruction points is increased, the effect is most visible for RMSE$_\phi$. The iteratively reweighted ℓ_1 algorithm yields an RMSE$_\beta$ larger than 50 deg for all integration times when δ_0=0.6 Hz.

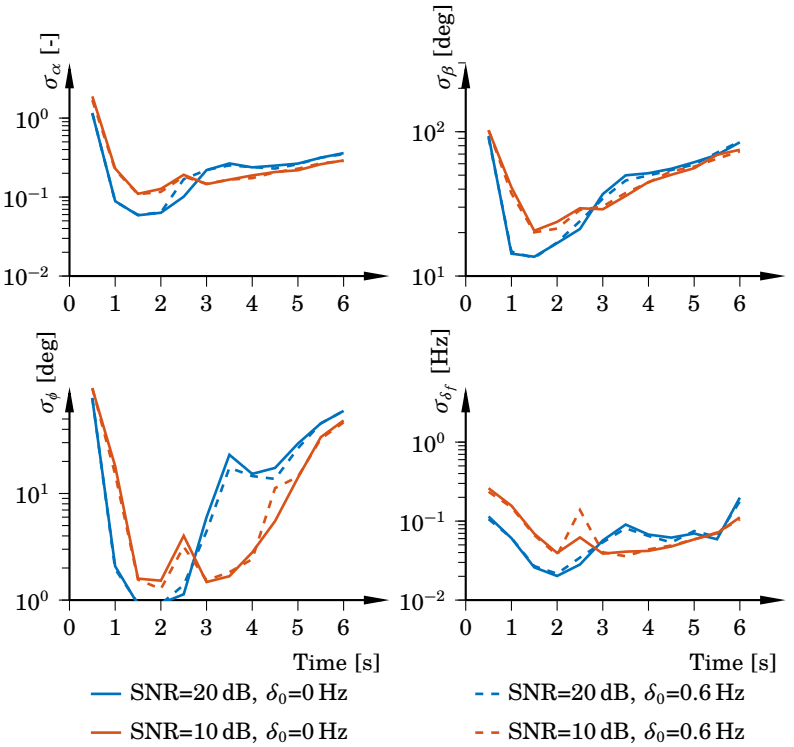

Figure 4.7 Standard deviations for the estimation error of complex MPC amplitude, AoA, and frequency error using SBL. It is estimated using 80% of the simulation results and presented as a function over the integration time. There is an increase in the standard deviation after 2.5 seconds when the SNR is 20 dB. The reason for better long-time performance at 10 dB is the fact that the algorithm at 20 dB relies on later measurements to the same extent as early measurements. Hence, these measurements will deteriorate the estimate since more error has been accumulated in the position estimate.

5

Fundamental Performance Bounds

Before investigating the estimation problem itself, we will look at the estimation performance bounds using the Cramér-Rao lower bound. We will study both batch estimation as well as recursive estimation since both will give valuable insights into the estimation problem at hand. For both scenarios a virtual array will be used which extends the traditional antenna array model with the time dimension. The investigation will explicitly look at the difficulty of joint estimation of AoA and frequency error. Sections 5.1 – 5.3 are based on [Mannesson and Bernhardsson, 2015].

Cramér-Rao Lower Bound

The Cramér-Rao lower bound (CRLB) [Cramér, 1999; Rao, 1945; Kay, 1993] is a concept closely related to estimation. In the simplest form, the bound is a lower limit of what variance an unbiased linear estimator can achieve given the measurement model and noise levels. Even so, the theorem can be used to, e.g., determine if a given system specification is realistic or not, or to determine if an estimator is the minimum variance estimator.

Assume that $\boldsymbol{y}$ is a vector of K measurements, $\boldsymbol{\psi}$ is a vector of real deterministic unknowns, and $\widehat{\boldsymbol{\psi}}$ are the estimated values given by an unbiased linear estimator. Then the theorem states that

$$\mathbb{E}_{\boldsymbol{y}|\boldsymbol{\psi}} \left\{ [\boldsymbol{\psi} - \widehat{\boldsymbol{\psi}}][\boldsymbol{\psi} - \widehat{\boldsymbol{\psi}}]^T \right\} \geq \boldsymbol{\mathcal{F}}^{-1}(\boldsymbol{\psi}) = \boldsymbol{\mathcal{C}}(\boldsymbol{\psi}) \tag{5.1}$$

where $\mathbb{E}_{\boldsymbol{y}|\boldsymbol{\psi}}\{\cdot\}$ denotes the expectancy operator with respect to the likelihood function $p(\boldsymbol{y}|\boldsymbol{\psi})$, $\boldsymbol{\mathcal{F}}(\boldsymbol{\psi})$ is the Fisher information matrix (FIM), and $\boldsymbol{\mathcal{C}}(\boldsymbol{\psi})$ is the CRLB for the parameters in $\boldsymbol{\Psi}$. For observations with additive zero mean circular symmetric complex Gaussian noise, $\boldsymbol{y}(\boldsymbol{\psi}) \sim \mathcal{CN}(\boldsymbol{h}(\boldsymbol{\psi}), \boldsymbol{\Sigma})$, the FIM is given in [Kay, 1993] as

$$\boldsymbol{\mathcal{F}}(\boldsymbol{\psi}) = -\mathbb{E}_{\boldsymbol{y}|\boldsymbol{\psi}} \left\{ \mathrm{Re}\, \frac{\partial^2 \mathcal{L}}{\partial \boldsymbol{\psi}\, \partial \boldsymbol{\psi}^T} \right\}, \tag{5.2}$$

where Re{·} denotes real part,

$$\mathcal{L} = \log p(\boldsymbol{y}|\boldsymbol{\psi}), \tag{5.3}$$

and $p(\boldsymbol{y}|\boldsymbol{\psi})$ is the probability distribution of the measurement noise given the parameters $\boldsymbol{\psi}$. If element (i, j) with $i \neq j$ of $\mathcal{F}$ equals zero, then variables i and j are said to be mutually decoupled.

Note that the Fisher information matrix is additive, i.e., if two independent measurements series with information matrices of $\mathcal{F}_1$ and $\mathcal{F}_2$ respectively are joined, the total information is the sum $\mathcal{F}_1 + \mathcal{F}_2$.

The Hybrid Cramér-Rao Lower Bound

If the observation model has both deterministic and stochastic latent variables, the formulation of the hybrid information matrix (HIM) [Bay et al., 2008] takes prior information on the stochastic variables into account. The definition of HIM is

$$\mathcal{H}(\boldsymbol{\psi}, \boldsymbol{\Omega}) = -\mathbb{E}_{\boldsymbol{y},\boldsymbol{\Omega}|\boldsymbol{\psi}} \left\{ \mathrm{Re} \begin{bmatrix} \dfrac{\partial^2 \mathcal{L}}{\partial \boldsymbol{\psi}\, \partial \boldsymbol{\psi}^T} & \dfrac{\partial^2 \mathcal{L}}{\partial \boldsymbol{\psi}\, \partial \boldsymbol{\Omega}^T} \\ \dfrac{\partial^2 \mathcal{L}}{\partial \boldsymbol{\Omega}\, \partial \boldsymbol{\psi}^T} & \dfrac{\partial^2 \mathcal{L}}{\partial \boldsymbol{\Omega}\, \partial \boldsymbol{\Omega}^T} \end{bmatrix} \right\} \triangleq \begin{bmatrix} \mathcal{H}_{\boldsymbol{\psi}\boldsymbol{\psi}^T} & \mathcal{H}_{\boldsymbol{\psi}\boldsymbol{\Omega}^T} \\ \mathcal{H}_{\boldsymbol{\Omega}\boldsymbol{\psi}^T} & \mathcal{H}_{\boldsymbol{\Omega}\boldsymbol{\Omega}^T} \end{bmatrix}, \tag{5.4}$$

where $\boldsymbol{\psi} \in \mathbb{R}^{n_\psi}$ and $\boldsymbol{\Omega} \in \mathbb{R}^{n_\Omega}$ are vectors containing the deterministic and stochastic latent variables respectively. Furthermore, the log-likelihood function $\mathcal{L}$ is the logarithm of the joint distribution,

$$\mathcal{L} = \log p(\boldsymbol{y}, \boldsymbol{\Omega}|\boldsymbol{\psi}) = \log p(\boldsymbol{y}|\boldsymbol{\Omega}, \boldsymbol{\psi}) + \log p(\boldsymbol{\Omega}), \tag{5.5}$$

where $p(\boldsymbol{\Omega})$ is the prior information on the stochastic latent variables. By using the matrix inversion lemma, the CRLB for the deterministic parameters $\boldsymbol{\psi}$ from (5.4) is obtained as

$$\mathcal{C}(\boldsymbol{\psi}) = \left[\mathcal{H}_{\boldsymbol{\psi}\boldsymbol{\psi}^T} - \mathcal{H}_{\boldsymbol{\psi}\boldsymbol{\Omega}^T} \mathcal{H}_{\boldsymbol{\Omega}\boldsymbol{\Omega}^T}^{-1} \mathcal{H}_{\boldsymbol{\Omega}\boldsymbol{\psi}^T} \right]^{-1}. \tag{5.6}$$

Note that when $\mathcal{H}_{\boldsymbol{\Omega}\boldsymbol{\Omega}^T}$ is large, i.e., the prior of $\boldsymbol{\Omega}$ is highly informative, the formulation converges to the Cramér-Rao lower bound obtained by $\mathcal{F}^{-1} = \mathcal{H}_{\boldsymbol{\psi}\boldsymbol{\psi}^T}^{-1}$ in (5.2).

Recursive Cramér-Rao Lower Bound

For the state-space models introduced in (4.1), the CRLB can be recursively updated as presented in [Taylor, 1979; Tichavsky et al., 1998; Gustafsson, 2010]. For a nonlinear system with states and measurements subject to additive white Gaussian noise processes, the recursively updated CRLB

$\mathcal{C}(\boldsymbol{x}_{k|k})$ propagates with the equations (4.2b) and (4.3b), found in the EKF, Algorithm 4.1. This means that the EKF produces the CRLB as a side result if the true state vector is supplied to the filter. However, the linearizations in the EKF require that the true state vector is available, i.e., the recursive Cramér-Rao lower bound can only be computed for simulations or when the true state vector has been acquired without any measurement uncertainty.

5.1 Cramér-Rao Lower Bound for Space-Time Arrays

The CRLB for AoA estimation for space-time arrays is inspired by [Dogandžić and Nehorai, 2001] where the CRLB for estimating range, velocity, and AoA is derived when using an active array in radar. The goal is to extend their work to cover joint estimation of AoA and frequency error using space-time arrays.

Equations (4.1) and (4.5) from [Dogandžić and Nehorai, 2001, p. 1129] are repeated here for completeness. The CRLB for azimuth and elevation angle $\{\phi, \theta\}$ is

$$\mathcal{C} = \mathcal{F}^{-1} = \begin{bmatrix} \mathcal{F}_{11} & \mathcal{F}_{12} \\ \mathcal{F}_{12} & \mathcal{F}_{22} \end{bmatrix}^{-1}, \tag{5.7}$$

where $\mathcal{F}$ is the Fisher information matrix. The components of the FIM $\mathcal{F}$ are given by

$$\mathcal{F}_{11} \propto \sin(\theta)^2[\mathcal{Q}_{xx}\sin(\phi)^2 + \mathcal{Q}_{yy}\cos(\phi)^2 - \mathcal{Q}_{xy}\sin(2\phi)] \tag{5.8a}$$

$$\mathcal{F}_{12} \propto \sin(\theta)^2\left\{\left[\frac{1}{2}(\mathcal{Q}_{xx} - \mathcal{Q}_{yy})\sin(2\phi) - \mathcal{Q}_{xy}\cos(2\phi)\right]\sin(\phi) + [\mathcal{Q}_{yz}\cos(\phi) - \mathcal{Q}_{xz}\sin(\phi)]\cos(\phi)\right\} \tag{5.8b}$$

$$\begin{aligned}\mathcal{F}_{22} \propto\ & [\mathcal{Q}_{xx}\cos(\phi)^2 + \mathcal{Q}_{yy}\sin(\phi)^2]\cos(\theta)^2 \\ & + \mathcal{Q}_{zz}\sin(\theta)^2 + \mathcal{Q}_{xy}\sin(2\phi)\cos(\theta)^2 \\ & - [\mathcal{Q}_{xz}\cos(\phi) + \mathcal{Q}_{yz}\sin(\phi)]\cos(2\theta),\end{aligned} \tag{5.8c}$$

where $\mathcal{Q}_{xx}$, $\mathcal{Q}_{yy}$, $\mathcal{Q}_{zz}$, $\mathcal{Q}_{xy}$, $\mathcal{Q}_{xz}$, and $\mathcal{Q}_{yz}$ describe the *moment of inertia tensor* of the array. To equate the notation from their work with ours, we have substituted the notation ψ in their work with $\pi/2 - \theta$ when the equations are repeated above. As seen in the equations the components of the moment of inertia tensor of the array has a direct connection to the estimation accuracy for AoA. This finding will be generalized here to cover the time dimension that follows with the introduction of frequency error estimation. The main difference is that we use a passive virtual antenna array, i.e., no signals are transmitted from the array. We assume

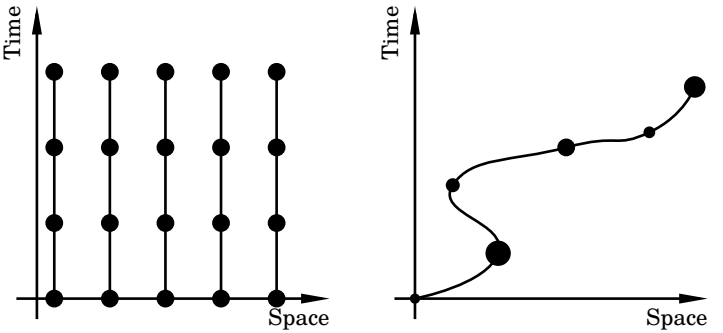

Figure 5.1 A traditional antenna array consisting of five stationary elements is shown in the left panel while a virtual antenna array with one moving receive antenna element is shown in the right panel. A dot marks the sampling time and the size of the dot indicates the SNR; a large dot represents higher SNR. Note that the virtual array can have non-equidistant sample points in both space and time as indicated in the figure. The space dimension is in $\mathbb{R}^3$.

that sources/transmitters/scatterers are stationary at a distance far away so that only AoA is to be estimated. Finally, our work captures the scenario of multiple impinging components and also analyses performance with respect to uncertainties in position and time which is not covered in [Dogandžić and Nehorai, 2001].

The work of [Collier, 2005] derives the Fisher information matrix for both plane wave and spherical wave propagation in a medium where there are random inhomogeneities, still with the limitation of a single impinging component, but it serves as a good introduction to the subject although it does not include any sensitivity analysis. The work of [Rendas and Moura, 1991] derives expressions for AoA estimation in an underwater multiple wave scenario. However, it does not capture the effects related to the use of a virtual antenna array. Furthermore, in [Friedlander, 1990] the influence of the receive antenna element position errors on the estimation performance was studied for a fixed array. The results show that the position errors impact the estimation performance but the work is limited to fixed arrays.

To illustrate the difference between previous works and ours, Figure 5.1 shows how a virtual antenna array can be moved arbitrarily in four dimensions compared to a traditional stationary antenna array. With the virtual array, one could have several measurements at the same location in space.

Signal and Noise Modeling

In this section, we derive and analyze the scenario of a SISO system with a single impinging component. For equations treating multiple components, see Appendix B. The signal model is a repetition from (2.33) in Section 2.4 with the assumptions that there are no clusters present and that there is one impinging component. The equation is also extended into three dimensions. Then, the measurements are given by

$$y_k = \alpha \exp\{-i(\beta + \langle \boldsymbol{p}_k, \boldsymbol{\varrho}(\phi, \theta)\rangle - \delta_f t_k)\} + e_k, \quad k = 1, \ldots, K, \tag{5.9}$$

where $t_k = T_s k$. Note that the parameters α, β, ϕ, and δ_f are assumed to be constant over the observations $\{1, \ldots, K\}$ in this analysis. The vector $\boldsymbol{\varrho}(\phi, \theta)$ is of unit length and pointing in the direction of (ϕ, θ), i.e.,

$$\boldsymbol{\varrho}(\phi, \theta) = \begin{bmatrix} \cos(\phi)\sin(\theta) & \sin(\phi)\sin(\theta) & \cos(\theta) \end{bmatrix}^T. \tag{5.10}$$

Remember that the position $\boldsymbol{p}$ in the argument of (5.9) is scaled with the term $2\pi\lambda^{-1}$, while the frequency error δ_f is scaled with 2π.

Motivating Example

Before going further, we will look at a motivating example of joint AoA and frequency error estimation. Let the receive antenna element be moved in a straight line with constant speed along the x-axis and acquire K samples. Since there is no extension of the array in the z-direction, only estimation of the azimuth angle ϕ and frequency error δ_f is considered. The estimation performance can be studied using the *ambiguity function* [Gu, 1996] defined as

$$f(\phi, \delta_f) = \frac{1}{K}\left|\sum_{k=1}^{K} \exp\{-i[(\cos(\phi_0) - \cos(\phi))p_{x,k}^2 + (\delta_0 - \delta_f)T_s^2 k^2]\}\right|^2, \tag{5.11}$$

where ϕ_0 and δ_0 denote AoA and frequency error given by an oracle. A high value of the ambiguity function indicates that the estimated values ϕ and δ_f are close to these values. In Figure 5.2 the ambiguity function is shown as a function of ϕ and δ_f. Obviously there are infinitely many combinations of ϕ and δ_f that equally well explain the measurements. Hence, a straight line movement can not be used to jointly estimate AoA and frequency error. If the same receive antenna element is moved along the x-axis but returned back to the starting position, the ambiguity function has a distinct peak as seen in Figure 5.3. The conclusion from this example is that when the movement is more informative, the ambiguity function gets a unique maximum and the two parameters can be estimated jointly. This example will be revisited and examined using the Fisher information matrix derived below.

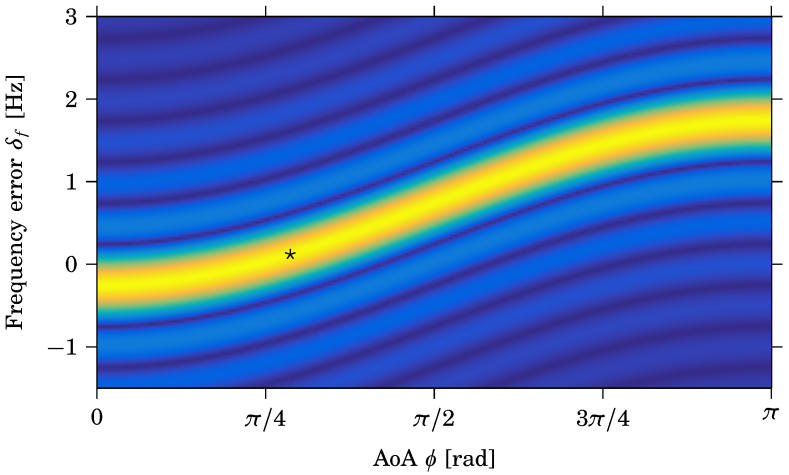

Figure 5.2 The ambiguity function for a straight line movement where the star marks the values of ϕ_0 and δ_0 given by an oracle. There are infinitely many combinations of ϕ and δ_f that equally well explain the measurements.

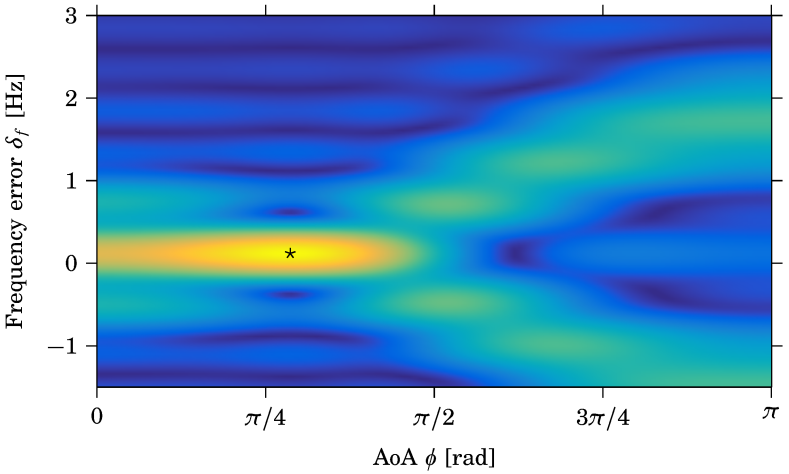

Figure 5.3 The ambiguity function for a back and forth movement where the star marks the values of ϕ_0 and δ_0. The peak of the ambiguity function is distinct when a more informative movement is used.

Signal Model Parameterization

To facilitate further analysis, the signal given on the form of (5.9) is parameterized. By applying the coordinate change $\chi \triangleq \log\{\alpha\}$ the observations $\boldsymbol{y} = \begin{bmatrix} y_1 & y_2 & \dots & y_K \end{bmatrix}^T$ are given by the column vector

$$\boldsymbol{y}(\boldsymbol{\Omega}, \boldsymbol{\gamma}, \chi, \beta) = \exp\{\chi - i\beta\} \exp\{-i\boldsymbol{\Omega}\boldsymbol{\gamma}\} + \boldsymbol{e} \in \mathbb{C}^K \tag{5.12}$$

where $\chi \in \mathbb{R}$, $\beta \in \mathbb{R}$, $\boldsymbol{e} = \begin{bmatrix} e_1 & \dots & e_K \end{bmatrix}^T \sim \mathcal{CN}(\boldsymbol{0}, \boldsymbol{\Sigma}_e)$,

$$\boldsymbol{\gamma} = \boldsymbol{f}(\boldsymbol{\mu}) = \begin{bmatrix} \cos(\phi)\sin(\theta) & \sin(\phi)\sin(\theta) & \cos(\theta) & \delta_f \end{bmatrix}^T, \tag{5.13}$$

with $\boldsymbol{\mu} = \begin{bmatrix} \phi & \theta & \delta_f \end{bmatrix}^T$, and

$$\boldsymbol{\Omega} = \begin{bmatrix} p_{x,1} & p_{y,1} & p_{z,1} & t_1 \\ \vdots & \vdots & \vdots & \vdots \\ p_{x,K} & p_{y,K} & p_{z,K} & t_K \end{bmatrix} \triangleq \begin{bmatrix} \boldsymbol{p}_x & \boldsymbol{p}_y & \boldsymbol{p}_z & \boldsymbol{t} \end{bmatrix} \in \mathbb{R}^{K \times 4}. \tag{5.14}$$

The parameters in $\boldsymbol{\Omega}$ will be referred to as the *stochastic latent variables* and

$$\boldsymbol{\psi} = \begin{bmatrix} \chi & \beta & \boldsymbol{\mu}^T \end{bmatrix}^T \in \mathbb{R}^5 \tag{5.15}$$

as the *deterministic latent variables*. Note that other separations of the variables are possible but this one suits our analysis aiming to understand the performance impact of position and timing errors of the measurements.

Single Component Scenario

In this section, the FIM for the single component scenario where $\boldsymbol{\Omega}$ is assumed to be known is presented. The multiple components scenario is presented in Appendix B.1.

Given the observation model (5.12), the log-likelihood function $\mathcal{L}$ becomes

$$\mathcal{L} = c - (\boldsymbol{y} - \boldsymbol{h})^* \boldsymbol{\Sigma}_e^{-1} (\boldsymbol{y} - \boldsymbol{h}) \tag{5.16}$$

where $(\cdot)^*$ denotes Hermitian transpose, $\boldsymbol{y}$ is the vector of observations, $\boldsymbol{h} = \exp\{\chi - i\beta\} \exp\{-i\boldsymbol{\Omega}\boldsymbol{\gamma}\}$, and c is a constant. With the deterministic latent variables

$$\boldsymbol{\psi} = \begin{bmatrix} \chi & \beta & \boldsymbol{\mu}^T \end{bmatrix}^T, \tag{5.17}$$

the Fisher information for $\boldsymbol{\mu}$ is given by

$$-\mathbb{E}_{\boldsymbol{y}|\boldsymbol{\psi}} \left\{ \mathrm{Re}\, \frac{\partial^2 \mathcal{L}}{\partial \boldsymbol{\mu}\, \partial \boldsymbol{\mu}^T} \right\} = 2 \exp\{2\chi\}\, \mathrm{Re} \left\{ \mathbf{F}^T \boldsymbol{\Omega}^T \mathbf{W}^* \boldsymbol{\Sigma}_e^{-1} \mathbf{W} \boldsymbol{\Omega} \mathbf{F} \right\}, \tag{5.18}$$

where $\mathbf{W} \triangleq \operatorname{diag}\{\exp\{-i\boldsymbol{\Omega}\boldsymbol{\gamma}\}\} \in \mathbb{C}^{K\times K}$ is a diagonal matrix with $\exp\{-i\boldsymbol{\Omega}\boldsymbol{\gamma}\}$ on the diagonal, and

$$\mathbf{F} = \frac{\partial \boldsymbol{f}(\boldsymbol{\mu})}{\partial \boldsymbol{\mu}^T} = \begin{bmatrix} -\sin(\phi)\sin(\theta) & \cos(\phi)\cos(\theta) & 0 \\ \cos(\phi)\sin(\theta) & \sin(\phi)\cos(\theta) & 0 \\ 0 & -\sin(\theta) & 0 \\ 0 & 0 & 1 \end{bmatrix}. \tag{5.19}$$

Furthermore, with $\boldsymbol{w} \triangleq \exp\{-i\boldsymbol{\Omega}\boldsymbol{\gamma}\} \in \mathbb{C}^K$ we have

$$-\mathbb{E}_{\boldsymbol{y}|\boldsymbol{\psi}}\left\{\operatorname{Re}\frac{\partial^2 \mathcal{L}}{\partial \chi^2}\right\} = 2\exp\{2\chi\}\operatorname{Re}\{\boldsymbol{w}^*\boldsymbol{\Sigma}_e^{-1}\boldsymbol{w}\}, \tag{5.20a}$$

$$-\mathbb{E}_{\boldsymbol{y}|\boldsymbol{\psi}}\left\{\operatorname{Re}\frac{\partial^2 \mathcal{L}}{\partial \chi\,\partial \beta}\right\} = -\mathbb{E}_{\boldsymbol{y}|\boldsymbol{\psi}}\left\{\operatorname{Re}\frac{\partial^2 \mathcal{L}}{\partial \chi\,\partial \boldsymbol{\mu}^T}\right\} = 0, \tag{5.20b}$$

$$-\mathbb{E}_{\boldsymbol{y}|\boldsymbol{\psi}}\left\{\operatorname{Re}\frac{\partial^2 \mathcal{L}}{\partial \beta^2}\right\} = 2\exp\{2\chi\}\operatorname{Re}\{\boldsymbol{w}^*\boldsymbol{\Sigma}_e^{-1}\boldsymbol{w}\}, \tag{5.20c}$$

$$-\mathbb{E}_{\boldsymbol{y}|\boldsymbol{\psi}}\left\{\operatorname{Re}\frac{\partial^2 \mathcal{L}}{\partial \beta\,\partial \boldsymbol{\mu}^T}\right\} = 2\exp\{2\chi\}\operatorname{Re}\{\boldsymbol{w}^*\boldsymbol{\Sigma}_e^{-1}\mathbf{W}\boldsymbol{\Omega}\mathbf{F}\}. \tag{5.20d}$$

Note that if the measurement errors are uncorrelated, $\boldsymbol{\Sigma}_e$ is diagonal and thereby $\boldsymbol{w}^*\boldsymbol{\Sigma}_e^{-1}\boldsymbol{w} = \operatorname{tr}\{\boldsymbol{\Sigma}_e^{-1}\}$, $\mathbf{W}^*\boldsymbol{\Sigma}_e^{-1}\mathbf{W} = \boldsymbol{\Sigma}_e^{-1}$, and $\boldsymbol{w}^*\boldsymbol{\Sigma}_e^{-1}\mathbf{W} = \mathbf{1}_K^T\boldsymbol{\Sigma}_e^{-1}$, where $\mathbf{1}_K \triangleq \begin{bmatrix}1 & 1 & \dots & 1\end{bmatrix}^T \in \mathbb{R}^K$ and $\operatorname{tr}\{\cdot\}$ denotes the matrix trace.

Similar to the result in [Dogandžić and Nehorai, 2001], the FIM for joint AoA and frequency error estimation, assuming error-free observations of $\boldsymbol{\Omega}$, is summarized in Theorem 5.1.

THEOREM 5.1
Consider observations given by

$$\boldsymbol{y}(\boldsymbol{\Omega}, \boldsymbol{\gamma}, \chi, \beta) = \exp\{\chi - i\beta\}\exp\{-i\boldsymbol{\Omega}\boldsymbol{\gamma}\} + \boldsymbol{e} \in \mathbb{C}^K \tag{5.21}$$

where $\exp\{\cdot\}$ is element-wise exponentiation, χ and β are real constants, $\boldsymbol{e} = \begin{bmatrix}e_1 & \dots & e_K\end{bmatrix}^T \sim \mathcal{CN}(\mathbf{0}, \boldsymbol{\Sigma}_e)$,

$$\boldsymbol{\gamma} = \boldsymbol{f}(\boldsymbol{\mu}) = \begin{bmatrix}\cos(\phi)\sin(\theta) & \sin(\phi)\sin(\theta) & \cos(\theta) & \delta_f\end{bmatrix}^T, \tag{5.22}$$

and

$$\boldsymbol{\Omega} = \begin{bmatrix}\boldsymbol{p}_x & \boldsymbol{p}_y & \boldsymbol{p}_z & \boldsymbol{t}\end{bmatrix} \in \mathbb{R}^{K\times 4}. \tag{5.23}$$

The Fisher information matrix for the unknown set of parameters $\boldsymbol{\psi} = \begin{bmatrix}\chi & \beta & \phi & \theta & \delta_f\end{bmatrix}^T$ with perfect knowledge of $\boldsymbol{\Omega}$ and uncorrelated mea-

surement noise is given by

$$\mathcal{F}(\boldsymbol{\psi}) = 2\exp\{2\chi\}\begin{bmatrix}\mathrm{tr}\{\boldsymbol{\Sigma}_e^{-1}\} & 0 & \mathbf{0}_3^T \\ 0 & \mathrm{tr}\{\boldsymbol{\Sigma}_e^{-1}\} & \mathbf{P}^T\mathbf{F} \\ \mathbf{0}_3 & \mathbf{F}^T\mathbf{P} & \mathbf{F}^T\mathcal{Q}\mathbf{F}\end{bmatrix} \in \mathbb{R}^{5\times 5} \tag{5.24}$$

where

$$\mathbf{F} = \begin{bmatrix}-\sin(\phi)\sin(\theta) & \cos(\phi)\cos(\theta) & 0 \\ \cos(\phi)\sin(\theta) & \sin(\phi)\cos(\theta) & 0 \\ 0 & -\sin(\theta) & 0 \\ 0 & 0 & 1\end{bmatrix} \in \mathbb{R}^{4\times 3}, \tag{5.25}$$

$$\mathbf{P} = \boldsymbol{\Omega}^T\boldsymbol{\Sigma}_e^{-1}\mathbf{1}_K \in \mathbb{R}^4, \tag{5.26}$$

and

$$\mathcal{Q} = \boldsymbol{\Omega}^T\boldsymbol{\Sigma}_e^{-1}\boldsymbol{\Omega} \in \mathbb{R}^{4\times 4}. \tag{5.27}$$

□

Proof See (5.18) - (5.20). □

Corollary 5.1
If the origin of the array frame $(\bar{p}_x, \bar{p}_y, \bar{p}_z, \bar{t})$ is chosen so that $\mathbf{P} = \mathbf{0}$, the Fisher information matrix is given as

$$\mathcal{F}(\boldsymbol{\psi}) = 2\exp\{2\chi\}\begin{bmatrix}\mathrm{tr}\{\boldsymbol{\Sigma}_e^{-1}\} & 0 & \mathbf{0}_3^T \\ 0 & \mathrm{tr}\{\boldsymbol{\Sigma}_e^{-1}\} & \mathbf{0}_3^T \\ \mathbf{0}_3 & \mathbf{0}_3 & \mathbf{F}^T\mathcal{Q}\mathbf{F}\end{bmatrix} \in \mathbb{R}^{5\times 5}. \tag{5.28}$$

This can be achieved by the affine transformation moving the origin to the center of gravity of the SNR weighted measurements, i.e.,

$$(p_{x,k}, p_{y,k}, p_{z,k}, t_k) \mapsto (p_{x,k} - \bar{p}_x, p_{y,k} - \bar{p}_y, p_{z,k} - \bar{p}_z, t_k - \bar{t}),\ \forall\, k, \tag{5.29}$$

with

$$\bar{p}_x = \frac{\sum_{k=1}^K p_{x,k}\sigma_k^{-2}}{\sum_{k=1}^K \sigma_k^{-2}},\ \bar{p}_y = \frac{\sum_{k=1}^K p_{y,k}\sigma_k^{-2}}{\sum_{k=1}^K \sigma_k^{-2}},\ \bar{p}_z = \frac{\sum_{k=1}^K p_{z,k}\sigma_k^{-2}}{\sum_{k=1}^K \sigma_k^{-2}}, \tag{5.30}$$

and

$$\bar{t} = \frac{\sum_{k=1}^K t_k\sigma_k^{-2}}{\sum_{k=1}^K \sigma_k^{-2}} \tag{5.31}$$

where σ_k^2 is the variance of the measurement noise e_k. □

The formulation in (5.24) reveals interesting structures in the relationship between the latent variables. Firstly, the amplitude of the impinging component is decoupled from all other variables. Secondly, the estimation accuracy for the AoA and frequency error is determined by the components of $\mathcal{Q}$ given in (5.27) describing the moment of inertia tensor for the structure that the virtual array constitutes in four-dimensional space-time. The measurement noise covariance matrix $\mathbf{\Sigma}_e$ can be interpreted as a re-weighting of the measurements; more weight is given to the ones from locations with high SNR and vice versa. Theorem 5.1 is an extension of the result of [Dogandžić and Nehorai, 2001] where the SNR is assumed to be equal for all measurements, the receive antenna elements are stationary, and the frequency error is unmodeled.

Motivating Example Revisited

It is now time to revisit the motivating example from Section 5.1. The first array which suffers from ambiguity between AoA and frequency error has a moment tensor $\mathcal{Q}$ in the x, t dimension of the form

$$\mathcal{Q}_1 = c \begin{bmatrix} 1 & 1 \\ 1 & 1 \end{bmatrix}, \quad c \in \mathbb{R}. \tag{5.32}$$

The movement of the array is illustrated in the space-time domain to the left in Figure 5.4. The figure clearly shows that the movement yields an array with the same moments in both space and time as well as for the product moment. Consequently, since the moment tensor $\mathcal{Q}_1$ does not have full rank, the AoA and frequency error can not be separated as seen in Figure 5.2. The second array, with back and forth movement, has a moment tensor of the form

$$\mathcal{Q}_2 = \begin{bmatrix} c_1 & 0 \\ 0 & c_2 \end{bmatrix}, \quad c_1, c_2 > 0, \tag{5.33}$$

and the corresponding movement is shown to the right in Figure 5.4. Since the moment tensor $\mathcal{Q}_2$ has full rank, the two unknowns can be estimated as seen in Figure 5.3.

5.2 Worst-case-optimal Array Configurations

As shown in (5.24), the CRLB for the AoA estimation in a given direction is related to the inverse of $\mathcal{Q}$, see (5.27). To illustrate the result, it is used to find an array that has a constant AoA estimation performance regardless of the direction. In a scenario where the SNR is constant for the observation interval the covariance matrix $\mathbf{\Sigma}_e$ equals $\sigma^2 \mathbf{I}_K$, where $\mathbf{I}_K$ denotes the identity matrix of size K. Then, the minimal eigenvalue of $\mathcal{Q}$

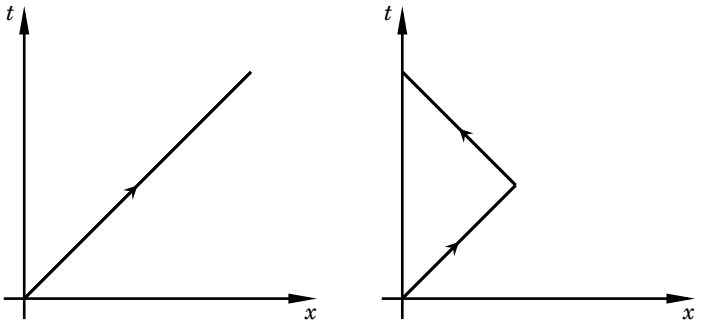

Figure 5.4 The space-time movements for the two arrays in the motivating example with the direction of movement indicated by the arrows. The left array suffers from ambiguity in the x, t dimension while the array to the right has $\mathcal{Q}_{xt} = 0$.

describes the worst-case estimation performance and a natural goal is hence to find the trajectory $\boldsymbol{p}$ of a given length that solves

$$\max_{\boldsymbol{p}_{1:K}} \min_i \lambda_i[\mathcal{Q}(\boldsymbol{p})], \tag{5.34}$$

where $\lambda[\mathcal{Q}]$ denotes the eigenvalues corresponding to the matrix $\mathcal{Q}$. We will assume that the antenna element can be moved with unit speed over a given finite time interval. Finally, a large number of observations are taken over a unit time interval at a constant sample rate, so the sums are replaced by integrals over the time interval $[0, 1]$.

Worst-case-optimal 2D Array

Let us assume that only positions in the plane $p_{z,k} = 0, \ \forall\, k$ are considered and that the frequency error is known. Thereby, $p_{z,k}$ and time t_k in (5.27) can be excluded from the optimization problem. The case with unknown frequency error is revisited in Section 5.2. For a two-dimensional movement, $\mathcal{Q}$ is with the choice of array center as stated in Corollary 5.1 defined by

$$\mathcal{Q} = \lim_{K\to\infty} \begin{bmatrix} \boldsymbol{p}_x & \boldsymbol{p}_y \end{bmatrix}^T \boldsymbol{\Sigma}_e^{-1} \begin{bmatrix} \boldsymbol{p}_x & \boldsymbol{p}_y \end{bmatrix} \triangleq \begin{bmatrix} \mathcal{Q}_{xx} & \mathcal{Q}_{xy} \\ \mathcal{Q}_{xy} & \mathcal{Q}_{yy} \end{bmatrix}, \tag{5.35}$$

with

$$\mathcal{Q}_{xx} = \int_0^1 p_x^2 \, dt - \left(\int_0^1 p_x \, dt \right)^2, \tag{5.36a}$$

$$\mathcal{Q}_{yy} = \int_0^1 p_y^2 \, dt - \left(\int_0^1 p_y \, dt \right)^2, \tag{5.36b}$$

$$\mathcal{Q}_{xy} = \int_0^1 p_x p_y \, dt - \int_0^1 p_x \, dt \int_0^1 p_y \, dt. \tag{5.36c}$$

Finding the array optimizing the worst-case AoA estimation performance can now be stated as an optimal control problem;

$$\begin{aligned} \underset{\dot{p}_x(t), \dot{p}_y(t)}{\text{maximize}} \quad & \mathcal{Q}_{xx}, \\ \text{subject to} \quad & \mathcal{Q}_{xy} = 0, \\ & \mathcal{Q}_{xx} = \mathcal{Q}_{yy}, \\ & \dot{p}_x^2(t) + \dot{p}_y^2(t) \leq 1. \end{aligned} \tag{5.37}$$

Note that the integrals in (5.36) are stated with a correction term to account for the displacement between the array frame and its mass center.

The first constraint of (5.37) can always be fulfilled since the array can be rotated such that the off-diagonal elements in $\mathcal{Q}$ become zero. The second constraint can be seen as a direct consequence of optimizing the worst-case performance. If a candidate solution is found where the estimation performance is different in the direction of the two eigenvectors of $\mathcal{Q}$, a better solution would be to lower the larger eigenvalue in order to increase the smaller one. It is easily seen that this can always be done, e.g., by rescaling the candidate solution. Consequently, the estimation performance in the direction of the two eigenvectors of $\mathcal{Q}$ should be equal. Finally, the last constraint limits the speed of the movement so that the length of the trajectory can not exceed 1.

The optimal control problem of (5.37) can be described using a seventh order state-space system as

$$\begin{cases} \dot{x}_1(t) = & u_1(t) \\ \dot{x}_2(t) = & u_2(t) \\ \dot{x}_3(t) = & x_1(t) \\ \dot{x}_4(t) = & x_2(t) \\ \dot{x}_5(t) = & x_1(t) x_2(t) \\ \dot{x}_6(t) = & x_1^2(t) \\ \dot{x}_7(t) = & x_2^2(t) \end{cases} \qquad x_n(0) = 0, \ \forall \, n \in \{1, \ldots, 7\} \tag{5.38}$$

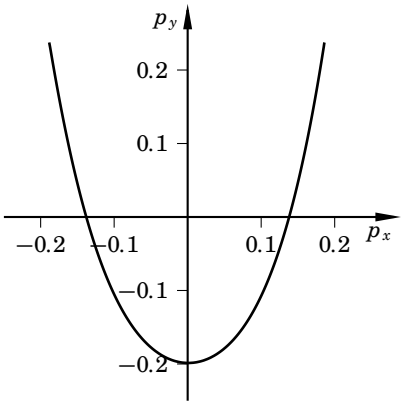

Figure 5.5 Worst-case-optimal 2D array configuration with $\mathcal{Q}_{xx} = \mathcal{Q}_{yy}$ and $\mathcal{Q}_{xy} = 0$ in the sense of (5.34). The array center $(\bar{p}_x, \bar{p}_y)$ has been moved to the origin to obtain a block diagonal FIM.

with the constraint $u_1^2(t) + u_2^2(t) \leq 1$, where $u_1(t)$ and $u_2(t)$ are the velocities in the x- and y- directions respectively and hence the control signals. The optimal control problem has been solved using jModelica [jModelica.org, 2016] which is an open source tool for solving nonlinear dynamic optimization problems. In the first scenario an open solution is wanted, i.e., the start and end points are not constrained to be equal, and the solution is presented in Figure 5.5 where the array center has been translated to the origin according to (5.29). Also note that the solution can be rotated around the origin, still yielding the same moment tensor $\mathcal{Q}$. Hence, there are an infinite number of solutions to the optimization problem but the one presented here is the one with the moments aligned with the coordinate axes. If the problem is further constrained so that $x_1(0) = x_1(1)$ and $x_2(0) = x_2(1)$, the solution becomes a circle.

The moments for four different array configurations are presented in Table 5.1. The L-shaped array consists of two equally long perpendicular segments while the square is a closed array, i.e., $x_1(0) = x_1(1)$ and $x_2(0) = x_2(1)$. The worst-case-optimal array configuration is approximately 41% better than the circle and 72% better than a square when comparing $\mathcal{Q}_{xx}$ (or $\mathcal{Q}_{yy}$). It is also seen that the moments of the L-shaped array are uneven in x and y, which is due to the array configuration.

Worst-case-optimal 3D Array

A similar problem to the one in (5.37) can be formulated to yield a solution in three dimensions with the constraint $\mathcal{Q}_{xx} = \mathcal{Q}_{yy} = \mathcal{Q}_{zz}$ on the moments and zeros everywhere else. A state-space model, similar to (5.38), with 12 states

Table 5.1 Moments for four different array configurations. All configurations have length 1, $\mathcal{Q}_{xy} = 0$, and $\mathcal{Q}_{xx} \leq \mathcal{Q}_{yy}$.

Shape	$\mathcal{Q}_{xx}$	$\mathcal{Q}_{yy}$
L-Shape	0.01042	0.04167
Square	0.01042	0.01042
Circle	0.01267	0.01267
Optimal (open)	0.01784	0.01784

Table 5.2 Moments for four different array configurations. All configurations have length 1 and for the worst-case-optimal configurations, $\mathcal{Q}_{xy} = \mathcal{Q}_{yz} = \mathcal{Q}_{xz} = 0$. Note that $\mathcal{Q}_{xx} \leq \mathcal{Q}_{yy} \leq \mathcal{Q}_{zz}$ for all configurations.

Shape	$\mathcal{Q}_{xx}$	$\mathcal{Q}_{yy}$	$\mathcal{Q}_{zz}$
Linear	0.003086	0.006173	0.03086
Helix	0.005509	0.005509	0.005509
Optimal (open-end)	0.006610	0.006610	0.006610
Optimal (closed-end)	0.003932	0.003932	0.003932

is used. The open- and closed-end solutions of the problem are presented in figures 5.6 and 5.7 respectively. Once again, the solutions presented here are aligned with the coordinate axes and the center of gravity in the origin to obtain a block diagonal FIM. The moments for four different array configurations are summarized in Table 5.2.

The linear array consists of three equally long perpendicular segments in the x, y, and z directions respectively and the helix antenna used for comparison is described by

$$\begin{cases} p_x(t) = \dfrac{\sqrt{1-l^2}}{r}\cos(rt) \\ p_y(t) = \dfrac{\sqrt{1-l^2}}{r}\sin(rt), \quad r \neq 0,\ 0 < l < 1. \\ p_z(t) = lt \end{cases} \tag{5.39}$$

By numerical optimization, parameters $r = 8.987$ and $l = 0.2571$ have been found and yield a helix configuration that maximizes the smallest eigen-

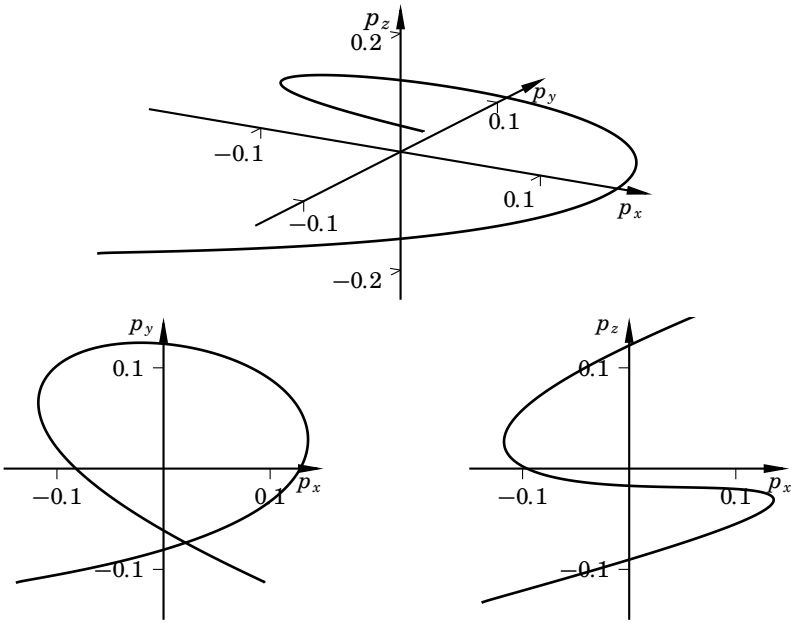

Figure 5.6 The curve indicates the open-end worst-case-optimal array configuration in 3D as well as projections $p_y(p_x)$ and $p_z(p_x)$ in the lower panels. The array center has been moved to the origin to obtain a block diagonal FIM.

value of $\mathcal{Q}$ for the corresponding FIM, see (5.34). In the 3D case the helix beats the worst-case-optimal closed-end array but the array configuration shown in Figure 5.6, i.e., the open-end array, performs approximately 20% better compared to the helix.

Joint AoA and Frequency Error Estimation

The worst-case-optimal arrays were defined assuming that the frequency error was known, see (5.35). If this is not the case, i.e., if the AoA and the frequency error have to be estimated jointly, then the AoA estimation performance will be affected. The effect can be studied using the Fisher information matrix with a prior distribution on the frequency error. If the prior is assumed to be Gaussian, the log-likelihood function in (5.16) is extended as

$$\mathcal{L} = c - (\boldsymbol{y} - \boldsymbol{h})^* \boldsymbol{\Sigma}_e^{-1} (\boldsymbol{y} - \boldsymbol{h}) - \frac{1}{2\sigma_{\delta,0}^2} (\delta_f - \delta_0)^2, \tag{5.40}$$

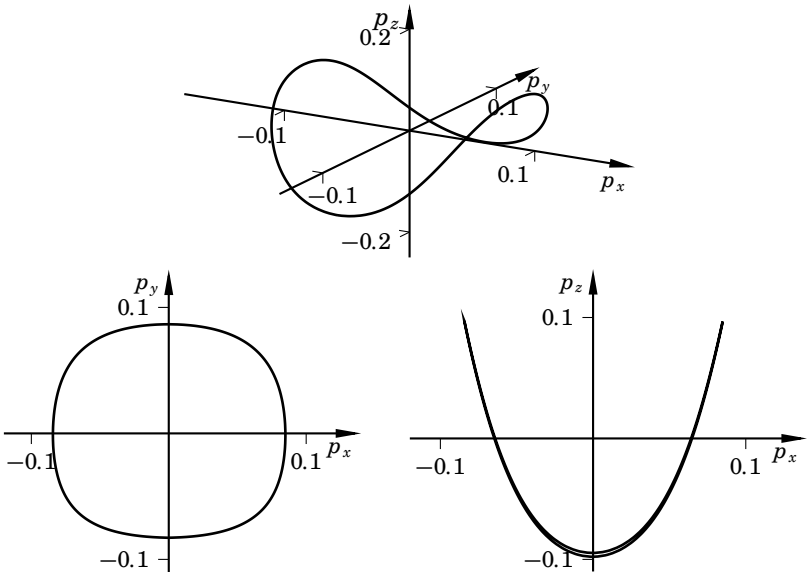

Figure 5.7 The curve indicates the closed-end worst-case-optimal array configuration in 3D as well as projections $p_y(p_x)$ and $p_z(p_x)$ in the lower panels. The array center has been moved to the origin to obtain a block diagonal FIM.

where δ_0 is the mean of the Gaussian prior, and $\sigma_{\delta,0}$ is the standard deviation. The other definitions remain unchanged. Consequently, the only element of the FIM that is changed is

$$-\mathbb{E}_{\boldsymbol{y}|\boldsymbol{\psi}}\left\{\mathrm{Re}\,\frac{\partial^2 \mathcal{L}}{\partial \delta_f^2}\right\} = 2\exp\{2\chi\}\,\mathrm{Re}\left\{\boldsymbol{t}^T\boldsymbol{\Sigma}_e^{-1}\boldsymbol{t}\right\} + \frac{1}{\sigma_{\delta,0}^2}. \tag{5.41}$$

By varying the standard deviation of the prior, scenarios with a highly informative prior ($\sigma_{\delta,0} \to 0$) to non-informative priors ($\sigma_{\delta,0} \to \infty$) can be investigated. The worst-case-optimal 2D open-end array is used for investigating its joint estimation performance under different levels of prior knowledge. The simulation result is presented in Figure 5.8. The result shows that for a highly informative prior, i.e., when the frequency error is known, the array has the same estimation performance regardless of the angle of arrival. This is expected from the assumptions underlying the design of the worst-case-optimal array. When the prior becomes more uninformative, the estimation performance is degraded. From the figure, it is clear that the estimation performance degradation is largest for AoA angles

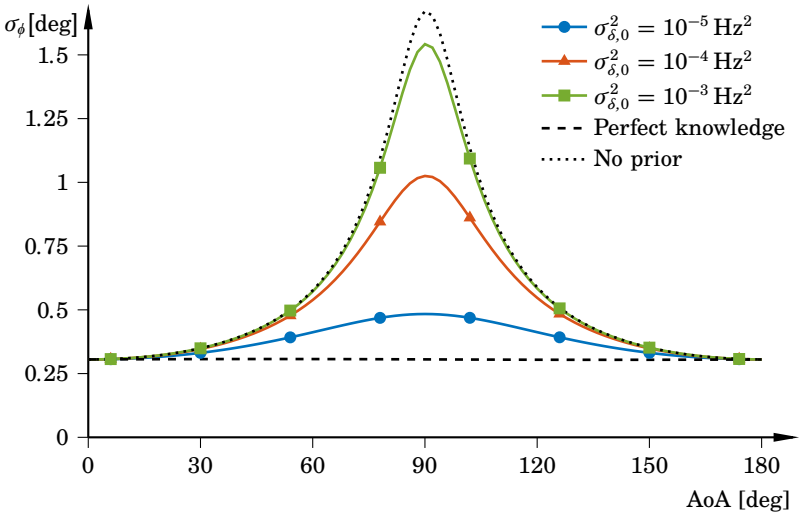

Figure 5.8 Estimation performance of ϕ as a function of AoA angle for three different levels of the standard deviation of the frequency error prior when the SNR is 20 dB. The dashed line is the performance with perfect knowledge of the frequency error and the dotted line when no prior information is available and the array is used for joint AoA and frequency error estimation. With perfect knowledge of the frequency error, the performance is equal for all angles as expected. When the prior becomes more uninformative, the estimation performance is affected with the largest deviation from the uniform case at 90 deg.

of 90 deg whereas for AoA angles of less than 30 deg or above 150 deg, the degradation is minor for all levels. The conclusion is that even though the array was constructed without taking the frequency error estimation into account, the array can often estimate the frequency error without a severe loss of performance.

5.3 Sensitivity Analysis

The worst-case-optimal array configuration presented in the previous section assumes perfect knowledge of the receive antenna element locations and that the clock signal is undisturbed. These assumptions can be fulfilled using a high precision tracking device and clock generator. However, if such equipment is unavailable, the accuracy of the estimated latent variables $\boldsymbol{\psi}$ will be degraded since the positions and time in $\boldsymbol{\Omega}$ are created using disturbed receiver locations and time stamps. To investigate the influence of disturbances in both space and time, the formulation of the hybrid infor-

mation matrix from (5.4) will be used. Here the analysis is limited to the single component scenario and the calculations for the multiple component scenario are provided in Appendix B.2.

The Hybrid Information Matrix

The calculations in (5.18) and (5.20) are reused for $\mathcal{H}_{\boldsymbol{\psi}\boldsymbol{\psi}^T}$ and the two additional matrices $\mathcal{H}_{\boldsymbol{\Omega}\boldsymbol{\Omega}^T}$ and $\mathcal{H}_{\boldsymbol{\psi}\boldsymbol{\Omega}^T}$ in (5.4) are derived below. It is assumed that the prior on $\boldsymbol{\Omega}$ is a Gaussian distribution and that the measurement noise is a zero mean circular symmetric complex Gaussian distribution. The log-likelihood function $\mathcal{L}$ for the distribution $p(\boldsymbol{y}, \boldsymbol{\Omega}|\boldsymbol{\psi})$ is then

$$\mathcal{L} = c - (\boldsymbol{y} - \boldsymbol{h})^* \boldsymbol{\Sigma}_e^{-1} (\boldsymbol{y} - \boldsymbol{h}) - \frac{1}{2} (\boldsymbol{\Omega} - \boldsymbol{\Omega}_0)^T \boldsymbol{\Sigma}_\Omega^{-1} (\boldsymbol{\Omega} - \boldsymbol{\Omega}_0), \tag{5.42}$$

where c is a constant, $\boldsymbol{y}$ the observations, $\boldsymbol{h} = \exp\{\chi - i\beta\} \exp\{-i\boldsymbol{\Omega}\boldsymbol{\gamma}\}$, $\boldsymbol{\Omega}_0$ is the mean of the Gaussian prior, and $\boldsymbol{\Sigma}_\Omega$ is its covariance. The matrix $\mathcal{H}_{\boldsymbol{\Omega}\boldsymbol{\Omega}^T}$ becomes

$$\mathcal{H}_{\boldsymbol{\Omega}\boldsymbol{\Omega}^T} = -\mathbb{E}_{\boldsymbol{y},\boldsymbol{\Omega}|\boldsymbol{\psi}} \left\{ \mathrm{Re} \frac{\partial^2 \mathcal{L}}{\partial \boldsymbol{\Omega}_v \, \partial \boldsymbol{\Omega}_v^T} \right\} = 2 \exp\{2\chi\} \, \mathrm{Re} \left\{ \boldsymbol{\Lambda}^T \mathbf{W}^* \boldsymbol{\Sigma}_e^{-1} \mathbf{W} \boldsymbol{\Lambda} \right\} + \boldsymbol{\Sigma}_\Omega^{-1}, \tag{5.43}$$

where

$$\begin{aligned} \boldsymbol{\Omega}_v &= \mathrm{vec}\{\boldsymbol{\Omega}\} \in \mathbb{R}^{4K}, \\ \boldsymbol{\Lambda} &= \boldsymbol{\gamma}^T \otimes \mathbf{I}_K \in \mathbb{R}^{K \times 4K}, \\ \boldsymbol{w} &= \exp\{-i\boldsymbol{\Omega}\boldsymbol{\gamma}\} \in \mathbb{C}^K, \end{aligned}$$

and $\mathbf{W} = \mathrm{diag}\{\boldsymbol{w}\} \in \mathbb{C}^{K \times K}$. Here $\otimes$ denotes the Kronecker product. The second element in the FIM becomes

$$\mathcal{H}_{\boldsymbol{\psi}\boldsymbol{\Omega}^T} = -\mathbb{E}_{\boldsymbol{y},\boldsymbol{\Omega}|\boldsymbol{\psi}} \left\{ \mathrm{Re} \frac{\partial^2 \mathcal{L}}{\partial \boldsymbol{\psi} \, \partial \boldsymbol{\Omega}_v^T} \right\} \tag{5.44}$$

with

$$-\mathbb{E}_{\boldsymbol{y},\boldsymbol{\Omega}|\boldsymbol{\psi}} \left\{ \mathrm{Re} \frac{\partial^2 \mathcal{L}}{\partial \chi \, \partial \boldsymbol{\Omega}_v^T} \right\} = \mathbf{0}_{4K}^T, \tag{5.45}$$

$$-\mathbb{E}_{\boldsymbol{y},\boldsymbol{\Omega}|\boldsymbol{\psi}} \left\{ \mathrm{Re} \frac{\partial^2 \mathcal{L}}{\partial \beta \, \partial \boldsymbol{\Omega}_v^T} \right\} = 2 \exp\{2\chi\} \, \mathrm{Re} \left\{ \boldsymbol{w}^* \boldsymbol{\Sigma}_e^{-1} \mathbf{W} \boldsymbol{\Lambda} \right\}, \tag{5.46}$$

and

$$-\mathbb{E}_{\boldsymbol{y},\boldsymbol{\Omega}|\boldsymbol{\psi}} \left\{ \mathrm{Re} \frac{\partial^2 \mathcal{L}}{\partial \boldsymbol{\mu} \, \partial \boldsymbol{\Omega}_v^T} \right\} = 2 \exp\{2\chi\} \, \mathrm{Re} \left\{ \mathbf{F}^T \boldsymbol{\Omega}^T \mathbf{W}^* \boldsymbol{\Sigma}_e^{-1} \mathbf{W} \boldsymbol{\Lambda} \right\}. \tag{5.47}$$

The expressions above simplify if the measurement noise is uncorrelated so $\boldsymbol{\Sigma}_e$ is diagonalized. This is summarized in Theorem 5.2.

THEOREM 5.2
Consider observations given by

$$\boldsymbol{y}(\boldsymbol{\Omega}, \boldsymbol{\gamma}, \chi, \beta) = \exp\{\chi - i\beta\} \exp\{-i\boldsymbol{\Omega}\boldsymbol{\gamma}\} + \boldsymbol{e} \in \mathbb{C}^K \tag{5.48}$$

where $\exp\{\cdot\}$ is element-wise exponentiation, χ and β are real constants, $\boldsymbol{e} = \begin{bmatrix} e_1 & \dots & e_K \end{bmatrix}^T \sim \mathcal{CN}(\boldsymbol{0}, \boldsymbol{\Sigma}_e)$,

$$\boldsymbol{\gamma} = \boldsymbol{f}(\boldsymbol{\mu}) = \begin{bmatrix} \cos(\phi)\sin(\theta) & \sin(\phi)\sin(\theta) & \cos(\theta) & \delta_f \end{bmatrix}^T, \tag{5.49}$$

and

$$\boldsymbol{\Omega} = \begin{bmatrix} p_{x,1} & p_{y,1} & p_{z,1} & t_1 \\ \vdots & \vdots & \vdots & \vdots \\ p_{x,K} & p_{y,K} & p_{z,K} & t_K \end{bmatrix} \triangleq \begin{bmatrix} \boldsymbol{p}_x & \boldsymbol{p}_y & \boldsymbol{p}_z & \boldsymbol{t} \end{bmatrix} \in \mathbb{R}^{K \times 4}. \tag{5.50}$$

The hybrid information matrix for the single component scenario with uncorrelated measurement noise and $\boldsymbol{\Omega} \sim \mathcal{N}(\boldsymbol{\Omega}_0, \boldsymbol{\Sigma}_\Omega)$ is given by

$$\mathcal{H}(\boldsymbol{\psi}) = \begin{bmatrix} \mathcal{H}_{\boldsymbol{\psi}\boldsymbol{\psi}^T} & \mathcal{H}_{\boldsymbol{\psi}\boldsymbol{\Omega}^T} \\ \mathcal{H}_{\boldsymbol{\Omega}\boldsymbol{\psi}^T} & \mathcal{H}_{\boldsymbol{\Omega}\boldsymbol{\Omega}^T} \end{bmatrix} \in \mathbb{R}^{(5+4K)\times(5+4K)}, \tag{5.51}$$

where $\boldsymbol{\psi} = \begin{bmatrix} \chi & \beta & \phi & \theta & \delta_f \end{bmatrix}^T \in \mathbb{R}^5$, and

$$\mathcal{H}_{\boldsymbol{\psi}\boldsymbol{\psi}^T} = 2\exp\{2\chi\} \begin{bmatrix} \operatorname{tr}\{\boldsymbol{\Sigma}_e^{-1}\} & 0 & \boldsymbol{0}_3^T \\ 0 & \operatorname{tr}\{\boldsymbol{\Sigma}_e^{-1}\} & \mathbf{P}^T\mathbf{F} \\ \boldsymbol{0}_3 & \mathbf{F}^T\mathbf{P} & \mathbf{F}^T\mathcal{Q}\mathbf{F} \end{bmatrix} \in \mathbb{R}^{5\times 5}, \tag{5.52}$$

$$\mathcal{H}_{\boldsymbol{\Omega}\boldsymbol{\Omega}^T} = 2\exp\{2\chi\}\boldsymbol{\Lambda}^T\boldsymbol{\Sigma}_e^{-1}\boldsymbol{\Lambda} + \boldsymbol{\Sigma}_\Omega^{-1} \in \mathbb{R}^{4K\times 4K}, \tag{5.53}$$

$$\mathcal{H}_{\boldsymbol{\psi}\boldsymbol{\Omega}^T} = 2\exp\{2\chi\} \begin{bmatrix} \boldsymbol{0}_{4K}^T \\ \mathbf{Q}^T \\ \mathbf{F}^T\boldsymbol{\Omega}^T\boldsymbol{\Sigma}_e^{-1}\boldsymbol{\Lambda} \end{bmatrix} \in \mathbb{R}^{5\times 4K}, \tag{5.54}$$

where

$$\mathbf{F} = \begin{bmatrix} -\sin(\phi)\sin(\theta) & \cos(\phi)\cos(\theta) & 0 \\ \cos(\phi)\sin(\theta) & \sin(\phi)\cos(\theta) & 0 \\ 0 & -\sin(\theta) & 0 \\ 0 & 0 & 1 \end{bmatrix} \in \mathbb{R}^{4\times 3}, \tag{5.55}$$

and

$$\mathbf{P} = \boldsymbol{\Omega}^T\boldsymbol{\Sigma}_e^{-1}\mathbf{1}_K \in \mathbb{R}^4 \tag{5.56}$$

$$\mathbf{Q} = \boldsymbol{\Lambda}^T\boldsymbol{\Sigma}_e^{-1}\mathbf{1}_K \in \mathbb{R}^{4K} \tag{5.57}$$

$$\boldsymbol{\Lambda} = \boldsymbol{\gamma}^T \otimes \mathbf{I}_K \in \mathbb{R}^{K\times 4K}. \tag{5.58}$$

The CRLB for the deterministic parameters $\boldsymbol{\psi}$ is obtained as

$$\mathcal{C}(\boldsymbol{\psi}) = \left[\mathcal{H}_{\boldsymbol{\psi}\boldsymbol{\psi}^T} - \mathcal{H}_{\boldsymbol{\psi}\boldsymbol{\Omega}^T}\mathcal{H}_{\boldsymbol{\Omega}\boldsymbol{\Omega}^T}^{-1}\mathcal{H}_{\boldsymbol{\Omega}\boldsymbol{\psi}^T}\right]^{-1}. \tag{5.59}$$

□

Acquisition Error Modeling

The acquisition error is characterized by the covariance matrix $\boldsymbol{\Sigma}_\Omega$ of the prior. For simplicity, it is assumed that the position error and time jitter are uncorrelated. The uncertainty in the sample time is due to jitter in the baseband clock signal and this will for ease of presentation be modeled as white Gaussian noise. For position errors, it is interesting to investigate both uncorrelated and correlated disturbances. We have found that this correlation has a significant impact on the resulting performance and therefore it should be carefully modeled. The uncorrelated case is applicable in virtual array solutions where the position of the receive antenna element is measured directly with limited accuracy. For a solution where the receiver unit is combined with an unaided IMU, the instantaneous positions are obtained by dead reckoning, see Figure 1.5. This is what is used in the initialization algorithm in Section 4.2 and also in [Yaqoob et al., 2013]. The double integration gives rise to significant correlation of position errors over time. The correlation is modeled using the state-space model,

$$\boldsymbol{p}_{k+1} = \boldsymbol{\Phi}\boldsymbol{p}_k + \boldsymbol{\Gamma}u_k \tag{5.60}$$

where $u_k \sim \mathcal{N}(\bar{u}_k, \sigma_k^2)$ is the noisy accelerometer signal. The double integrator is obtained with

$$\boldsymbol{\Phi} = \begin{bmatrix} 1 & T_s \\ 0 & 1 \end{bmatrix}, \quad \boldsymbol{\Gamma} = \begin{bmatrix} T_s^2/2 \\ T_s \end{bmatrix} \tag{5.61}$$

and the state vector $\boldsymbol{p}_k = \begin{bmatrix} p_{x,k} & v_{x,k} \end{bmatrix}^T$. The correlation matrix $\boldsymbol{\Sigma}_p = \mathbb{E}\{\boldsymbol{p}_x\boldsymbol{p}_x^T\}$ is then given by

$$[\boldsymbol{\Sigma}_p]_{(n,m)} = \sigma_p^2 \left[\sum_{k=1}^{\min(n,m)} \boldsymbol{\Phi}^{n-k}\boldsymbol{\Gamma}\boldsymbol{\Gamma}^T[\boldsymbol{\Phi}^{m-k}]^T\right]_{(1,1)}, \tag{5.62}$$

when the stochastic process u_k is considered stationary, i.e., $\sigma_p^2 = \sigma_k^2 \; \forall \, k \in \{1, \ldots, K\}$, making the correlation matrix $\boldsymbol{\Sigma}_p$ linear in σ_p^2. If the correlating effect of a gyroscope in the inertial measurement unit is neglected, the uncertainty in position can be modeled as uncorrelated between the three axes. With these assumptions, the covariance matrix of the prior will be block diagonal with $[\boldsymbol{\Sigma}_x, \boldsymbol{\Sigma}_y, \boldsymbol{\Sigma}_z, \boldsymbol{\Sigma}_t]$ on the diagonal.

Results for 2D Array

To illustrate the results of Theorem 5.2, the worst-case-optimal open-end 2D array derived in Section 5.2 is used again. As before, estimation of the elevation angle θ is not considered for the 2D array since it can not determine elevation angles. The distribution for the time jitter is zero mean with covariance $\mathbf{\Sigma}_t = \sigma_t^2 \mathbf{I}_K$.

Furthermore, for the position errors two different scenarios are investigated, uncorrelated position noise, and second-order correlated position noise. For simplicity it is assumed that the noise in x and y have the same distribution. The covariance matrices for the uncorrelated case are set to $\mathbf{\Sigma}_x = \mathbf{\Sigma}_y = \sigma_p^2 \mathbf{I}_K$, while the correlated covariance matrices are given by (5.62). The sample frequency is set to 250 Hz and the measurement noise level is set to 20 dB. The CRLB for the azimuth angle ϕ and frequency error δ_f, denoted σ_ϕ and σ_δ respectively, are shown in Figure 5.9 as a function of position RMSE for three different levels of time jitter RMSE levels σ_t for both scenarios.

There is a clear performance degradation when the time jitter noise increases as well as when the position RMSE increases. The performance degrades linearly with increasing position RMSE. The correlation of the position errors also lowers the tolerable position RMSE level with a factor of approximately 2.5. For the frequency error, the same factor is 10 indicating that the array performance for frequency error estimation is more sensitive to correlated position errors. From the results it is seen that the array has similar sensitivity to position RMSE and time jitter RMSE levels for both AoA and frequency error estimation.

Summary

In the single ray scenario, the relationship between the CRLB and the components of the moment of inertia tensor in space-time was made clear and presented as Theorem 5.1. The result was illustrated by finding arrays in both 2D and 3D that maximize the worst-case estimation performance by numerically solving an optimal control problem. The arrays were presented in Figure 5.5 for an open-end 2D array and figures 5.6 and 5.7 for the 3D arrays. The analysis was taken further by investigating the AoA estimation performance of the worst-case-optimal array with a prior on the frequency error. The result showed that the performance became dependent on the AoA even though the array was constructed with uniform estimation performance. The conclusion of the analysis is that the array is still usable for AoA estimation.

To investigate performance degradation when perfect knowledge of position and time is unavailable, an analysis was carried out using the formulation of the hybrid information matrix where prior information on the

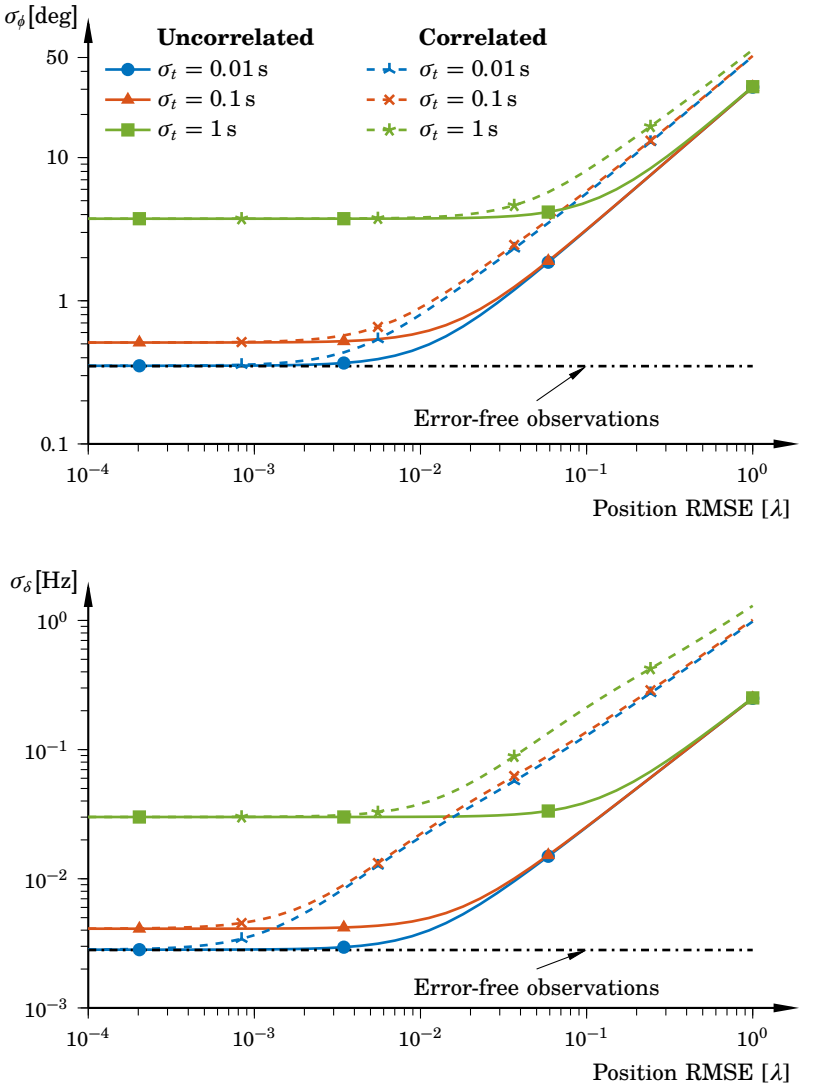

Figure 5.9 CRLB for ϕ and δ_f for uncorrelated and correlated position errors and uncorrelated time jitter. The dash-dotted line marks the CRLB calculated when there are no disturbances on $\mathbf{\Omega}$, i.e., the formulation from Theorem 5.1. The SNR is 20 dB and the AoA ϕ_0 is 30 deg. There is a clear performance degradation in both ϕ and δ_f estimation due to increasing levels of jitter as well as position uncertainties. Note that the frequency estimation is more sensitive to correlation of the position errors compared to the AoA estimation.

receive antenna element locations and the clock signal was included. The formulation was presented as Theorem 5.2. This theorem provides an understanding of how position and time inaccuracies degrade the performance of the virtual array. It was found that the correlation in position error which typically arises when using an IMU had significant impact on the result and therefore needs to be taken into account.

5.4 Recursive Cramér-Rao Lower Bound

From the previous section we know that the CRLB can efficiently be calculated for a scenario where the angle of arrival and amplitudes of the multipath components are considered constant during the acquisition period. We will now study the joint problem where the location is estimated simultaneously with the AoA and amplitude of the MPC as well as the frequency error. For this purpose, the recursive Cramér-Rao lower bound formulation for the state-space model derived in Section 3.3 will be used. The CRLB is calculated using the extended Kalman filter presented as Algorithm 4.1. Since the recursive estimation in subsequent chapters will be carried out on a 2×2 MIMO system, the CRLB analysis is for MIMO as well. An analysis assuming SISO can be found in [Mannesson, 2013].

In the analysis, the movement of the receiver on the x-axis is given by

$$p_x(t) = 3\lambda \sin(\pi t). \tag{5.63}$$

There is no movement along neither the y-axis nor the z-axis. The receiver is moving for one minute and is then left resting at $p_x = 0$ for two minutes. The radio channel is configured as having one, two, or three impinging specular MPCs, all with the same amplitude and a noise power equivalent to an SNR of 20 dB. The three simulation results are given in figures 5.10, 5.11, and 5.12 where the standard deviation of the positions (p_x, p_y), amplitude α, frequency error δ_f, and AoA ϕ is presented as a function of time. In Table 5.3, the slopes for the standard deviation growth rate for the different states in the model are given, assuming an unaided IMU. For β no individual noise processes n_β are present. Consequently the uncertainty in phase is coming from the uncertainty in frequency error δ_f.

The result with one impinging MPC reveals that even though the phase information of the radio signal is used, there is no change of the growth rate in the uncertainty of the position estimate. This is consistent with previous results; tracking one MPC does not provide any information perpendicular to the AoA, see Figure 2.8, and the uncertainty can therefore increase in this direction. Hence, one MPC alone can not significantly increase the accuracy of the estimated position. Looking at the AoA state ϕ_1^R, the algorithm is able to limit the growth of the uncertainty. This is different

Table 5.3 Slope of the standard deviation growth rate for the recursive model when the IMU is unaided.

State		Slope
Position	p_x, p_y	2.5
Angle of arrival	ϕ	0.5
Amplitude	α	0.5
Phase	β	1.5
Frequency error	δ_f	0.5

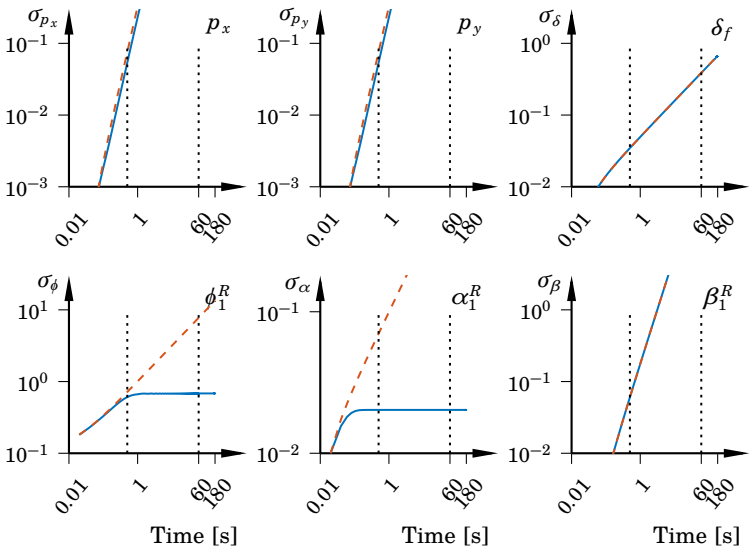

Figure 5.10 Cramér-Rao lower bound of state estimation with one MPC impinging on the receiver with a sinusoidal movement along the x-axis. The plots show standard deviation versus time for the states p_x, p_y, δ_f, ϕ_1^R, α_1^R, and $\beta_{1,1}^R$ at an SNR of 20 dB. The dashed lines show the case when no radio signal is supplied. The first vertical dotted line marks when the receiver reaches the maximum deviation from the origin the first time and the second when the movement has stopped. The only states that exhibit any considerable improvement in estimation accuracy is AoA and amplitude and there is a small performance gain of $\sqrt{2}$ for p_x and p_y.

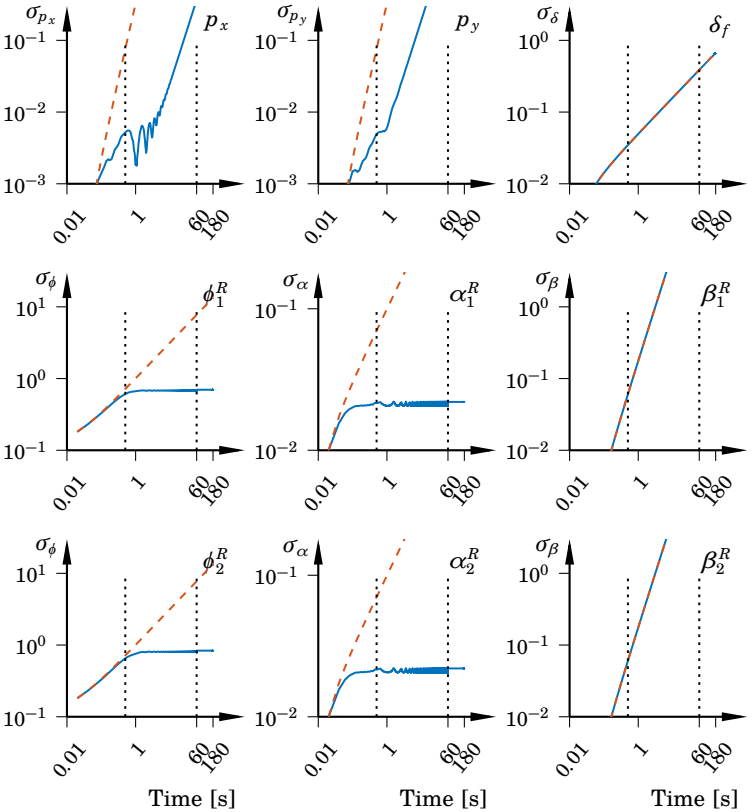

Figure 5.11 Same as Figure 5.10 but for two MPCs. The improvement in position accuracy is approximately 32 dB but the asymptotic growth rate is unaffected. The variance of the AoA is limited and the stationary level is dependent on the AoA. The estimation variance of the amplitude varies over time, which is due to the change in distance to the origin when the receiver is moving.

from previously published results in [Mannesson et al., 2015b; Mannesson, 2013] and the reason is the MIMO system used in this set-up. Since the receiver is equipped with two antennas with a separation of 0.6λ, compared to one receive antenna in the previous results, the AoA can be estimated since the physical displacement and orientation between the two antennas is assumed to be known. The uncertainty in the amplitude and frequency error is in line with the previous results. The amplitude, which the measurements are linearly dependent on, can be estimated while the frequency

error variance still grows at a constant rate.

The result with two impinging MPCs, see Figure 5.11, shows a performance improvement of approximately 32 dB for the position estimate but the asymptotic growth rate is unaffected. Also, the variance of the phase of the components is still growing without any change. Furthermore, the amplitude that before reached a static level now fluctuates with the movement and settles on a static level once the receiver stops moving. In the SISO case, the variance of the amplitude estimation starts growing after the receiver is stopped. The conclusion is that two multipath components do not provide enough information to improve either the position nor the frequency error estimation performance significantly.

With three impinging MPCs the result is clearly different from the previous cases. The uncertainty of the position estimates is now bounded, and the accuracy depends on the movement. As the receiver is moving away from the origin, the uncertainty grows and when it turns back, the uncertainty is reduced again. Clearly there is a dependence between the distance from the origin and with what accuracy the position can be estimated. This is due to the AoA modeling of the MPCs for the radio channel. A small variation of ϕ when the receiver is far away from the origin will have a bigger impact on the phase of the received signal compared to if the receiver is kept close to the origin. The uncertainty in the frequency error is now bounded which directly impacts the argument state β for all the components. However, with three components, the amplitude and AoA estimates are now varying with the movement but when the receiver stops, the uncertainty grows again. The conclusion from these simulation results is that as long as the receiver is moving, an estimator would be able to estimate the states of the joint position and radio channel state-space model with a non-growing uncertainty and that at least three multipath components must be available in order to estimate all the states with good performance.

The recursive Cramér-Rao lower bound calculations show promising results for the joint estimation problem. If the movement is rich enough and at least three MPCs impinge on the array, all states can be estimated and with bounded growth rate of the variance assuming that the receiver is moving. This is a huge fundamental improvement of what can be achieved in terms of estimation and accuracy using the joint position and radio channel tracking model compared to the unaided IMU case.

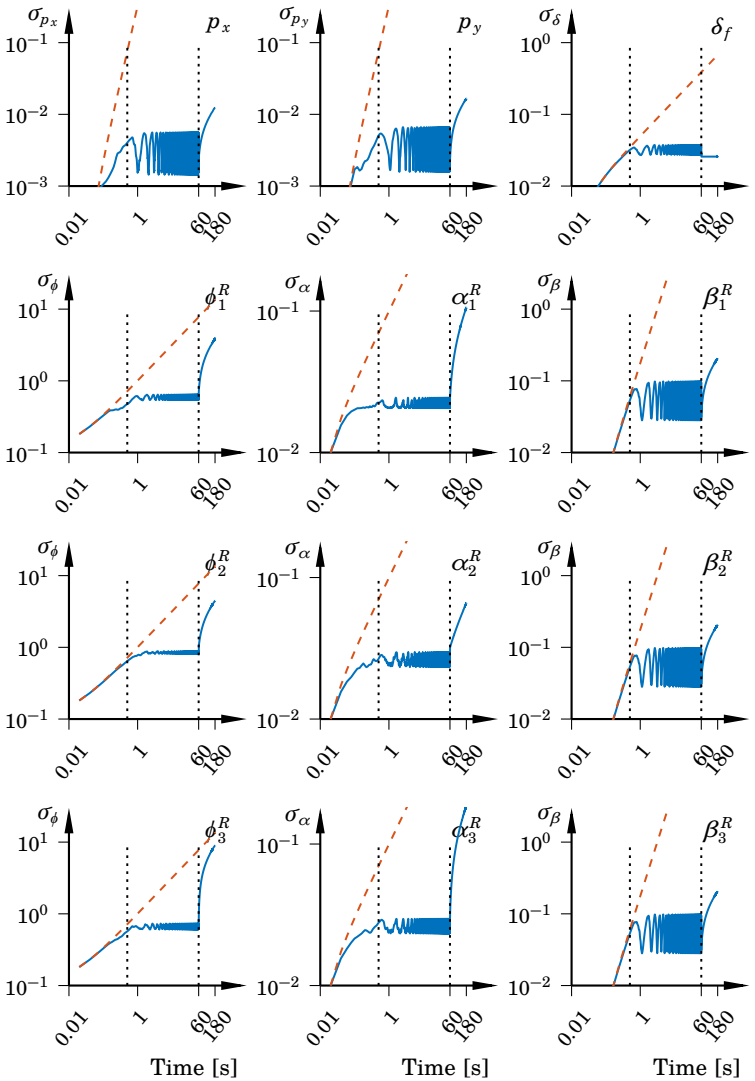

Figure 5.12 Same as Figure 5.11 but with three impinging MPCs. The improvement in position accuracy is clearly noticeable and the growth rate has been restrained. Also, the performance improvement when it comes to AoA and amplitude compared to the unaided scenario is similar to the result in Figure 5.11. For the frequency error and thereby the argument β, the growth rate is also restrained as long as the receiver is moving.

6

Joint Positioning and Radio Channel Estimation

With the performance studies from the last chapter we are ready to simulate the marginalized particle filter to investigate its estimation performance on synthetic signals. We will specifically investigate scenarios where all impinging multipath components are considered to be scattered by point sources and also scenarios with one cluster present in the environment. We limit the analysis to a SISO system and a 2×2 MIMO system. For the SISO system, the antenna is assumed to be aligned with the IMU center. In the MIMO system, the antennas are separated 10 cm which is justified by the size of cellular phones available today. In all simulations, the carrier frequency is set to 1.8 GHz which corresponds to a wavelength of 16.7 cm. Consequently, the antenna separation for the MIMO system is $0.6\,\lambda$.

The marginalized particle filter, presented as Algorithm 4.3, is implemented in MATLAB. For all simulations in this chapter, a trajectory spanning approximately 50 by $50\,\lambda$ in the x and y dimensions is generated and sampled at 50 Hz. The sample frequency is chosen to suit the velocity reached when walking and the wavelength is approximately 16.7 cm. The movement starts and ends in the origin and the full movement takes 60 seconds to complete. The maximum velocity during the movement is $7.5\,\lambda$/s. The trajectory is converted to accelerometer readings with additive white Gaussian noise with intensity similar to what is seen in an IMU of consumer grade. During the movement, the device is assumed to have a fixed orientation, i.e., the gyroscope signal is only white Gaussian noise with intensity similar to what is seen in a consumer grade IMU. This is however not known by the filter which still estimates orientation. For this trajectory, no random walk processes for the accelerometer or the gyroscope are included. The reason is that for time periods of 60 seconds, the additive white Gaussian noise is still the dominant part of the noise signal. See Table 1.1 for data sheet values. Constant bias in the sensors has also been neglected

Table 6.1 Nominal settings used for simulations in this chapter.

	Value
Carrier frequency [GHz]	1.8
Sample rate [Hz]	50
SNR [dB]	30
Angle of arrival change rate [deg/$\sqrt{\text{s}}$]	0.5
Amplitude change rate [1/$\sqrt{\text{s}}$]	0.1
Frequency error change rate [Hz/$\sqrt{\text{s}}$]	0.1
Accelerometer noise intensity [m/s/$\sqrt{\text{h}}$]	0.085
Gyroscope noise intensity [deg/$\sqrt{\text{h}}$]	1.5

Table 6.2 The nominal initial distributions of the states where $[\cdot]^\star$ denotes the true state value obtained by the sparse Bayesian learning algorithm presented in Section 4.2.

State		**Distribution**
Angle of arrival [deg]	ϕ	$\mathcal{N}(\phi^\star, 5)$
Amplitude [-]	α	$\mathcal{N}(\alpha^\star, 0.2)$
Phase [deg]	β	$\mathcal{N}(\beta^\star, 12)$
Frequency error [Hz]	δ_f	$\mathcal{N}(\delta_f^\star, 5 \cdot 10^{-2})$

since the calibration error is assumed to be small compared to other errors. The positioning results from the simulations with the filter are compared to the dead reckoning performance of the IMU signal. The nominal parameter setting for the simulations are given in Table 6.1. Note that the SNR is defined as an average value over the whole dataset, the instantaneous SNR can consequently be higher or lower.

In all the simulations it is assumed that the sparse Bayesian learning algorithm has been able to find an estimate of the angle of arrival, complex amplitude, and frequency error and the states are therefore initialized according to Table 6.2. These values are justified by the results in Figure 4.7.

6.1 Simulations for SISO Configuration

The filter performance for the SISO system is investigated when the number of impinging MPCs is varied from three up to six. The angles of arrival for the MPCs are randomly chosen from the range $[-\pi, \pi]$ with a constraint that two components can never be closer than 36 deg from each other. This restriction is introduced to avoid coinciding components which would make them similar to a cluster. In Figure 6.1, one run of the analysis with four MPCs is presented and in Figure 6.2 the mean position RMSE is presented when the number of particles is varied for the four different cases.

In Figure 6.1 position RMSE, amplitude, AoA, and frequency error are shown. It is seen that the filter tracks both position in x and y as well as the states associated with the MPCs. The position RMSE is never higher than $2.5\,\lambda$ during the whole movement and the average position RMSE for the whole trajectory is $0.6\,\lambda$ which equals 10 cm at the given wavelength. This is the most successful run and not average performance which is approximately 4 times worse. At 30 s, the distribution for the AoA ϕ_3 widens. Since the amplitude for the same MPC at the same time instant is low, the filter estimate of the amplitude is close to zero which makes the contribution from the erroneous AoA estimate negligible. There is also a clear widening in the distribution for the position at the same time instant which can be due to reduced information obtained from MPC 3. Also note that the AoA for the third component is approximately 240 deg which is the direction the receiver is moving in at the specific time instant. From our findings concerning estimation performance, it is known that the estimation performance is worse as the receiver travels towards or away from the impinging MPC.

Looking at the cumulative distributions in Figure 6.2, we see that as the number of MPCs present in the environment is increased from three to four, the mean position RMSE is almost halved. Compared to the performance obtained by a stand-alone consumer grade IMU, the filter-based solution performs 22 times better on average. For five MPCs, the mean position RMSE for the best 50% of the cases is marginally lowered but for the worst 50% it is clearly worse compared to the scenario with four MPCs. This effect is emphasized even more with six MPCs. The explanation for the deteriorated behavior is the increased number of states for the estimation problem with six MPCs. This is also seen in Figure 6.3 where the number of particles has been varied instead and the number of MPCs is fixed to five. The improvement in mean position RMSE when the number of particles is increased is clear. For 500 particles, the filter fails to benefit from the data given by the radio channel estimates; the nonlinearities in the measurement equation are too severe and the state-space dimension is too large to be well covered by 500 particles. When the number of particles is increased, the filter can benefit from the extra information and the plateau

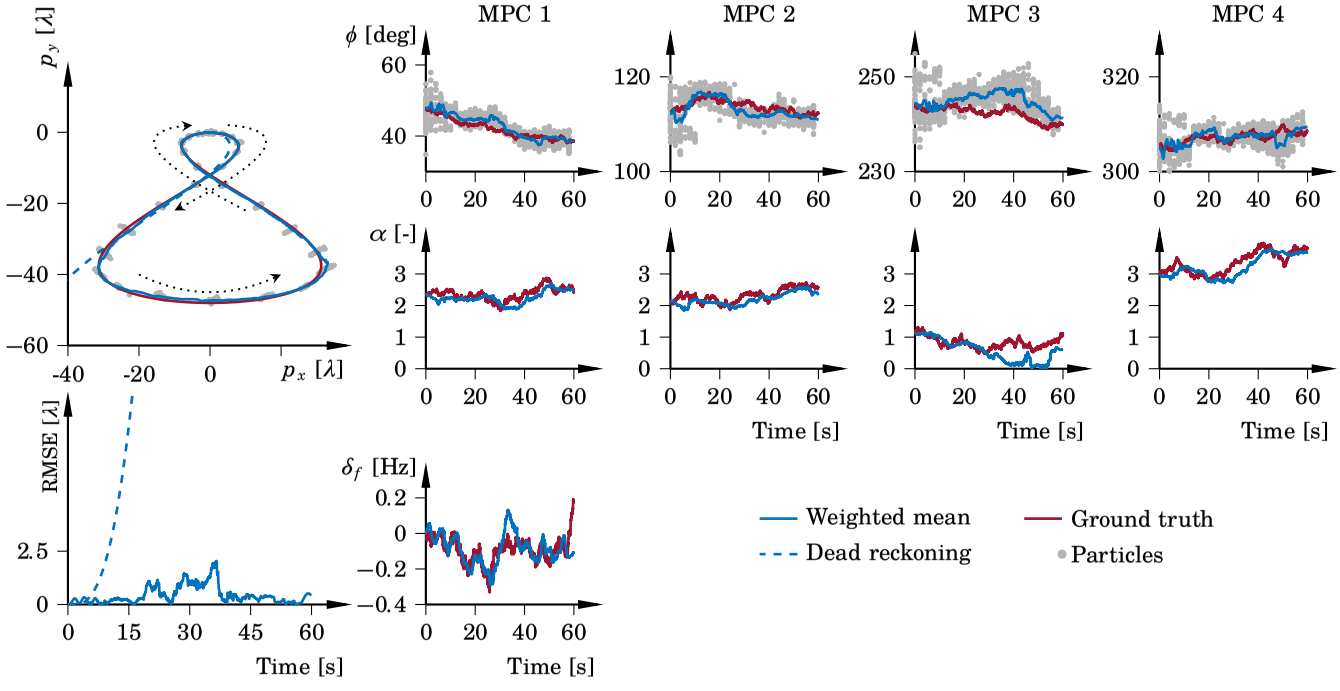

Figure 6.1 SISO simulation result when tracking four MPCs with 5000 particles and an SNR of 30 dB. The left panel shows the position estimation and the position RMSE over time. The right panel shows the estimates for the states associated with the MPCs. In the figures, the 50 highest weighted particles are shown every other second. The mean position RMSE for the trajectory is 0.6 λ. At 30 seconds there is some deviation in the frequency error estimation as well as for the AoA of the third MPC. The mean position RMSE using dead reckoning for the dataset is 113 λ.

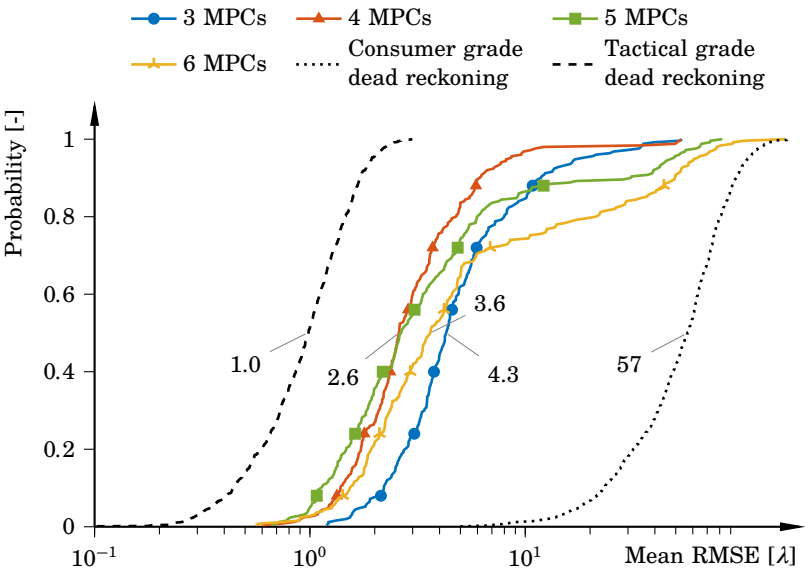

Figure 6.2 The cumulative distributions for mean position RMSE in the SISO case when the number of MPCs is varied. The change rates for the states used in the simulations are found in Table 6.1. The numbers indicate the median of cumulative mean position RMSE for each distribution. The number of particles is 5000 and the distributions are created from 250 simulations. When the number of MPCs is increased from three to four, the performance is improved. If more MPCs are present, more particles would be needed to maintain the performance. The dashed and dotted curves indicate the performance of dead reckoning with different IMU grades without using radio channel information.

which indicates where the filter completely fails to estimate the state vector is pushed upwards. Hence, it is believed that the performance seen for four and five MPCs can be reached when more MPCs are present given that the number of particles can be increased accordingly. The reason for not doing this here is simulation time.

6.2 Simulations for MIMO Configuration

For the MIMO case we study scenarios with four MPCs originating from point sources and cases where one of the four MPCs is exchanged for a cluster. For the case with only point sources, we investigate how the width of the prior distribution on β affects the results since this is believed to have a major impact on the estimation performance, at least with the number

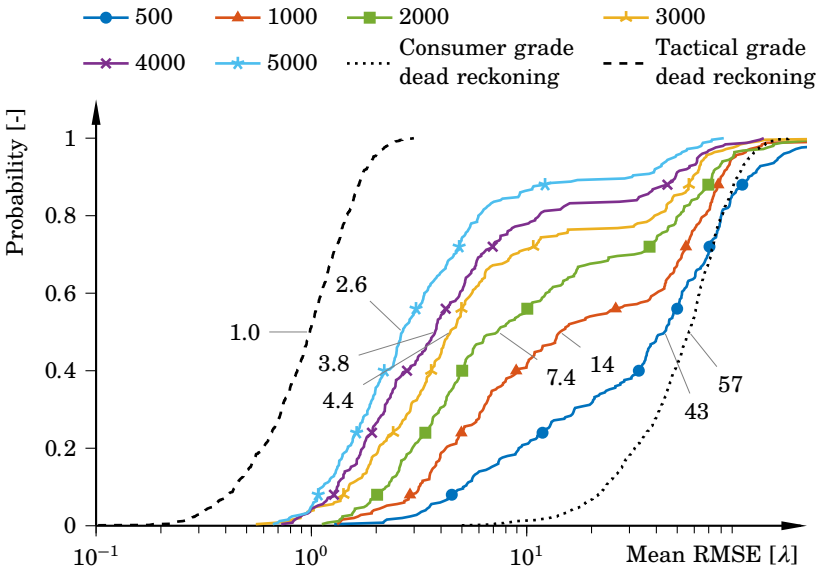

Figure 6.3 The cumulative distributions for mean position RMSE in SISO when tracking five MPCs using different number of particles. The numbers indicate the median of cumulative mean position RMSE for each distribution. There is a clear decrease in mean position RMSE when the number of particles is increased. Note that the median performance for 5000 particles is equal to the performance at 4000 particles with four MPCs, compare Figure 6.2. The dashed and dotted curves indicate the performance of dead reckoning with different IMU grades without using radio channel information.

of particles we have used. We also investigate how the angle of arrival and frequency error change rate influence the estimation performance and finally also the performance when the SNR is varied.

In Figure 6.4, position, amplitude, AoA, and frequency error are presented for a single particle filter run. The mean position RMSE for the whole trajectory is approximately 0.8 λ which equals 13.5 cm at the current wavelength. The result is an improvement compared to the SISO case in Figure 6.2, mainly since there are four channel estimates used for the estimation. The estimates of the amplitude and AoA are also good with some deviation on the AoA for the third MPC at 30 seconds. This is also seen in a degraded RMSE at 30 seconds, similar to what is seen in the SISO case.

In Figure 6.5, the estimation performance is compared to the recursive Cramér-Rao lower bound. The CRLB is calculated in the same way as in Section 5.4. The filter is able to almost reach the CRLB for position and it

actually outperforms the bound for amplitude estimates, see the lower part of Figure 6.5. The reason for this can be bias in the estimates or that the particle filter has recently resampled which lowers the state variance. For the AoA in the middle part and the frequency error the filter is close to the CRLB. The result indicates that there is almost no more information to extract from the measurements.

In Figure 6.6, the cumulative distributions of the mean position RMSE are shown when the number of particles is varied and also when the width of the prior distribution on β is varied. As expected, the median value of the mean position RMSE distribution is lowered as the number of particles is increased. Compared to the SISO case, the performance for all numbers of particles is improved. Worth noting is that the performance in 80% of the cases is better than for a tactical grade IMU using dead reckoning. The reason for fewer simulations where the filter fails to track the state vector with MIMO compared to SISO is that the distance and orientation of the two receive antennas is known. The filter is therefore able to exploit the knowledge of this correlation between the measurements and produce a better estimate with less particles. It is also clear that when the prior on β is less informative, the performance is degraded. The 4000 particle filter performance with a wider prior equals the 3000 particle filter performance with a narrower prior. The conclusion is that if the prior becomes less informative, the performance can be regained by increasing the number of particles.

In Figure 6.7, the AoA change rate is varied and the SNR is lowered to 20 dB. Compared to the results from Figure 6.6 where the change rate was $0.5\,\mathrm{deg}/\sqrt{\mathrm{s}}$ at 30 dB, there is only a minor difference due to the lowered SNR. The reason for the slightly increased performance at the top of the distribution is due to tuning of the filter while the median remains unchanged. As the AoA change rate is increased, the performance is worsened. The AoA change rate sets the rate at which the map over the fading pattern becomes useless. A consequence of the higher change rate is that position estimates that were unlikely at a lower change rate become likely since the map provides less information. Hence, the filter will not be able to discard these hypotheses and they are thereby deteriorating the position estimates. Also, as the rate increases, the filter must spread out the particles wider in the state-space which makes the particle representation a worse approximation of the true underlying distribution. This is what causes lowered performance as the change rate increases. It is believed that increasing the number of particles can regain some of the lost performance but to what extent is yet unknown.

The next investigation on parameter variation is SNR variations. Figure 6.8 shows the cumulative distributions for mean position RMSE with 250 simulations when the average SNR is varied from 0 dB to 20 dB. The dif-

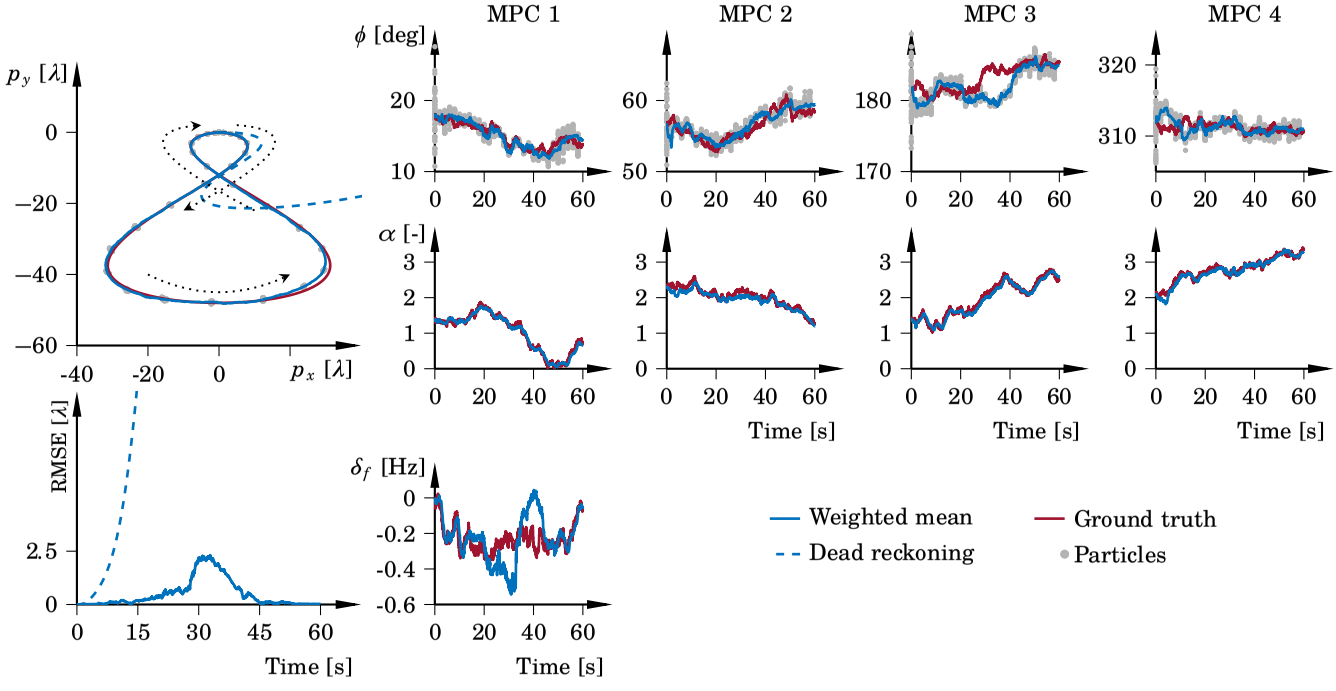

Figure 6.4 Simulation result for a typical MIMO case using 4000 particles and an SNR of 30 dB. The left panel shows the position estimates and the position RMSE over time. The mean position RMSE is 0.82 λ for the whole trajectory. The right panel shows the estimated amplitude, AoA, and frequency error compared to the true values. For the nonlinear states, the 50 highest weighted particles are shown every other second. The mean position RMSE using dead reckoning for the dataset is 154 λ.

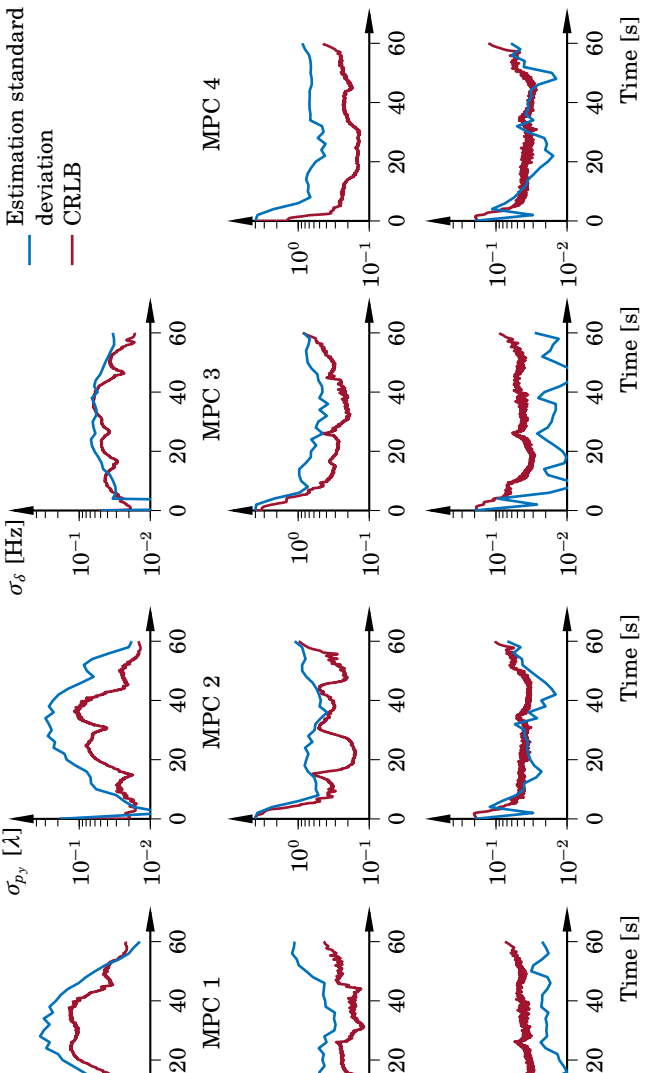

Figure 6.5 CRLB and standard deviation of the estimate for the dataset shown in Figure 6.4. The standard deviation is the mean standard deviation of 25 particle filter runs on the same dataset. The filter is able to reach the CRLB for the frequency error σ_δ and occasionally for the angle of arrival estimation. Note that for the amplitude, the filter outperforms the CRLB.

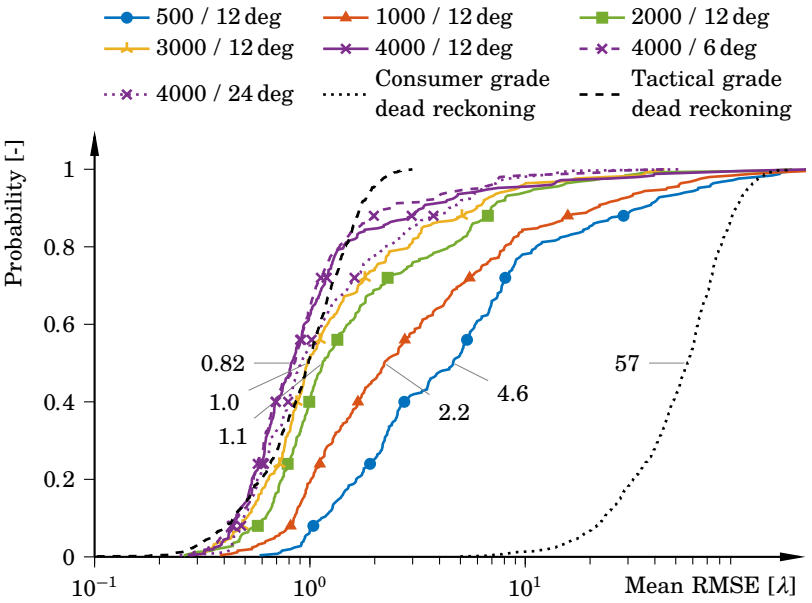

Figure 6.6 The cumulative distribution for mean position RMSE in the MIMO case. The change rates for the states used in the simulations are found in Table 6.1. When the number of particles is increased, the mean position RMSE is lowered as expected. The difference in performance when the prior becomes less informative is noticeable; the 4000 particle filter performance is similar to the 3000 particle filter performance with a smaller prior. The dashed and dotted curves indicate the performance of dead reckoning with different IMU grades without using radio channel information. Note that the particle filter solution with 4000 particles outperforms the dead reckoning performance of a tactical grade IMU in 80% of the cases. Compared to the consumer grade IMU, the mean position RMSE is almost 70 times lower.

ference between the distributions is small which indicates that the filtering solution is capable of handling low SNR situations as well. An explanation of the good performance, even for the low SNR scenarios, can be traced back to the dead reckoning equations. As mentioned in Section 1.2, the main contribution to the positioning error in dead reckoning is the noise from the gyroscope which causes orientation errors. The incorrect orientation leads to a non-zero residual term when gravity has been canceled. This residual term is then integrated twice. The noise from the accelerometer gives, compared to this error, a minor contribution to the final position error. Consequently, any particles in the filter that hold an incorrect hypothesis of the orientation will quickly have an incorrect position and thereby be

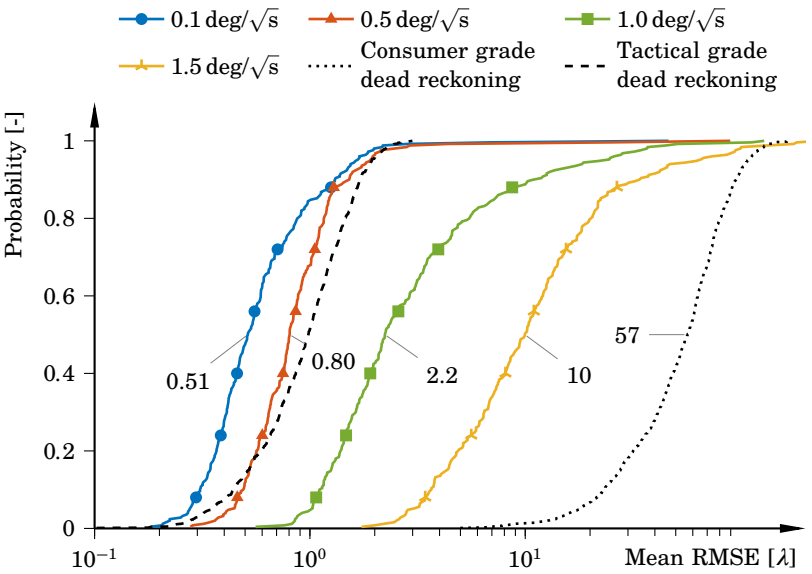

Figure 6.7 The cumulative distributions for mean position RMSE in the MIMO case with 4000 particles and an SNR of 20 dB. As the change rate for the AoA is increased, the filtering performance deteriorates. The reason for this is that the same number of particles is expected to cover larger filtering distributions and that the map changes too rapidly between consecutive time samples. It is believed that some of the lost performance can be regained if the number of particles is increased.

removed in the next resampling step of the filter. This holds regardless of the number of antennas on the receiver side. The conclusion is that if only the orientation can be obtained with high accuracy, the accelerometer signal with a negligible residual from gravity left can be used for calculating the position and this is what is done by the filter.

Note that the states in the filter have been correctly initialized according to Table 6.2 regardless of the average SNR. In a scenario where the initialization of the filter has to be done at an SNR of 0 dB, it is unlikely that the sparse Bayesian learning algorithm would find all MPCs and the initialization of the filter would therefore be erroneous. The performance in such a case would be seriously affected. Instead, the simulations can be seen as what would happen if the SNR drops after the filter has been correctly initialized, for instance when the receiver moves into an area with worse reception.

To test the ability of the filter to track larger frequency errors, three different levels of frequency error are tested at an SNR of 20 dB. The cu-

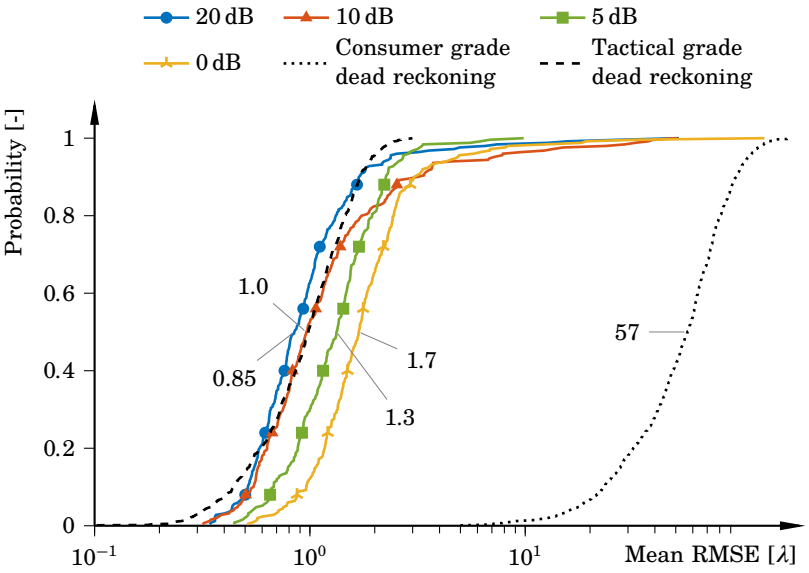

Figure 6.8 The cumulative distributions for mean position RMSE in the MIMO case with 4000 particles and varying average SNR. The difference between the distributions is small. The reason why the 10 dB distribution crosses the lower SNR distributions is unclear but a possible explanation is tuning of the filter. Separate tuning of the particle filter parameters has been performed for each case.

mulative distributions for 250 Monte Carlo simulations for one MIMO case and three SISO cases are shown in Figure 6.9. The MIMO case is at large unaffected by the increased frequency error which can be explained by how the frequency error is modeled. In the model, it is a common contribution on all receive antenna signals. Hence, the dual antenna unit can partition the phase change that is seen in the received signals into two components: one contribution from the movement and another one from the frequency error. In the SISO case, the filter can not separate the contributions and the positioning performance is thereby negatively affected by the increased frequency error.

Simulations for MIMO Configuration With Clusters

For the cluster simulation, one MPC is exchanged for a cluster chosen from Table 2.1. As before, the particle filter is initialized according to Table 6.2. In Figure 6.10, the cumulative distribution of the mean position RMSE is shown. Regardless of cluster type, the performance is negatively affected when the cluster is introduced. The mean position RMSE is doubled and

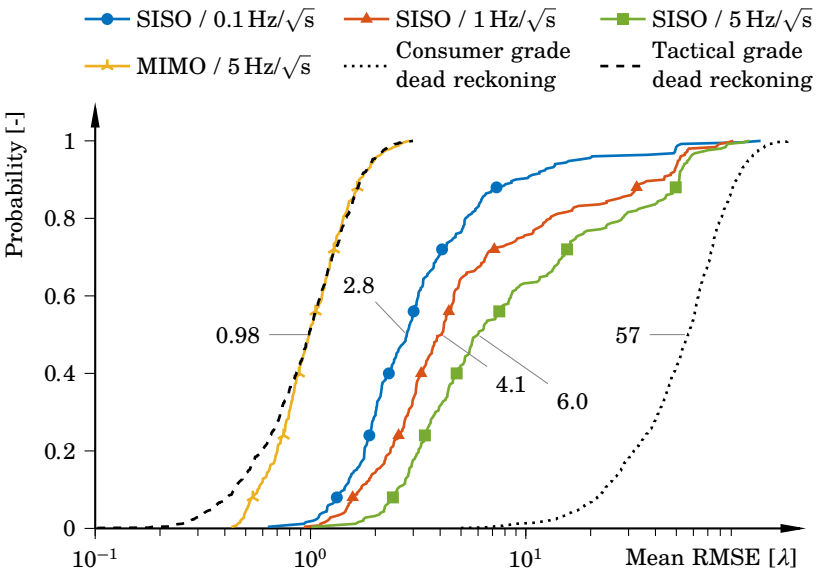

Figure 6.9 The cumulative distributions for the mean position RMSE in the SISO and MIMO cases with 4000 particles and an SNR of 20 dB. As the change rate for the frequency error is increased, the performance in the SISO case is negatively affected since the filter can not determine if the change in phase is due to the movement or due to frequency error. In the MIMO case, the two contributions can be separated and the performance is thereby not significantly affected.

the worst 50% of the runs are even more affected. Still, the performance compared to the dead reckoning is impressive and it is believed that by increasing the number of particles some performance can be regained.

In Figure 3.3, cluster type two is indicated to be the hardest cluster to track since it introduces the largest amplitude variations. Figure 6.10 shows that cluster type one yields the worst mean performance. The reason for this is not clear but it might be due to the large standard deviation of the azimuth spread for cluster type one.

6.3 Summary and Discussion

The positioning performance seen in the simulations is very good compared to the performance of a consumer grade IMU. For the MIMO case, the performance also beats a tactical grade IMU in 80% of the cases. The MIMO case performs approximately three times better than the SISO configura-

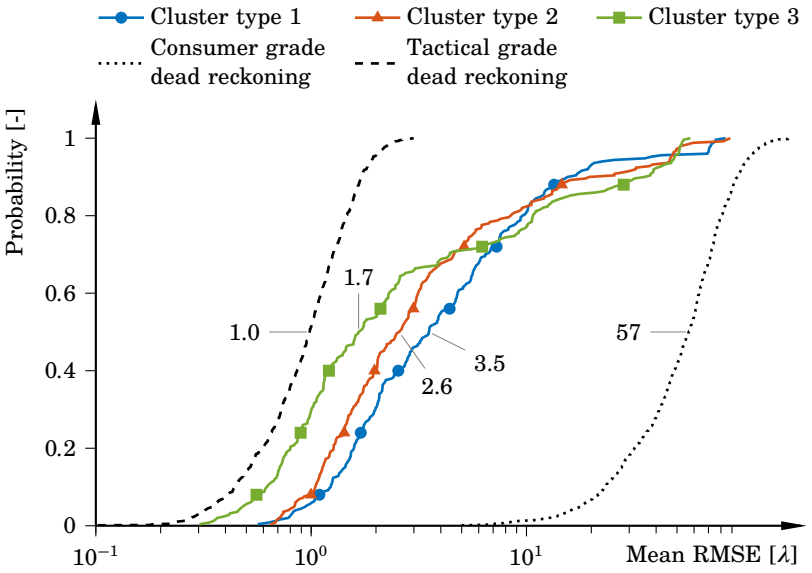

Figure 6.10 The cumulative distributions for mean position RMSE in the MIMO case with one cluster and three specular components with 4000 particles in the filter. The performance is negatively affected by all cluster types. Compared to the scenario with four specular components, the presence of a cluster type 3 yields a median RMSE that is a factor of two worse.

tion. The main reason for the improvement is believed to be the fact that four times the data in terms of channel estimates is supplied to the filter in the MIMO configuration. Another benefit of the MIMO configuration is that the yaw angle, i.e., the rotation around the z-axis, is determined since a rotation will be observed in both the channel estimates and the gyroscope signals. In the simulation the measurement noise on the two receive antennas is assumed to be uncorrelated. If the noise is correlated due to, e.g., coupling between the antenna elements, the MIMO case is believed to degrade in performance and become similar to the SISO configuration. Also, in the MIMO case, the mutual location of the receive antennas is assumed to be known with high precision. By this assumption, the phase difference introduced by differences in travel distance can be accounted for. In a real world MIMO system, the mutual location might be unknown and needs to be estimated using some prior information. This is also believed to degrade the performance in the MIMO case.

We also saw that the number of particles is crucial for the performance of the filtering solution. If the number of particles is too low, the underlying state distributions are not well represented which leads to erroneous state

estimates. The upper performance limit that can be obtained by increasing the number of particles is yet unknown and the CRLBs presented in Figure 6.5 indicate that there is more performance to be gained and more particles might be the answer to how to achieve this. It is also obvious from Figure 6.7 that if the filter is to track a rapidly changing channel when it comes to AoA, more particles are needed. The need for particles has to be balanced with the computational effort of the filter which increases linearly with the number of particles.

When a cluster was included in the environment, a degradation in performance was noticed. This is as expected since the contribution given by the cluster is described in a similar way as a single MPC. In the current implementation, the filter lacks the ability to distinguish between contributions which can be modeled as a single component and contributions from clusters. This ability is a feature that has to be added before the filter can be used in rich multipath environments. Still, the cluster simulations reveal that the filtering solution is able to track the components originating from point sources.

In the investigations we have reused the same movement trajectory that spans approximately 8 m in both x and y directions. From the performance bound investigation presented in Chapter 5, it is known that the movement trajectory influences the estimation performance. For instance, a straight line movement yields bad estimation performance in the movement direction. Consequently, moving towards an impinging MPC for a longer period of time could worsen the performance but in a real world multipath environment, this kind of movement would be a rare occasion. Still, other trajectories can improve or worsen the performance and the full potential of the estimator is yet unknown.

Another topic not discussed here is tuning of the filter. The variances of the state noise processes are assumed to be known in the simulations and tuned accordingly. In a real world scenario, the noise parameters of the accelerometer and the gyroscope as well as frequency error can be obtained. To obtain change rates for AoA and amplitude is more challenging. There exist extensions to the particle filter like particle smoothing with expectation maximization (PSEM) [Olsson et al., 2008] where the variance level, seen as a parameter, can be estimated. This challenge is left for future research.

7

Positioning Experiments

7.1 Hardware

Inertial Measurement Unit

The IMU used in this thesis is delivered by Phidgets [Phidgets, 2016] at a price of $150 and measures 30 × 35 mm, see Figure 7.1. This IMU contains one accelerometer, one gyroscope and one magnetometer along each principal axis and gives in total nine degrees of freedom. The performance of the device is comparable to what is available in cellular phones today where the same performance costs a fraction of the Phidgets device. The magnetometers have not been used in this thesis. The software for communication with the device is implemented in LabVIEW.

Characterization and Calibration The Allan deviation technique described in Section 3.1 is used for characterization of the noise sources in the IMU. The IMU is placed on a table and data is gathered for 30 minutes

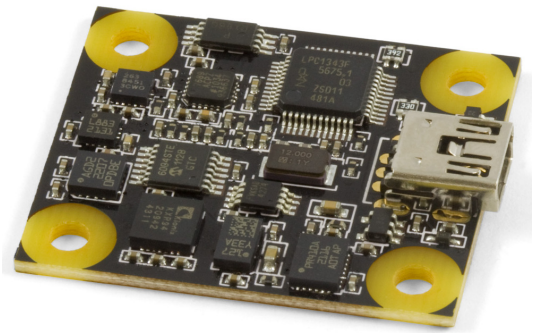

Figure 7.1 IMU 1044 from Phidgets used for the experiments. The circuit board measures 30 × 35 mm and is connected to a computer via USB.

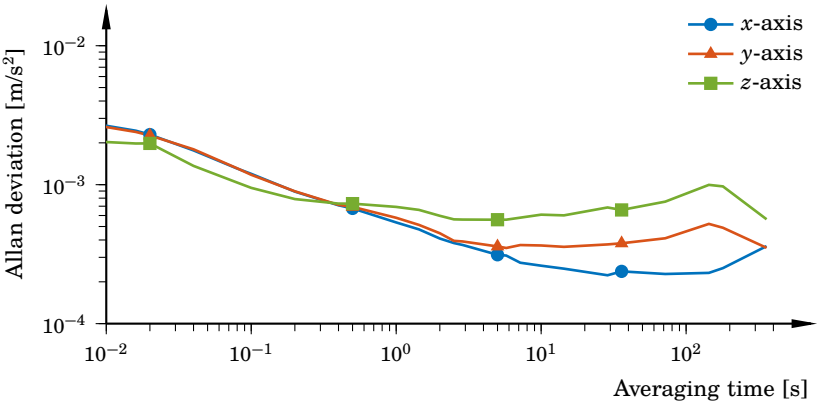

Figure 7.2 Allan deviation for the three accelerometers. In the x- and y-axis, the noise performance is similar while the z-axis has more noise for longer averaging times.

Table 7.1 Accelerometer noise parameters estimated from measurements presented in Figure 7.2.

	***x*-axis**	***y*-axis**	***z*-axis**
Bias instability [m/s/h]	0.8	1.3	2.0
Bias instability time [s]	29	5.7	5.0
Velocity random walk [m/s/$\sqrt{\text{h}}$]	0.032	0.035	0.042

at a data rate of 250 Hz. The Allan deviation results for the accelerometers and for the gyroscopes are presented in figures 7.2 and 7.3 respectively.

The performance of the x- and y-axis accelerometers is comparable while the z-axis accelerometer has a larger noise level and also exhibits a higher bias instability level. The reason for the uneven performance of the three accelerometers is unknown. The IMU is among the inexpensive ones and this is reflected in the performance of the unit. The gyroscopes show an even performance for all units.

Before the IMU is used for measurements, its accelerometers are calibrated with respect to alignment, constant bias, and orthogonality. The calibration scheme used is presented in [Skog and Händel, 2006]. The rea-

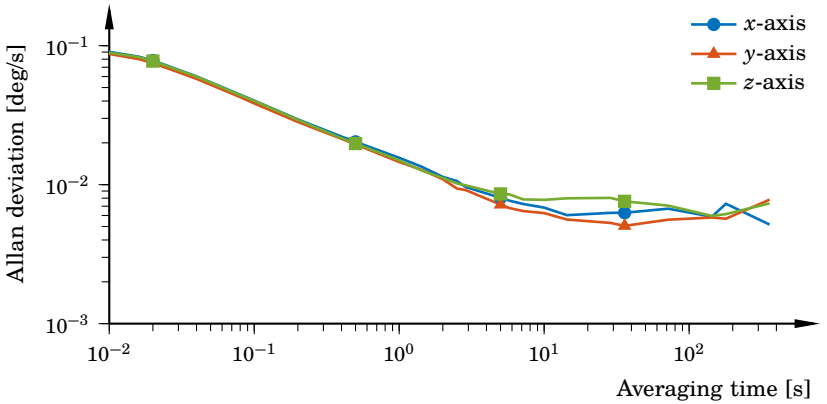

Figure 7.3 Allan deviation for the three gyroscopes. The performance resembles the ideal response in Figure 3.2.

Table 7.2 Gyroscope noise parameters estimated from measurements presented in Figure 7.3.

	***x*-axis**	***y*-axis**	***z*-axis**
Bias instability [deg/h]	19	18	21
Bias instability time [s]	359	36	144
Angle random walk [deg/$\sqrt{\text{h}}$]	0.9	0.9	0.9

son for not calibrating the gyroscopes is lack of equipment since the device has to be rotated at a known angular velocity.

Radio Equipment

To be able to have a controlled radio environment for the experiments, a complete transmitter-receiver chain has been configured. For this purpose a channel sounder known as RUSK LUND [MEDAV, 2016] is used, see Figure 7.5. The equipment consists of one transmitter and one receiver unit and has the capability of measuring the radio channel impulse response from one transmit antenna to many receive antennas for radio channel characterization and analysis.

Since the radio channel is reciprocal, i.e., the channel transfer function

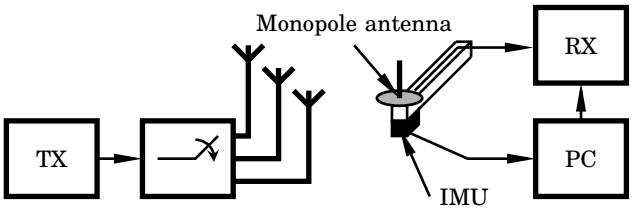

Figure 7.4 Block diagram of the equipment used for experiments. The RUSK TX is connected to a high-speed multiplexer feeding the three patch antennas. The IMU and a monopole antenna with a ground plane are fixed to a wooden stick and the measurement signals are fed to a PC and the receiver respectively. Note that RUSK has several receivers and one transmitter but due to the reciprocal property of the channel, it can be considered to have several transmitters and one receiver. When the experiment starts, the PC triggers the receiver to initiate data recording.

from the transmitter to the receiver is the same as it is for the channel in the other direction, it does not matter which one of the receiver and the transmitter that is moving. Hence, the description of the channel sounder from here on is written as if it were to have one receiver and many transmitters where the transmitters act as controlled scattering objects generating one MPC each. By switching transmission frequency and transmit antenna at a high speed, the individual channel impulse responses at different frequencies are obtained. One benefit with this configuration is the possibility to evaluate the radio channel's individual impulse responses from each transmit antenna to each receive antenna. The transmitter and receiver are synchronized to minimize uncontrolled frequency error in the experiments. A semi-schematic illustration of the equipment configuration is presented in Figure 7.4.

The transmitter antennas are patch antennas, suitable for the frequency band of 2.4 GHz. The antennas are assumed to have high directivity and are carefully placed so that the receive antenna is within the main lobe of these antennas. The receive antenna is a monopole antenna for the same frequency band with a ground plane to eliminate unwanted reflections. The monopole can be considered to be isotropic in the plane aligned with the ground plane.

7.2 Data Gathering

The IMU data recording is synchronized with the recording of the radio signal. The IMU sensors are recorded at 250 Hz but later down sampled to 50 Hz by averaging over five samples. This gives sufficiently many samples

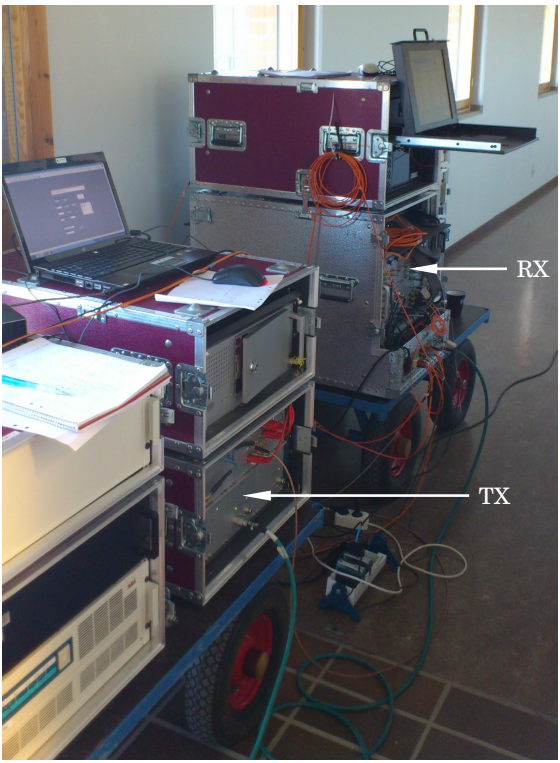

Figure 7.5 The channel sounder RUSK with transmitter unit closest to the viewer and receiver unit behind it.

per revolution of the measurement signal in the complex plane for velocities up to 10 λ/s. The IMU is mounted together with the monopole antenna on a wooden stick, see Figure 7.6, making it easy to move them by hand without interfering with the receive antenna. The experiments are carried out outdoors on a rooftop with clear line of sight between the transmitter antennas and the receiver on the stick. A total number of 129 frequency points between 2.40 GHz and 2.48 GHz are recorded but only the one on 2.40 GHz is used for the evaluation in this work. The wavelength λ is 12.5 cm for this choice of frequency. The noise level in the measurement scenario is approximately 15 dB.

The three transmitter antennas are placed as shown in Figure 7.7 with a table holding the stick to give stationary measurements during a short startup sequence. A photo of the test area is shown in Figure 7.8 where the transmitter antennas are marked. Also, the start and stop positions

Table 7.3 The initial distributions of the states where $\phi^\star$ denotes the true AoA. When initializing the filter, an initial estimate of the AoA is assumed to be obtained by the sparse Bayesian learning algorithm presented in Section 4.2.

State		**Distribution**
Angle of arrival [deg]	ϕ	$\phi^\star + \mathcal{U}(-20, 20)$
Amplitude [-]	α	$\mathcal{N}(1, 0.3)$
Phase [rad]	β	$\mathcal{U}(-\pi, \pi)$
Frequency error [Hz]	δ_f	$\mathcal{N}(0, 7 \cdot 10^{-2})$

are carefully tracked; the interim trajectory is however not tracked due to lack of equipment. No exact ground truth is therefore available. In the evaluation of the filtering results, the dead reckoned positions are adjusted with a polynomial to fit the end point of the movement to the starting point but it can not be considered to be the exact movement. The distances to the transmitters are measured using a laser distance measuring unit and the expected AoA is calculated. Therefore, AoA denoted as "known" might be a few degrees off compared to the true values. For the complex MPC amplitude and frequency error, nothing is known about the true values of these states.

Two different sets of measurements are performed. In the first set the stick is kept on the table while moving it in a circle at a maximum speed of approximately 1 m/s. By holding the stick on the table, the influence of phase shifts due to elevation changes is reduced. For the second measurement, the stick is initialized on the table but then lifted a few wavelengths from it and an eight-shaped movement is performed in free air. Therefore, this dataset is considered to be more difficult compared to the first one since a small error in the orientation will quickly deteriorate the position estimates. After the movement is completed, the stick is placed on the table. In both measurements the start and stop positions on the table are within centimeters from each other.

The same implementation of the marginalized particle filter for SISO systems as used in Chapter 6 is reused here. The state initialization is according to Table 7.3. Since the transmitter and the receiver are synchronized, the frequency error becomes negligible. Thus, the white noise process on the state modeling the frequency error is set to track slow changes.

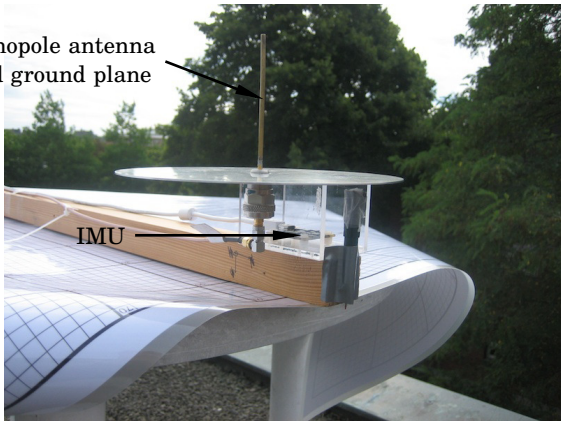

Figure 7.6 IMU and monopole antenna with ground plane mounted on the wooden stick.

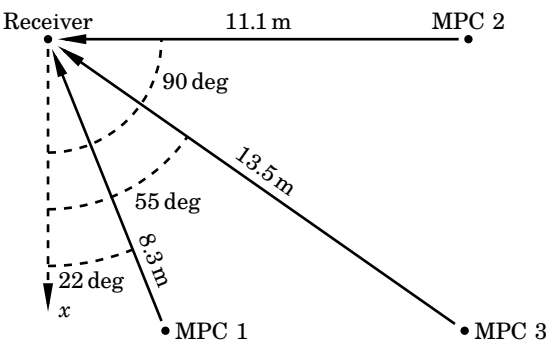

Figure 7.7 Layout of the test area with the three transmitters and the IMU-equipped receive antenna in the upper left corner. Note that the x-axis is defined as pointing downwards in the figure. The y-axis points from the receiver towards MPC 2.

Figure 7.8 The test area with the table holding the IMU and receive antenna closest to the viewer. The three transmitter antennas acting as scattering objects are marked in white.

7.3 Experiment Results and Analysis

The result of the first experiment is presented in Figure 7.9. Since the true movement trajectory is not known, the adjusted dead reckoned result is presented as ground truth. The number of particles is set to 4000 and the result for estimated position is clearly following the circular movement. The filter settles to zero velocity after the movement has stopped at 16 seconds. The AoA is also tracked well with some offset to the true values. The error at the end position is negligible and the maximum position RMSE is 2.7 λ or 34 cm with the current wavelength. The average position RMSE for the whole trajectory is approximately 0.75 λ or 9.4 cm. The same value with dead reckoning is 47 λ or 5.9 m. The peculiar behavior of α for MPC 2 in the beginning indicates that the filter has resampled and prefers low amplitude on that specific MPC. When the movement begins, the filter increases the amplitude quickly in order to explain the measurements.

To investigate how the number of particles influence the result, 200 Monte Carlo simulations with different numbers of particles are executed. The result is presented as a cumulative distribution over the mean position RMSE for the whole trajectory in Figure 7.10. As expected, increasing the number of particles yields a better estimate while increasing it beyond 2000 does not significantly improve the median position RMSE but rather reduces the number of simulations with large errors, i.e., the simulation is more likely to converge if the number of particles is increased.

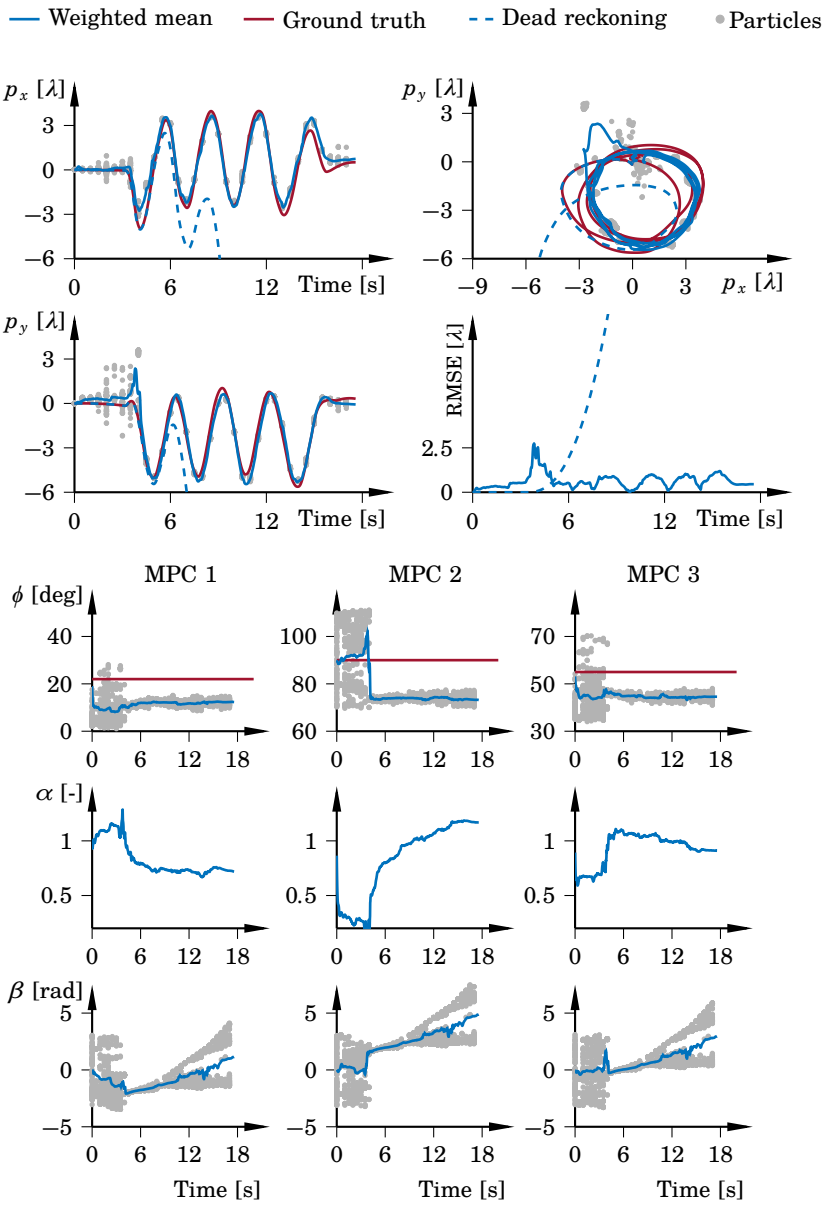

Figure 7.9 The upper panel shows the result for the position states, compared to the dead reckoned result and the ground truth trajectory. The lower panel shows the estimate of AoA and complex MPC amplitude with the same color coding as above. Note how the filter keeps multiple hypotheses of all states until the movement begins at approximately 4 seconds.

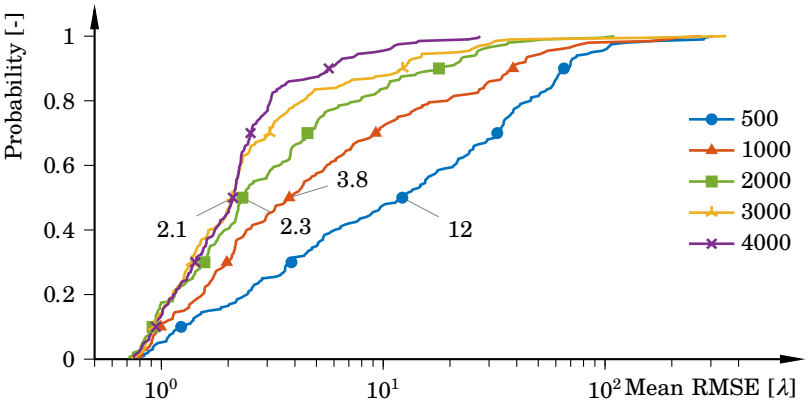

Figure 7.10 The cumulative distributions for the mean position RMSE for the dataset shown in Figure 7.9. It is evaluated for 200 Monte Carlo runs for five different levels of number of particles. The cases with 3000 and 4000 has similar performance for 70% of the runs while the 4000 particle filter has better performance on the last 30%. The median value for each case is marked in the figure.

The second experiment is presented in Figure 7.11. As before, the number of particles is 4000 and the positioning result follows the adjusted dead reckoned ground truth very well. The filter also settles to zero velocity after the movement has stopped and the stick is placed on the table again. The error at the end position is negligible and the maximum position RMSE is around 2.7 λ or 34 cm with the current wavelength. The average position RMSE for the whole trajectory is 1.2 λ or 15 cm. The same result for the dead reckoning is 25 λ or 3.2 m so the improvement in positioning is remarkable. As with the previous dataset, the number of particles is varied and the mean position RMSE is presented as a cumulative distribution over 200 Monte Carlo simulations in Figure 7.12. The shapes of the curves resembles what is seen in Figure 7.10 but with a slightly higher median RMSE.

7.4 Discussion

The positioning results shown is a clear and remarkable improvement compared to the dead reckoned result. The filter is able to fuse the information from the radio receiver and the IMU and the multiple hypotheses, represented by the particles, evaluated by the filter is believed to be necessary for convergence. The choice of movement will of course influence the performance. From previous chapters, we know that the estimation performance is related to the components of the moment of inertia tensor of the virtual

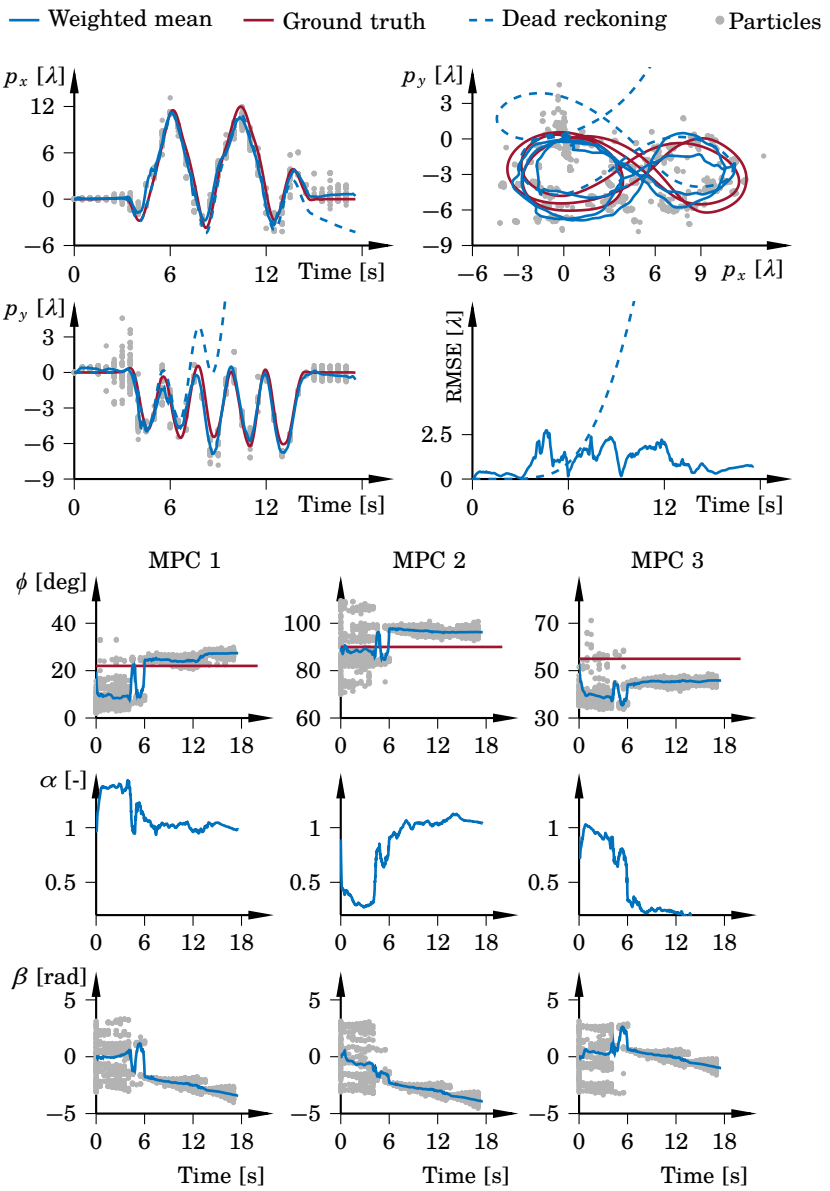

Figure 7.11 Same as Figure 7.9 but for another dataset. The results are comparable in performance. Here there are multiple hypotheses for the position in x but as soon as more data is gathered, they can be discarded. Note that the dead reckoning in x is very good until 15 seconds while in y it fails after 7 seconds.

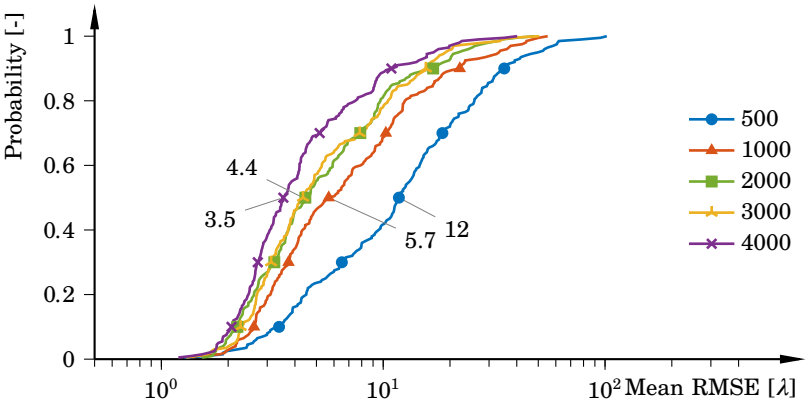

Figure 7.12 The cumulative distributions for the mean position RMSE for the dataset shown in Figure 7.11. It is evaluated for 200 Monte Carlo runs for five different levels of number of particles. The curves resembles the result from Figure 7.10 with a slightly higher median value which is marked for each curve in the figure.

array and the circle was found to be superior which justifies the circular movements used here.

Even though the measurement scenario is carefully arranged with respect to antenna placement and measurement of start and stop position, there are error sources that are hard to eliminate. The derivation of (2.24) in Section 2.2 assumes that the receiver and transmitters are in the same plane. If not, the elevation angle will influence the argument of the received signal. Since it is hard to keep a free-hand movement in a plane, this effect will be present and will be altering the phase of the received signal. This might be an explanation for the worse performance seen in the second dataset, shown in Figure 7.11, where the stick is lifted from the table in the beginning of the experiment. Another source of errors is unaccounted multipath wave propagation. Since the filter can not detect the number of components to track, it is configured to track the three most dominant components but there might be more multipath components. One way to investigate this is to use a receive antenna with several elements and perform a high resolution AoA investigation of the environment.

Even though the experimental situation has been chosen to be application-friendly, compared to what could be expected in worst-case situations, the belief is that the experiments can be taken as proof of concept for the state-space model and the suggested state estimator. The limits of performance and the full potential of the method is however an area for future research.

8

Link Adaptation

In this chapter we will study and investigate link adaptation with the joint position and multipath radio channel model estimated by the particle filter. The material presented in this Chapter is based on [Mannesson et al., 2015a].

8.1 Introduction

The concept of link adaptation is to adjust transmission parameters to suit the radio channel conditions that exist when the data is sent [Cavers, 1972]. The transmission parameters can be coding, power level, and modulation scheme [Goldsmith and Chua, 1997; Chung and Goldsmith, 2001; Zhou et al., 2005]. By link adaptation, the average spectral efficiency of the fading radio channel can be increased without deteriorating the bit error rate (BER) for other users in the network. For this reason, link adaptation is used in many commercially available wireless communication system, e.g., UMTS/HSPA [3GPP, 2016b], LTE [3GPP, 2016a], and WiFi [IEEE S.A., 2016].

Link adaptation relies on channel estimation and a feedback link between the receiver and the transmitter. In the feedback link, the channel conditions as seen by the receiver are shared with the transmitter. As we know from Section 1.1, the channel response is constantly being estimated using pilot symbols for high performance networks. However, for any pilot based system there is an inevitable delay between the time instant when the channel is estimated and when the symbol is transmitted. An exception is if time division duplex is used and channel reciprocity holds. Since there is no guarantee that the channel transfer function remains unchanged during the time period between the channel estimation and the next transmission, the transmission parameters used might be unsuitable for the channel conditions that reside at the transmission instant. Hence, it would be beneficial

if the channel could be predicted so that the transmitter can adjust the coding in advance.

With the MPC-based tracking model we have derived previously, the channel fluctuations caused by small scale fading can now be predicted to a large extent and used for link adaptation. To investigate the benefit for the end user, we apply our proposed channel predictor and link adaptation technique to the LTE system [3GPP, 2016a], [Ghosh et al., 2011] with the limitation of bit rate and modulation scheme adaptation.

Previous Work

A common radio channel model is the *tapped delay line model* [Molisch, 2005]; its coefficients can be estimated using the pilot symbol sequence. An early work using this approach is [Duel-Hallen et al., 2000] where the authors investigate the performance of long range channel prediction using autocorrelation of the pilot data. Their conclusion was that the approach allowed for prediction ranges of approximately $0.5\,\lambda$ in most scenarios. This work was followed by [Ekman, 2002] where filtered regressors are used for prediction. The filtering makes the prediction less sensitive to estimation errors of the individual coefficients of the taps in the tapped delay line model. The results are similar to what is presented in [Duel-Hallen et al., 2000].

Another approach is to use sinusoidal modeling of the channel impulse response, which can be found in [Hwang and Winters, 1998] and [Andersen et al., 1999]. Here the channel is modeled as superimposed sinusoids with a fixed phase shift and Doppler shift for each sinusoid. This technique is extended in [Chen and Viberg, 2009] into non-stationary sinusoidal parametric modeling where the Doppler shifts are modeled as a polynomial function instead. The results show that a predictor with a state-space model for this extended sinusoidal model can improve the channel prediction compared to a linear channel predictor.

8.2 System Overview

LTE System Overview

The wireless system considered for our work is the eighth release of the LTE system [3GPP, 2016a]. LTE uses both MIMO and OFDM and the system bandwidth is at maximum 20 MHz divided into subchannels of 15 kHz [Ghosh et al., 2011], compare Figure 1.4. These subchannels are considered to be frequency flat, i.e., the narrowband assumption holds for each subchannel. The temporal spacing of 1 ms is called a subframe and twelve subchannels and seven temporal samples constitute a resource block if normal cyclic prefix is used. [Ghosh et al., 2011].

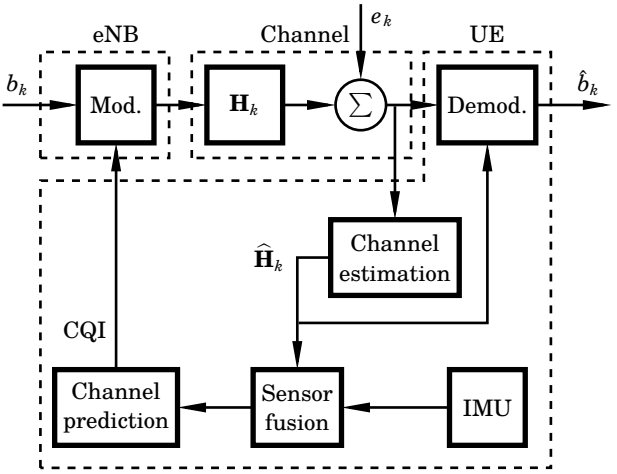

Figure 8.1 The extended downlink chain for a single subchannel with the sensor fusion-based radio channel model. The subchannel is considered to be frequency flat and k denotes sample index. The modulator is similar to what is found in the LTE system. It includes amongst other modulation, turbo coder, and rate adjuster.

In the LTE specification, the user equipment (UE) should report a channel quality indicator (CQI) value to the base station (eNB) [Ghosh et al., 2011]. This value can be reported for every resource block or for the full system bandwidth depending on the mode of operation. The CQI value reported by the UE is a 4-bit value that suggests a predefined modulation and coding rate in order to meet a certain threshold of the block error rate (BLER) of the demodulated blocks at the UE. Due to the coding of the blocks, modulation and bit rate are closely related to the data throughput to the UE and it is therefore important to choose the most suitable CQI-value in order to maximize throughput.

Downlink With Sensor Fusion-Based CQI Feedback

An overview of the downlink chain, i.e., the link from the eNB to the user equipment, for our system is shown in Figure 8.1. The chain includes the sensor fusion block that estimates the MPC-based state-space model using information from the IMU and the channel estimates. The estimates are fed to the channel predictor.

The modulator block is similar to what is found in the LTE standard. The bits b_k enter the modulator where several steps of signal processing is done, among them are outer channel coding and modulation mapping. The basic channel coding in LTE is a rate 1/3 turbo coder with a subse-

Table 8.1 Modulation and code bit rates for LTE CQI values.

Modulation	Rate [x/1024]	CQI
4-QAM	{78, 120, 193, 308, 449, 602}	$\{1, \ldots, 6\}$
16-QAM	{378, 490, 616}	$\{7, \ldots, 9\}$
64-QAM	{446, 567, 666, 772, 873, 938}	$\{10, \ldots, 15\}$

quent rate matcher to adjust the bit rate of the code [Ghosh et al., 2011]. Furthermore, LTE uses quadrature amplitude modulation (QAM) and the available schemes are 4/16/64-QAM, which equals two, four, and six bits per transmitted symbol respectively [Ghosh et al., 2011]. The output of the modulator is the symbols transmitted over the frequency flat subchannel with transfer function $\mathbf{H}_k$. For a MIMO system with M_R receiver antennas and M_T transmitter antennas, $\mathbf{H}_k \in \mathbb{C}^{M_R \times M_T}$. The received symbols are subject to zero mean circular symmetric complex Gaussian noise, denoted $\boldsymbol{e}_k \in \mathbb{C}^{M_R}$, before the demodulator can reverse the operations of the modulator to obtain the most likely transmitted bits $\hat{b}_k$. In order for the demodulator to compensate for the influence of the channel, it needs an estimate of $\mathbf{H}_k$ and this is supplied by the channel estimator algorithm using the pilot sequences. The channel estimates are also used for channel prediction and CQI feedback discussed in the previous section. The implementation of the channel prediction is not specified in the system standard and its design is decided by the implementer.

8.3 Particle CQI Prediction

LTE Downlink Throughput

The channel coder for the LTE system that we are considering is an adjustable rate turbo code [Ghosh et al., 2011; Berrou et al., 1993]. With the three different levels of QAM symbol coding, 15 different combinations of modulation orders and code rates are specified in the LTE standard (Table 7.2.3-1 [3GPP, 2009]) and summarized in Table 8.1.

A higher modulation order and rate yields higher throughput since more bits are packed into every transmitted symbol but it also requires a higher SINR level for successful decoding. The iterative scheme used by the turbo coder yields a very sharp block error rate (BLER) curve with respect to SINR. When the SINR exceeds the threshold, which is dependent on the rate and modulation type, in practice all symbols of the block are successfully decoded. To calculate the throughput for each level of CQI at

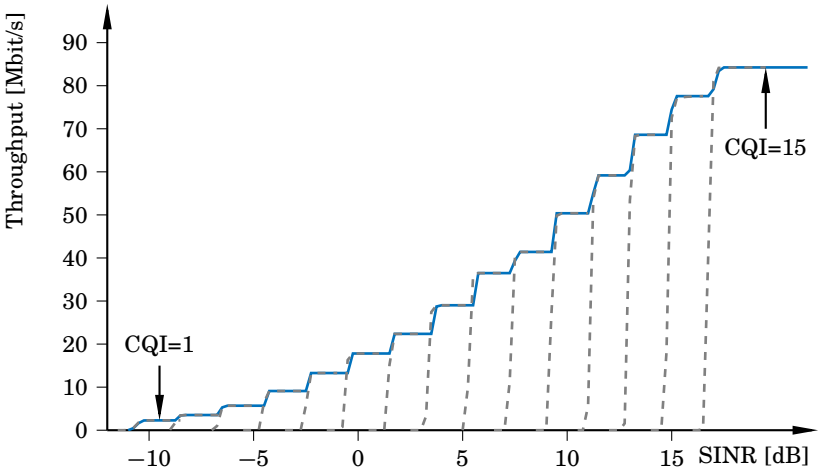

Figure 8.2 Physical layer throughput in Mbit/s for one stream as a function of SINR for a system utilizing 20 MHz bandwidth under an AWGN channel and no H-ARQ. The dashed curves indicate the throughput associated with each CQI value. The maximum throughput is approximately 84 Mbit/s for SINR over 18 dB. The simulated throughput is approximately 16% lower than the theoretical limit which does not include any channel overhead data.

a given SINR level, the LTE downlink simulator by [Schwarz et al., 2013] is used. The setup is an additive white Gaussian noise (AWGN) channel and a 2×2 MIMO system utilizing 20 MHz system bandwidth, equivalent to 100 resource blocks. The throughput as a function of SINR is presented in Figure 8.2. Note that retransmissions with a hybrid automatic repeat request (H-ARQ) protocol are for simplicity not considered in the simulation. Furthermore, a normal cyclic prefix is used.

There are several suggestions in the literature on how to average the estimated SINR over time and space, see, e.g., [Ghosh et al., 2011]. In our work, no averaging is considered at all. Instead Figure 8.2 is used as a look-up table (LUT) for translating an estimated SINR via a CQI value to a throughput. This LUT is applied independently to all subchannels of the MIMO system. The flat fading assumption is mainly for simplicity to reduce simulation time. For frequency-selective channels with large delay spread, a more involved filter, performing filtering in the frequency domain, is needed.

Particle Channel Predictor

The state-space model introduced in Section 3.3 with the state vector given in (3.17) will be the basis of our channel predictor. The goal of the channel

predictor is to obtain an estimate of the SINR for future transmissions and thereby enabling requesting a suitable coding rate according to Table 8.1. Our channel predictor will be based on the particle method used for the state estimation.

To obtain a predicted SINR, the first step is to predict the state vector (3.17) given the information of the states at the current time instant. Since the channel prediction is intended to be used for prediction horizons ranging up to half a second, a reduced state vector is predicted instead of the full one from (3.17). Firstly, the phase offset β is assumed to be constant in the model and can therefore be omitted. The same holds for the bias states since they do not affect the predicted positions for short time periods. If the position is predicted with an uncertainty, the quaternion representing the orientation does not have to be predicted either. Finally, since the measurements in (3.18) do not depend on the position along the z-axis this state is also omitted. Hence, the state vector that is to be predicted becomes

$$\boldsymbol{x} = \begin{bmatrix} p_x & p_y & v_x & v_y & \boldsymbol{\phi}^T & \boldsymbol{\alpha}^T & \delta_f \end{bmatrix}^T \in \mathbb{R}^{5+2N_R}. \tag{8.1}$$

Given the state posterior distributions delivered by the state estimator, the particle predictor draws L_p particles out of these distributions and uses (3.13) and (3.16) to propagate the particles forward in time with the noise levels used by the state estimator. Each predicted particle is also a representation of a channel transfer matrix $\mathbf{H}_{k+p|k}$, where k is the current sample index and p is the number of prediction steps. This matrix is obtained by the observation model in (3.18). Each predicted channel transfer matrix is transformed into an SINR value assuming an MMSE receiver. For a predicted channel matrix $\mathbf{H}_{k+p}$, the SINR at time $k+p$ of the mth subchannel is given by [Paulraj et al., 2003]

$$\begin{aligned} \mathrm{SINR}_{m,k+p} &= \frac{\gamma}{M_T} \boldsymbol{h}_m^* \boldsymbol{\Omega}_m^{-1} \boldsymbol{h}_m \\ \boldsymbol{\Omega}_m &= \mathbf{I}_{M_R} + \frac{\gamma}{M_T} \sum_{\substack{j=1 \\ j \neq m}}^{M_T} \boldsymbol{h}_j \boldsymbol{h}_j^*, \end{aligned} \tag{8.2}$$

where $\gamma = E_s/N_0$, E_s is the average energy for an OFDM symbol, and N_0 is the intensity of the additive zero mean circular symmetric complex Gaussian noise of the received signal including interference and receiver imperfections. Furthermore, $\boldsymbol{h}_m$ is the mth column of $\mathbf{H}_{k+p}$, i.e., the response of the mth transmitted stream on all RX antennas. The variance of the noise N_0 is assumed to be estimated by the UE and varies on a longer time scale compared to the prediction horizon. Since the influence of the precoder is not a part of the study, it is set to the identity matrix.

The final step of the predictor is to choose the CQI value that will maximize the throughput using the LUT from Figure 8.2. For each subchannel m, the requested CQI value is given by

$$\begin{aligned} \mathrm{CQI}_{\mathrm{req}}^{m} &= \arg\max_{x} \sum_{l=1}^{L_p} \mathcal{I}(x, \mathrm{CQI}_{l}^{m}) \\ \mathcal{I}(x, \mathrm{CQI}_{l}^{m}) &= \begin{cases} T(x) & \text{if } \mathrm{CQI}_{l}^{m} \geq x \\ 0 & \text{if } \mathrm{CQI}_{l}^{m} < x \end{cases} \end{aligned} \tag{8.3}$$

where CQI_{l}^{m} is the CQI value of particle l for subchannel m, and $T(\cdot)$ is the LUT function from Figure 8.2. This is a good approximation of the average throughput of the turbo decoder. The channel predictor described above is summarized in Algorithm 8.1.

Algorithm 8.1—The particle channel predictor

Input: Prediction horizon: P
Initial distribution: $p(\boldsymbol{x}_0)$
Number of particles: L_p

1: Draw L_p particles from initial distribution $p(\boldsymbol{x}_0)$
2: **for** $p = 1$ **to** P **do**
3: **for** $l = 1$ **to** L_p **do**
4: Propagate state vector (8.1) using (3.13) and (3.16).
5: Calculate predicted channel matrix $\mathbf{H}_{k+p}$ using (3.18).
6: Calculate SINR_m for each subchannel m, (8.2).
7: Request $\mathrm{CQI}_{\mathrm{req}}^{m}$ for each subchannel m, (8.3).
8: **end for**
9: **end for**

Output: Requested $\mathrm{CQI}_{\mathrm{req}}^{m}$ for subchannel m ■

The operations of the particle predictor is illustrated in Figure 8.3. The distribution of the particles are shown as circles where most particles suggest CQI 10 to be requested. However, the expected throughput is slightly higher at a requested CQI of 9.

SINR Prediction Illustrated

Before investigating the throughput the particle based predictor can yield, we return to a simulated MIMO case from last chapter. In Figure 8.4, the prediction of SINR is investigated at two different points in time. At the prediction instant, the reduced state vector of (8.1) is predicted using the same noise intensities that is used by the particle filter solution. The SINR is calculated using (8.2) for the predicted channel matrices and weighted mean is presented in the lower panel of Figure 8.4. The weighted mean

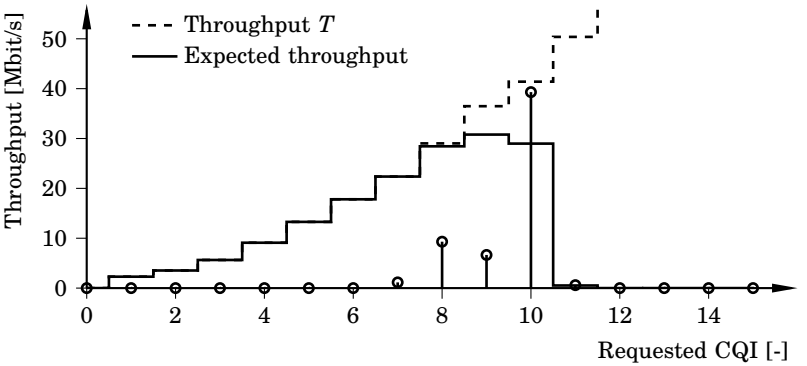

Figure 8.3 The throughput T from Figure 8.2 and expected throughput as a function of requested CQI. The circles mark the particle likelihood distribution. CQI value 9 yields the highest expected throughput.

SINR follows the true SINR well for about 100 ms and the true SINR is within one standard deviation up until 200 ms. The weighted mean value of the prediction is thereby well tracked for approximately $0.5\,\lambda$.

8.4 Simulations

Simulation Setup

To investigate the performance of the proposed predictor, Monte Carlo simulations are used. To decrease the simulation time needed and also to explicitly study the performance of the predictor without influence from the estimation performance of the particle filter, the predictor and the particle filter are not co-simulated. Instead, it is assumed that the state estimates have reached a posterior distribution that can be described as $\mathcal{N}(\boldsymbol{x}_0, \mathbf{P}_0)$ in the simulations shown in Chapter 6. An example of SINR prediction using the particle filter is shown in Figure 8.4. The initial variances for the different states are given in Table 8.3 and they are obtained from realistic particle filter simulations presented in previous chapters. To mimic a CQI reporting period of 2 ms, which is the preferred setting according to the LTE specification [Ghosh et al., 2011], the sample frequency of the simulations below is set to 500 Hz. Both data and the channel estimates have an average SNR of 20 dB and the carrier frequency is set to 1.8 GHz which yields a wavelength of 16.7 cm. The simulation parameters are summarized in Table 8.2.

For each Monte Carlo run, a set of reference channel matrices $\mathbf{H}_{k+p|k},\ p = 1, \ldots, P$ is generated using four multipath components. The

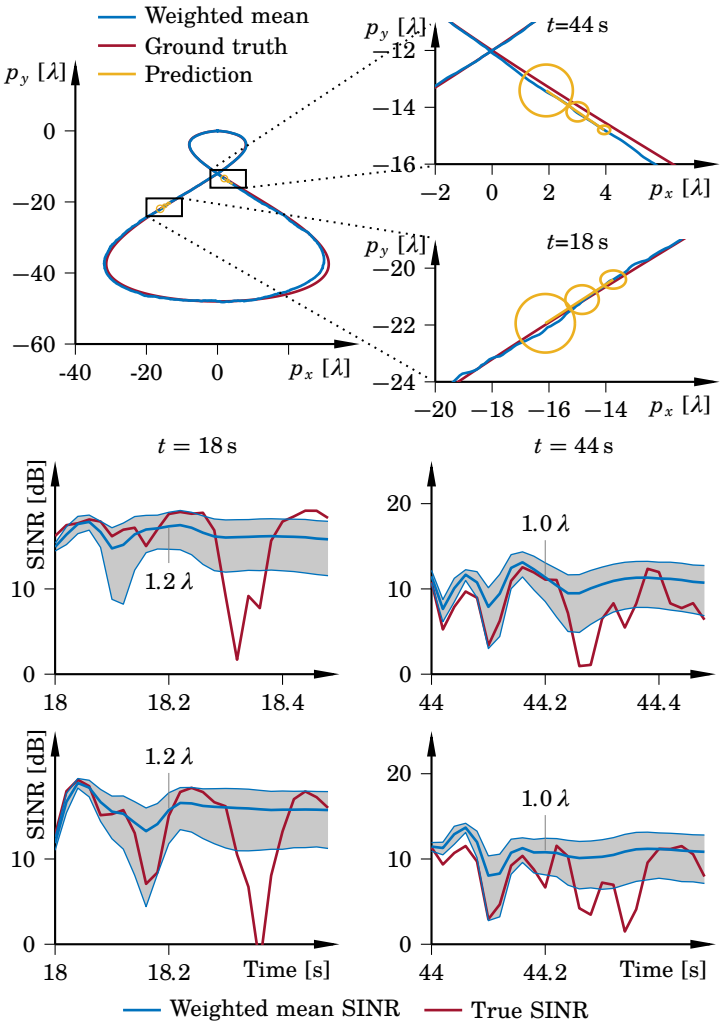

Figure 8.4 SINR prediction for two time instances using the same dataset shown in Figure 6.4. The locations and corresponding time when predictions are performed is shown in the upper panel where the circles mark the 95% confidence interval for position of the predicted particles. The standard deviation in x and y is approximately 0.35 λ. In the lower panel, the SINR predictions for the two parallel MIMO streams are shown together with one standard deviation of the predicted SINR as the shaded area. In the figures, the physical distance predicted is also indicated. The predictor is close to the true SINR for approximately 100 ms. The true SINR lies within one standard deviation of the predicted mean for 200 ms.

Table 8.2 Simulation parameters used for the channel predictor.

	Value
Sample rate [Hz]	500
Average SNR [dB]	20
Carrier frequency [GHz]	1.8
Wavelength [cm]	16.7
Number of MPCs [-]	4
Channel realizations [-]	20000

AoA ϕ for each component is drawn from the uniform distribution $\mathcal{U}(-\pi, \pi)$, with a complex amplitude α initialized to 1 while the argument β is randomly drawn from $\mathcal{U}(-\pi, \pi)$. Finally, the frequency error is initialized to 0 Hz without loss of generality. The UE is assumed to move in a straight line, i.e., there is no acceleration acting on the device during the time of the prediction but this is unknown to the estimator which instead assumes the unconstrained motion model described in Section 3.2. The obtained set of reference matrices is normalized according to

$$\begin{aligned} \overline{\mathbf{H}}^{\star}_{k+p} &= c\mathbf{H}^{\star}_{k+p}, \quad p = 1, \cdots, P \\ c &= \sqrt{\frac{PM_RM_T}{\sum_{p=1}^{P} \|\mathbf{H}^{\star}_{k+p}\|_F^2}}, \end{aligned} \tag{8.4}$$

where P is the prediction horizon, and $\|\cdot\|_F$ denotes Frobenius norm. Thus, the normalization yields a channel matrix with $\mathbb{E}\{\|\overline{\mathbf{H}}^{\star}\|_F^2\} = M_RM_T$.

A second set of channel matrices is constructed, configured as above but with an initial variance $\mathbf{P}_0$ added to the amplitude, AoA, velocity, and frequency error states, given in Table 8.3. The channel predictor in Algorithm 8.1 supplies the optimal requested CQI value for these predicted matrices. Finally, the requested CQI value is evaluated against the CQI value associated with $\overline{\mathbf{H}}^{\star}$ in (8.4) for the corresponding subchannel. Using the requested $\mathrm{CQI}^m_{\mathrm{req},p}$ value, the throughput at time $k+p$ for subchannel m is denoted $t_{m,p}$ and given by

$$t_{m,p} = \begin{cases} T(\mathrm{CQI}^m_{\mathrm{req},p}) & \text{if } \mathrm{CQI}^m_{\mathrm{req},p} \leq \mathrm{CQI}^m_p \\ 0 & \text{if } \mathrm{CQI}^m_{\mathrm{req},p} > \mathrm{CQI}^m_p, \end{cases} \tag{8.5}$$

Table 8.3 Nominal initial variance $\mathbf{P}_0$ and noise process intensity σ for the different states. Note that all MPCs use the same initial variance and process intensity for amplitude and AoA.

Inital variance		**Value**
Amplitude [-]	$\mathbf{P}_{0,\alpha}$	10^{-3}
Angle of arrival [deg^2]	$\mathbf{P}_{0,\phi}$	10^{-1}
Velocity [m^2/s^2]	$\mathbf{P}_{0,v}$	10^{-3}
Frequency error [Hz^2]	$\mathbf{P}_{0,\delta}$	10^{-4}
Change rate		**Value**
Amplitude [1/s]	σ_α^2	$1.0 \cdot 10^{-2}$
Angle of arrival [deg^2/s]	σ_ϕ^2	$2.5 \cdot 10^{-1}$
Velocity [m^2/s^3]	σ_v^2	$1.6 \cdot 10^{-1}$
Frequency error [Hz^2/s]	σ_δ^2	$2.0 \cdot 10^{-3}$

where CQI_p^m is the CQI-value that corresponds to the SINR of the mth subchannel at time instant $k+p$ for $\overline{\mathbf{H}}^\star$.

For evaluation of the proposed channel predictor, two additional predictors are implemented. The first one assumes that the latest channel estimate is valid for the entire prediction horizon. This is referred to as the *naive predictor*. The second one is a linear predictor using the two latest channel estimates $\widehat{\mathbf{H}}_{k-1}$ and $\widehat{\mathbf{H}}_k$ for predicting the future channel. This predictor will be referred to as the *first-order predictor*. Finally, an oracle with perfect channel knowledge is included in the simulations as an upper limit. These three predictors use the same LUT as the particle-based predictor to translate the channel matrices to SINR and finally to throughput.

The nominal values of the noise processes for amplitude, AoA, velocity, and frequency error are given in Table 8.3. The process variance σ^2 for amplitude and AoA describes a slowly varying channel. The variance for velocity is chosen to yield an uncertainty in position with a standard deviation of $0.5\,\lambda$ after 0.5 seconds. The presented results are the averages over 20000 channel realizations.

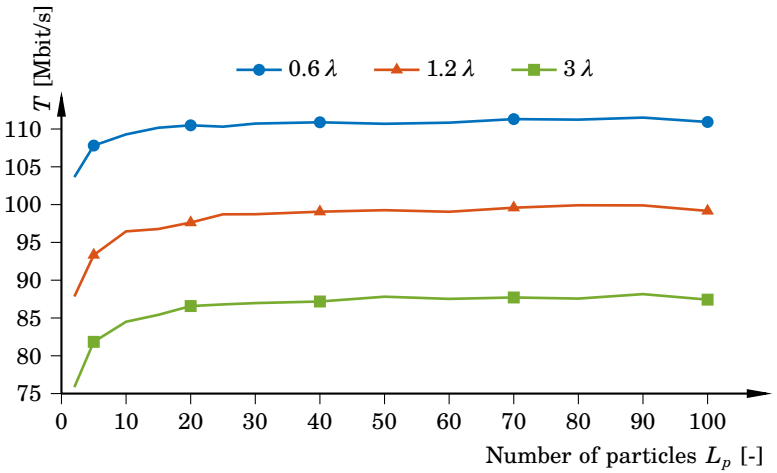

Figure 8.5 Throughput T as a function of the number of particles in the predictor for three different prediction horizons assuming a velocity of 6 λ/s. After 30 particles, the performance is stable.

Simulation Results

The first test is to investigate the predictor performance as a function of the number of particles L_p used in the predictor when using the nominal noise settings $\mathbf{P}_0$ and $\boldsymbol{n}_0$ given in Table 8.3. The simulation result is shown in Figure 8.5. The result indicates that 30 particles are enough for describing the non-Gaussian posterior channel distributions. To test the robustness of the proposed predictor to different channel conditions and erroneous initializations, five different scenarios are defined and simulated below. The first scenario varies the speed of the UE while the remaining four scenarios use the velocity 6 λ/s which corresponds to 1 m/s at a carrier frequency of 1.8 GHz.

Nominal Initialization In the first scenario, three different velocities are investigated, 6 λ/s, 18 λ/s, and 30 λ/s. The lower speed equals walking, while the higher corresponds to running or cycling at the given carrier frequency. The result using the nominal noise levels is presented in Figure 8.6. The result shows a significant performance increase of the particle based channel predictor compared to the naive and first order predictors. At the lower speed, the predictor settles on a 30% increase in throughput compared to the naive predictor. When the speed increases, the prediction horizon corresponds to less time and thereby less uncertainty accumulated in the states and thereby a better channel prediction performance of the particle based channel predictor. However, since a longer distance is pre-

dicted, the likelihood that the radio channel has significantly changed is increased. In such a case, the predictor is believed to perform badly. The naive and linear predictors do not depend on speed at all. Worth noting is that the first-order predictor is better than the naive predictor in the first few samples but falls off rapidly due to extrapolation of the channel impulse response. The ripple seen in the performance of the naive predictor is due to the correlation of the channel over the prediction horizon.

Incorrect Heading Initialization For the next simulation, the speed of the receiver, which has been estimated by the particle filter, is assumed correct but the heading is incorrect. The simulation result is shown in Figure 8.7. At an error of 10 deg the performance of the sensor fusion based predictor is reduced for shorter prediction horizons. It settles around the same level as the correctly initiated particle predictor. When the heading error is 45 deg, the performance for shorter prediction horizons is only slightly better than the naive predictor but the performance increases as the horizon extends. This is due to the accumulation of uncertainty in the position state which the filter accounts for. The heading error leads to a linearly increasing position error while the double integrator of the position state has a standard deviation growth rate of $t^{3/2}$. The nominal noise setting of the velocity corresponds to a standard deviation in the position of $0.5\,\lambda$ at a prediction horizon of $3\,\lambda$. Hence, the particle predictor will underestimate the position error for prediction horizons below $3\,\lambda$ and overestimate the error for larger horizons.

Amplitude Uncertainty Here the robustness of the predictor to uncertainty in the initialization of the MPC amplitudes and the change rate of the amplitudes is investigated. The simulation results are shown in Figure 8.8 and Figure 8.9 respectively. The influence of the two parameters is similar. At short horizons, the performance is degraded if the channel is rapidly changing or the particle filter yields a higher posterior distribution variance for the amplitude. The performance of the predictor at a change rate of $10\,\mathrm{s}^{-1}$ shows a noticeable degradation for all horizons. This change rate is similar to what is seen in the larger clusters, compare Figure 3.3. Hence, the performance of the predictor when clusters are present in the environment needs further studies.

Angle of Arrival Uncertainty In this scenario the robustness of the predictor to uncertainty in AoA estimation and AoA change rate is investigated. The simulation results are presented in Figure 8.10 and Figure 8.11. As seen in the figures, the predictor is not very sensitive to the change rate of the AoA while there is a critical level of the initial standard deviation at approximately 5 deg. If the estimation accuracy given by the particle filter is worse, the performance of the predictor is negatively affected.

Velocity Uncertainty The final scenario which is investigated is the robustness of the predictor to initial uncertainty in velocity and velocity change rate. The simulation results are presented in Figure 8.12 and Figure 8.13. The result is significantly influenced by both parameters. For initial uncertainty, the performance for short horizons is affected while at larger horizons the influence is negligible. The explanation is that the initial variance does not influence the position variance in the long run. In Figure 8.13, it is seen that the prediction performance for larger horizons is limited by the noise variance of the velocity state and that the nominal simulation setup is on the edge of the performance curve at short prediction horizons.

Discussion

The simulation results show great improvement in the throughput to the end user when the predictor is initialized with the nominal values from Table 8.3. The improvement compared to a first-order predictor is almost three times at a prediction horizon of $1\,\lambda$. The robustness to incorrect heading initialization is considerable for a slowly changing channel. As the other simulations show, the critical factor for the performance of the predictor is the accuracy of the predicted position and velocity, see Figure 8.13. Given the simulation results, a reasonable prediction horizon is $0.5\,\lambda$ under the given channel parameters but could be $2\,\lambda$ if a better prediction of the position was available.

Since the prediction model relies on the state estimates given by the particle filter, a case where the filter has not reached the underlying true distribution will heavily degrade the performance of the prediction algorithm. Such cases have not been investigated here. The convergence of the filter is as discussed previously dependent on initialization of the state vector, the number of particles and also the number of MPCs with significant contribution to the channel matrix. The performance of the channel predictor in a dense multipath environment with many minor contributions to the channel matrix is left for future research.

An aspect of the LTE system not considered here is retransmissions using the H-ARQ protocol [Ghosh et al., 2011] briefly mentioned before. Without H-ARQ, a single bit error will trigger a full package error with a retransmission of all bits of the package as a consequence. However, this will be wasteful if almost all bits were received correctly. The H-ARQ protocol will retransmit a fraction of the encoded bits to facilitate successful decoding of the original package. This functionality will improve the link capacity even in poor channel conditions and result in a higher throughput than indicated by Figure 8.2.

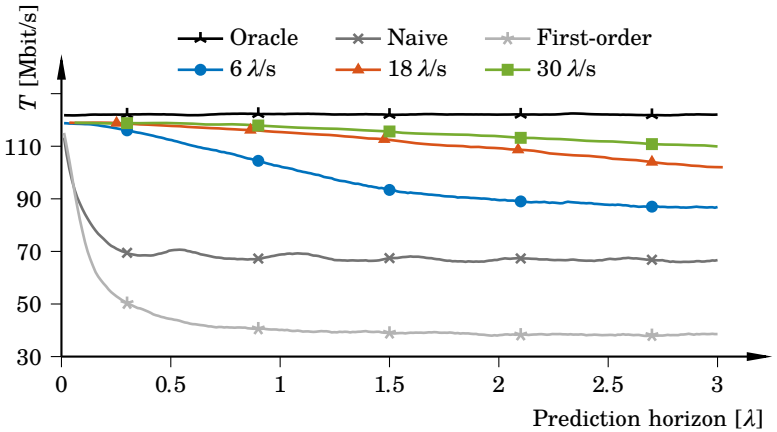

Figure 8.6 Throughput T as a function of prediction horizon with correct initialization of all states for 6 λ/s, 18 λ/s, and 30 λ/s compared to the naive and first-order predictor. The difference in throughput between the three cases increases with the prediction horizon since at a lower velocity, a horizon of 3 λ will accumulate more uncertainty compared to a higher velocity and thereby less prediction time. The performance at the lower speed settles at a level which is 30% higher than the naive predictor.

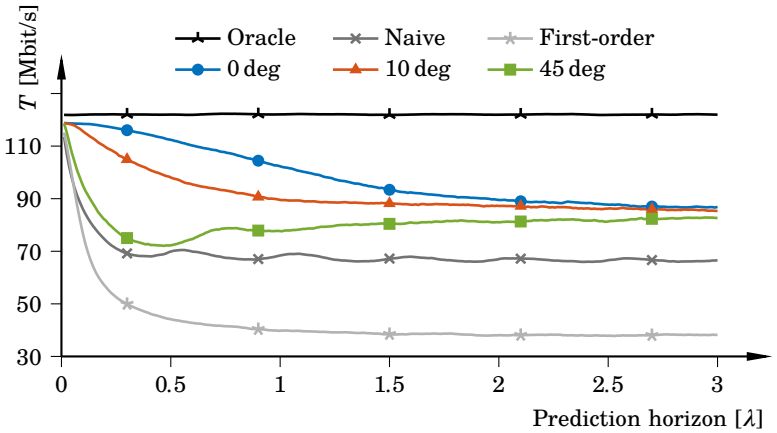

Figure 8.7 Throughput T as a function of prediction horizon with heading error of 0, 10, and 45 deg when the velocity is 6 λ/s. A moderate heading error of 10 deg slightly decreases the throughput at short horizons whereas 45 deg reduces the throughput significantly for short horizons. Note that the performance is regained as the horizon increases due to accumulated uncertainty in the position state.

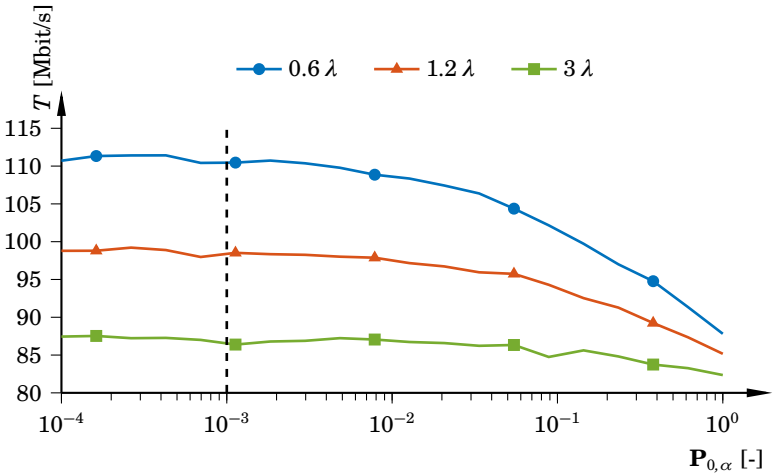

Figure 8.8 Throughput T as a function of initial variance $\mathbf{P}_{0,\alpha}$ of the amplitude for three different prediction horizons at a speed of 6 λ/s. The vertical dashed line marks the nominal case. The influence is noticeable for short horizons while for large horizons, the performance is stable under parameter variations.

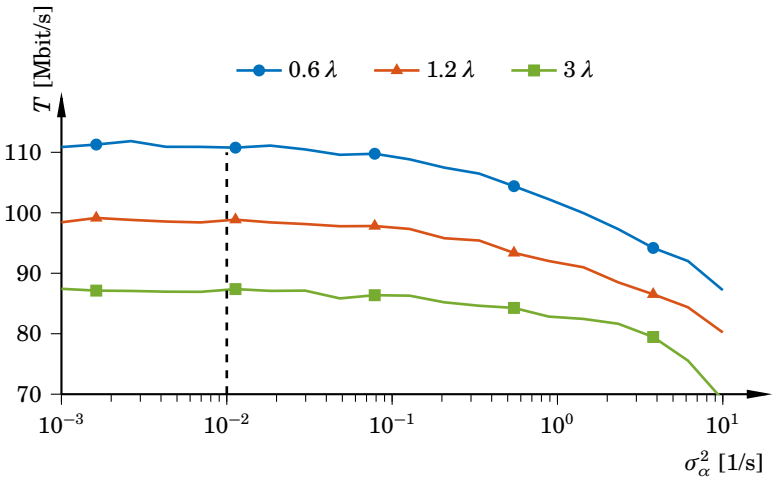

Figure 8.9 Throughput T as a function of amplitude change rate σ_α^2 for three different prediction horizons at a speed of 6 λ/s. The vertical dashed line marks the nominal case. As the change rate exceeds 1/s, the predictor performance degrades rapidly.

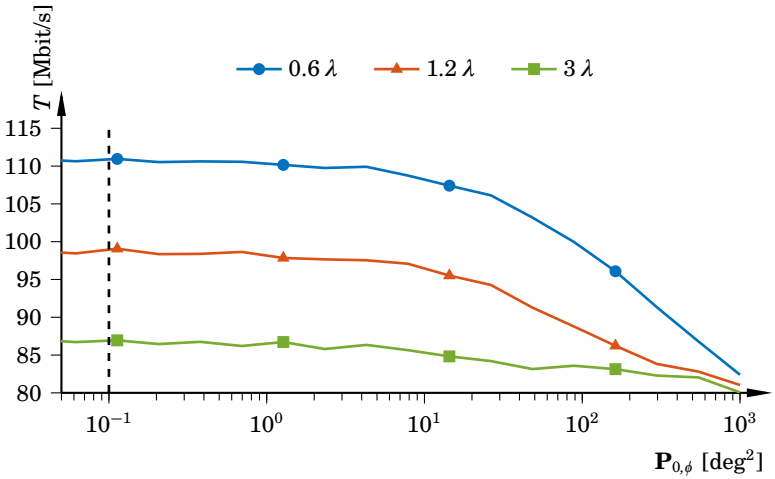

Figure 8.10 Throughput T as a function of initial variance $\mathbf{P}_{0,\phi}$ of the AoA for three different prediction horizons at a speed of 6 λ/s. The vertical dashed line marks the nominal case. If the standard deviation of the AoA estimation given by the particle filter is larger than 5 deg, the performance of the predictor is negatively affected. However, this critical level is approximately 15 times higher than the nominal level.

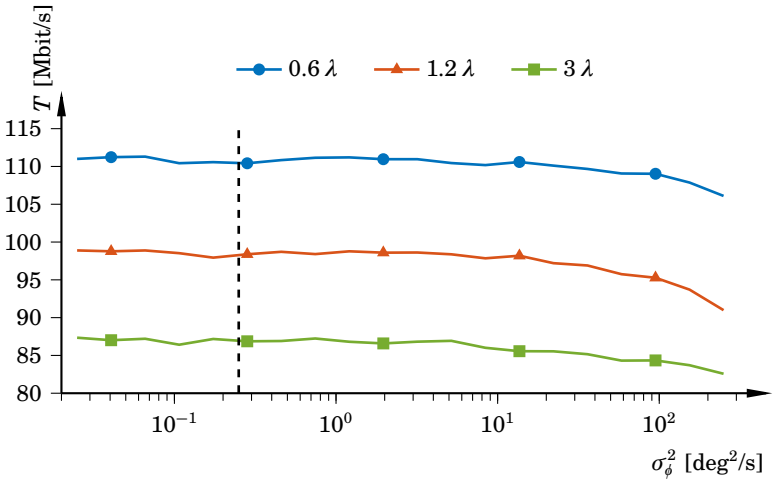

Figure 8.11 Throughput T as a function of AoA change rate σ_ϕ^2 for three different prediction horizons. The vertical dashed line marks the nominal case. The performance is stable for all horizons.

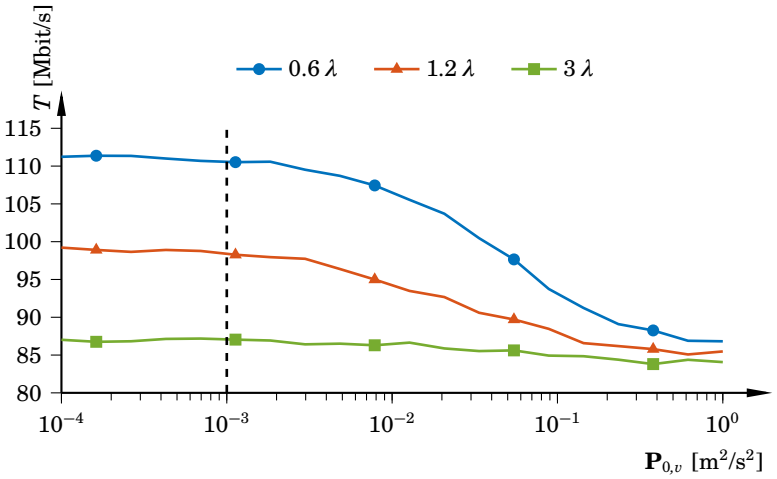

Figure 8.12 Throughput T as a function of initial velocity variance $\mathbf{P}_{0,v}$ for three different prediction horizons at a speed of 6 λ/s. The vertical dashed line marks the nominal case. There is a clear influence on the performance for short horizons due to the initial variance.

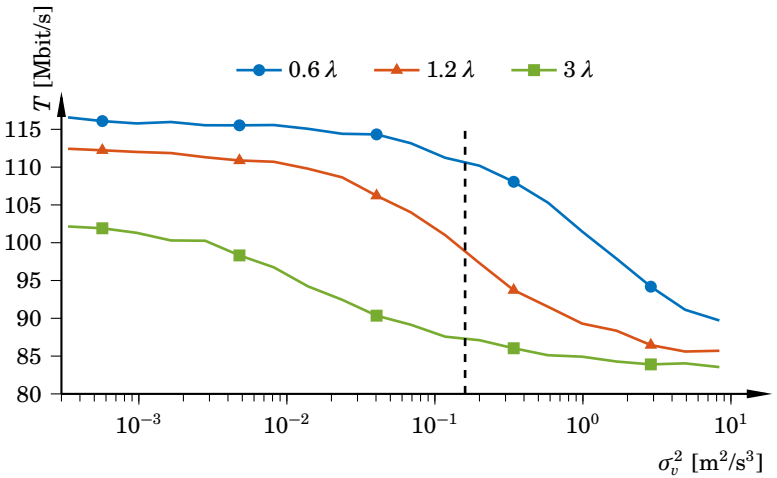

Figure 8.13 Throughput T as a function of velocity change rate σ_v^2 for three different prediction horizons at a speed of 6 λ/s. The vertical dashed line marks the nominal case. The influence of the velocity change rate is significant. Hence, the position uncertainty of the receiver in the future is the limiting factor for prediction performance. This could be improved if a more reliable movement model was available.

9

Summary and Conclusions

In this thesis we investigated the improvements that can be achieved in long-term IMU-based positioning performance, radio channel prediction, and link adaptation. The enabler for this improvement was the joint position and multipath radio channel state-space model. The target application of the work was a hand-held device, equipped with an accelerometer, a gyroscope, and a radio receiver for a pilot based communication system.

In the derivation of the state-space model, a narrowband description of the radio channel was assumed. The implication of this description is that the contribution from an individual multipath component can not be resolved. Instead, each MPC was described by a complex amplitude and its angle of arrival which were included in the state-space model. We also derived the relationship between the location of the receiver and the radio channel impulse response which allowed fusion of accelerometer and gyroscope sensor data and radio channel estimates. Furthermore, we identified the frequency error in the local oscillator of the receiver as being crucial for the success of the approach and it was therefore included in the resulting state-space model. To account for the occurrence of clusters in the environment, their contributions to the channel impulse response was investigated. It was decided to model the contribution as a single component in the state-space model but with a higher change rate on the amplitude compared to the specular components. The state-space model was estimated using a marginalized particle filter capable of estimating the nonlinear model. Since the filter is sensitive to initialization, two different techniques for obtaining the number of MPCs, their complex amplitude, and also their angle of arrival were investigated. It was concluded that the sparse Bayesian learning algorithm, developed in Section 4.2, was superior to the iteratively reweighted ℓ_1 solution since the former was also capable of correcting for the frequency error which causes large estimation errors for the latter. We also investigated the performance bounds for the estimation problem at hand. An extension of known results from the radar literature was presented regarding the connection between the Cramér-Rao lower bound and the

components describing the moment of inertia tensor for space-time virtual arrays and the findings were presented as Theorem 5.1 and Theorem 5.2. With the established connection, we also created worst-case-optimal arrays as a result of an optimal control problem. These arrays have equal estimation performance regardless of the angle of arrival. We also studied how jitter in sampling time and specifically correlated position errors affected the estimation performance. It was concluded that the correlated position errors degrade the performance by a factor of two in angle of arrival estimation and a factor of ten in frequency error estimation. Following that investigation, we looked at the how the state estimation is affected by the number of multipath components present in the environment. The conclusion was that three components is the lower limit if all parameters of the state-space model are to be estimated with a bounded variance growth rate. This is a huge fundamental improvement of what can be achieved in terms of estimation and accuracy compared to the unaided IMU case.

To investigate the positioning and radio channel state tracking performance, both simulation studies and experiments were performed. The simulations served as an enabler for the experiments and the gain in long-term positioning performance is remarkable. Comparing the performance improvement between a SISO system and a 2×2 MIMO system revealed that the MIMO system was approximately three times better than the SISO system and almost 70 times better on average compared to the unaided IMU simulation scenario for a one minute movement. We also studied how the number of particles, AoA and frequency error change rate, and SNR variation affected the result. The conclusion is that the filter-based solution is capable of delivering positioning performance that on average is within a few decimeters in good channel conditions. When introducing clusters in the model, the performance was degraded but for small indoor clusters the degradation was limited. This confirms the belief that the technique is suitable for high accuracy indoor positioning. Experimental results show that the mean position RMSE for a 20 second movement is kept within a few decimeters on average. The experimental results can be seen as a proof of concept for the modeling and estimation approach. Further experiments with other movement patterns are needed in order to understand the full potential of the method.

Finally, we investigated the performance that can be achieved in data throughput if a particle predictor is used for the channel prediction. The results show that under slow channel fluctuations, the channel can be predicted for at least $0.5\,\lambda$ with sufficient accuracy to increase the throughput to the end user. For the naive and first-order predictors, the prediction horizon was well below $0.5\,\lambda$. The number of particles needed for the prediction was low and the computational cost of the predictor would therefore be small in a real-time implementation.

9.1 Directions for Future Work

The material presented opens up for interesting research directions for the future. Below is a collection of ideas that are worthy candidates of investigation in order to improve the methods described in this thesis.

Modeling Improvement

As touched upon previously, the modeling in Section 3.3 has implications for the estimation of the state vector. As the formulation is currently given, a small change in the angle of arrival when $\boldsymbol{p}$ is large yields a larger change in the measurement signal compared to when $\boldsymbol{p}$ is smaller. This means that when $\boldsymbol{p}$ is large, most predicted hypotheses in the particle filter will be discarded which triggers resampling. If the two properties, angle of arrival change rate and position, can be separated, the estimation performance will be independent of how far the receiver has been moved since β was initialized.

Multipath Component Detection and Classification

In this thesis we have investigated cases where the number of multipath components is assumed to be known and fixed for the whole simulation time. In a real world scenario, this would in general not be the case. Instead, multipath components appear and disappear as the receiver is moved. The current state of the model and the filter is such that it can remove a component by setting its amplitude to zero but no new components can be detected and added. This is a crucial feature for a future implementation. A potential detection measure would be the residuals of the measurement signal. Such an approach has been suggested in [Chen and Viberg, 2009; Angelosante et al., 2009]. If most components are detected and estimated, the residuals should be close to the noise level of the current measurement. If the residual is larger, then there are most likely undetected components present. Also, in the implementation investigated here, there is a clear distinction between whether the signal contribution is from a cluster or a single point source. In the real world, this must also be adaptively detected by the filter.

Antenna Radiation Pattern Estimation

The directivity of the antennas has been excluded in this thesis even though in the experiments, the antenna pattern is of course present. However, antennas in general and especially the ones used in hand-held devices show a high directivity, see, e.g., [Krogerus et al., 2007]. Also, the directivity is for example dependent on whether the device is held in open air or closer to the body. This would require the filter to account for the antenna pattern's influence on the received signals.

Initialization Using MIMO Measurements

For initialization with the sparse Bayesian learning algorithm, data from one receive antenna is used. This is a clear waste since the data available from the other receive antennas could give a considerable contribution to the estimation performance. A MIMO formulation of the regularized convex approach is available in [Wipf and Rao, 2007] but for the sparse Bayesian learning, no extension appears to exist yet.

Wideband Channel Extension

This work is restricted to single-frequency pilots. As seen in Figure 1.4, pilots are transmitted on several subchannels. If all the available pilots are taken into account by the filter, the performance can be increased assuming there are some states that are common for different frequencies. A potential candidate would be the angle of arrival. If the subchannel frequencies, and thereby the wavelengths, are close to each other the phase information in the different subchannels is almost the same. This corresponds to the maps from figures 2.8, 2.9, and, 2.10 being almost identical for different subchannels. The effect in such a case would consequently be similar to an increased SNR level. If the subchannel frequencies are further apart the gain would be larger. This is used in radio standards with aggregated frequency bands that are in many cases several hundreds of MHz apart. However, extending the algorithm to use more frequency bands will also introduce more states that need to be estimated and a real time implementation of the marginalized particle filter tracking several MPCs on different frequencies might be difficult to achieve.

Performance in a Dense Multipath Environment

In the work of [Poutanen et al., 2010] the contribution of dense/diffuse multipath components (DMC) to the total received power was investigated. It was concluded that in an indoor environment under NLOS, the main contribution to the received power comes from the DMC, especially when the distance between the receiver and the transmitter is large. Furthermore, in [Leitinger et al., 2015] the authors investigate the achievable positioning performance under the existence of DMC using time delay measurements in an UWB network. It is shown that there is a clear connection between the positioning performance and the SINR where the DMCs are considered as interference. A similar study of the particle filter based positioning solution would be of interest to see how the performance will be affected.

Bibliography

3GPP (2009). *Technial specification; evolved universal terrestrial radio access (E-UTRA); physical layer procedures (release 8)*. 3rd Generation Partnership Project. URL: http://www.3gpp.org/DynaReport/36213.htm (visited on 2016-02-08).

3GPP (2016a). 3rd Generation Partnership Project. URL: http://www.3gpp.org/technologies/keywords-acronyms/98-lte (visited on 2016-02-08).

3GPP (2016b). 3rd Generation Partnership Project. URL: http://www.3gpp.org/technologies/keywords-acronyms/99-hspa (visited on 2016-02-08).

Andersen, J., J. Jensen, S. Jensen, and F. Frederiksen (1999). "Prediction of future fading based on past measurements". In: *IEEE VTS 50th Vehicular Technology Conference*. Vol. 1. Amsterdam, The Netherlands, pp. 151–155.

Anderson, B. and J. Moore (2012). *Optimal Filtering*. Dover Books on Electrical Engineering. Dover Publications.

Angelosante, D., E. Biglieri, and M. Lops (2009). "Sequential estimation of multipath MIMO-OFDM channels". *IEEE Transactions on Signal Processing* **57**:8, pp. 3167–3181.

Arulampalam, S., S. Maskell, N. Gordon, and T. Clapp (2001). "A tutorial on particle filters for on-line non-linear/non-Gaussian Bayesian tracking". *IEEE Transactions on Signal Processing* **50**, pp. 174–188.

Babacan, S., R. Molina, and A. Katsaggelos (2010). "Bayesian compressive sensing using Laplace priors". *IEEE Transactions on Image Processing* **19**:1, pp. 53–63.

Bailey, T. and H. Durrant-Whyte (2006a). "Simultaneous localization and mapping (SLAM): Part I". *IEEE Robotics and Automation Magazine* **13**:2, pp. 99–110.

Bailey, T. and H. Durrant-Whyte (2006b). "Simultaneous localization and mapping (SLAM): Part II". *IEEE Robotics and Automation Magazine* **13**:3, pp. 108–117.

Bay, S., B. Geller, A. Renaux, J.-P. Barbot, and J. Brossier (2008). "On the hybrid Cramér-Rao bound and its application to dynamical phase estimation". *IEEE Signal Processing Letters* **15**, pp. 453–456.

Berrou, C., A. Glavieux, and P. Thitimajshima (1993). "Near Shannon limit error-correcting coding and decoding: turbo-codes". In: *Proceedings of IEEE International Conference on Communications (ICC)*. Vol. 2. Geneva, Switzerland, pp. 1064–1070.

Boyd, S. and L. Vandenberghe (2004). *Convex optimization*. Cambridge university press.

Broumandan, A., T. Lin, A. Moghaddam, D. Lu, J. Nielsen, and G. Lachapelle (2007). "Direction of arrival estimation of GNSS signals based on synthetic antenna array". In: *Proceedings of the 20th International Technical Meeting of the Satellite Division of the Institute of Navigation (ION GNSS'07)*. Fort Worth, TX, USA, pp. 728–738.

Candes, E. J., M. B. Wakin, and S. P. Boyd (2008). "Enhancing sparsity by reweighted ℓ_1 minimization". *Journal of Fourier Analysis and Applications* **14**:5, pp. 877–905.

Capon, J. (1969). "High-resolution frequency-wavenumber spectrum analysis". *Proceedings of the IEEE* **57**:8, pp. 1408–1418.

Carvalho, H., P. Del Moral, A. Monin, and G. Salut (1997). "Optimal nonlinear filtering in GPS/INS integration". *IEEE Transactions on Aerospace and Electronic Systems* **33**:3, pp. 835–850.

Cavers, J. K. (1972). "Variable-rate transmission for Rayleigh fading channels". *IEEE Transactions on Communications* **20**:1, pp. 15–22.

Chen, M. and M. Viberg (2009). "Long-range channel prediction based on nonstationary parametric modeling". *IEEE Transactions on Signal Processing* **57**:2, pp. 622–634.

Chung, S. T. and A. Goldsmith (2001). "Degrees of freedom in adaptive modulation: a unified view". *IEEE Transactions on Communications* **49**:9, pp. 1561–1571.

Collier, S. L. (2005). "Fisher information for a complex Gaussian random variable: beamforming applications for wave propagation in a random medium". *IEEE Transactions on Signal Processing* **53**:11, pp. 4236–4248.

Coutsias, E. A. and L. Romero (1999). *The quaternions with an application to rigid body dynamics*. Tech. rep. Dept. of Mathematics and Statistics, University of New Mexico Albuquerque, NM, USA.

Cramér, H. (1999). *Mathematical Methods of Statistics*. Princeton Mathematical Series. Princeton University Press.

CVX (2016). URL: `http://cvxr.com` (visited on 2016-02-08).

Davison, A. J. (2003). "Real-time simultaneous localisation and mapping with a single camera". In: *Proceedings of the 9th IEEE International Conference on Computer Vision*. Nice, France, pp. 1403–1410.

Dogandžić, A. and A. Nehorai (2001). "Cramér-Rao bounds for estimating range, velocity, and direction with an active array". *IEEE Transactions on Signal Processing* **49**:6, pp. 1122–1137.

Doucet, A., N. de Freitas, K. Murphy, and S. Russell (2000a). "Rao-Blackwellised particle filtering for dynamic Bayesian networks". In: *Proceedings of the 16th Conference on Uncertainty in Artificial Intelligence (UAI)*. Stanford, CA, USA, pp. 176–183.

Doucet, A., S. Godsill, and C. Andrieu (2000b). "On sequential Monte Carlo sampling methods for Bayesian filtering". *Statistics and Computing* **10**, pp. 197–208.

Duel-Hallen, A., S. Hu, and H. Hallen (2000). "Long range prediction of fading signals: enabling adaptive transmission for mobile radio channels". *IEEE Signal Processing Magazine* **17**, pp. 62–75.

Ekman, T. (2002). *Prediction of mobile radio channels, Modeling and Design*. PhD thesis. Uppsala University, Uppsala, Sweden.

Fessler, J. A. and A. O. Hero (1994). "Space-alternating generalized expectation-maximization algorithm". *IEEE Transactions on Signal Processing* **42**:10, pp. 2664–2677.

Fink, A., H. Beikirch, M. Voss, and C. Schroder (2010). "RSSI-based indoor positioning using diversity and inertial navigation". In: *Proceedings of 2010 International Conference on Indoor Positioning and Indoor Navigation (IPIN)*. Zurich, Switzerland, pp. 1–7.

Fleury, B., M. Tschudin, R. Heddergott, D. Dahlhaus, and K. Ingeman Pedersen (1999). "Channel parameter estimation in mobile radio environments using the SAGE algorithm". *IEEE Journal on Selected Areas in Communications* **17**:3, pp. 434–450.

Friedlander, B. (1990). "Sensitivity analysis of the maximum likelihood direction-finding algorithm". *IEEE Transactions on Aerospace and Electronic Systems* **26**:6, pp. 953–968.

Ghosh, A., J. Zhang, J. Andrews, and R. Muhamed (2011). *Fundamentals of LTE*. Pearson Education.

Godsill, S. J., A. Doucet, and M. West (2004). "Monte Carlo smoothing for nonlinear time series". *Journal of the American Statistical Association* **99**:465, pp. 156–168.

Goldsmith, A. J. and S. G. Chua (1998). "Adaptive coded modulation for fading channels". *IEEE Transactions on Communications* **46**:5, pp. 595–602.

Goldsmith, A. and S.-G. Chua (1997). "Variable-rate variable-power MQAM for fading channels". *IEEE Transactions on Communications* **45**:10, pp. 1218–1230.

Gordon, N., D. Salmond, and A. F. M. Smith (1993). "Novel approach to nonlinear/non-Gaussian Bayesian state estimation". *IEE Proceedings F - Radar and Signal Processing* **140**:2, pp. 107–113.

Gu, H. (1996). "Ambiguity function and Cramér-Rao bound in the multisignal case". *IEE Proceedings - Radar, Sonar and Navigation* **143**:4, pp. 227–231.

Gustafsson, F. (2010). *Statistical Sensor Fusion*. Studentlitteratur.

Hol, J. D., F. Dijkstra, H. Luinge, and T. B. Schön (2009). "Tightly coupled UWB/IMU pose estimation". In: *Proceedings of 2009 IEEE International Conference on Ultra-Wideband (ICUWB)*. Vancouver, BC, Canada, pp. 688–692.

Hwang, J.-K. and J. Winters (1998). "Sinusoidal modeling and prediction of fast fading processes". In: *Proceedings of 1998 IEEE Global Telecommunications Conference (GLOBECOM)*. Vol. 2. Sydney, Australia, pp. 892–897.

IEEE S.A. (2016). IEEE Standards Association. URL: `http://standards.ieee.org/about/get/802/802.11.html` (visited on 2016-02-08).

IEEE Std 952-1997 (1998). *IEEE Standard Specification Format Guide and Test Procedure for Single-Axis Interferometric Fiber Optic Gyros*. Tech. rep.

Ji, S., Y. Xue, and L. Carin (2008). "Bayesian compressive sensing". *IEEE Transactions on Signal Processing* **56**:6, pp. 2346–2356.

jModelica.org (2016). URL: `http://www.jmodelica.org/` (visited on 2016-02-08).

Jourdan, D. B., J. J. Deyst, M. Z. Win, and N. Roy (2005). "Monte Carlo localization in dense multipath environments using UWB ranging". In: *2005 IEEE International Conference on Ultra-Wideband (ICU)*. Zurich, Switzerland, pp. 314–319.

Julier, S. and J. Uhlmann (2004). "Unscented filtering and nonlinear estimation". *Proceedings of the IEEE* **92**:3, pp. 401–422.

Kalman, R. (1960). "A new approach to linear filtering and prediction problems". *Transactions of the ASME–Journal of Basic Engineering* **82**:Series D, pp. 35–45.

Karlsson, R., T. Schön, and F. Gustafsson (2005). "Complexity analysis of the marginalized particle filter". *IEEE Transactions on Signal Processing* **53**:11, pp. 4408–4411.

Kasdin, N. J. (1995). "Discrete simulation of colored noise and stochastic processes and $1/f^{\alpha}$; power law noise generation". *Proceedings of the IEEE* **83**:5, pp. 802–827.

Kay, S. M. (1993). *Fundamentals of statistical signal processing: Estimation theory*. Prentice Hall.

Kirkelund, G., G. Steinbock, X. Yin, and B. Fleury (2008). "Tracking of the temporal behaviour of path components in the radio channel - a comparison between methods". In: *Proceedings of Annual IEEE Conference Student Paper*. Aalborg, Denmark, pp. 1–5.

Krim, H. and M. Viberg (1996). "Two decades of array signal processing research: the parametric approach". *IEEE Signal Processing Magazine* **13**:4, pp. 67–94.

Krogerus, J., J. Toivanen, C. Icheln, and P. Vainikainen (2007). "Effect of the human body on total radiated power and the 3-D radiation pattern of mobile handsets". *IEEE Transactions on Instrumentation and Measurement* **56**:6, pp. 2375–2385.

Kuipers, J. B. (1999). *Quaternions and rotation sequences: A primer with applications to orbits, aerospace, and virtual reality*. Princeton university press.

Leitinger, E., P. Meissner, C. Rudisser, G. Dumphart, and K. Witrisal (2015). "Evaluation of position-related information in multipath components for indoor positioning". *IEEE Journal on Selected Areas in Communications* **33**:11, pp. 2313–2328.

Li, W. W.-L., R. Iltis, and M. Win (2013). "A smartphone localization algorithm using RSSI and inertial sensor measurement fusion". In: *Proceedings of 2013 IEEE Global Telecommunications Conference (GLOBECOM)*. Atlanta, GA, USA, pp. 3335–3340.

Li, X. R. and V. P. Jilkov (2003). "Survey of maneuvering target tracking. Part I. dynamic models". *IEEE Transactions on Aerospace and Electronic Systems* **39**:4, pp. 1333–1364.

Liu, L., C. Oestges, J. Poutanen, K. Haneda, P. Vainikainen, F. Quitin, F. Tufvesson, and P. Doncker (2012). "The COST 2100 MIMO channel model". *IEEE Wireless Communications* **19**:6, pp. 92–99.

Malioutov, D., M. Cetin, and A. Willsky (2005). "A sparse signal reconstruction perspective for source localization with sensor arrays". *IEEE Transactions on Signal Processing* **53**:8, pp. 3010–3022.

Mannesson, A. (2013). *Joint Pose and Radio Channel Estimation*. Licentiate Thesis ISRN LUTFD2/TFRT–3263–SE. Department of Automatic Control, Lund University, Sweden.

Mannesson, A. and B. Bernhardsson (2015). “Cramér-Rao lower bound for imprecise space-time virtual antenna arrays”. *IEEE Transactions on Signal Processing*. Submitted.

Mannesson, A., B. Bernhardsson, and F. Tufvesson (2015a). “Link adaption for MIMO systems using sensor fusion based channel prediction”. *IEEE Transactions on Wireless Communications*. Submitted.

Mannesson, A., M. A. Yaqoob, B. Bernhardsson, and F. Tufvesson (2015b). “Tightly coupled positioning and multipath radio channel tracking”. *IEEE Transactions on Aerospace and Electronic Systems*. Accepted.

MEDAV (2016). URL: `http://www.channelsounder.de` (visited on 2016-02-08).

Molisch, A. F. (2005). *Wireless Communications*. Wiley.

Ohlsson, H., L. Ljung, and S. Boyd (2010). “Segmentation of ARX-models using sum-of-norms regularization”. *Automatica* **46**:6, pp. 1107–1111.

Olama, M., S. Djouadi, and C. Charalambous (2006). “Position and velocity tracking in cellular networks using particle and Kalman filtering with comparison”. In: *Proceedings of 45th IEEE Conference on Decision and Control (CDC)*. San Diego, CA, USA, pp. 1315–1320.

Olsson, J., O. Cappé, R. Douc, and É. Moulines (2008). “Sequential monte carlo smoothing with application to parameter estimation in nonlinear state space models”. *Bernoulli* **14**:1, pp. 155–179.

Paulraj, A., R. Nabar, and D. Gore (2003). *Introduction to Space-Time Wireless Communications*. Cambridge University Press.

Pedersen, T. (2009). *Contributions in Radio Channel Sounding, Modeling, and Estimation*. PhD thesis. The Faculty of Engineering, Science, Navigation, and Communications, Aalborg University, Denmark.

Phidgets (2016). URL: `http://www.phidgets.com/docs/1044_User_Guide` (visited on 2016-02-08).

Poutanen, J., K. Haneda, L. Liu, C. Oestges, F. Tufvesson, and P. Vainikainen (2011). “Parameterization of the COST 2100 MIMO channel model in indoor scenarios”. In: *Proceedings of the 5th European Conference on Antennas and Propagation (EUCAP)*. Rome, Italy, pp. 3606–3610.

Poutanen, J., J. Salmi, K. Haneda, V. M. Kolmonen, F. Tufvesson, and P. Vainikainen (2010). “Propagation characteristics of dense multipath components”. *IEEE Antennas and Wireless Propagation Letters* **9**, pp. 791–794.

Rao, C. R. (1945). “Information and the accuracy attainable in the estimation of statistical parameters”. *Bulletin of the Calcutta Mathematical Society* **37**, pp. 81–91.

Rendas, M.-J. D. and J. M. Moura (1991). "Cramér-Rao bound for location systems in multipath environments". *IEEE Transactions on Signal Processing* **39**:12, pp. 2593–2610.

Richter, A., M. Enescu, and V. Koivunen (2005). "State-space approach to propagation path parameter estimation and tracking". In: *Proceedings of 6th IEEE Workshop on Signal Processing Advances in Wireless Communications (SPAWC)*. New York, NY, USA, pp. 510–514.

Robert, C. (2007). *The Bayesian Choice. From Decision-Theoretic Foundations to Computational Implementation*. 2nd ed. Springer.

Roy, R. and T. Kailath (1989). "ESPRIT-estimation of signal parameters via rotational invariance techniques". *IEEE Transactions on Acoustics, Speech, and Signal Processing* **37**:7, pp. 984–995.

Sabatini, A. M. (2006). "Quaternion-based extended Kalman filter for determining orientation by inertial and magnetic sensing". *IEEE Transactions on Biomedical Engineering* **53**:7, pp. 1346–1356.

Sabatini, A. M., C. Martelloni, S. Scapellato, and F. Cavallo (2005). "Assessment of walking features from foot inertial sensing". *IEEE Transactions on Biomedical Engineering* **52**:3, pp. 486–494.

Schmidt, R. O. (1986). "Multiple emitter location and signal parameter estimation". *IEEE Transactions on Antennas and Propagation* **34**:3, pp. 276–280.

Schön, T. (2006). *Estimation of nonlinear dynamic systems: Theory and applications*. PhD thesis. Department of Electrical Engineering, Linköping University, Sweden.

Schön, T., F. Gustafsson, and P.-J. Nordlund (2005). "Marginalized particle filters for mixed linear/nonlinear state-space models". *IEEE Transactions on Signal Processing* **53**:7, pp. 2279–2289.

Schwarz, S., J. Ikuno, M. Simko, M. Taranetz, Q. Wang, and M. Rupp (2013). "Pushing the limits of LTE: a survey on research enhancing the standard". *IEEE Access* **1**, pp. 51–62.

Skog, I. and P. Händel (2006). "Calibration of a MEMS inertial measurement unit". In: *Proceedings of XVIII IMEKO World Congress*. Rio de Janeiro, Brazil, pp. 1445–1451.

Skog, I., J.-O. Nilsson, and P. Händel (2010). "Evaluation of zero-velocity detectors for foot-mounted inertial navigation systems". In: *Proceddings of International Conference on Indoor Positioning and Indoor Navigation (IPIN)*. Zurich, Switzerland, pp. 1–6.

Staszewski, R., C. Fernando, and P. Balsara (2005). "Event-driven simulation and modeling of phase noise of an RF oscillator". *IEEE Transactions on Circuits and Systems—Part I: Fundamental Theory and Applications* **52**:4, pp. 723–733.

Sukkarieh, S., E. M. Nebot, and H. F. Durrant-Whyte (1999). "A high integrity IMU/GPS navigation loop for autonomous land vehicle applications". *IEEE Transactions on Robotics and Automation* **15**:3, pp. 572–578.

Systron (2016). URL: http://www.systron.com/imus/sdi500-tactical-grade-imu-inertial-measurement-unit (visited on 2016-02-08).

Taylor, J. (1979). "The Cramér-Rao estimation error lower bound computation for deterministic nonlinear systems". *IEEE Transactions on Automatic Control* **24**:2, pp. 343–344.

Tibshirani, R. (1996). "Regression shrinkage and selection via the Lasso". *Journal of the Royal Statistic Society*. B **58**:1, pp. 267–288.

Tichavsky, P., C. Muravchik, and A. Nehorai (1998). "Posterior Cramér-Rao bounds for discrete-time nonlinear filtering". *IEEE Transactions on Signal Processing* **46**:5, pp. 1386–1396.

Tipping, M. E. and A. C. Faul (2003). "Fast marginal likelihood maximisation for sparse Bayesian models". In: *Proceedings of The 9th International Workshop on Artificial Intelligence and Statistics*. Key West, FL, USA.

Tipping, M. E. (2001). "Sparse Bayesian learning and the relevance vector machine". *Journal of Machine Learning Research* **1**, pp. 211–244.

Titterton, D. and J. Weston (2004). *Strapdown Inertial Navigation Technology, 2nd Edition*. IET.

Van Trees, H. L. (2004). *Detection, estimation, and modulation theory, optimum array processing*. John Wiley & Sons.

Veen, A.-J. van der, M. Vanderveen, and A. Paulraj (1997). "Joint angle and delay estimation using shift-invariance properties". *IEEE Signal Processing Letters* **4**:5, pp. 142–145.

Verdone, R. and A. Zanella, (Eds.) (2012). *Pervasive Mobile and Ambient Wireless Communications. COST Action 2100*. 1st ed. Signals and Communication Technology. Springer.

Wipf, D. and B. Rao (2007). "An empirical Bayesian strategy for solving the simultaneous sparse approximation problem". *IEEE Transactions on Signal Processing* **55**:7, pp. 3704–3716.

Woodman, O. (2010). *Pedestrian Localisation for Indoor Environments*. PhD thesis. University of Cambridge, U.K.

Woodman, O. and R. Harle (2008). "Pedestrian localisation for indoor environments". In: *Proceedings of 10th International Conference Ubiquitous Computing*. UbiComp '08. Seoul, Korea, pp. 114–123.

Xsens (2016). URL: https://www.xsens.com/products/mti-1-series/ (visited on 2016-02-08).

Yanying, G., A. Lo, and I. Niemegeers (2009). “A survey of indoor positioning systems for wireless personal networks”. *IEEE Communications Surveys and Tutorials* **11**:1, pp. 13–32.

Yaqoob, M. A., A. Mannesson, F. Tufvesson, and B. Bernhardsson (2013). “Direction of arrival estimation with arbitrary virtual antenna arrays using low cost inertial measurement unit”. In: *Proceedings of IEEE International Conference on Communications - Workshop*. Budapest, Hungary, pp. 79–83.

Zhou, Z., B. Vucetic, M. Dohler, and Y. Li (2005). “MIMO systems with adaptive modulation”. *IEEE Transactions on Vehicular Technology* **54**:5, pp. 1828–1842.

Zhu, M., G. Eriksson, and F. Tufvesson (2013). “The COST 2100 channel model: parameterization and validation based on outdoor MIMO measurements at 300 MHz”. *IEEE Transactions on Wireless Communications* **12**:2, pp. 888–897.

A

The Particle Filter

This appendix presents a derivation of the particle filter equations. The recursive formulation of the filter is summarized in Algorithm 4.2. The derivation of the particle filter follows [Schön, 2006] closely.

The dynamic and measurement equations of (4.1) can be written as distributions where $\boldsymbol{x}_k$ and $\boldsymbol{y}_k$ are given as

$$\boldsymbol{x}_{k+1} \sim p(\boldsymbol{x}_{k+1}|\boldsymbol{x}_k), \tag{A.1a}$$

$$\boldsymbol{y}_k \sim p(\boldsymbol{y}_k|\boldsymbol{x}_k). \tag{A.1b}$$

Now consider the posterior distribution density

$$p(\boldsymbol{x}_k|\boldsymbol{y}_{1:k}) = p(\boldsymbol{x}_k|\boldsymbol{y}_k, \boldsymbol{y}_{1:k-1}), \tag{A.2}$$

where $\boldsymbol{y}_{1:k} = \{\boldsymbol{y}_1, \ldots, \boldsymbol{y}_k\}$. Using Bayes' rule

$$p(x|y) = \frac{p(y|x)p(x)}{p(y)}$$

and the Markov property of dynamic systems, (A.2) can be transformed into

$$p(\boldsymbol{x}_k|\boldsymbol{y}_{1:k}) = \frac{p(\boldsymbol{y}_k|\boldsymbol{x}_k, \boldsymbol{y}_{1:k-1})p(\boldsymbol{x}_k|\boldsymbol{y}_{1:k-1})}{p(\boldsymbol{y}_k|\boldsymbol{y}_{1:k-1})} = \frac{p(\boldsymbol{y}_k|\boldsymbol{x}_k)p(\boldsymbol{x}_k|\boldsymbol{y}_{1:k-1})}{p(\boldsymbol{y}_k|\boldsymbol{y}_{1:k-1})}, \tag{A.3}$$

where the denominator can, using marginalization, be written with known densities as

$$p(\boldsymbol{y}_k|\boldsymbol{y}_{1:k-1}) = \int p(\boldsymbol{y}_k|\boldsymbol{x}_k)p(\boldsymbol{x}_k|\boldsymbol{y}_{1:k-1})\, d\boldsymbol{x}_k. \tag{A.4}$$

For the prediction step, the strategy with marginalization used above is reused as

$$\begin{aligned} p(\boldsymbol{x}_k|\boldsymbol{y}_{1:k-1}) &= \int p(\boldsymbol{x}_k, \boldsymbol{x}_{k-1}|\boldsymbol{y}_{1:k-1})\, d\boldsymbol{x}_{k-1} \\ &= \int p(\boldsymbol{x}_k|\boldsymbol{x}_{k-1}, \boldsymbol{y}_{1:k-1})p(\boldsymbol{x}_{k-1}|\boldsymbol{y}_{1:k-1})\, d\boldsymbol{x}_{k-1} \\ &= \int p(\boldsymbol{x}_k|\boldsymbol{x}_{k-1})p(\boldsymbol{x}_{k-1}|\boldsymbol{y}_{1:k-1})\, d\boldsymbol{x}_{k-1}. \end{aligned} \tag{A.5}$$

The integrals in (A.4) and (A.5) are usually not analytically solvable. However, if the distributions are Gaussian and the dynamic system is linear, the integrals above are solvable and yield the Kalman filter equations presented in Algorithm 4.1. For the more general case, an approximation of the integrals can be used instead.

Introduce a particle as a sample from the posterior distribution

$$\boldsymbol{x}_k^{(i)} \sim p(\boldsymbol{x}_k|\boldsymbol{y}_{1:k}), \ \forall\, i \in \{1, \ldots, N_p\}, \tag{A.6}$$

where N_p is the number of such particles. They can now be used to make an approximation of the posterior distribution as

$$p(\boldsymbol{x}_k|\boldsymbol{y}_{1:k}) \approx \sum_{i=1}^{N_p} w_{k|k}^{(i)} \delta(\boldsymbol{x}_k - \boldsymbol{x}_k^{(i)}), \tag{A.7}$$

where $\delta(\cdot)$ is the Dirac delta function and

$$\sum_{i=1}^{N_p} w_{k|k}^{(i)} = 1, \quad w_{k|k}^{(i)} \geq 0, \ \forall\, i \in \{1, \ldots, N_p\}.$$

By using the approximation above, the integrals in (A.3) and (A.5) can be solved approximately. Starting with the prediction step in (A.5) and replacing the posterior distribution with its approximation from (A.7) yields

$$\begin{aligned} p(\boldsymbol{x}_k|\boldsymbol{y}_{1:k-1}) &= \int p(\boldsymbol{x}_k|\boldsymbol{x}_{k-1}) p(\boldsymbol{x}_{k-1}|\boldsymbol{y}_{1:k-1})\, d\boldsymbol{x}_{k-1} \\ &\approx \int p(\boldsymbol{x}_k|\boldsymbol{x}_{k-1}) \sum_{i=1}^{N_p} w_{k-1|k-1}^{(i)} \delta(\boldsymbol{x}_{k-1} - \boldsymbol{x}_{k-1}^{(i)})\, d\boldsymbol{x}_{k-1} \\ &= \sum_{i=1}^{N_p} w_{k-1|k-1}^{(i)} p(\boldsymbol{x}_k|\boldsymbol{x}_{k-1}^{(i)}). \end{aligned} \tag{A.8}$$

To regain a set of particles instead of a distribution, N_p new particles should be drawn from (A.8). However, it is difficult to directly generate samples from this distribution. Instead, importance sampling can be used to generate the samples [Gordon et al., 1993]. From the sampling it is given that the importance weights w are calculated as

$$w = \frac{p(\boldsymbol{x}_k|\boldsymbol{y}_{1:k-1})}{q(\boldsymbol{x}_k|\boldsymbol{x}_{k-1}, \boldsymbol{y}_{1:k})}, \tag{A.9}$$

where the numerator is the target distribution and the denominator is the proposal distribution from which samples can be drawn. The first step of

importance sampling is to draw new particles from the proposal distribution as

$$\tilde{\boldsymbol{x}}_k^{(i)} \sim q(\boldsymbol{x}_k|\boldsymbol{x}_{k-1}^{(i)}, \boldsymbol{y}_{1:k}), \ \forall\, i \in \{1, \dots, N_p\}. \tag{A.10}$$

The weights w for the new samples are computed as

$$w_{k|k-1}^{(i)} = \frac{p(\tilde{\boldsymbol{x}}_k^{(i)}|\boldsymbol{y}_{1:k-1})}{q(\tilde{\boldsymbol{x}}_k^{(i)}|\boldsymbol{x}_{k-1}^{(i)}, \boldsymbol{y}_{1:k})}, \ \forall\, i \in \{1, \dots, N_p\}.$$

By choosing

$$q(\boldsymbol{x}_k|\boldsymbol{x}_{k-1}, \boldsymbol{y}_{1:k}) = p(\boldsymbol{x}_k|\boldsymbol{x}_{k-1}) \tag{A.11}$$

as proposal distribution, which is the state dynamics from (A.1a), the following relation is obtained

$$\begin{aligned} w_{k|k-1}^{(i)} = \frac{p(\tilde{\boldsymbol{x}}_k^{(i)}|\boldsymbol{y}_{1:k-1})}{p(\tilde{\boldsymbol{x}}_k^{(i)}|\boldsymbol{x}_{k-1}^{(i)})} &\approx \frac{\int p(\tilde{\boldsymbol{x}}_k^{(i)}|\boldsymbol{x}_{k-1}) \sum_{i=1}^{N_p} w_{k-1|k-1}^{(i)} \delta(\boldsymbol{x}_{k-1} - \boldsymbol{x}_{k-1}^{(i)})\, d\boldsymbol{x}_{k-1}}{p(\tilde{\boldsymbol{x}}_k^{(i)}|\boldsymbol{x}_{k-1}^{(i)})} \\ &= w_{k-1|k-1}^{(i)}, \ \forall\, i \in \{1, \dots, N_p\}. \end{aligned} \tag{A.12}$$

There are other suggestions on how to choose the proposal distribution $q(\boldsymbol{x}_k|\boldsymbol{x}_{k-1}, \boldsymbol{y}_k)$, see, e.g., [Gustafsson, 2010]. The approximation of the prediction step is then

$$\hat{p}(\boldsymbol{x}_k|\boldsymbol{y}_{1:k-1}) = \sum_{i=1}^{N_p} w_{k|k-1}^{(i)} \delta(\boldsymbol{x}_k - \tilde{\boldsymbol{x}}_k^{(i)}). \tag{A.13}$$

To solve the measurement update in (A.3), start with (A.4) and use the previous result to get an approximation as

$$\begin{aligned} \hat{p}(\boldsymbol{y}_k|\boldsymbol{y}_{1:k-1}) &= \int p(\boldsymbol{y}_k|\boldsymbol{x}_k) \sum_{i=1}^{N_p} w_{k|k-1}^{(i)} \delta(\boldsymbol{x}_k - \tilde{\boldsymbol{x}}_k^{(i)})\, d\boldsymbol{x}_k \\ &= \sum_{i=1}^{N_p} w_{k|k-1}^{(i)} p(\boldsymbol{y}_k|\tilde{\boldsymbol{x}}_k^{(i)}). \end{aligned} \tag{A.14}$$

Substituting this into (A.3) yields the approximation of the posterior distribution as

$$\begin{aligned} \hat{p}(\boldsymbol{x}_k|\boldsymbol{y}_{1:k}) = \frac{p(\boldsymbol{y}_k|\boldsymbol{x}_k)\hat{p}(\boldsymbol{x}_k|\boldsymbol{y}_{1:k-1})}{\hat{p}(\boldsymbol{y}_k|\boldsymbol{y}_{1:k-1})} &\approx \sum_{i=1}^{N_p} \frac{w_{k|k-1}^{(i)} p(\boldsymbol{y}_k|\tilde{\boldsymbol{x}}_k^{(i)})}{\hat{p}(\boldsymbol{y}_k|\boldsymbol{y}_{1:k-1})} \delta(\boldsymbol{x}_k - \tilde{\boldsymbol{x}}_k^{(i)}) \\ &\propto \sum_{i=1}^{N_p} w_{k|k}^{(i)} \delta(\boldsymbol{x}_k - \tilde{\boldsymbol{x}}_k^{(i)}). \end{aligned} \tag{A.15}$$

B

Information Matrices for Multiple Components

This appendix provides the derivation and resulting Fisher and hybrid information matrices for the multiple components scenario.

B.1 Fisher Information Matrix for Multiple Components

The observation model for multiple components with a single parameter δ_f denoting the frequency error is given by

$$\boldsymbol{y}(\boldsymbol{\Psi}, \delta_f, \boldsymbol{\Omega}_p) = \boldsymbol{\Delta} \sum_{r=1}^{N_R} \exp\{\chi_r - i\beta_r\} \exp\{-i\boldsymbol{\Omega}_p \boldsymbol{\gamma}_r\} + \boldsymbol{e} \in \mathbb{C}^K \tag{B.1}$$

where N_R is the number of impinging components, and

$$\boldsymbol{\Delta} = \operatorname{diag}\{\exp\{-i\delta_f \boldsymbol{t}\}\}, \tag{B.2}$$

$$\boldsymbol{\Omega}_p = \begin{bmatrix} \boldsymbol{p}_x & \boldsymbol{p}_y & \boldsymbol{p}_z \end{bmatrix} \in \mathbb{R}^{K\times 3}, \tag{B.3}$$

$$\boldsymbol{\Psi} = \begin{bmatrix} \boldsymbol{\psi}_1 & \boldsymbol{\psi}_2 & \dots & \boldsymbol{\psi}_{N_R} \end{bmatrix} \in \mathbb{R}^{4\times R}, \tag{B.4}$$

$$\boldsymbol{\psi}_r = \begin{bmatrix} \alpha_r & \beta_r & \boldsymbol{\gamma}_r^T \end{bmatrix}^T, \tag{B.5}$$

$$\boldsymbol{\gamma}_r = \boldsymbol{f}(\boldsymbol{\mu}_r) = \begin{bmatrix} \cos(\phi_r)\sin(\theta_r) & \sin(\phi_r)\sin(\theta_r) & \cos(\theta_r) \end{bmatrix}^T. \tag{B.6}$$

Since time is excluded from $\boldsymbol{\Omega}_p$ there are only two parameters associated with each component, ϕ and θ, while the frequency error δ_f is common for all components. This is a natural model when the deterministic parameters to be estimated are $\boldsymbol{\Psi}$ together with δ_f and the stochastic parameters are $\boldsymbol{\Omega}_p$ together with $\boldsymbol{t}$.

Assuming that $\boldsymbol{\Omega}_p$ and $\boldsymbol{t}$ are known, the Fisher information matrix $\mathcal{F}(\boldsymbol{\Psi}, \delta_f)$ is defined as

$$-\mathbb{E}_{\boldsymbol{y}|\boldsymbol{\Psi}}\left\{\operatorname{Re}\begin{bmatrix} \frac{\partial^2 \mathcal{L}}{\partial \boldsymbol{\psi}_1 \partial \boldsymbol{\psi}_1^T} & \cdots & \frac{\partial^2 \mathcal{L}}{\partial \boldsymbol{\psi}_1 \partial \boldsymbol{\psi}_{N_R}^T} & \frac{\partial^2 \mathcal{L}}{\partial \boldsymbol{\psi}_1 \partial \delta_f} \\ \vdots & \ddots & \vdots & \vdots \\ \frac{\partial^2 \mathcal{L}}{\partial \boldsymbol{\psi}_{N_R} \partial \boldsymbol{\psi}_1^T} & \cdots & \frac{\partial^2 \mathcal{L}}{\partial \boldsymbol{\psi}_{N_R} \partial \boldsymbol{\psi}_R^T} & \frac{\partial^2 \mathcal{L}}{\partial \boldsymbol{\psi}_{N_R} \partial \delta_f} \\ \frac{\partial^2 \mathcal{L}}{\partial \delta_f \partial \boldsymbol{\psi}_1^T} & \cdots & \frac{\partial^2 \mathcal{L}}{\partial \delta_f \partial \boldsymbol{\psi}_{N_R}^T} & \frac{\partial^2 \mathcal{L}}{\partial \delta_f^2} \end{bmatrix}\right\} \tag{B.7}$$

where

$$-\mathbb{E}_{\boldsymbol{y}|\boldsymbol{\Psi}}\left\{\operatorname{Re}\frac{\partial^2 \mathcal{L}}{\partial \boldsymbol{\psi}_n \partial \boldsymbol{\psi}_m^T}\right\} = 2\operatorname{Re}\begin{bmatrix} \boldsymbol{w}_n^* \boldsymbol{\Sigma}_w^{-1} \boldsymbol{w}_m & -i\boldsymbol{w}_n^* \boldsymbol{\Sigma}_w^{-1} \boldsymbol{w}_m & -i\boldsymbol{w}_n^* \boldsymbol{\Sigma}_w^{-1} \mathbf{W}_m \boldsymbol{\Omega}_p \mathbf{F}_m \\ i\boldsymbol{w}_n^* \boldsymbol{\Sigma}_w^{-1} \boldsymbol{w}_m & \boldsymbol{w}_n^* \boldsymbol{\Sigma}_w^{-1} \boldsymbol{w}_m & \boldsymbol{w}_n^* \boldsymbol{\Sigma}_w^{-1} \mathbf{W}_m \boldsymbol{\Omega}_p \mathbf{F}_m \\ i\mathbf{F}_n^T \boldsymbol{\Omega}_p^T \mathbf{W}_n^* \boldsymbol{\Sigma}_w^{-1} \boldsymbol{w}_m & \mathbf{F}_n^T \boldsymbol{\Omega}_p^T \mathbf{W}_n^* \boldsymbol{\Sigma}_w^{-1} \boldsymbol{w}_m & \mathbf{F}_n^T \boldsymbol{\Omega}_p^T \mathbf{W}_n^* \boldsymbol{\Sigma}_w^{-1} \mathbf{W}_m \boldsymbol{\Omega}_p \mathbf{F}_m \end{bmatrix}, \tag{B.8}$$

with $\boldsymbol{w}_n = \boldsymbol{\Delta} \exp\{\chi_n - i\beta_n\} \exp\{-i\boldsymbol{\Omega}_p \boldsymbol{\gamma}_n\}$, $\mathbf{W}_n = \operatorname{diag}\{\boldsymbol{w}_n\}$, and

$$\mathbf{F}_n = \begin{bmatrix} -\sin(\phi_n)\sin(\theta_n) & \cos(\phi_n)\cos(\theta_n) \\ \cos(\phi_n)\sin(\theta_n) & \sin(\phi_n)\cos(\theta_n) \\ 0 & -\sin(\theta_n) \end{bmatrix} \in \mathbb{R}^{3\times 2}. \tag{B.9}$$

Furthermore,

$$-\mathbb{E}_{\boldsymbol{y}|\boldsymbol{\Psi}}\left\{\operatorname{Re}\frac{\partial^2 \mathcal{L}}{\partial \boldsymbol{\psi}_n \partial \delta_f}\right\} = 2\operatorname{Re}\begin{bmatrix} -i\boldsymbol{w}_n^* \boldsymbol{\Sigma}_w^{-1} \mathbf{T} \sum_r \boldsymbol{w}_r \\ \boldsymbol{w}_n^* \boldsymbol{\Sigma}_w^{-1} \mathbf{T} \sum_r \boldsymbol{w}_r \\ \mathbf{F}_n^T \boldsymbol{\Omega}_p^T \mathbf{W}_n^* \boldsymbol{\Sigma}_w^{-1} \mathbf{T} \sum_r \boldsymbol{w}_r \end{bmatrix}, \tag{B.10}$$

and

$$-\mathbb{E}_{\boldsymbol{y}|\boldsymbol{\Psi}}\left\{\operatorname{Re}\frac{\partial^2 \mathcal{L}}{\partial {\delta_f}^2}\right\} = 2\operatorname{Re}\left\{\sum_r \boldsymbol{w}_r^* \mathbf{T} \boldsymbol{\Sigma}_w^{-1} \mathbf{T} \sum_r \boldsymbol{w}_r\right\}. \tag{B.11}$$

where $\mathbf{T} = \operatorname{diag}\{\boldsymbol{t}\}$. The first line of (B.8) reveals that the amplitude χ_n is decoupled from β_m, $\boldsymbol{\gamma}_m$, and δ_f if $n = m$. All other elements of the FIM are potentially non-zero. Note that the CRLB $\mathcal{F}(\boldsymbol{\Psi}, \delta_f)^{-1}$ is a full matrix.

B.2 Hybrid Information Matrix for Multiple Components

The Hybrid information matrix for the observation model in (B.1) is given by

$$\mathcal{H} = \begin{bmatrix} \mathbf{A} & \mathbf{B} \\ \mathbf{B}^T & \mathbf{C} \end{bmatrix} \tag{B.12}$$

where $\mathbf{A}$ is given by (B.7). Furthermore,

$$\mathbf{B} = -\mathbb{E}_{\boldsymbol{y},\boldsymbol{\Omega}_p|\boldsymbol{\Psi}} \left\{ \mathrm{Re} \begin{bmatrix} \dfrac{\partial^2 \mathcal{L}}{\partial \boldsymbol{\psi}_1 \, \partial \boldsymbol{\Omega}_{p,v}^T} \\ \vdots \\ \dfrac{\partial^2 \mathcal{L}}{\partial \boldsymbol{\psi}_{N_R} \, \partial \boldsymbol{\Omega}_{p,v}^T} \\ \dfrac{\partial^2 \mathcal{L}}{\partial \delta_f \, \partial \boldsymbol{\Omega}_{p,v}^T} \end{bmatrix} \right\} \tag{B.13}$$

where $\boldsymbol{\Omega}_{p,v} = \mathrm{vec}\{\boldsymbol{\Omega}_p\}$,

$$-\mathbb{E}_{\boldsymbol{y},\boldsymbol{\Omega}_p|\boldsymbol{\Psi}} \left\{ \mathrm{Re} \frac{\partial^2 \mathcal{L}}{\partial \boldsymbol{\psi}_n \, \partial \boldsymbol{\Omega}_{p,v}^T} \right\} = 2 \, \mathrm{Re} \left\{ \begin{bmatrix} -i \boldsymbol{w}_n^* \boldsymbol{\Sigma}_w^{-1} \boldsymbol{\Gamma} \\ \boldsymbol{w}_n^* \boldsymbol{\Sigma}_w^{-1} \boldsymbol{\Gamma} \\ \mathbf{F}_n^T \boldsymbol{\Omega}_p^T \mathbf{W}_n^* \boldsymbol{\Sigma}_w^{-1} \boldsymbol{\Gamma} \end{bmatrix} \right\}, \tag{B.14}$$

and $\boldsymbol{\Gamma} = \sum_{r=1}^{N_R} \mathbf{W}_r (\boldsymbol{\gamma}_r^T \otimes \mathbf{I}_K)$ in $\mathbf{B}$. The last element is given by

$$-\mathbb{E}_{\boldsymbol{y},\boldsymbol{\Omega}_p|\boldsymbol{\Psi}} \left\{ \mathrm{Re} \frac{\partial^2 \mathcal{L}}{\partial \delta_f \, \partial \boldsymbol{\Omega}_p^T} \right\} = 2 \, \mathrm{Re} \left\{ \sum_r \boldsymbol{w}_r^* \mathbf{T} \boldsymbol{\Sigma}_w^{-1} \boldsymbol{\Gamma} \right\}. \tag{B.15}$$

Finally, $\mathbf{C}$ is given by

$$\mathbf{C} = -2\mathbb{E}_{\boldsymbol{y},\boldsymbol{\Omega}_p|\boldsymbol{\Psi}} \left\{ \mathrm{Re} \frac{\partial^2 \mathcal{L}}{\partial \boldsymbol{\Omega}_p \, \partial \boldsymbol{\Omega}_p^T} \right\} = 2 \, \mathrm{Re} \left\{ \boldsymbol{\Gamma}^* \boldsymbol{\Sigma}_w^{-1} \boldsymbol{\Gamma} \right\} + \boldsymbol{\Sigma}_\Omega^{-1}. \tag{B.16}$$